STAVEBNÍ OBZOR
ČÍSLO 2/2019

Obsah čísla:

MONITORING DYNAMIC DEFORMATION OF SHUTTLE STEEL SHELVES BY DIGITAL PHOTOGRAPHY

Chengxin Yu[1], Guojian Zhang[2], Xinhua Ding[3], Yongqian Zhao[4] and Guangli Guo[5]

1. *Business School, Shandong Jianzhu University, Fengming Road 1000, 250101 Jinan, Shandong, China; ycx1108@126.com (Corresponding author)*
2. *NASG Key Laboratory of Land Environment and Disaster Monitoring & School of Environmental Science and Spatial Informatics, China University of Mining and Technology, Daxue Road 1, 221116 Xuzhou, Jiangsu, China; g_j_zhang@cumt.edu.cn*
3. *Map Institute of Shandong Province, Jinan, Shandong; 250001, China, email: ding_xin_hua@126.com*
4. *School of Science, Shandong Jianzhu University, Fengming Road 1000, 250101 Jinan, Shandong, China; Yongqian_Zhao@126.com*
5. *NASG Key Laboratory of Land Environment and Disaster Monitoring & School of Environmental Science and Spatial Informatics, China University of Mining and Technology, Daxue Road 1, 221116 Xuzhou, Jiangsu, China; guo_gli@126.com*

ABSTRACT

Shuttle steel shelves (steel shelves equipped with shuttles) are popular in modern logistics. The safety of shuttle steel shelves is an issue due to the complicated dynamic load that develops when the shuttles are in operation. As deformation is an important index of structural safety, this study uses a DPS (digital photography system) based on the PST-IM-MP (photograph scale transformation-image matching-motion parallax) method to monitor shuttle steel shelves: a digital camera (SONY350) was used to monitor the dynamic deformation of shuttle steel shelves when the shuttles began to move, accelerated, moved at constant speed, decelerated and stopped. Then, the deformation trends of the shuttle steel shelves were depicted to study the moving trajectory in a local area. Moreover, we analysed the stresses in the shuttle steel shelves based on these monitoring data. The results showed that the PST-IM-MP method can meet the accuracy requirements in monitoring the dynamic deformation of steel shelves as the maximum and minimum measurement errors were 0.74 pixels and 0.34 pixels in the comprehensive direction, respectively. The shuttle steel shelves were robust because the deformations were elastic and within the allowed10mm. Shear and tension stresses developed in the shuttle steel shelves when the shuttles were in operation. Thus, in the future DPS will become popular for monitoring shuttle steel shelves in real time to warn of possible dangers and mitigate hazards. Additionally, the monitoring data can be used to study the stability of the shuttle steel shelves to improve the related stability design theory.

KEYWORDS

DPS (digital photography system), Shuttle steel shelf, Dynamic deformation, Safety monitoring, PST-IM-MP (photograph scale transformation-image matching-motion parallax) method

INTRODUCTION

As the logistics business grows with the development of society, logistics systems become increasingly important. Warehouse shelves are indispensable equipment for logistics systems and the premise to the normal operation of the logistics systems [1]. Steel shelves are widely used in the storage of warehouse goods due to the high strength, light weight, good ductility and strong earthquake resistance of these shelves. The safety associated with steel shelves is an outstanding problem. Although scholars have studied the stabilities of steel shelf components (shelf columns [2], shelf beams [3] and shelf nodes [4]) and the stabilities of shelves overall [5] by theoretical analyses, structural tests and numerical simulations, and the rich research results have improved the stability design of steel shelf [6]. However, many accidents still occur during the use of steel shelf, especially shuttle steel shelves. The dynamic influences of shuttle operation cause certain areas to develop large wobbles and deformation, which makes traditional steel shelf design theory unable to meet the safety design requirements of shuttle steel shelves [7,8]. Thus, the safety of shuttle steel shelves is an urgent issue that needs to be addressed. Considering that deformation is an important index of structural safety, monitoring the dynamic deformation of shuttle steel shelves in operation is an important way to study this safety problem.

Traditional surveying methods such as use of the level instruments and the total stations can measure the static deformation of a target with high precision but cannot monitor the dynamic deformation over time. Such a task is technically possible for a physical sensor but is practically challenging due to the limited application of physical sensors for local deformation and the vulnerability of sensors in direct contact with the target. GPS (global positioning system) has proved effective in monitoring dynamic deformation [9]. However, the use of this method is restricted indoors because GPS cannot always receive a satellite signal. Although three-dimensional laser scanning has high measurement accuracy in monitoring the global deformation of a static object, this method cannot capture instantaneous dynamic deformation [10]. Digital photography is a non-contact measurement technique that continuously uses a non-metric digital camera to photograph an object to record its global and local dynamic deformation of the object over time.

Digital photography has been used to monitor the dynamic deformation of engineering structures such as masonry walls [11], bridge structures [12] and steel structures [13]. Certain researchers used digital photography to monitor the vibration deformation of steel shelves [1]. These examples suggest that using digital photography is feasible for monitoring dynamic deformation of shuttle steel shelves to study the safety issues when the shuttles are in operation.

The aim of this study is to use digital photography to monitor dynamic deformation of shuttle steel shelves over time when the shuttles are in operation. Real-time deformation trends depicted by a DPS (digital photography system) are used to assess the safety of shelves on site and to give timely warning of possible dangers. Moreover, the monitoring data is provided to facilitate the study of the stability of shuttle steel shelves to improve the design theory of these shelves.

DOI 10.14311/CEJ.2019.02.0012

DIGITAL PHOTOGRAPHY SYSTEM

The DPS (digital photography system) consists of hardware (a SONY350 camera and a computer) and software (data processing software for steel shelves). The key techniques of the DPS are detailed in the following sections.

Accuracy assessment of the digital camera

A Sony350 camera is used in this study. The view and parameters of the camera are showed in Figure 1 and Table 1, respectively. The distortion of the camera in the photographic system plays a major role in the measurement accuracy [14]. Assuming that the digital camera and the object do not move during testing, research shows that the distortion errors are linear near the centers of the resulting images. Thus, we adopt a grid method in the study to eliminate the distortion of the digital camera [15].

(a) *(b)* *(c)*

Fig.1 - Images of the Sony350 camera

Tab. 1 - Parameters of the Sony-350 camera

Type	Ser	Sensor sc	Focal lengt	Active pixels
Sony DSLR A350 (Sony-350)	C(	23.5×15.7	35mm (27-3	4592×3056 pixe

After correcting the distortion, we used the direct linear transformation (DLT) method [16,17] to assess the measurement accuracy of the digital camera:

(1) the forward: we use the spatial and pixel coordinates of reference points C_0-C_7 (in Table 2 of [18]) to solve for the coefficient between the spatial coordinates and pixel coordinates of the points in the photo;

(2) the inversion: we use the coefficient between the spatial coordinates and pixel coordinates of the points (in Table 3 of [18]) in the photo and the pixel coordinates of the points on the photographs to be solved for determining the spatial coordinates. Note that at least two photographs from different positions had to be taken to compute spatial coordinates for accuracy test.

Based on the relative data (in Table 2) and Equation (1), we obtain the measurement accuracy (in Table 3) of the digital camera:

$$\delta = \sqrt{\frac{[\Delta\Delta]}{n}} \tag{1}$$

where Δ is the true error, n is the number of true errors, and δ is the mean squared error.

In Table 3, the mean squared error of the Sony350 camera is 0.58mm. This result suggests that the camera used in this study meets the accuracy requirements for deformation observation. In Table 2, L represents the differences between the actual coordinates and the calculated coordinates of the deformation points. In Table 3, E (L) represents the mathematically expected value of L, and Δ is equal to E (L) minus L. Leica TM30 measurement robot was used to monitor 3D-coordinates of the necessary points. The angular accuracy and ranging accuracy of Leica TM30 are 0.5 seconds and 0.6mm+1ppm, respectively. In the test, the ranging accuracy of this measurement robot is approximately 0.6mm because the measuring distance is short.

Tab. 2- Spatial coordinates of deformation points U0 and U1

Name	Actual coordinates/r	Calculated coordinates/r	Differences(L)/mm
U0-X	108.8250	108.8260	1.0
U0-Y	95.8870	95.8880	1.0
U0-Z	99.4410	99.4400	1.0
U1-X	109.0670	109.0650	2.0
U1-Y	96.9350	96.9340	1.0
U1-Z	99.3940	99.3940	0.0

Tab. 3- Accuracy assessments of the digital camera/mm

L	1.0	1.0	1.0	2.0	1.0	0.0
E (L)	1.0					
Δ	0.0	0.0	0.0	-1.0	0.0	1.0
δ	0.58					

Photograph scale transformation-motion parallax method

The motion parallax method uses a camera to photograph an object before and after deformation to obtain the zero and successive images. The camera is in the same position and the optical axis of the camera is perpendicular to the object during measurement. The zero and successive images should be obtained with the same internal and external orientation elements. However, the internal and external orientation elements are always changing during the measurement process. Sometimes we cannot ignore the influence of this phenomenon on the coordinates of the image points. Then, the image matching-motion parallax (IM-MP) method is used to correct the influence of this phenomenon on the measurement results and to improve the measurement accuracy. However, sometimes the reference points and the deformation points are not on the same plane. Thus, this paper provides the photograph scale transformation-image matching-motion parallax method (PST-IM-MP) method to solve this problem.

In Figure 2 (a), we assume that point a (x_1^d, z_1^d) and point b (x_2^d, z_2^d) are the coordinates of the same deformation point on the zero and successive images, respectively. (dx_1^d, dz_1^d) and (dx_2^d, dz_2^d) are the systematic errors of the corresponding deformation point on the zero and

successive images, respectively. $(\Delta p_x^d, \Delta p_z^d)$ are the parallaxes of the deformation point on the image plane. Equation (2) can be expressed as:

$$\left.\begin{aligned}(x_2^d - x_1^d) - (dx_2^d - dx_1^d) - \Delta p_x^d = 0\\ (z_2^d - z_1^d) - (dz_2^d - dz_1^d) - \Delta p_z^d = 0\end{aligned}\right\} \quad (2)$$

On the object plane, Δx^d and Δz^d of the corresponding deformation point are:

$$\left.\begin{aligned}\Delta x^d = m \cdot \Delta p_x^d\\ \Delta z^d = m \cdot \Delta p_z^d\end{aligned}\right\} \quad (3)$$

where m is the photograph scale on the reference plane and Δx^d and Δz^d are the horizontal and vertical deformations of the deformation point on the object plane. Δp_x^d and Δp_z^d are the horizontal and vertical parallaxes of the corresponding image point on the image plane. Note that there are systematic errors in Δp_x^d and Δp_z^d .

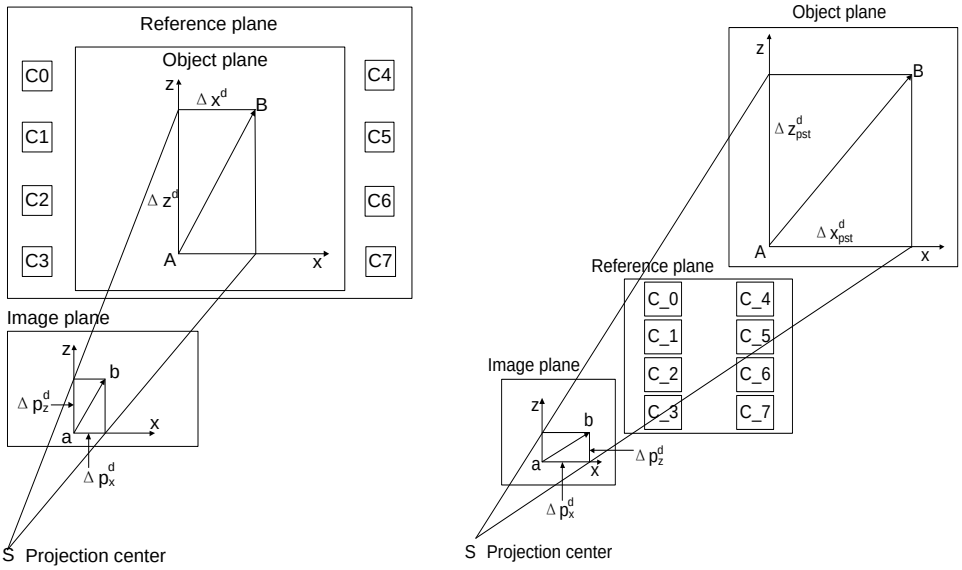

(a) Principle of the IM-MP method (b) Principle of the PST-IM-MP method

Fig. 2 - Principles of image matching- time baseline parallax

For the reference points, Equation (2) can be expressed as：

$$\left.\begin{aligned}(x_2^r - x_1^r) - (dx_2^r - dx_1^r) = 0\\ (z_2^r - z_1^r) - (dz_2^r - dz_1^r) = 0\end{aligned}\right\} \quad (4)$$

where (x_1^r, z_1^r) and (x_2^r, z_2^r) are the coordinates of the same reference point on the zero and successive images, respectively. (dx_1^r, dz_1^r) and (dx_2^r, dz_2^r) are systematic errors of the corresponding reference point on the zero and successive images, respectively.

Δp_x^r [17] is the parallax of the reference point, and the equation for this term can be expressed as:

$$\left.\begin{aligned} \Delta p_x^r &= (x_2^r - x_1^r) = (dx_2^r - dx_1^r) = \Delta p_x^{r0} + \delta p_x^r \\ \Delta p_x^{r0} &= (-\frac{\Delta Z_S}{Z} - \frac{\Delta f}{f})x_1^r + \Delta\kappa z_1^r + (-\frac{f}{Z}\Delta X_S - f\Delta\varphi - \Delta x_0) - \frac{x_1^{r2}}{f}\Delta\varphi - \frac{x_1^r z_1^r}{f}\Delta\omega \\ \delta p_x^r &= -(\frac{\Delta p_x^r dZ_{S2}}{Z}) - \frac{2\Delta p_x^r x_1^r}{f}d\varphi_2 - \frac{\Delta p_x^r z_1^r}{f}d\omega_2 - \frac{\Delta p_z^r x_1^r}{f}d\omega_2 + \Delta p_z^r d\kappa_2 - \frac{df_2}{f}\Delta p_z^r \end{aligned}\right\} \quad (5)$$

where $(X_S, Z_S, \varphi, \omega, \kappa, f, x_0)$ are the internal and external orientation elements of the zero and successive images and $(\Delta X_S, \Delta Z_S, \Delta\varphi, \Delta\omega, \Delta\kappa, \Delta f, \Delta x_0)$ are the changes in the internal and external orientation elements of the successive image relative to the zero image. Δp_x^{r0} is the function of the reference point coordinates on the image plane, $(dZ_{S2}, d\varphi_2, d\omega_2, d\kappa_2, df_2)$ are the internal and external orientation elements of the successive image themselves, $(\Delta p_x^r, \Delta p_z^r)$ are the parallax of reference points on the image plane, and δp_x^r is the parallax caused by the errors of the internal and external orientation elements of the images themselves and $(\Delta p_x^r, \Delta p_z^r)$.

Δp_x^{r0} can also be expressed as Equation (6):

$$\Delta p_x^{r0} = a_x x^r + b_x z^r + c_x + d_x x^{r2} + e_x x^r z^r \quad (6)$$

where $a_x = -\frac{\Delta Z_S}{Z} - \frac{\Delta f}{f}$, $b_x = \Delta\kappa$, $c_x = -\frac{f}{Z}\Delta X_S - f\Delta\varphi - \Delta x_0$, $d_x = -\frac{\Delta\varphi}{f}$, $d_x = -\frac{\Delta\omega}{f}$, (a_x, b_x) and (a_z, b_z) are the parallax coefficients in the X- and Z-direction respectively, (c_x, d_x) are the constant parallax coefficients in the X- and Z-direction respectively, and (x^r, z^r) are the coordinates of the reference points on the image plane.

As $(\Delta p_x^{r0}, \Delta p_z^{r0})$ are tiny amounts, their quadratic terms are negligible, and Equation (7) is obtained:

$$\left.\begin{aligned} \Delta p_x^{r0} &= a_x x^r + b_x z^r + c_x \\ \Delta p_z^{r0} &= a_z x^r + b_z z^r + c_z \end{aligned}\right\} \quad (7)$$

In this case, we only need three or more reference points to obtain (a_x, b_x, c_x) and (a_z, b_z, c_z). After barycentralizing the image point coordinates, we obtain the coordinates $(x^r{}', z^r{}')$ and the systematic error $(\Delta p_x^{r0}{}', \Delta p_z^{r0}{}')$ of the reference point in the barycentric coordinate system. Equation (8) is obtained when $(\Delta p_x^{r0}{}', \Delta p_z^{r0}{}')$ only have random errors:

$$\left.\begin{aligned} \Delta p_x^{r0}{}' &= a_x x^r{}' + b_x z^r{}' \\ \Delta p_z^{r0}{}' &= a_z x^r{}' + b_z z^r{}' \end{aligned}\right\} \quad (8)$$

Based on the error equation of (8), we obtain the parallax coefficients (a_x, b_x) and (a_z, b_z) of the image point in the X- and Z-direction, respectively. Then, we obtain the systematic errors of the deformation points:

$$\left.\begin{aligned} \Delta p_x^{d0}{}' &= a_x x^d{}' + b_x z^d{}' \\ \Delta p_z^{d0}{}' &= a_z x^d{}' + b_z z^d{}' \end{aligned}\right\} \quad (9)$$

where (x^d', z^d') and $(\Delta p_x^{d0}', \Delta p_z^{d0}')$ are the coordinates and the systematic error of the deformation point in the barycentric coordinate system, respectively.

Then, the corrected parallaxes of the corresponding deformation points are obtained:

$$\left.\begin{aligned} c\Delta p_x^d' &= \Delta p_x^d' - \Delta p_x^{d0}' \\ c\Delta p_z^d' &= \Delta p_z^d' - \Delta p_z^{d0}' \end{aligned}\right\} \quad (10)$$

where $(c\Delta p_x^d', c\Delta p_z^d')$ are the corrected parallaxes of the deformation points in the barycentric coordinate system.

Then, we obtain the corrected displacements of the deformation points based on the reference plane:

$$\left.\begin{aligned} c\Delta x^d &= m \cdot c\Delta p_x^d' \\ c\Delta z^d &= m \cdot c\Delta p_z^d' \end{aligned}\right\} \quad (11)$$

where $(c\Delta x^d, c\Delta z^d)$ are the corrected displacements of the deformation points based on the reference plane

Based on the photograph scale transformation principle [18], we obtain the real displacements on the object plane of a deformation point:

$$\left.\begin{aligned} \Delta x_{pst}^d &= \Delta pstc \cdot c\Delta x^d \\ \Delta z_{pst}^d &= \Delta pstc \cdot c\Delta z^d \end{aligned}\right\} \quad (12)$$

where Δx_{pst}^d and Δz_{pst}^d are the real displacements on the object plane of a deformation point, and $\Delta pstc$ is the coefficient of the photograph scale transformation

Note that the PST-IM-MP method is the IM-MP method when $\Delta pstc$ is equal to 1.

SHUTTLE STEEL SHELF TESTS

Test process

Figure 3 shows the test field of the steel shelf. Before the test, the camera was set 5m from the steel shelf and was levelled. Moreover, we adjusted the camera parameters (focal length 35mm) and turned on the flash to obtain a clear image. Deformation points labelled U0-U5 were set on the columns of the steel shelf where monitoring was needed. The reference system should not be influenced by the shuttles. Therefore, we selected another small steel shelf and set reference points labelled C0-C5 on the shelf to form the reference system. Furthermore, the direction photographed was perpendicular to the reference system and the columns of steel shelf. In addition, the shuttles labelled S1-S3 were mounted on the corresponding tracks. For convenience, we define the direction photographed as north (in Figure 3 (b)).

Note that in the test the reference plane is very close to the object plane. The deformation points and the reference points can be considered to be on the same plane. Thus, in this paper, $\Delta pstc$ is approximately equal to 1.

The testing process is detailed as follows: First, before the shuttles moved the SONY350 camera was used to photograph the steel shelf as a zero image (the reference image).

Second, the camera was used to photograph the steel shelf in successive images when the shuttles S2 and S3 began to move, accelerated, moved at constant speed, decelerated and stopped from the south to the north.

Third, the camera was used to photograph the steel shelf in successive images when the shuttles S2 and S3 began to move, accelerated, moved at constant speed, decelerated and stopped from the north to the south.

Last, thirteen successive images were obtained. In this paper, we define photographing the steel shelf one time as one test. Thus, we completed thirteen tests and obtained the relative deformation of the steel shelf in operation thirteen times.

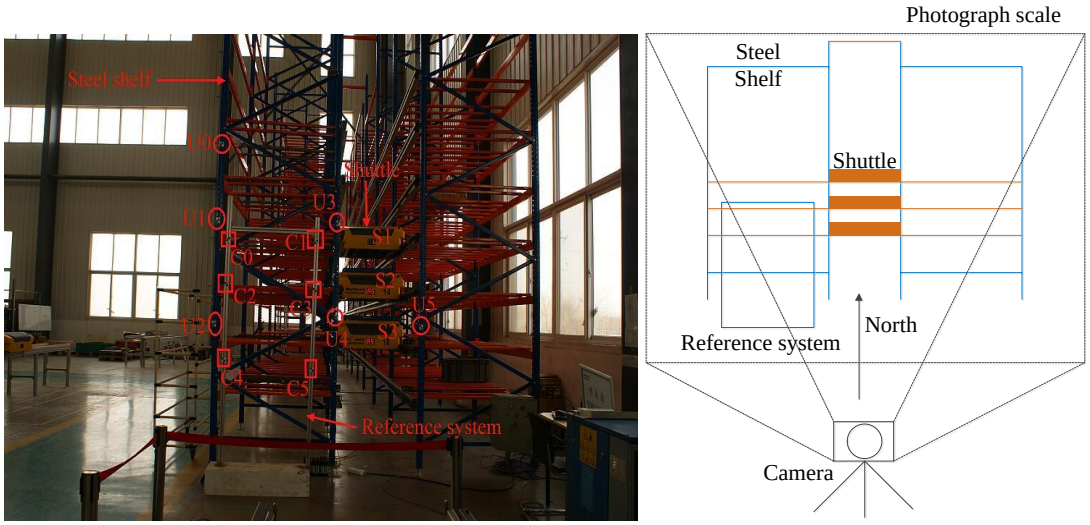

(a) Front view of the test field (taken by Yongqian Zhao)

(b) Relative positions of the camera and steel shelf

Fig. 3 - Test field of the steel shelf

Test results and analysis

In the tests, the pixel displacements of the reference points were zero in theory. However, the pixel displacements of the reference points were not zero in the PST-IM-MP method. As such, these values were considered to be the measurement accuracies of the PST-IM-MP method.

Through data processing, the measurement accuracy of the PST-IM-MP method (Table 4) and deformation values of the deformation points (Table 5) were obtained. In Table 4, |X| represents the absolute value of the measurement accuracy in the X-direction, |Z| represents the absolute value of measurement accuracy in the Z-direction, and CD represents the absolute value of measurement accuracy in the comprehensive direction. The measurement accuracy of

the PST-IM-MP method reaches the sub-pixel level. The maximum and minimum average measurement errors are 0.63 pixels and 0.10 pixels in the X-direction, respectively, 0.37 pixels and 0.28 pixels in the Z-direction, respectively, 0.74 pixels and 0.34 pixels in the comprehensive direction, respectively. The photograph scale is 1.11mm/pixel in the reference system. Note that in this paper, we use the pixel displacements of all six reference points to reflect the measurement accuracy of the PST-IM-MP method. In consideration of space in the civil engineering journal of publication, only a selection of data are shown in Table 4.

In Table 5, the positive and negative X represent the deformation points moving right and left, respectively. The positive and negative Z represent the deformation points moving up and down, respectively. To study visually the stability of the shuttle steel shelves, the deformation trends (Figure 4) were depicted by DPS. Figure 4 clearly shows the maximum deformation, the minimum deformation and the movement trajectory of each deformation point in the X-, Z- and comprehensive directions. Moreover, the deformations of U0-U5 are elastic, and within the allowed deviation (10mm) [19]. These results suggest that the steel shelves are safe.

Tab. 4 - Measurement accuracies/pixel

Test	C0			C1			C2			C3		
	|X|	|Z|	CD	|X|	|Z|	CD	|X|	|Z|	CD	|X|	|Z|	CD
1	0.51	0.02	0.51	0.2	0.77	0.80	0.37	0.37	0.52	0.04	0.04	0.06
2	0.52	0.23	0.57	0.21	0.22	0.30	0.37	0.33	0.50	0.04	0.33	0.33
3	0.99	0.22	1.01	0.01	0.3	0.30	0.01	0.41	0.41	0.00	0.24	0.24
4	0.52	0.59	0.79	0.21	0.77	0.80	0.37	0.55	0.66	0.04	0.87	0.87
5	0.52	0.12	0.53	0.21	0.93	0.95	0.37	0.12	0.39	0.03	0.20	0.20
6	0.99	0.12	1.00	0.01	0.06	0.06	0.01	0.12	0.12	0.00	0.20	0.20
7	0.51	0.88	1.02	0.21	0.93	0.95	0.37	0.12	0.39	0.03	0.20	0.20
8	0.42	0.49	0.65	0.42	0.02	0.42	0.37	0.74	0.83	0.38	0.08	0.39
9	0.62	0.01	0.62	0.03	0.23	0.23	0.33	0.37	0.50	0.01	0.04	0.04
10	0.52	0.12	0.53	0.21	0.01	0.21	0.37	0.08	0.38	0.03	0.08	0.09
11	0.99	0.22	1.01	0.01	0.3	0.30	0.01	0.58	0.58	0.00	0.24	0.24
12	0.13	0.12	0.18	0.13	0.06	0.14	0.3	0.12	0.32	0.70	0.20	0.73
13	0.99	0.59	1.15	0.01	0.22	0.22	0.01	0.45	0.45	0.00	0.87	0.87
Avera	0.63	0.29	0.74	0.14	0.37	0.44	0.25	0.34	0.47	0.10	0.28	0.34

Tab. 5- Pixel displacements of U0-U5/pixel

Test	U0		U1		U2		U3		U4		U5	
	X	Z	X	Z	X	Z	X	Z	X	Z	X	Z
1	0.24	0.58	0.00	1.33	-1.35	0.06	1.49	-0.43	0.08	-0.06	-0.13	-0.57
2	1.24	1.10	0.00	0.57	-0.36	-0.09	1.49	1.26	0.08	0.30	0.86	0.09
3	0.46	0.88	-0.50	0.97	-0.50	1.15	1.06	0.62	-0.04	0.42	0.12	0.25
4	0.36	0.44	-0.86	0.78	-1.23	1.29	0.26	-0.04	-0.18	0.05	-0.35	0.56
5	1.35	-0.36	0.13	0.05	-1.23	0.66	1.26	0.22	-0.18	-0.60	-0.35	-0.08
6	-0.53	0.64	-0.50	0.05	-1.49	0.66	0.06	0.22	-0.04	0.39	0.12	-0.08
7	1.35	0.64	0.13	0.05	-0.24	0.66	1.26	0.22	-0.18	-0.60	-0.35	-0.08
8	-0.52	0.68	-1.15	0.71	-0.70	-0.2	0.38	1.35	-0.31	0.08	-0.13	-0.10
9	-1.00	1.58	-0.92	1.33	-1.85	0.06	1.08	0.56	0.05	-0.06	0.53	-0.57
10	1.46	1.33	0.25	0.41	-0.11	0.56	0.03	0.16	-1.43	-1.08	-1.56	-0.90
11	-0.53	1.99	-0.50	1.10	-0.50	1.27	1.06	-0.6	-0.04	0.16	0.11	-0.97
12	-0.72	0.64	-1.41	1.05	-1.06	0.66	0.12	0.22	-0.66	0.39	0.51	-0.08
13	-0.53	0.44	-0.50	0.78	-0.50	0.30	1.06	0.95	-0.04	0.05	0.12	-0.43

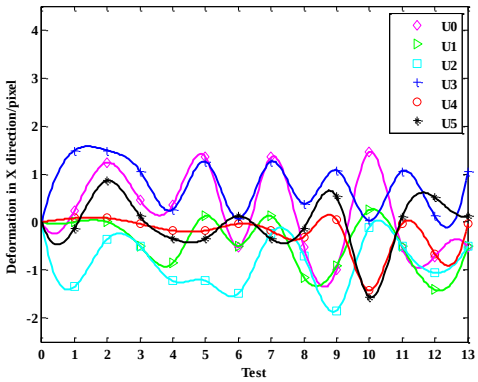

(a)deformation in the X-direction

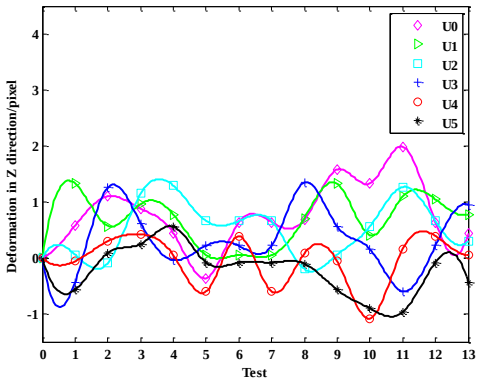

(b) deformation in the Z-direction

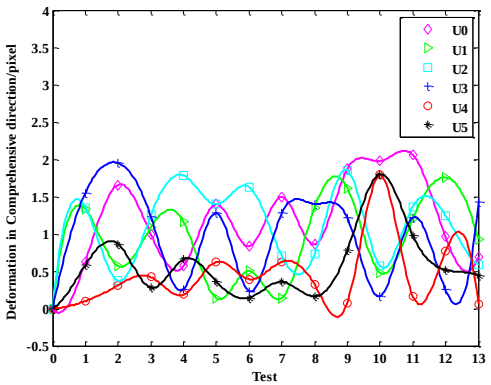

(c) deformation in the comprehensive direction

Fig. 4 - Deformation trends of the shuttle steel shelves

As the maximum deformation is the key to study the stability of the steel shelf, we analyse the maximum deformations of U0-U5 in the X-, Z- and comprehensive directions: U0 moved

right 1.46 pixels in test 10, up 1.99 pixels in test 11, and 2.06 pixels in the comprehensive direction in test 11. U1 moved left 1.41 pixels in test 12, up 1.33 pixels in tests 1 and 9, and 1.76 pixels in the comprehensive direction in test 12. U2 moved left 1.85 pixels in test 9, up 1.29 pixels in test 4, and 1.85 pixels in the comprehensive direction in test 9. U3 moved right 1.49 pixels in tests 1 and 2, up 1.35 pixels in test 8, and 1.95 pixels in the comprehensive direction in test 2. U4 moved left 1.43 pixels, down 1.08 pixels, and 1.79 pixels in the comprehensive direction in test 10. U5 moved left 1.56 pixels in test 10, down 0.97 pixels in test 11, and 1.80 pixels in the comprehensive direction in test 10.

Thus, it is necessary to further analyse the operation situations of the shuttle steel shelves in tests 1, 2, 4, 8, 9, 10, 11 and 12. Figure 3 shows the locations of the deformation points on the columns before (the red circles) and after (the blue asterisks) the tests. The changes in the locations of deformation points directly reflect the operational situations of the steel shelves. In Figure 3, the red lines represent the original locations of the columns. The blue curves represent the locations of the corresponding columns after the tests. The arrows represent the movement directions of the deformation points. The distances between the columns and the lengths of the column decrease by certain proportions.

Figure 5 (a) shows the changes in the locations of the deformation points when the shuttles began to move from the south side. Strong tensile stress developed between column 1 and column 2 because U2 moved left 1.35 pixels and U3 moved right 1.49 pixels. Strong shear stress developed between U1 and U2 because U2 moved left 1.35 pixels and U1 remained in the same location.

Figure 5 (b) shows the changes in the locations of the deformation points when the shuttles accelerated from the south to the north. Strong shear stress developed between U0 and U1 because U0 moved right 1.24 pixels and U1 remained in the same location. Strong tensile stress developed between column 1 and column 2 because U1 remained in the same location and U3 moved right 1.49 pixels. Strong tensile stress developed between column 2 and column 3 because U4 moved right 0.08 pixels and U5 moved right 0.86 pixels.

Figure 5 (c), (d) and (e) shows the changes in the locations of the deformation points when the shuttles decelerated from the south to the north, accelerated from the north to the south and moved at constant speed from the north to the south, respectively. Strong tensile stresses also developed between column1 and column2 in these tests.

Figure 5 (f) shows the changes in the locations of the deformation points at the moment when the shuttles decelerated from the north to the south. Strong shear stress developed between U0 and U1. Strong compressive stress developed between column 1 and column 2 due to U4 moving left 1.43 pixels and U3 moving right 0.03 pixels. Moreover, U4 and U5 were more stable than the other deformation points because these points were on the bottom of the shuttle steel shelves. However, U4 and U5 developed more deformation in test 10 when the shuttle decelerated from the north to the south. U4 and U5 moved down 1.08 pixels and 0.97 pixels, respectively. These points also moved left 1.43 pixels and 1.56 pixels, respectively. These results suggests that the bottoms of the shuttle steel shelves bear high impacts when the shuttle decelerates. In turn, deceleration makes the top left corner of the shuttle steel shelves wobble strongly, such as U0 moving right 1.46 pixels and up 1.33 pixels.

Figure 5 (g) and (h) shows the changes in the locations of the deformation points when the shuttles decelerated from the north to the south. Strong tensile stresses developed between column 1 and column 2 in tests 11 and 12. In test 12, tensile stress developed between column 2 and column 3.

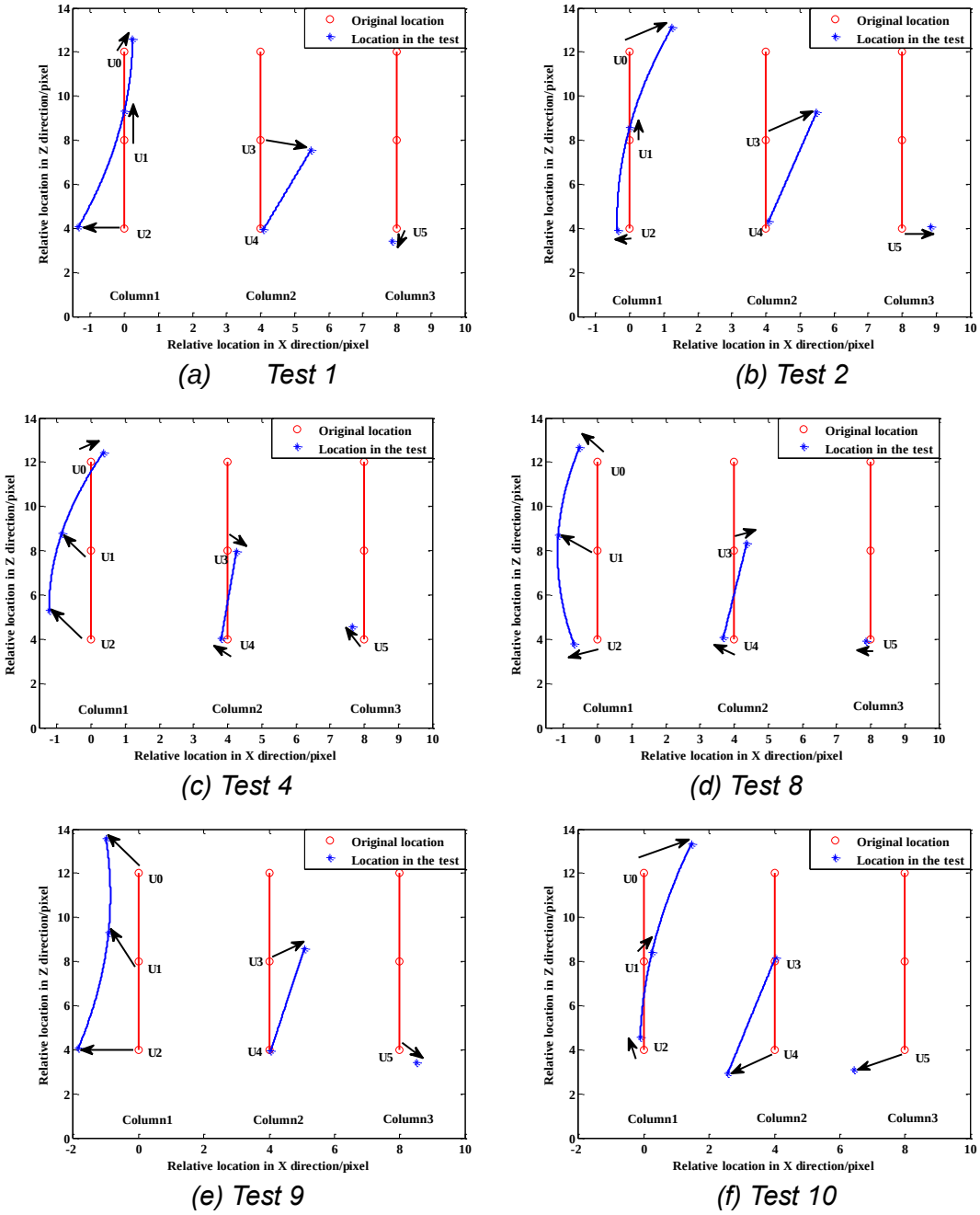

Fig. 5 - Changes in the locations of the deformation points

DOI 10.14311/CEJ.2019.02.0012

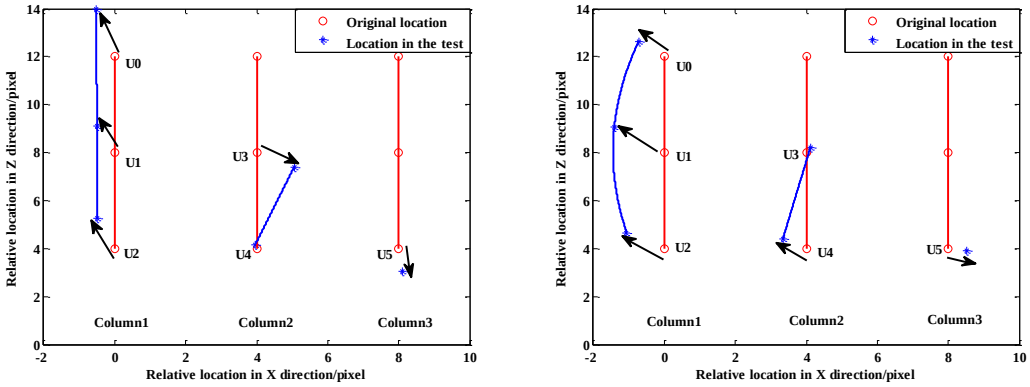

(g) Test 11 *(h) Test 12*

Fig. 5 - Changes in the locations of the deformation points

In conclusion, the stresses on the shelves are complicated when the shuttles are in operation. The beams between the columns bear the tension and shear caused by the shuttle movement, which is different from traditional steel shelves. If the shelves were full and the components were in extreme equilibrium, the tension and shear caused by the shuttle movement would cause the beams to yield and result in damage to the steel shelf or even in collapse. Moreover, only two shuttles were in operation in the test. The stresses on the shelves would be more complicated if the shuttle steel shelves were normally used as multiple shuttles would be in operation. Thus, a DPS can be used to monitor the safety of shuttle steel shelves and depict their deformation trends in real time. A DPS can warn of possible dangers and mitigate hazards based on these real-time deformation trends. Furthermore, the data from the DPS in this study can be used to study the stability of shuttle steel shelves to improve the stability of their design.

CONCLUSION

This study used a DPS (digital photography system) to monitor the dynamic deformation of shuttle steel shelves to warn of possible dangers and mitigate hazards when the shuttles were in operation. The PST-IM-MP (photograph scale transformation-image matching-motion parallax) method was used to process these images over time. The stresses in the shuttle steel shelves were analysed based on the data. The conclusions from the study are the following:

(1) The measurement accuracy of the PST-IM-MP method reaches the sub-pixel level because the maximum and minimum measurement errors are 0.63 pixels and 0.10 pixels in the X-direction, respectively, 0.37 pixels and 0.28 pixels in the Z-direction, respectively, and 0.74 pixels and 0.34 pixels in the comprehensive direction, respectively.

(2) The beams between the columns bear the tension and shear stresses caused by the shuttle movement, which differs from the response of traditional steel shelves.

(3) The top left of the shuttle steel shelf wobbles more than other positions when the shuttles are in operation.

(4) The bottoms of the shuttle steel shelves bears high impacts when the shuttles decelerate. In turn, deceleration makes the top left corner of the steel shelf wobble strongly.

(5) The shuttle steel shelves are robust as the deformations of the shelves are elastic and within the allowed10mm.

(6) The DPS in this study can monitor dynamic deformations of shuttle steel shelves in real time to warn of possible dangers and mitigate hazards.

As the dynamic deformation data of shuttle steel shelves in operation is of great importance in the safety related to the shelves, it is essential to use a DPS to monitor the dynamic deformation of the shuttle steel shelves during operation. The DPS can process the images and depict the deformation trends over time, which can be used to warn of possible dangers on site and mitigate hazards. Thus, DPS will be popular in monitoring the safety of shuttle steel shelves in operation in the future and will provide data support to improve the stability design of shuttle steel shelves.

ACKNOWLEDGMENTS

This study was supported by Postgraduate Research & Practice Innovation Program of Jiangsu Province (Grant No.: KYCX19_2162)，the National Key Research and Development Program (2018YFC0604704), the Science and Technology Project of the Shandong Province of China (Grant No. 2010GZX20125), PhD research fund project of Shandong Jianzhu University, 2016 (Grant No. XNBS1635) and the Science and Technology Project of Shandong's Department of Housing and Urban-rural Construction (Grant No. 2017-K2-001). The funders Chengxin Yu and Yongqian Zhao were involved in the writing, editing, and approval of the manuscript and decision to publish this paper.

REFERENCES

[1] Yu CX, Ding XH, Chen MZ, Xiao P (2013) The Application of Digital Cameras in Monitoring Dynamic Deformation of Steel Shelf. Applied Mechanics & Materials 405-408:873-877
[2] Kwon YB, Hancock GJ (1992) Tests of Cold-Formed Channels with Local and Distortional Buckling. Journal of Structural Engineering 118 (7):1786-1803
[3] Chen B, Yin ZJ, Yang J, Wang CY (2011) Integration Research for Steel Shelf CAD/CAE Calculation and Analysis System. Advanced Materials Research 243-249:6154-6158
[4] Gilbert BP, Rasmussen KJR (2011) Determination of the base plate stiffness and strength of steel storage racks. Journal of Constructional Steel Research 67 (6):1031-1041
[5] Aguirre C (2005) Seismic behavior of rack structures. Journal of Constructional Steel Research 61 (5):607-624
[6] White DW, Hajjar JF (1997) Accuracy and simplicity of alternative procedures for stability design of steel frames. Journal of Constructional Steel Research 42 (3):209-261
[7] Tian Qiu (2016) Analysis of the loading capacity and seismic resistance and the motion of the shuttle bus of automated warehouse. Master' thesis, Kunming University of Science and Technology. (in Chinese)
[8] Yongqian Zhao (2016) Research on the stability and deformation monitoring of the dense channels accessing-sorting racks system. PhD thesis, Shandong University. (in Chinese)
[9] Lovse JW, Teskey WF, Lachapelle G, Cannon ME (1995) Dynamic Deformation Monitoring of Tall Structure Using GPS Technology. Journal of Surveying Engineering 121 (1):35-40
[10] Ma DL, Cui J, Wang SY (2014) Application and Research of 3D Laser Scanning Technology in Steel Structure Installation and Deformation Monitoring. Applied Mechanics & Materials 580-583:2838-2841
[11] Ghorbani R, Matta F, Sutton MA (2015) Full-Field Deformation Measurement and Crack Mapping on Confined Masonry Walls Using Digital Image Correlation. Experimental Mechanics 55 (1):227-243
[12] Jiang R, Jauregui DV (2010) Development of a digital close-range photogrammetric bridge deflection measurement system. Measurement 43 (10):1431-1438
[13] Yu CX, Xia X, Qin FH, Xiao P (2014) The Application of Digital Photography Techniques in

Structure Deformation Measurement. Applied Mechanics & Materials 475-476:204-208
[14] Yanagi H, Chikatsu H (2012) Factors and Estimation of Accuracy in Digital Close Range Photogrammetry using Digital Cameras. Journal of the Japan Society of Photogrammetry 50 (1):4-17
[15] Zhang G, Guo G, Li L, Yu C (2018) Study on the dynamic properties of a suspended bridge using monocular digital photography to monitor the bridge dynamic deformation. Journal of Civil Structural Health Monitoring 8 (2):1-13
[16] Zhang G, Guo G, Yu C, Li L (2018) Monitoring dynamic global deflection of a bridge by monocular digital photography. Civil Engineering Journal 27 (2):168-182. doi:10.14311/CEJ.2018.02.0014
[17] Shapiro, R. (1978). Direct linear transformation method for three-dimensional cinematography. Res. Quart. 49, 197-205.
[18] Zhang G, Guo G, Yu C, Li L, Hu S, Wang X (2018) Monitoring Instantaneous Dynamic Displacements of Masonry Walls in Seismic Oscillation Outdoors by Monocular Digital Photography. Mathematical Problems in Engineering 2018. doi:10.1155/2018/4316087
[19] Institute RM (2012) Specification for the Design, Testing, and Utilization of Industrial Steel Storage Racks. Springer Netherlands.

Article no. 13

THE CIVIL ENGINEERING JOURNAL 2-2019

BENDING FATIGUE PROPERITIES RESEARCH OF POLYURETHANE CEMENT (PUC)

Kexin Zhang[1,2], Quansheng Sun[2]

1. *School of Transportation Engineering, Shenyang Jianzhu University, Shenyang,110168, China; zkx0204@yahoo.com*
2. *School of Civil Engineering, Northeast Forestry University, Harbin, 150040, China; hrbsqs@126.com*

ABSTRACT

In order to study the fatigue properties of polyurethane cement (PUC), the newly bridge reinforcement material, three different densities of PUC beams were tested. The studies indicate that the fatigue life of PUC material obeys two parameters Weibull distribution, and the double logarithm fatigue equation with different failure probability is established by this mathematical model. The fatigue life equations of the PUC with three different densities (PUC1500, PUC1200 and PUC800) were established when the failure rate was 0.5. The fatigue life of PUC1500 is the largest, and the fatigue life of PUC material decreases with the decrease of its density. Under the action of bending fatigue load, the fatigue strain of PUC material can be divided into three phases.

KEYWORDS

Polyurethane Cement (PUC), Fatigue, Bending, Four-point Loading, Weibull Distribution, Failure Probability

INTRODUCTION

The availability of many tests and the number of projects demonstrate that the use of polyurethane cement (PUC) materials to strengthen bridge structures is becoming a feasible technique [1-6]. PUC material can make the repair or retro-fitting of bridge elements more effective, easier to handle, and cheaper because of its very simple method of implementation and its excellent properties and flexural behaviour [1].

Usually polyurethane cement (PUC) material is a new type of composite material, with light weight, high strength, high toughness and good bonding performance [2-3]. In previous studies, ordinary Portland cement is used as filler and polyurethane raw material is used as cementing material. PUC has excellent bonding for the retrofitting of beams. Ten pieces of reinforced concrete beams were tested and studied by Haleem [1]. The external strengthened beams with PUC material showed an increase in the ultimate load. The maximum load capacity of retrofitted specimens reached values of about 170% comparing with control beam. Moreover, cracks were reduced around 58% comparing with control beam at the maximum applied load stage of control beam. To investigate the feasibility of the PUC-strengthened bridge, load tests were conducted before and after strengthening. The results of concrete strain and deflection show that the capacity of the repaired bridge, including the bending strength and stiffness, is enhanced [2]. The crack width measurement also indicates that this technique could increase the durability of the bridge. The PUC material is used as the embedded material of steel wire ropes in reinforcement [5], and the results showed significantly enhanced strength, stiffness, and ability to constrain cracks. The PUC also increases the durability of the steel wire ropes and promotes secure anchoring.

Nevertheless, a majority of previous studies were focused on the static performance between strength and density of the PUC material. In recent literatures, no studies were reported with

respect to the flexural fatigue behaviour of PUC material. Actually, the fatigue behaviour of PUC material is an important design parameter for the strengthened structures, which have to be subjected to repetitive fatigue load. The PUC material in structural reinforcement is subjected to the repeated action of vehicle load. It is of great interest for both researchers and engineers to investigate the fatigue behaviour of PUC material.

The primary goal of this study is to investigate the flexural fatigue behaviour of PUC as strengthening material. The effective density and static flexural strength of PUC were detected prior to fatigue test. A laboratory testing program was applied to collect the fatigue lives of PUC at various stress levels. To incorporate the effects of stress level S and survival probability, equivalent fatigue-life was employed to study the fatigue equation of PUC. The fatigue prediction models for the PUC and the flexural fatigue behaviour of PUC800, PUC1200 and PUC1500 was compared.

EXPERIMENTAL PROGRAM AND TESTING METHODS

The main components of PUC are polyurethane and cement, mixed together [3-6]. The hardness range of this material is 10-100 (IRHD), and it possesses good chemical resistance, flexibility, adhesion and film-forming properties. The cement used in this study was produced under Chinese specifications. Ordinary Portland cement was used. The type of polyol used was polyether polyol. The acid value of the polyether polyol was ⩽5 mg KOH/g, and the hydroxyl value of the polyether polyol was 350±10 mg KOH/g. The density of the polyether polyol was 1.13 g/cm^3. The mixing containers used are plastic buckets. Firstly, the weighed polyether polyol and the silicone oil with different water content were poured into the container. Secondly, the Portland cement is poured into the mixture after being weighed and dried. Finally, the isocyanate was poured into the container. The raw materials for the polyurethane and cement were mixed for 3 min in a mixing container. The mixture was electrically stirred at a rate of 1500 revolutions per minute, seeFigure1.

Polyurethane is a high performance polymer elastic material, polyols and the polyisocyanate, are the main chemical components forming the polyurethane segment block, and the ether linkages. Small quantity of water can play very important role in forming the polyurethane densities due to the chemical reaction of water with polyol and polyisocyanate which produced foam composite with an air bubbles which affect the density of final product. All components of the polyurethane are liquid material and were used in this research mixed with cement powder.

Three kinds of polyurethane cement materials with different densities (800 kg/m^3, 1200 kg/m^3 and 1500kg/m^3) were prepared in this experiment, which were respectively represented by PUC800, PUC1200 and PUC1500. The distribution of materials with different densities is shown in Table 1.

Pour the mixed polyurethane cement material into the sample mould of 100×100×400mm^3 [7], as Figure 2. The specimens were demoulded the next day. Thereafter, they were transferred into the curing room and stored at 20 ± 2℃ until preparation for testing. The specimens were removed from the curing room after 28 days. Sensors were pasted onto the prism specimens to measure the strain during loading, as Figure3.

Fig. 1 - Polyurethane cement (PUC) mixing diagram

Tab. 1 - Mixing ratio PUC materials for all cases

component	Ratio of PUC		
	PUC800 (800 kg/m^3)	PUC1200 (1200 kg/m^3)	PUC1500 (1500 kg/m^3)
Cement	50.00	50.00	50.00
Polyisocyanate	24.64	24.87	25.00
polyether polyol	25.13	25.12	25.00
silicone oil	0.20	0.00	0.00
Water	0.03	0.01	0.00

Fig. 2 - Casting drawing of specimens

Fig. 3 - Fatigue test

DOI 10.14311/CEJ.2019.02.0013

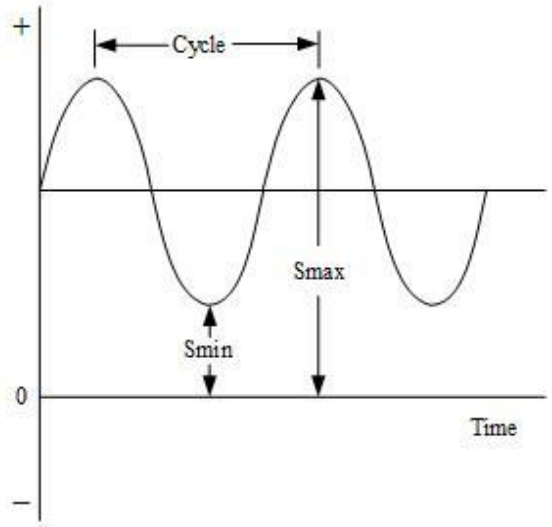

Fig. 4 - Fatigue test loading system

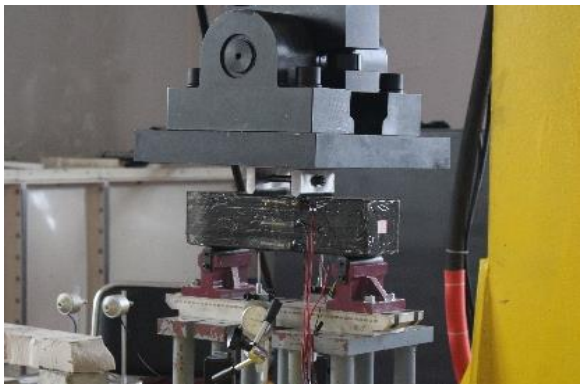

Fig. 5 - Fatigue test details

Strengthening analysis

In the static load test, there are three specimens for each density polyurethane cement composite, and the average value of ultimate flexural strength is shown in Table 2. It was found in the test that the flexural strength of PUC specimens increased with the increase of material density. The average flexural strength of high density polyurethane cement materials is 38.4MPa, which is far higher than that of ordinary Portland cement concrete and higher than that of general resin concrete [8-9].

Tab.2 - Average flexural strength of PUC for all cases

All case	PUC800	PUC1200	PUC1500
Flexural Strength（Mpa）	12.8	27.1	38.4

Tab 3 - Fatigue life of the specimen (PUC1500)

Fatigue life				survival rate L_R	$\ln\ln(1/L_R)$
S=0.90	S=0.85	S=0.75	S=0.65		
270	1526	4489	14810	0.8571	-1.8698
528	3944	8342	28210	0.7143	-1.0892
1934	6934	16365	59290	0.5714	-0.5805
5066	11484	48521	139140	0.4286	-0.1657
6512	81804	197512	349968	0.2857	0.2254
9867	164322	293698	886523	0.1429	0.6657

Fatigue strength results

Fatigue life statistical analysis

The fatigue life of PUC1500 specimens with different stress levels is shown in Table 3. It can be seen from Table 3 that the fatigue life test of PUC is discrete to a certain extent. Only by adopting reasonable and scientific methods for analysis can the reliable results be obtained with a small sample. There are many mathematical probability models used in the statistical description of fatigue data, among which the most commonly used are logarithmic normal distribution and Weibull distribution. As the logarithmic normal distribution function decreases with the increase of fatigue life, it is obvious that this violates the physical phenomenon of gradual deterioration caused by the fatigue process of materials. However, the risk function of Weibull's probability density function gradually increases with the increase of time, which can more accurately describe the fatigue data and conform to the actual situation of fatigue test. Therefore, it is commonly used to describe fatigue data with Weibull distribution in recent years [10-11]. In this paper, the fatigue properties of PUC are studied by means of Weibull distribution. The probability density function $f(n)$ and cumulative distribution function $F_N(n)$ of the Weibull probability distribution can be expressed by the following Equations (1) and (2), respectively, under the conditions $n \geqslant n_0$, $\alpha > 0$, and $u > n_0$:

$$f(n) = \frac{\alpha}{u - n_0}\left(\frac{n - n_0}{u - n_0}\right)^{\alpha-1} \exp\left[-\left(\frac{n - n_0}{u - n_0}\right)^{\alpha}\right] \quad (1)$$

$$F_N(n) = 1 - \exp\left[-\left(\frac{n - n_0}{u - n_0}\right)^{\alpha}\right] \quad (2)$$

Where n is the specific value of the random variable N; α is the shape parameter; u is the scale parameter; and n_0 is the location parameter.

The survivorship function $L_R(n)$ may be given as:

$$L_R(n) = \exp\left[-\left(\frac{n - n_0}{u - n_0}\right)^{\alpha}\right] \quad (3)$$

Considering the dispersion of materials, the minimum life parameter n_0 is 0, then Equation (3) can be rewritten as:

$$L_R(n) = \exp\left[-\left(\frac{n}{u}\right)^{\alpha}\right] \quad (4)$$

Take the logarithms twice on both sides of Equation (4), it holds Equation (5):

$$\ln\left[\ln\frac{1}{L_R}\right] = \alpha\ln(N) - \alpha\ln(u) \quad (5)$$

Equation (5) can be expressed as a simple linear relationship $Y = \alpha X - b$, where $Y = \ln\left[\ln\frac{1}{L_R}\right]$ and $X = \ln(N)$.

Under the given stress level S, the K fatigue test data obtained from the test were arranged from small to large in ascending order (the serial number is I), and the reliability L_R can be calculated as follows:

$$L_R = 1 - \frac{i}{k+1} \quad (6)$$

The survival rate and $\ln\ln(1/L_R)$ calculated by Eq. (6) are shown in Table 3, and the results of regression according to Equation (5) are shown in Table 4. It can be seen from Table 4 that $\ln\ln(1/L_R)$ has a good statistical linear relationship with $\ln(N)$. The correlation coefficients were 0.961, 0.918, 0.937 and 0.961, respectively. The results show that the fatigue life of PUC can obey the two-parameter Weibull distribution well.

Tab. 4- Regression coefficients at different stress levels (PUC1500)

stress level	regression coefficient a	regression coefficient b	u=exp（b/a）	correlation index R^2
0.90	0.6194	5.2121	4513	0.961
0.85	0.4886	5.1211	35638	0.918
0.75	0.5226	5.9312	84915	0.937
0.65	0.5823	7.179	226092	0.961

Tab. 5 - Fatigue life under different survival rates (PUC1500)

stress level	u	a	L_R					
			0.95	0.9	0.8	0.7	0.6	0.5
0.90	4513	0.6194	37	119	400	854	1526	2497
0.85	35638	0.4886	82	356	1654	4321	9013	16832
0.75	84915	0.5226	289	1145	4813	11810	23483	42111
0.65	226092	0.5823	1378	4741	17202	38494	71333	120484

Establishment of fatigue equation

The fatigue life is calculated by Equation (3) :

$$N = u\left|\ln\left(L_R\right)\right|^{1/\alpha} \quad (7)$$

The fatigue life under different survival probability was calculated by using Weibull function fitting results and Equation (7), as shown in Table 5.

In engineering, the dual logarithmic fatigue equation is generally adopted for fatigue analysis:

$$\lg S = \lg\alpha - b\lg N \quad (8)$$

The relation curve and regression equation of *S-N* are shown in Figure 6.

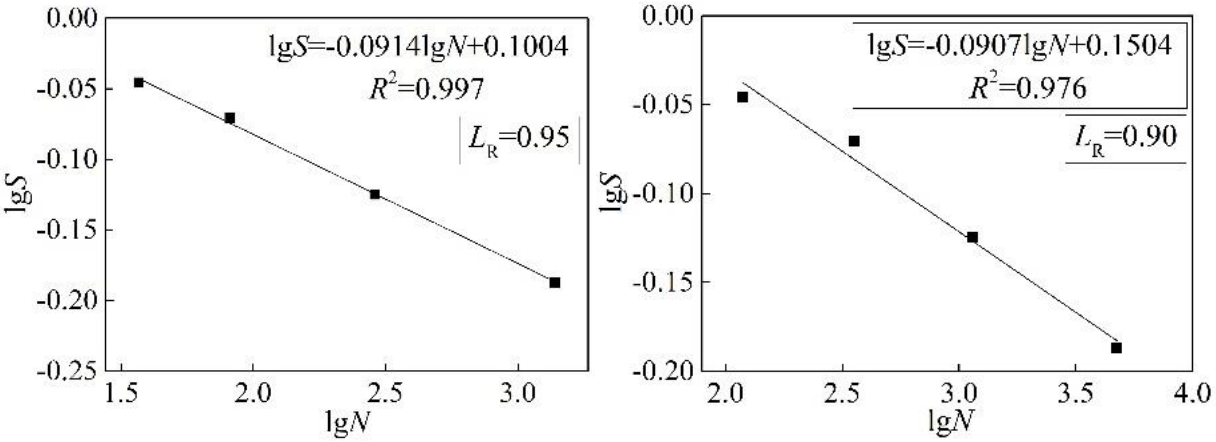

(a) L_R=0.95

(b) L_R=0.90

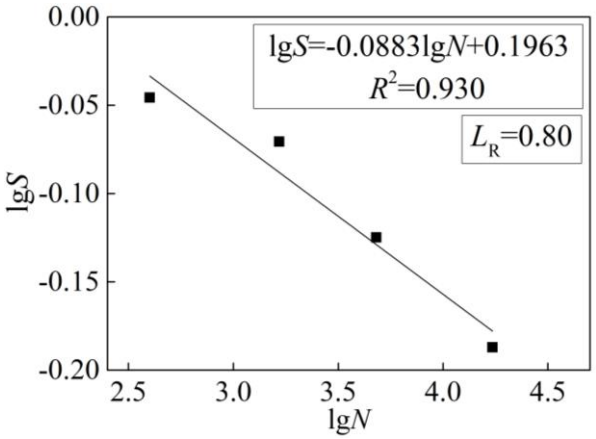

(c) L_R=0.80

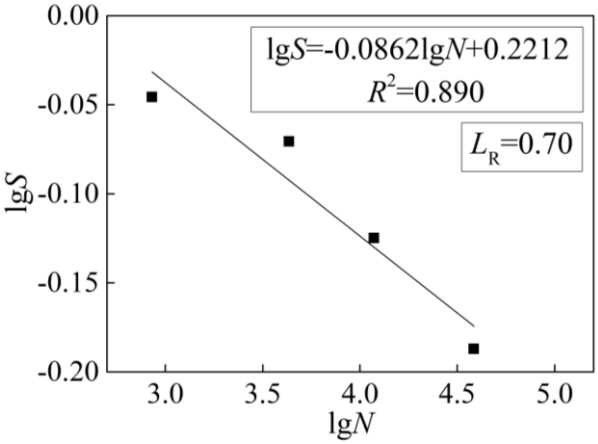

(d) L_R=0.70

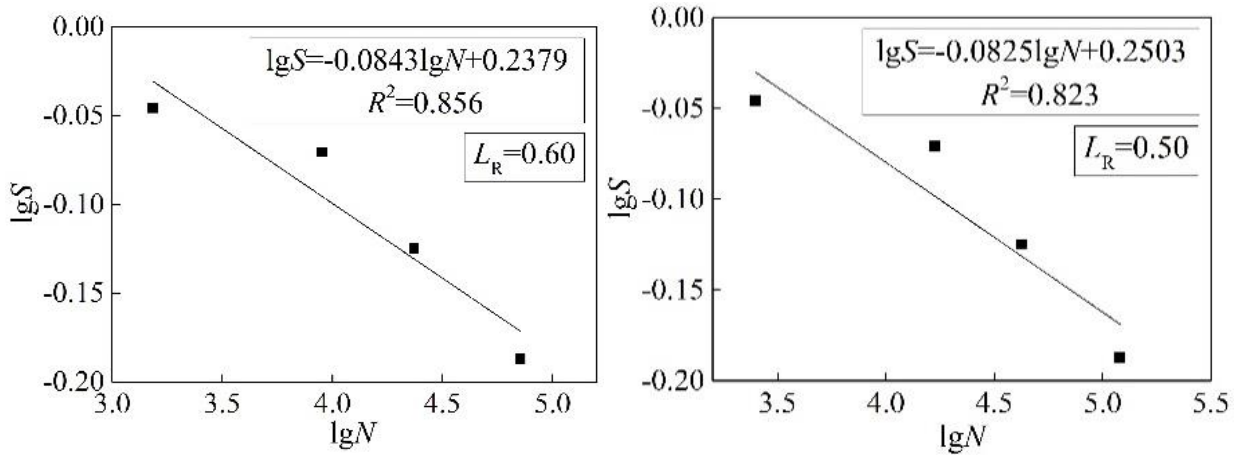

(e) L_R=0.60 *(f) L_R=0.50*

Fig. 6 - S-N regression curve and PUC fatigue equation (PUC1500)

The *S-N* fitting line equation with a survival rate of 0.5 in PUC1500 is shown in Equation (9) :

$$\lg S = -0.08820\lg N + 0.2910 \qquad R^2 = 0.991 \qquad (9)$$

The failure probability of PUC1200 and PUC800 specimens was analysed. The results show that the fatigue life of PUC1200 and PUC800 also conforms to Weibull distribution, and the S-N relation curve with the survival rate of 0.5 is as follows:

$$\lg S = -0.08430\lg N + 0.2754 \qquad R^2 = 0.982 \qquad (10)$$

$$\lg S = -0.09329\lg N + 0.3248 \qquad R^2 = 0.992 \qquad (11)$$

According to the S-N curve, the lgN and lgS of PUC1500, PUC1200 and PUC800 at the survival rate of 0.5 all conform to the linear relationship and fit well. According to the fatigue curves of PUC materials at different densities, the fatigue life of PUC1500 is the largest.

Strain analysis

Based on the dynamic strain acquisition instrument, PUC1500 samples were tested for the relationship between longitudinal maximum and minimum strain and fatigue life under flexural fatigue load. The resulting PUC1500 ε-N curve is shown in Figure 7.

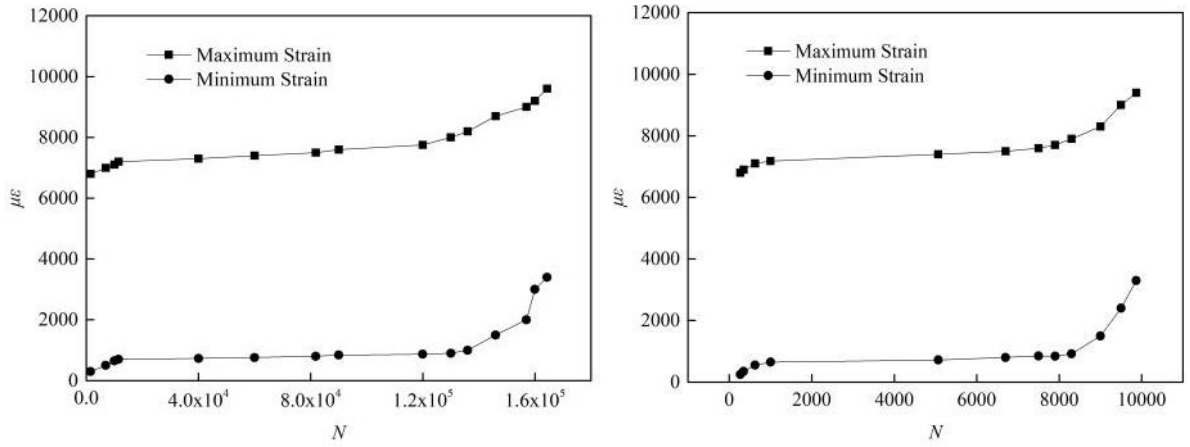

(a) L_R=0.90 *(b) L_R=0.85*

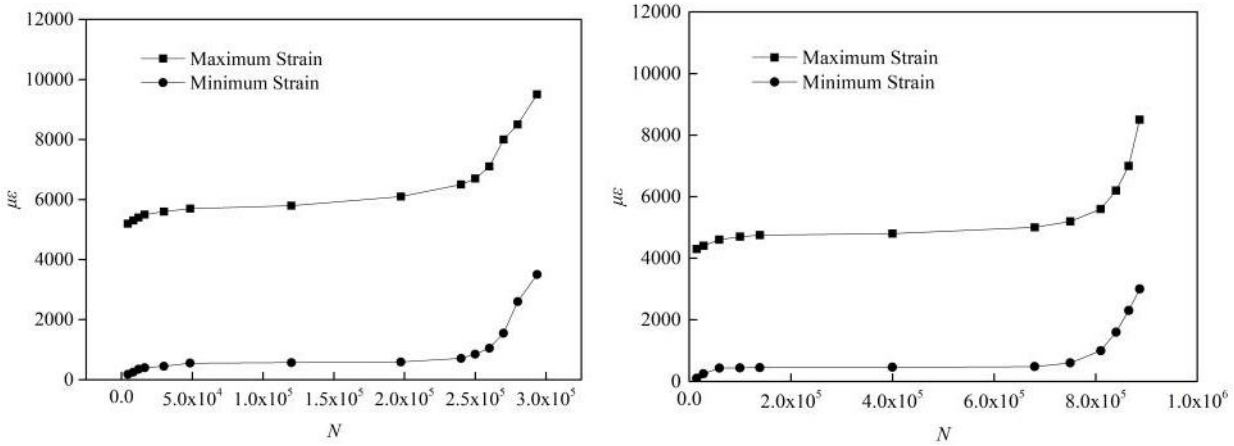

(c) L_R=0.75 *(d) L_R=0.65*

Fig. 7 - Curve of PUC1500 strain - fatigue life under different stress levels

As shown in Figure 7, under bending fatigue load, the variation rule of PUC1500 fatigue strain can be roughly divided into three stages: In the first stage, the fatigue strain increases rapidly. In the second stage, the fatigue strain increases linearly with the increase of fatigue times. In the third stage, the fatigue strain increases rapidly, which eventually leads to instability and failure.

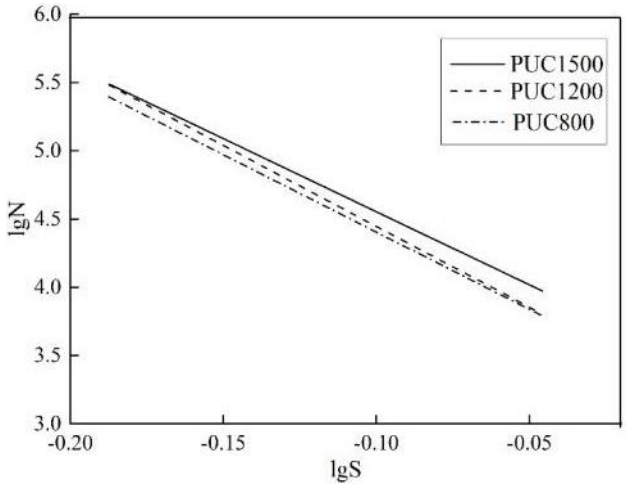

Fig. 8- Comparison of fatigue performance of PUC for all cases

The fatigue life equations for a survival probability of 0.5 were presented in Figure 8. Result indicates that PUC1500 has the maximum fatigue life among all the mixtures investigated. The fatigue life in descending order is PUC1500, PUC1200, and PUC800. Therefore, using the high density could enhance the flexural fatigue strength of PUC.

CONCLUSION

Through trabecular flexural fatigue tests, PUC material fatigue life basic obeys two parameter Weibull distribution, and through the mathematical model established the double logarithm fatigue equation under different failure probability.

According to the fatigue performance of PUC with three densities, the fatigue life equation of PUC1500, PUC1200 and PUC800 with a failure probability of 0.5 was obtained. PUC1500 has the highest fatigue life, and the fatigue life of PUC material decreases with the decrease of material density.

Under flexural fatigue load, the variation rule of the fatigue strain of PUC can be roughly divided into three stages.

The fatigue life equations of PUC with different density for a survival probability of 0.5 were compared. The result indicates that PUC1500 has the maximum fatigue life among all the mixtures investigated. The fatigue life in descending order is PUC1500, PUC1200, and PUC800.

REFERENCES

[1] Haleem KH, Zhang LZ, liu GW. An experimental study on strengthening reinforced concrete T-beams using new material poly-urethane-cement (PUC) [J]. Construction and Building Material, 2013, 40:104-117.
[2] Kexin Zhang, Quansheng Sun. Strengthening of a Reinforced Concrete Bridge with Polyurethane-cement Composite (PUC) [J]. The Open Civil Engineering Journal,2016,10(1):768-781.
[3] Haleem K.H., Liu G.W., Yu W.Y. Experimental study to investigate mechanical properties of new material polyurethane-cement composite (PUC)[J]. Construction and Building Materials, 2014; 50(15): 200-208.
[4] Liu G.W., Otsuka H., Mizuta Y., Shimitsun A. A foundational study on static mechanical characteristics of the super lightweight and high strength material using fly-ash[J]. Journal of the Society of Materials Science Japan, 2006; 55(8): 738-745.
[5] Kexin Zhang, Quansheng Sun. Experimental Study of Reinforced Concrete T-Beams Strengthened with a Composite of Prestressed Steel Wire Ropes Embedded in Polyurethane Cement (PSWR–PUC)[J]. International Journal of Civil Engineering, 2017:1-15.
[6] Kexin Zhang, Quansheng Sun. The use of Wire Mesh-Polyurethane Cement (WM-PUC) composite to strengthen RC T-beams under flexure[J]. Journal of Building Engineering, 2017, 15.
[7] Chinese Nation Standards, Test method of cement and concrete (JTG E30-2005), Ministry of Communications of PRC, Beijing, 2005.
[8] Min Xu, Yushi Li, Ping Zhang. Fatigue test of epoxy resin concrete[J]. Journal of China & Foreign Highway. 2009,29(1):200-203.
[9] Weiwei Sun, Sai Lu, Yuan Zhang. Experimental study on flexural fatigue damage of high strength resin concrete[J]. Building Structure,2016,46(5):56-59.
[10] Yongqing Yang, Meng Yan, Xiaobin Li. Transverse load distribution theory and experimental study on reinforced hollow slab bridge with polymer modified concrete [J]. Bridge Construction, 2014, 44(6): 63-68.
[11] Juanlan Zhou, Mulian Zheng, Qi Wang, Jiangang Yang and Tianfa Lin. Flexural fatigue behavior of polymer-modified pervious concrete with single sized aggregates [J]. Construction and Building Materials, 2016; 124, 897-905.
[12] Kyu-Seok Yeona, Yoon-Sang Choi b, Kwan-Kyu Kima, Jung Heum Yeonc. Flexural fatigue life analysis of unsaturated polyester-methyl methacrylate polymer concrete [J]. Construction and Building Materials, 2017; 140, 336-343.

Article no. 14

THE CIVIL ENGINEERING JOURNAL 2-2019

CALCULATION MODEL AND EXPERIMENTAL STUDY ON SEDIMENT EROSION OF SLOPE UNDER EXTERNAL-SOIL SPRAY SEEDING

Can Li[1], Haiqing Zhou[1,2], Qianghui Song[1,3], Yang Liu[1], Yixin He[4]*

1. *Army Logistics University, Chongqing Key Laboratory of Geomechanics & Geoenvironment Protection, Chongqing, Daxue North 1st Road 20, 401331 Chongqing, P.R.China; 443743832@qq.com, 821580249@qq.com*
2. *Chongqing University of Science and Technology, Chongqing, East Road 20, 401331 Chongqing, P.R.China; 976922172@qq.com*
3. *Chongqing Institute of Geology and Mineral Resources, Lanxin Road 111, 400042 Chongqing,* P.R.China; *songbook@126.com (Corresponding author)*
4. *School of Geography Sciences, SWU, Tiansheng Road 2,400715 Chongqing, P.R.China; 88206879@qq.com*

ABSTRACT

Due to the current lack of theoretical study on rain erosion of the slope under external-soil spray seeding, the calculation model applicable to slope sediment erosion under external-soil spray seeding was derived from hydraulics theory and energy method. Designed slope scouring test on indoor model, conducted 3 separate scouring tests under 3 different slope rates (1:0.75, 1:1, 1:1.25) and 3 different rainfall intensities (120, 150, 180mm/h). The rationality of the calculation model was verified by the experimental data. Meanwhile, also analysed the developing regularities of slope erosion and relationship among sediment erosion, rainfall duration, rainfall intensity and slope rate. The results show that the relative error between the theoretical value and measured data is within 18%, and the calculation model can accurately predict the sediment erosion of the slope under external-soil spray seeding to some extent; the slope under external-soil spray seeding is lack of erosion resistant ability, and the slope erosion is mainly rill erosion and layered surface erosion; the amount of sediment erosion is positively correlated with rainfall intensity and slope rate. The relationship between growth rate and rainfall duration basically remained the same during the first 20 minutes, and then gradually decreased.

KEYWORDS

External-soil spray seeding, Slope erosion, Energy method. Model test

INTRODUCTION

In the 1980s, Japan was the first country to carry out study on external-soil spray seeding technology [1], which China has introduced in the early 1990s and successively carried out experimental study in south China and loess plateau [2]. Since the 20th century, external-soil spray seeding technology, as the most important ecological protection technology, has been widely applied nationwide [3]. This technology is able to spray soil mixture evenly into the bare rock or soil slope through the mixing and spraying pump for external soil, advanced processing and meshing on the slope is generally required. The soil mixture consists of base material soil, fertilizer, water retaining agent, pH regulator, water, and various selected plant seeds etc. allocated by reasonable proportions, which will and finally protect the environment and beautify the slope. It has the

advantages of sound slope protection effect, wide application range, economic, beautiful and strong sustainability etc. [4].

In rainy cities, due to the sudden torrential rains, the external-soil spray seeding is susceptible to heavy rainfall after its completion. Surface runoff on the slope can take away a lot of sediment, which will leads to serious sediment erosion [5]. As for external-soil spray seeding on the highway subgrade slope, Wang Yimin et al. [6] studied the resistant ability of the slope under external-soil spray seeding for rain scouring at the initial stage after construction and vegetation growth. The result shows that at early spraying, the slope is lack of ability to resist rain scouring, and protective measures must be taken to protect the plant seeds. In practical engineering application, put a layer of non-woven cloth on the slope after construction is the normal practice adopted to prevent or reduce the sediment erosion caused by rainfall on the slope. However, in case of heavy rainfall, sediment erosion phenomenon is still serious, even with the help of protective measures. As shown in Figure 1, a slope for external-soil spray seeding with non-woven fabric was built in the west campus of the college. After heavy rain, a lot of gullies have occurred on the slope, mesh steel material was exposed, large sediment erosion was occurred and the plant is difficult to completely cover the slope in the later stage, because a large number of plant seeds were taken away by runoff on the slope. For abovementioned reasons, re-construction is needed and may lead to serious economic losses.

Fig. 1 - Sediment erosion

Therefore, considering the larger sediment erosion resulted from rain scouring on the slope under external-oil spray seeding after construction; it is necessary to conduct theoretical calculation on its sediment erosion. It would be of theoretical guidance to practical engineering to derive calculation model through theories, verify the accuracy of model by designing test and accurately grasp the developing regularities of sediment generated from external-soil spray seeding under multiple conditions.

Calculation Model for Sediment Erosion

Hydraulic Analysis of Water Flow on the Slope

Simulated water flow on the slope is as shown in Figure 2; flow rate at L point of the slope could be derived from Manning Formula, see Equation (1).

$$v_L = \frac{1}{n} h_\alpha^{\frac{2}{3}} \tan^{0.5}\theta \tag{1}$$

In the above formula, h_α refers to confluent depth, n refers to roughness ratio and θ refers to the angle between the slope and horizontal surface.

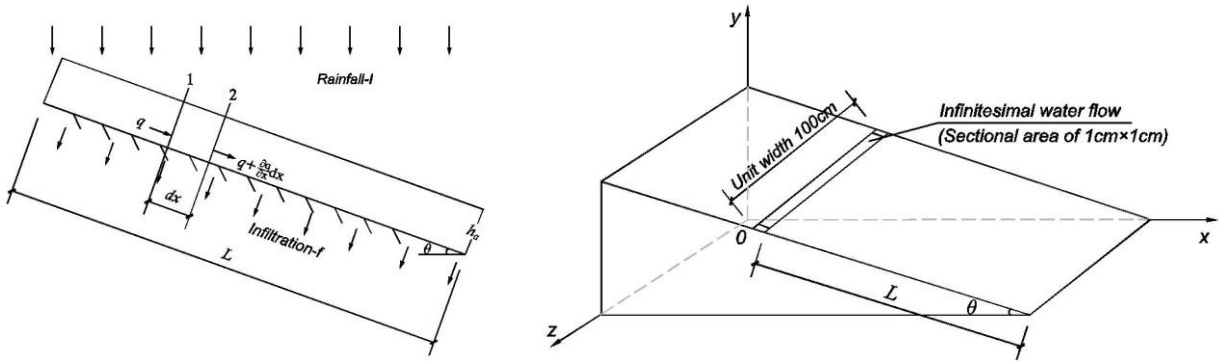

(a) Water flow analysis *(b) Water and soil flow model*

Fig. 2 - Analysis of water flow on the slope

The relationship between micro-segment flow and increased runoff (determined by rainfall intensity and infiltration rate) can be established by reference to the infinitesimal water flow relationship between section 1 and section 2. Refer to the single-width flow formula derived by Horton [7] in calculating the critical slope under soil erosion at the slope length of L and make some modifications, take α as the angle between the rainfall direction and the vertical direction of the slope. When the rainfall direction is vertical, the value is equal to the angle between the slope and the horizontal plane. Please refer to Equation (2) for the specific formula.

$$q = \int_0^L \frac{\partial q}{\partial x} dx = \int_0^L (\mathrm{I} - f) dx \cos\alpha = (\mathrm{I} - f) L \cos\alpha \tag{2}$$

According to the hydraulics theory, the single-width flow can also be expressed as the product of flow velocity and confluent water depth, and it can be combined into the Equation (2) as follows:

$$q = v_L h_\alpha = \frac{1}{n} h_\alpha^{\frac{5}{3}} \tan^{0.5}\theta = (\mathrm{I} - f) L \cos\alpha \tag{3}$$

Finally, the confluent water depth could be derived from the Equation (3), see Equation (4).

$$h_\alpha = [\frac{n(\mathrm{I} - f) L \cos\alpha}{\tan^{0.5}\theta}]^{0.6} \tag{4}$$

With reference to the “Designing Specification on Highway Drainage” [8], catchment time of the slope is:

$$t = 1.445(\frac{nL}{\sqrt{\tan\theta}})^{0.467} \tag{5}$$

In the above formula, I refers to the standard rainfall intensity, f refers to the infiltration rate, and both units are m/min.

Derivation of the Energy Method Formula

At present, there are many methods for calculating the amount of sediment erosion on the slope, such as establishing empirical models based on a large number of measured data [9], establishing mathematical equations based on hydraulic theory [10], and using neural networks to predict the amount of sediment erosion [11,12] etc. However, there are certain problems in the above methods, such as excessive influence factors of sediment erosion on the slope [13]; difficult to clarify the relationship between various factors; over complicated mathematical formula and

insufficient accuracy of the results etc. Li Zhigang et al [14] proposed to calculate the amount of sediment erosion by using the energy conservation law for the first time, and successfully applied this method to calculate the amount of sediment erosion in geotechnical structures. Based on the hydraulics theory, the energy method is to calculate the sediment erosion on the slope by the energy conservation law, which is not only simple in terms of the mathematical formula, but can also reflect the relationship among influence factors to some extent.

Energy distribution and transformation during slope erosion obey the energy conservation and conversion law [15]. According to the variation of water flow in soil and energy during rain scouring and erosion, the energy balance equation of slope soil under scouring is established as follows:

$$E_0 + E_1 = E_2 + E_3 \tag{6}$$

In the formula, E_0 refers to the potential energy of water flow in soil, E_1 refers to the initial kinetic energy of water flow in soil, E_2 refers to the frictional energy dissipation, and E_3 refers to the kinetic energy of water flow in soil.

During the movement of water flow in soil, the friction is the product of the positive pressure of the moving material on the slope and the friction coefficient. In the formula, the friction coefficient is expressed by the roughness rate n. At the same time, it is assumed that the variation of mass along the path of water flow in soil is linear, and the frictional energy dissipation E_2 can be obtained by the frictional force integration along the movement distance. See Equation (7).

$$E_2 = \int_0^L ng(m_1 + \frac{\Delta m}{L}x)\cos\theta = ngL(m_1 + \frac{\Delta m}{2})\cos\theta \tag{7}$$

The external-soil spray seeding technology is widely used for the cutting slope. Basically, there is no catchment at the top of the slope. The initial kinetic energy of water flow in soil E_1 is equal to 0. The kinetic energy of water flow in soil can be derived by taking the velocity v_L at the foot of the slope, and energy balance equation for the simulated slope is obtained:

$$m_1 gL\sin\theta + \frac{1}{2}m_1 v_1^2 = ngL(m_1 + \frac{1}{2}\Delta m)\cos\theta + \frac{1}{2}(m_1 + \Delta m)v_2^2 \tag{8}$$

$$\Delta m = m_1 \frac{2gL\sin\theta - 2ngL\cos\theta - v_2^2}{ngL\cos\theta + v_2^2} \tag{9}$$

Δm is the variation of water flow in soil, including the increased sediment m_2 and the increased rainwater ΔQ, i.e.

$$\Delta m = m_2 + \Delta Q \Rightarrow m_2 = \Delta m - qt \tag{10}$$

By substituting Equations (1), (4), and (5) into Equations (9) and (10), a function of the sediment erosion m_2 on the slope could be derived:

$$m_2 = F(\mathrm{I}, f, \mathrm{L}, n, \theta, \alpha) \tag{11}$$

The catchment on the slope is equal to the total flow at the foot of the slope, i.e. $M = \rho qtB = \rho v_L h_\alpha tB$, where B is the slope width, ρ is the water density, and t is the catchment time of the slope.

The initial mass of the infinitesimal water flow on a single width area is:

$$m_1 = \rho \times 10^{-4} = 0.1\mathrm{kg} \tag{12}$$

The total amount of sediment erosion on the slope is

$$\Delta M = \frac{m_2}{m_1} M \tag{13}$$

Scouring Test on Indoor Slope Model

Test Device

The scouring test on indoor slope model was carried out by using a self-made test vehicle. It is mainly composed of a frame, a guide frame, a model frame, a support system and a rainfall system, as shown in Figure 3(a).

(1) Frame

There are 4 universal wheels with brakes at the bottom of the frame. The frame is made of unequal angle iron, with a height of 50cm, a base size of 1.5*0.6m and an angle iron specification of 70*50*8mm. Slanting rod of the frame is connected to the frame base by a hinge, and four holes are reserved on the slanting rod for connecting the model frame.

(2) Guide Frame

The guide frame is composed of equilateral angle iron (with a specification of 30*30*3mm and a length of 30cm) and steel bar (with a diameter of 18mm and a length of 35cm); the two form a triangular support with the frame base. The top surface of the triangular support has a slope of 15°; laying a wooden board with a size of 40*90*8mm on the support and fixing it with the triangular structure by iron wire. It is a trenched wooden board, as shown in Figure 3(b), with a position left for the hinge at the upper end of the wooden board, which enables the wooden board to be embedded under the model frame, so as to ensure that the groove can be completely used for collecting rainwater. Side plates with a height of 8cm are arranged on both sides of the wooden board and the water outlet; a plastic film is laid in the guide groove to prevent rainwater flow out from the assembling gap of the wooden board and makes it easy to collect the sediment brought by scouring.

(3) Model Box

The model box is made of 2cm thick wood, with an inner frame size of 800*1200*1200mm. Put nails on the bottom plate, hang the thin wire netting, lay fine stone concrete (2cm thick), and finally roll the slope with the roller. Hang the thin wire netting could prevent the concrete from cracking and ensure a complete slope.

(4) Support System and Rainfall System

The support system is mainly composed of a support rod and a support baffle, which changes the slope rate by adjusting the supporting points. Learned from the designing experience of rainfall simulators in existing studies [16-19], the rainfall system designed in this test consists of a wooden bracket, a wire mesh frame, a spray device, and a voltage stabilizing and flow control device. The wire mesh is hold up on the wooden support and parallel to the slope. The spray device is composed of 10 copper nozzles and rubber tube, with a size of 400*800mm, as shown in Figure 3(c), which is fixed on the iron grid by the self-locking nylon cable tie. The copper nozzle is adjustable mist sprayer, with a specification of the following: diameter of the nozzle orifice is 1.2cm, operating pressure (0.2-0.5Mpa), spraying diameter (0-60 cm), spraying flow rate (0-140L/h); inner diameter and outer diameter of the rubber tube is 8mm and 12mm respectively. The nozzle is 50cm above the ground, with its orifice vertical to the slope. Modify the spraying diameter of the nozzle and its position before the test, so as to ensure uniform rainfall distribution in the model box;

meanwhile, to prevent rainfall distribution outside the model box, no wind is allowed in the room. Based on abovementioned prerequisites, the uniformity of rainfall distribution is determined as 86.5%. The maximum rainfall intensity of the rainfall simulator is 800mm/h; kinetic energy of the rainfall is 33.45 $\mathrm{J \cdot m^{-2} \cdot mm^{-1}}$,41.79 $\mathrm{J \cdot m^{-2} \cdot mm^{-1}}$ and 50.13 $\mathrm{J \cdot m^{-2} \cdot mm^{-1}}$ under a rainfall intensity of 120mm/h, 150mm/h and 180mm/h respectively. Without changing the opening status of the nozzle and valve, the rainfall intensity of the sprayer is stable with the help of voltage stabilizing and flow control device.

(a) Model test vehicle

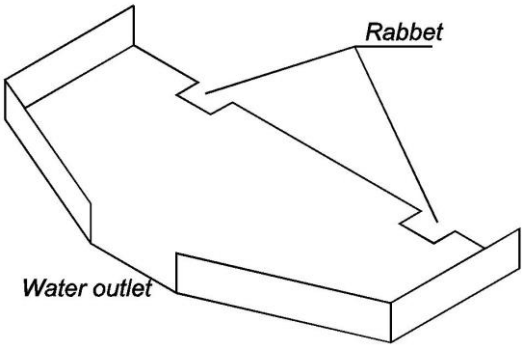

(b) Guide groove

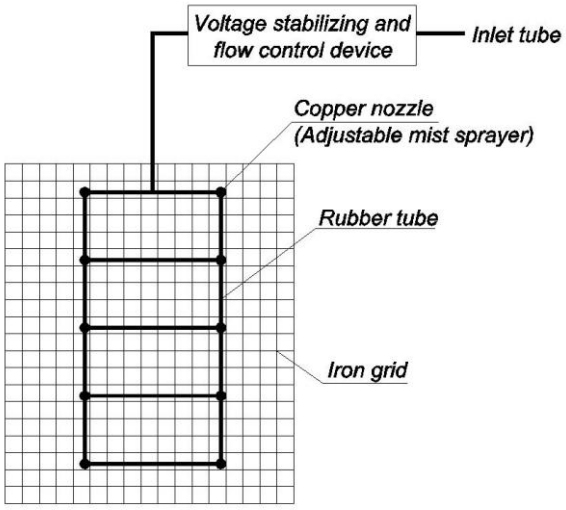

(c) Rainfall system

Fig. 3 - Test device

Test Plan Design

(1) Rainfall Intensity

Rainfall intensity of the test is determined and derived in accordance with the storm intensity formula and specifications [20]. The selected area of the storm intensity formula is Shapingba, where the campus is located, see Equation (14).

$$q = \frac{1132(1+0.958\lg P)}{(t+5.408)^{0.595}} \quad (L/s \cdot hm^2) \tag{14}$$

Where P is the recurrence period of the design, the unit is year (a);

q is the intensity of torrential rain, the unit is $L/s \cdot hm^2$;

t is the duration of the rain, the unit is min.

According to the requirements of the specification [20], take $P=3$, t=$5min$. It can be calculated by taking the formula (14) that $q = 409.26L/s \cdot hm^2$, based on the conversion formula, the rainfall intensity under standard unit is:

$$I = \frac{q}{166.67} \times 60 = 147mm/h \quad (15)$$

The designed rainfall simulator controls the rainfall intensity by flow rate, the calculated rainfall intensity needs to be converted for the convenience of the test. In the preparation stage, the rainfall is ensured to be distributed completely on the designed slope as far as possible, thus the minor rainfall outside the slope can be ignored. Therefore, the derived flow rate is Q=2.3568 L/min, which is based on a slope area of 0.96m^2 and a rainfall intensity of $\mathrm{I} = 147\mathrm{mm/h}$. In order to control the test easier, take Q=2.4 L/min and correspondent rainfall intensity $\mathrm{I} = 150\mathrm{mm/h}$. Meanwhile, considered a fluctuation of 20% to simulate situation under heavy rain and torrential rain, namely $\mathrm{I} = 120\mathrm{mm/h}$ (rainfall area is 0.96 m^2, correspondent flow rate Q=1.9 L/min) and $\mathrm{I} = 180\mathrm{mm/h}$ (rainfall area is 0.96 m^2, correspondent flow rate Q=2.9 L/min).

(2) Experiment Material

The slope material for external-soil spray seeding is mainly composed of organic nutrient soil. Considering that the calculation model is mainly used to calculate sediment erosion after the slope engineering, the situation after vegetation growth is not considered in this calculation model. Therefore, various additives used to assist plant growth in the external-soil spray seeding are not considered in the test, and the test soil is only organic nutrient soil.

(3) Model Making

Measuring the water content of the organic nutrient soil in advance, adding correspondent proportion of water according to the water content required by the test, putting together the mixture with a soil mixing tool, and then infiltrated for 24 hours. The soil is paved in the model box by layered compaction method, each layer with a thickness of 1cm. After compacting one layer, scrape off the excess part with a scraper, then shave the surface of the soil with a geo-knife and compact it, 5 layers in total.

(4) Artificial Rainfall

The artificial rainfall adopts nozzle for simulated water spray, reasonably control the nozzle spacing and angle to ensure uniform rainfall. A bucket was placed at the water outlet of the guide frame to collect the mixture of rainwater and sediment brought by the scouring on the slope surface. The designed rainfall duration is 60 minutes, and the data was collected every 10 minutes, 6 groups of data in total.

(5) Test Group

In order to consider the influence of different rainfall intensity and slope rate on the sediment erosion under external-soil spray seeding, three slope rates were selected for comparison, namely 1:0.75, 1:1, 1:1.25. Based on the standard rainfall intensity derived from the intensity of torrential rain, with a fluctuation of 20%. The conditions of heavy rain and torrential rain were simulated respectively. The test group is as shown in Table 1.

Tab. 1- Test group

Working Condition	Slope Rate	Rainfall Intensity/ (mm/h)
1	1:0.75	120
2	1:0.75	150
3	1:0.75	180
4	1:1	120
5	1:1	150
6	1:1	180
7	1:1.25	120
8	1:1.25	150
9	1:1.25	180

TEST RESULTS

Slope Erosion

Under the action of rainfall erosion, the erosion process of slope generally follows the sequence of raindrop erosion - layered surface erosion - rill erosion [21, 22]. Taking the experimental group with a slope rate of 1:1 and a rainfall intensity of 150mm/h for erosion effect analysis. From the beginning of rainfall, record the status of slope erosion by every 10 minutes. The rainfall lasted for 60 minutes and was recorded for 6 times. See Figure 4.

In the early stage of rainfall, the soil is in the state of natural moisture, with strong water absorption capacity. The initial process of slope erosion occurs while most rainwater infiltrates into the soil and erodes the slope. The impact of raindrops on the slope causes the surface soil to become loose, and the floating soil begins to roll along the slope with raindrops as they hit. As the soil gradually became saturated and rainfall intensity became greater than the infiltration rate, the slope surface began to fall and formulate a fluid or a shallow flow along the slope. At this moment, the kinetic energy of water flow is small, and the runoff is also scattered and broad, which can only take away suspended or condensed fine soil particles and dissolved substances on the surface, and result in a layered surface erosion mainly eroded by a thin layer of water flow. Due to the small pits formed by raindrop erosion in the early stage, and the micro-topographic fluctuation on the slope, the sheet flood produces differentiated erosion on the slope, and then gradually develops into the thin water flow with obvious flow path. The hydraulic drop appears under the action of thin water flow, indicating that the rill erosion begins to form, which is an important cut-off point of erosion mode variation.

When the rainfall lasted for 10min, visible ridges were formed in the lower right part of the slope, with a depth of 0.2cm-0.8cm. The upper left part of the slope was less eroded and the slope is smooth. Other areas of the slope have different degree of layered surface erosion. When the rainfall lasted for 20min, the ridge continued to develop, and the depth reached about 1cm. At the same time, a new rill began to form in the lower left part of the slope. The layered surface erosion still occurs in the upper left area of the slope, Surface erosion on remaining parts of the slope was deepened, and shows obvious scale-like shape. When the rainfall lasted for 30 minutes, the rill in the lower right region began to develop upward, and the depth gradually deepened. New rill was formed in the middle and lower regions, and the rest of the slope was in the state of layered surface erosion, with more obvious scale-like shape. After 40 minutes of rainfall, the rill began to widen and the deepening trend began to slow down. At the same time, new rill began to branch from the existing rill and developed into various directions, among which the vertical rill is the

fastest developed one. A pit was formulated in the left and right area, which is mainly due to a puddle was gradually formed by accumulated rainfall during its horizontal development process on the basis of the rill, with sediment at the bottom of the pit taking away by the water flow, a visible pit was gradually formed. When the rainfall lasted for 50min and 60min, the existing rill continued to develop, the surface erosion became more obvious, and the slope erosion began to stabilize.

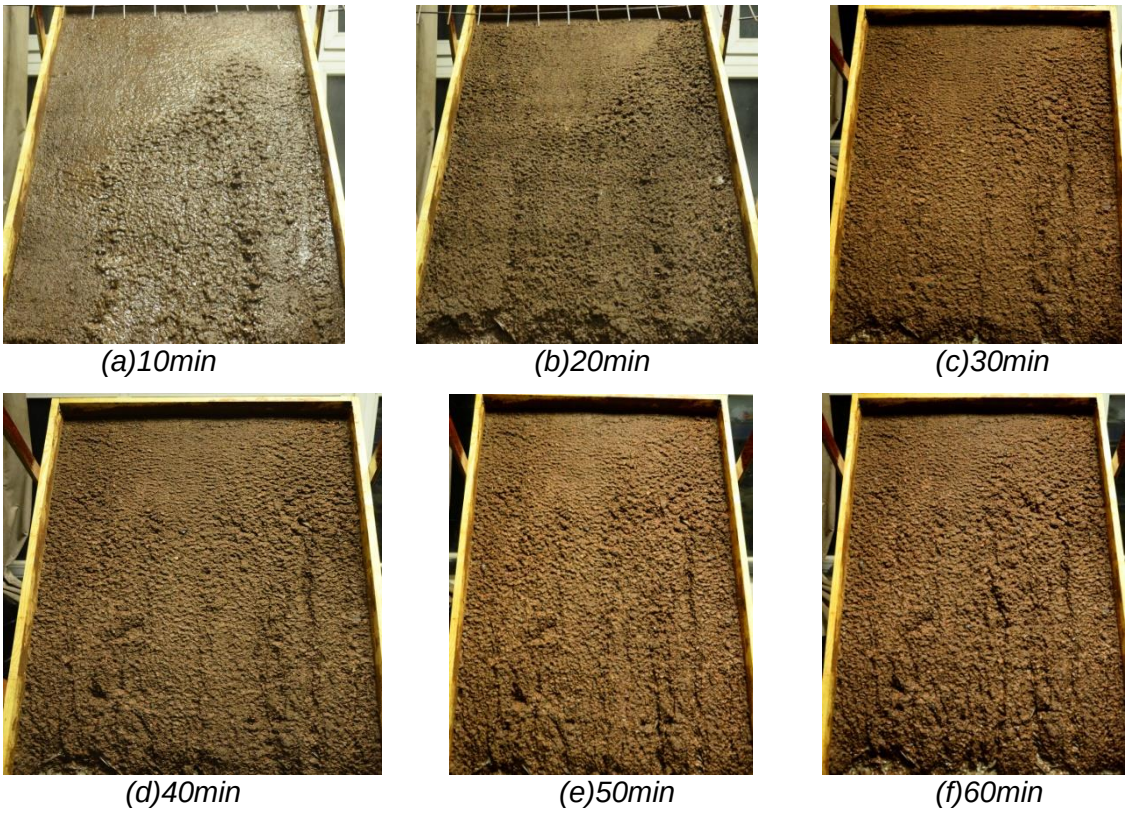

(a)10min *(b)20min* *(c)30min*

(d)40min *(e)50min* *(f)60min*

Fig. 4 - Slope erosion

Analysis of Sediment Erosion

Keep each group of bucket static for 24 hours, carefully separate mud and rain, ensure no sediment outflow, then use iron plate to collect the remained mixture of sediment and water. Put it into the drum wind drying oven with a temperature of 110 ° C, measure the weight of dried soil after 24 hours and record the sediment concentration in each group. Plot the relationship curve between accumulated sediment erosion and rainfall duration, as shown in figure 5.

It can be found from the three sets of curves that sediment erosion increases with the increase of rainfall duration under each working condition. For the working conditions under rainfall intensity of 120mm/h and 150mm/h, the increasing trend basically increases linearly before the rainfall duration of 20min, and then slows down after 20min. However, in the case of rainfall intensity of 180mm/h, the sediment growth rate began to slow down after the rainfall lasted for 30min, the decelerated increase rate appears later at the slope rate of 1:0.75, and began to decelerate after the rainfall lasted for 40min. This regularity indicates that under higher rainfall intensity and steeper slope, the longer the linear increase of sediment erosion is maintained, the more serious the slope erosion damage is. In the late rainfall duration, the growth rate of sediment erosion seems slowdown, which reflects that rill development and surface erosion tends to be stable in the late stage of the actual slope erosion. There is no sudden increase of large rill, with sediment on existing rills gradually taken away under the erosion of runoff on surface, gully

gradually appears. The sediment erosion during this process was less than that in the initial stage and its growth rate was relatively stable.

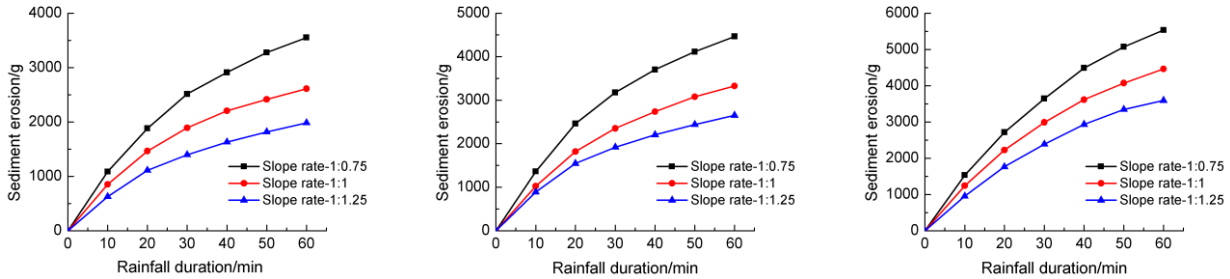

(a)Rainfall Intensity-120mm/h (b)Rainfall Intensity-150mm/h (c)Rainfall Intensity-180mm/h

Fig. 5 - Curve of sediment erosion and rainfall duration

In order to analyse the influence of rainfall intensity and slope rate on sediment erosion in a comprehensive manner, taking rainfall intensity and slope rate as the horizontal coordinate, and the sediment erosion under a rainfall duration of 60 minutes as the vertical coordinate to draw curves, as shown in Figure 6 and Figure 7.

From the relationship curve of sediment erosion and rainfall intensity, the sediment erosion increases with the increase of rainfall intensity. The curve tends to be concave under a slope rate of 1:1 and 1:1.25, which indicates that under the rainfall intensity of 120-150mm/h, the rainfall intensity and sediment erosion increase slowly. Sediment erosion increases faster under the rainfall intensity of 150-180mm/h; under the slope rate of 1:0.75, the increase rate of sediment erosion is relatively consistent, and the curve is basically linear.

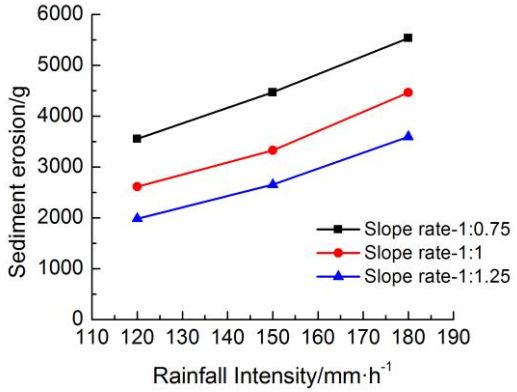

Fig. 6 - Relationship between sediment erosion and rainfall intensity

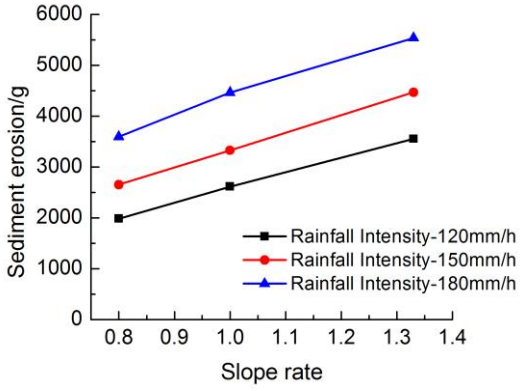

Fig. 7 - Relationship between sediment erosion and slope rate

As can be seen from the relationship curve between sediment erosion and slope rate, sediment erosion increases with the increase of slope rate. Under the working condition with a rainfall intensity of 120mm/h, the curve is convex, indicating that sediment erosion increases rapidly at the slope rate of 1:1.25 - 1:1, and slowly at the slope rate of 1:1-1:0.75. Under the working condition with a rainfall intensity of 150mm/h and 180mm/h, the curve is linear, indicating that the increase rate of sediment erosion is relatively consistent.

Regression Analysis

In order to reflect the relationship between sediment erosion and rainfall duration under various working conditions, the nonlinear regression analysis of test data was carried out. Through multiple fitting, the regression equation with the largest determination coefficient was selected, as shown in equation (16). Where, the value of x in the fitting formula is limited to the duration of rainfall in this experiment, i.e. $0 \le x \le 60$. The fitting curve is as shown in Figure 8.

$$y = a + b\ln(x + c) \tag{16}$$

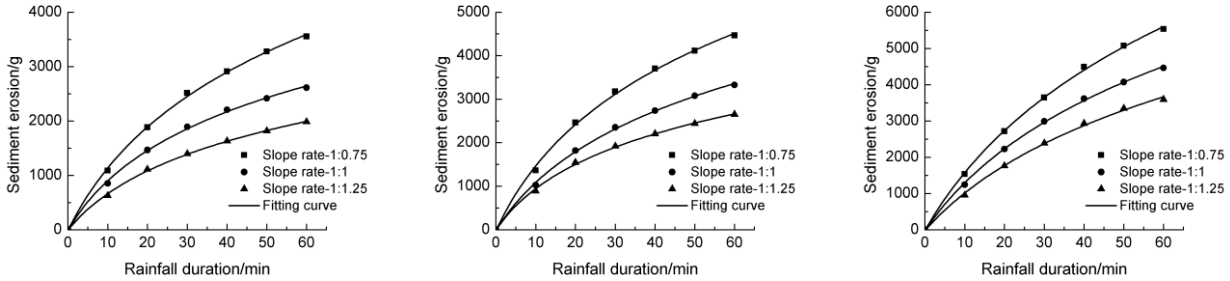

(a)Rainfall Intensity-120mm/h (b)Rainfall Intensity-150mm/h (c)Rainfall Intensity-180mm/h

Fig. 8 - Fitting curve of sediment erosion and rainfall duration

The specific results of nonlinear fitting are shown in Table 2. By observing the determination coefficient R^2 in the table, it is found that it is greater than 0.997 in each working condition, indicating that the nonlinear fitting result is very good, and equation (16) can soundly reflect the relationship between sediment erosion amount and rainfall duration under external-soil spray seeding.

Tab. 2- Regression analysis

Working Condition	a	b	c	R^2
1	-5963.61868	2214.8242	14.66493	0.99874
2	-6859.74208	2649.35689	13.18338	0.99795
3	-13431.63497	4314.6354	22.38974	0.99907
4	-3515.05999	1443.44149	11.31882	0.99823
5	-5228.44849	1998.54593	13.57112	0.99866
6	-10007.57583	3307.58463	20.48106	0.99914
7	-2844.49467	1129.78831	12.31032	0.99869
8	-3133.98194	1365.19371	9.85304	0.99834
9	-9088.22272	2885.61775	23.12692	0.99777

At the same time, regression analysis was conducted on the relationship among sediment erosion amount, rainfall intensity and slope rate under the rainfall duration of 60 minutes. Considering that there are few data in each group and the overall trend of the relationship between them is linear, linear equation $y = a + bx$ was selected for regression analysis. The fitting results of the relationship between sediment erosion and rainfall intensity are shown in Figure 9 and equation (17). The value range of x is the rainfall intensity range involved in this test, i.e. $120 \le x \le 180$. See Figure10 and equation (18) for the fitting results of the relationship between sediment erosion and the slope rate, and the value range of x is the slope rate interval involved in this experiment, namely $0.8 \le x \le 1.33$.

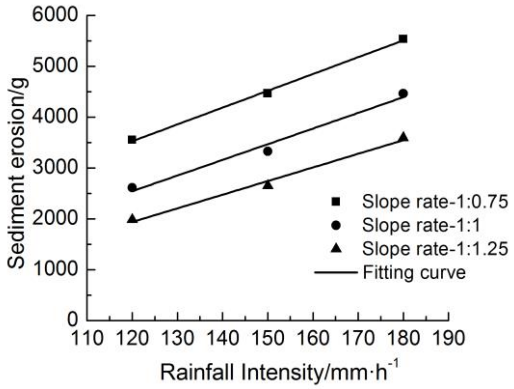

Fig. 9 - Fitting curve of relationship between sediment erosion and rainfall intensity

$$\begin{aligned} &\text{Slope rate-1:0.75:} && y = -439.2 + 33.1x,\ R^2 = 0.99582 \\ &\text{Slope rate-1:1:} && y = -1155.1 + 30.81x,\ R^2 = 0.96622 \\ &\text{Slope rate-1:1.25:} && y = -1280.3 + 26.8x,\ R^2 = 0.98092 \end{aligned} \quad (17)$$

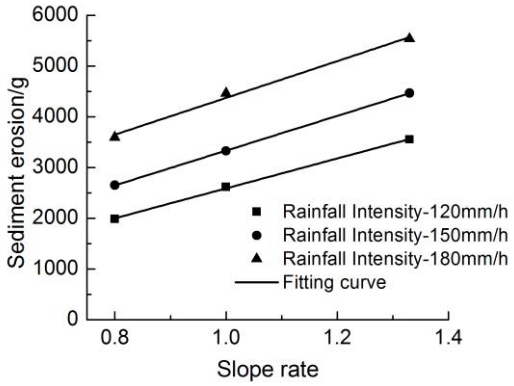

Fig. 10 - Fitting curve of relationship between sediment erosion and slope rate

$$\begin{aligned} &\text{rainfall intensity-120mm/h:} && y = -360.9 + 2948.9x,\ R^2 = 0.99855 \\ &\text{rainfall intensity-150mm/h:} && y = -92.7 + 3425x,\ R^2 = 0.99994 \\ &\text{rainfall intensity-180mm/h:} && y = 748.2 + 3623.9x,\ R^2 = 0.98724 \end{aligned} \quad (18)$$

Comparison of Theoretical Calculation and Experimental Results

According to the experimental conditions of scouring test on indoor slope model, reasonably select the parameters in function (11) and put them into the function to calculate the sediment erosion amount under different slope rates and rainfall intensities. The total sediment erosion after 60min of rainfall was selected for comparative analysis, and the theoretical calculation value was compared with the test results as shown in Figure 11.

By comparing the histogram, it can be found that the measured values were greater than the theoretical value under the rainfall intensity of 120mm/h, which is less than the theoretical value under the rainfall intensity of 150mm/h and 180mm/h. The reason for this phenomenon may be that slope collapse phenomenon exists under the rainfall intensity of 120mm/h, this part was collectively counted as the final sediment erosion. It could also be that the rainfall intensity is not

accurately controlled and the rainfall intensity is high. The regularities of the theoretical value and the measured value is consistent, both decrease with the increase of slope rate.

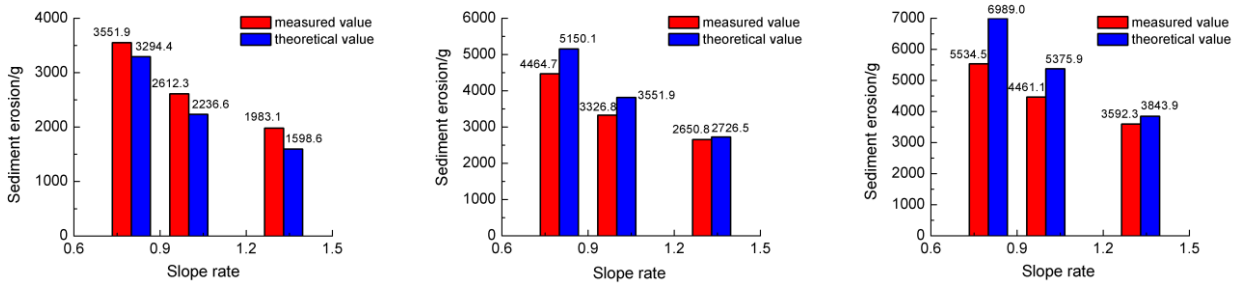

(a)Rainfall intensity-120mm/h (b)Rainfall intensity-150mm/h (c)Rainfall intensity-180mm/h

Fig. 11 - Comparison of theoretical and measured values

The relative errors under each working condition were collected, as shown in Table 3. It can be seen from the error statistics that the relative error under all other working conditions except for working condition 3 and 7 were all less than 18%. Among which the relative error of working condition 1, 8 and 9 were all less than 10% and that of working condition 8 was only 2.78%, the closest one between theoretical and measured values. The above results shown that the calculation model for sediment erosion derived from hydraulics and the energy method can accurately predict the actual sediment erosion to larger extent, which is of theoretical significance to practical external-soil spray seeding engineering.

Tab. 3- Error statistics

Working Condition	1	2	3	4	5	6	7	8	9
Relative Error/%	7.82	13.31	20.81	16.80	12.77	17.02	24.05	2.78	6.56

CONCLUSION

(1) The slope without vegetation is lack of anti-scouring ability after external-soil spray seeding engineering. A large number of gully is formed and slope erosion is relatively serious, surface erosion on the slope is mainly composed of layered erosion and rill erosion, with faster rill developmental rate and obvious surface corrosion phenomenon, effective measures must be taken to avoid engineering failure resulted from heavy rain.

(2) Sediment erosion of the slope under external-soil spray seeding increases with the increase of rainfall intensity and slope rate. With the increase of rainfall duration, the increase rate remains the same in the first 20min and gradually decreases after 20min. Meanwhile, carried out regression analysis of the experimental data, the equation $y = a + bln(x + c)$ can well adapt to the relationship between sediment erosion and rainfall duration, and the equation $y = a + bx$ can well adapt to the relationship among sediment erosion, rainfall intensity and slope rate.

(3) The calculation model applicable to the sediment of slope under external-soil spray seeding was derived from hydraulics and the energy method, which revised the traditional energy method formula to some extent. By comparing the theoretical value and measured data of the designed test, it is found that the relative error of the theoretical value and measured data under most working conditions is within 18%, which indicating that this calculation model can accurately predict the sediment of slope under external-soil spray seeding.

ACKNOWLEDGEMENTS

This study was substantially supported by the Natural Science Foundation of Chongqing, China (Grant No. cstc2017shmsA0581), the Special funding for Chongqing postdoctoral research project (Grant No. Xm2017006), the Science and Technology Plan Project of Chongqing planning and Natural Resources Bureau (Grant No. KJ-2017019) and the National Natural Science Foundation of China (Grant No.51408603).

REFERENCES

[1] Hongrong C., 1997. The Grass Planting Technology for Highway Slope Lawn and Its Function in Slope Protection. Rural Eco-environment, 1.
[2] Chen X.P., Jiang Y.L., Song Z.Q., 2007. The Use of Hydroseeding Technology for Side Slope Revegetation on Loess Plateau. *Research of Soil and Water Conservation*, 84(1),266-269.
[3] Li Y.Q., Wang X.R., 2017. Construction Technology of Slope Greening and Guest Soil Spraying. West-china Exploration Engineering, (10),1-4.
[4] Jiang Y., Yan T., Wei G.U., Liu B., Yu H.L., 2007. Assessment on Vegetation Restoration by Soil Spray Seeding Technique on Road Verge Slopes of Expressway. Journal of Highway and Transportation Research and Development, 24(7),147-152.
[5] Vargas-Luna A.E.S., Crosato A., Uijttewaal W.S., 2015. Effects of vegetation on flow and sediment transport: comparative analyses and validation of predicting models. Earth Surface Processes and Landforms, 40(2),157-176.
[6] Wang Y.M., Li Q.Z., Zhang L.J., 2009. Test on Soil Spray-Sowing for Subgrade Slope Scour Protection Of Expressway. Subgrade Engineering, (06):15-17.
[7] Horton R.E.,1945. Erosional development of streams and their drainage basins; hydrophysical approach to quantitative morphology. Geological society of America bulletin, 56(3),275-370.
[8] Ministry of Transport of the People's Republic, 2012. JTG/T D33-2012 Highway drainage design code 88 pp.
[9] Jakeman A.J., Hornberger G.M., 1993. How much complexity is warranted in a rainfall-runoff model?. Water Resources Research, 29(8),2637-2649.
[10] Chai G.H., Chai W., 2010. Analysis of Runoff Capacity on Surface of Highway Slope during Construction. Technology of Highway and Transport, (1):6-7, 11.
[11] Gholami V., Booij M.J., Nikzad T.E., 2018. Spatial soil erosion estimation using an artificial neural network (ANN) and field plot data. Catena, 163,210-218.
[12] Lagos-Avid., María Paz., Carlos A., Bonilla., 2017. Predicting the particle size distribution of eroded sediment using artificial neural networks. Science of the Total Environment, 581,833-839.
[13] Wu B., Wang Z., Zhang Q., 2018. Evaluation of shear stress and unit stream power to determine the sediment transport capacity of loess materials on different slopes. Journal of Soils and Sediments, 18(1),116-127.
[14] Li Z.G., Zhang X.Y., 2005. A energy-based erosion calculation model of the slopes for civil ergineering structures. China Civil Engineering Journal, 38(6),122-124, 136.
[15] Li F., Wu F.B., Wu J.T., 2016. Erosion Quantity Calculation and Experimental Study of Sandy Slope. Journal of Wuhan University of Technology(Transportation Science & Engineering), 40(2),289-292.
[16] Kavka P., Strouhal L., Jachymova B., 2018. Double size fulljet field rainfall simulator for complex interrill and rill erosion studies. The Civil Engineering Journal, (2),183-194.
[17] Meyer L.D., 2017. Rainfall simulators for soil erosion research. Soil erosion research methods. Routledge, 83-104.
[18] Lassu T.A.S., Seeger M., Peters P., 2015. The Wageningen rainfall simulator: Set-up and calibration of an indoor nozzle-type rainfall simulator for soil erosion studies. Land degradation development, 26(6),604-612.
[19] Lora M., Camporese M., Salandin P., 2016. Design and performance of a nozzle-type rainfall simulator for landslide triggering experiments. Catena, 140,77-89.

[20] Ministry of Housing and Urban-Rural Development of the People's Republic of China, 2016. GB 50014-2006Outdoor drainage design specification 258pp.
[21] Owoputi L.O., Stolte W.J., 1995. Soil detachment in the physically based soil erosion process: a review. Transactions of the ASAE (USA).
[22] Govindaraju R.S., Kavvas M.L., 1991. Modeling the erosion process over steep slopes: approximate analytical solutions. Journal of Hydrology, 127(1-4),279-305.

Articleno. 15

THE CIVIL ENGINEERING JOURNAL 2-2019

AN ANALYSIS OF DIURNAL AIR TEMPERATURE RANGE CHANGE AND ITS COMPONENTS IN SHAHEED BENAZIR ABAD SINDH

Nadeem ul karim Bhatti[1], Saleem Raza Samo[2], Manthar Ali Keerio[3], Ahsan Ali[4], Abdul Aziz Ansari[5]*

1. *Department of Civil Engineering, Quaid-e-Awam University College of Engineering, Science and Technology, Larkana, Sindh, Pakistan Email: knadeem_b@quest.edu.pk*
2. *Energy and Environment Engineering Department, Quaid-e-Awam University of Engineering, Science and Technology Nawabshah, Sindh, Pakistan. Email: sfaizsamo@yahoo.com*
3. *Department of Civil Engineering, Quaid-e-Awam University College of Engineering, Science and Technology, Larkana, Sindh, Pakistan Email: mantharali99@quest.edu.pk*
4. *Department of Civil Engineering, Quaid-e-Awam University College of Engineering, Science and Technology, Larkana, Sindh, Pakistan Email: ahsanone@gmail.com*
5. *Department of Civil Engineering, MUET, Shaheed Zulifquar Ali Bhutto Campus Khairpur, Sindh, Pakistan Email: dransari@quest.edu.pk*

ABSTRACT

A study has been carried out to analyse the temporal and seasonal patterns in the trends of diurnal air temperature range (DTR) and its components in Shaheed Benazir Abad for the time period 1996–2014.The magnitude, the slope and the significance of trends were investigated by using the linear regression method, the trend magnitude, the Mann-Kendall test and the Sen's estimator of slope. The Mann-Kendall test and Sen's estimator of slope were calculated by using Addinsoft's XLSTAT 2015 software. The hypothesis of Mann-Kendall test was investigated at 95% confidence level for all variables. The result shows that minimum temperature of Shaheed Benazir Abad has increased at the rate of 0.063°C per year during study period while the maximum temperature for all months exhibits no change. This increase of minimum temperature contributed to the decreasing trend of diurnal temperature range. The DTR decreased at the rate of 0.057°C /year in Shaheed Benazir Abad. The investigation of seasonal DTR trends revealed that Summer and Spring seasons also witnessed a decreasing trends at the rate of 0.26 °C/year and 0.047°C/year respectively. Winter and aseasons, on the other hand, have experienced the increasing trends of DTR at the rate of 0.136 °C/year and 0.115 °C/year respectively. It is found by MK test that Tmax (winter), Tmax (Spring) and Tmin (Spring) exhibited the significant positive trends at the rate of 0.21°C/year, 0.368 °C/year and 0.421°C/year respectively. The increasing trends of Tmax of winter and spring indicate that winter and spring are warmer now.

KEYWORDS

Diurnal temperature range, Climate change, Mann-Kendall test, the Sen's slope, Shaheed Benazir Abad

INTRODUCTION

It is important to investigate the regional climate variations in order to understand the exertion of complex influence of climate on natural system. This needs the quantitative and descriptive analysis of regional climate variations. The DTR is a suitable measure of climate

variations [1]. For central Sindh, no quantitative work has been carried out on diurnal basis. Diurnal temperature range (DTR) change has far reaching effects on natural ecosystem and socio-economic system because it is suitable sign of climatic change along with mean temperature changes [2]. Various researchers have conducted studies on diurnal temperature range and its components which show the variation of DTR in different regions of the world [3-6]. DTR demonstration on regional basis assumes special importance in context of global warming because its pattern is not uniform across the globe [7]. It has been observed that the warming of land surface is due to the relatively larger increase in daily minimum temperatures than in maximum temperatures [6, 8-9]. Various studies have indicated that the trend of DTR is decreasing globally since the mid of twenty century. The data of five stations (Islamabad, Lahore, Jhelum, Faisalabad and Multan) of Pakistan also display the decreasing trend of DTR [1, 10-11]. Dai et al. have studied the impacts of winds, soil moisture, cloud cover and precipitation on DTR [12]. They found that these hydrological variables have damping effects on DTR. Beside these variables, land cover and land use, deforestation, irrigation and urbanization of the region are identified as responsible factors for variation of DTR trend [13-15].Therefore the variation of DTR in different regions has a peculiar characteristics which is the outcome of complicated interaction of anthropogenic factors and local climatic conditions [1, 9-10].

The primary objective of this study is to examine the historical (1996–2014) variability in DTR and its components (Tmax and Tmin) over Shaheed Benazir Abad, Sind, Pakistan. Monthly and seasonal trends of DTR and its component are examined for whole period. Generally in Shaheed Benazir Abad, twelve months of year are divided in four seasons. So this study has considered four seasons, namely; winter (December- February), spring (March- April), summer (May -September), autumn (October- November).

DATA AND METHODOLOGY

Study Area Description

Geographically, Shaheed Benazir Abad is at the center of Sindh province of Pakistan. It is located between 25° 59' to 27° 15' North latitude and 67° 52' to 68° 54' East longitude .The Indus river flows at west border of district which is about 90 km long in the district. The net area of district is 451 thousand hectares out of which 189 thousand hectares are cropped areas. The study area is in tropical climate which is hotter environment. The total projected population of the city was 1676000 in 2014.The average rainfall in the district is 18.39 cm.

The surface air temperature data of Pakistan Meteorological Department (PMD) station at the airport of Nawabshah (OPNH-417490) was used for this study [16].

Methods

Surface air temperature Data on minimum maximum, monthly as well as annual have been compiled for the years 1996 – 2014. Diurnal Temperature Range (DTR) was calculated. Graphs were plotted for the maximum temperature, minimum temperature and DTR against the 12 months for each year. The monthly graphs were subsequently merged in a spreadsheet with the minimum, maximum and DTR against the 228 months and season-wise and also trend lines for each variable were plotted.

The many statistical procedures and techniques are used to detect and estimate of trends in different parameters of climate because the detecting and estimating the temporal and spatial trends are very important for various studies and monitoring program related to the environment.

The following four statistical methods were used to detect and estimate the trends of temperature.

The linear regression method

The behaviour of all parameters were computed and analysed with following linear trend model by using linear regression method [17-18].

$$y = \alpha x + \beta \quad (3.1)$$

$$\alpha = (\sum y_j \sum x_j^2 - \sum x_j \sum x_j y_j) / n \sum x_j^2 - (\sum x_j)^2 \quad (3.2)$$

$$\beta = n \sum y_j x_j - \sum x_j y_j / n \sum x_j^2 - (\sum x_j)^2 \quad (3.3)$$

Where x_j represents "years" and y_j represents “Parameters”

This method is frequently used to determine the trend. If the sign of α is positive then the trend is increasing and if the sign of α is negative then the trend is decreasing when the value of α is equal to zero then there is no trend in time series.

The trend magnitude

The second method was trend magnitude which was used to find out the magnitude of trend. The magnitude of trend was calculated by using the following equation.

$$\Delta y = y(\text{initial time}) - y(\text{terminate time}) \quad (3.4)$$

Where Δy indicates the total trend magnitude while y (initial time) and y (terminate time) represent the beginning and the end point of the trend equation respectively. However the positive and negative sign of Δy show the decreasing and increasing trend respectively.

The Mann-Kendall Test

This is the third statistical method which was used to analyse the significance of trends of all-time series. It is non-parametric test which is usually used in hydrological and climatological time series [19]. This test has been suggested by the World Meteorological Organization (WMO) for assessing the temporal trends in the time series of environmental data [20].This method is used to detect the statistically significant trends of long term data. There are two hypotheses to be tested in the Mann-Kendall test. One hypothesis is null hypothesis H_0 which means that the concerned time series has no trend while other one is alternative hypothesis Ha. This alternative hypothesis assumes that the concern time series possesses the significant trend.

The computation of the M-Kendall statistic is the main procedure for the application of MK test. The Mann-Kendall Statistic (S) is computed as follows:

$$S = \sum_{i=1}^{n-1} \sum_{j=i+1}^{n} Sign(Tj - Ti) \quad (3.5)$$

Where

$$\text{Sign}(Tj - Ti) = \begin{cases} 1 \; if \; (Tj - Ti) > 0 \\ 1 \; if \; (Tj - Ti) = 0 \\ -1 \; if \; (Tj - Ti) < 0 \end{cases} \quad (3.6)$$

Here Tj and Ti represent the data points at the time i and j respectively where j > i and *n* is the last period in the time series. If *n* > 10 then the Statistic *S* approximately normally distributed with the mean of *S* is zero and the variance statistic Var (*S*) is computed as:

$$V(S) = 1/18 \; n(n-1) \; (2n+5) \quad (3.7)$$

Kendall's tau (τ) is another statistic which is obtained by applying Mann-Kendall test. It represents the correlation between two variables which means the value of tau describes the relationship between two variables [21]. Mann-Kendall Tau is given by:

$$\tau = S / n\,(n-1) / 2 \qquad 3.8$$

Here,

S represents the Mann-Kendall statistic and

n shows the number of data pairs

The probability p is determined to know the confidence level in the hypothesis of Mann-Kendall test and it is computed as follows:

$$p = [1-f\,(Z)] \cdot 100 \qquad 3.9$$

Z is standard normal test statistics which is computed by using following equation:

$$Z = \begin{cases} \frac{S-1}{\sigma} & if\ S > 0 \\ 0 & if\ S = 0 \\ \frac{S+1}{\sigma} & if\ S < 0 \end{cases} \qquad 3.10$$

In the equation 3.9, *f*(Z) is a function of probability density and it is calculated by following equation:

$$f(Z) = 1/\sqrt{2\pi}\ exp\ (-z^2/2) \qquad 3.11$$

The value of p is very important for accepting and rejecting the hypothesis of Mann-Kendall test. The level of chosen significance is represented by Alpha (α = 0.05). If the calculated value of p is greater than the value of Alpha then H_o cannot be rejected.

If the value of p is less than the value of Alpha then Ha should be accepted [22].

The Sen's estimator of slope

This method is used to calculate the magnitude of linear trends which exist in the time series data. The slope (m) of all pairs of data is computed by following equation.

$$mi = xj-xk / j-k \quad i = 1,\ldots..,N \qquad 3.12$$

In the above equation, x_j and x_k are used to represent data values at the time j and k respectively where j is greater than k. The Sen's estimator of slope is the median of these N values of m_i and computed by following equation.

$$Q_{med} = \begin{cases} \frac{1}{2}\left(m_{N/2} + m_{\frac{N+2}{2}}\right) \text{if N is even} \\ m_{(N+1/2)} \text{ if N is odd} \end{cases} \qquad 3.13$$

The sign of Q_{med} indicates the reflection of trend of time series data. The positive sign of Q_{med} represents the increasing trend while negative sign shows the decreasing trend [23]. Addinsoft's XLSTAT 2015 is the software which was used for Mann-Kendall test and Sen's estimator of slope. The hypothesis was tested at 95% confidence level for all variables.

RESULTS AND ANALYSIS

Trend analysis by linear regression and trend magnitude

The trends of monthly diurnal air temperature range, maximum air temperature, and minimum air temperature of the Shaheed Benazir Abad have been illustrated in Figure 1 from years 1996–2014. A steadily decreasing trend of DTR can be identified statistically, with the decreasing rate of 0.057°C /year during study period despite the fluctuations from year to year because of various climatic factors.

(a) Monthly DTR

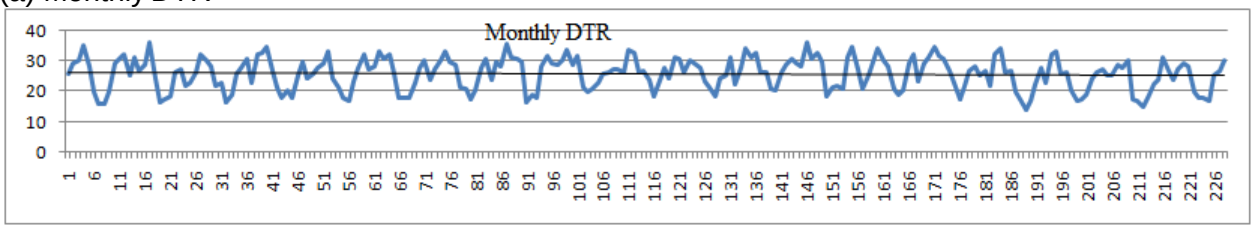

(b)MonthlyTmax

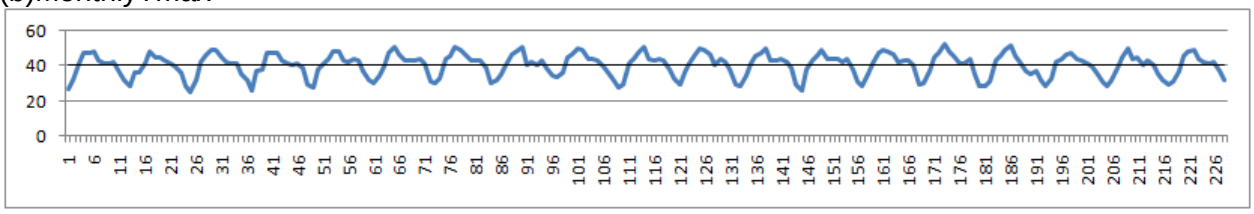

(c)MonthlyTmin

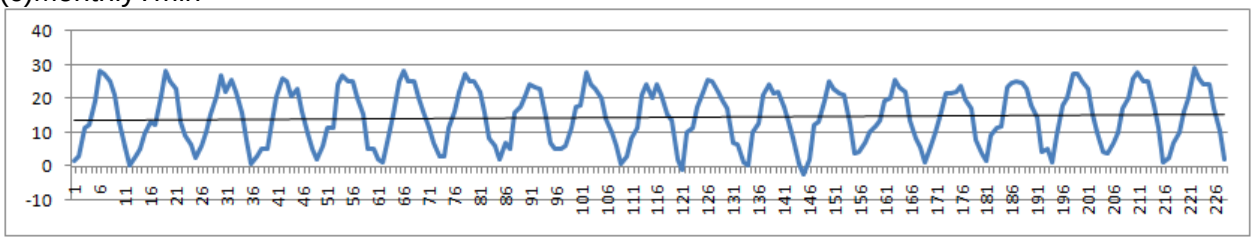

Fig.1- All month temperature variations in Shaheed Benazir Abad (a) monthly diurnal air temperature (b) maximum air temperature (c) minimum air temperature.

The rate of change of the monthly maximum air temperature is almost zero during study period but the monthly minimum air temperature is rising at the rate of 0.063158°C per year as demonstrated in Figure 1. So, the significantly increasing trend of minimum temperature contributes to the decrease of DTR trend. This decrease in DTR may have profound effect on human comfort and as well as on the agricultural ecosystem of this region. The increase in minimum temperature prevents the nocturnal cooling which is very essential to neutralize the maximum temperature of hot day especially during the summer season.

The special report of an IPCC also notes that the economies of agrarian countries are under threat due to global warming of 1.5°C above pre-industrial levels [24]. This change has reaching effects for the strength and timing of precipitation patterns of this region. The energy and agriculture sectors of this region are also adversely affected by climate change which are exclusively depend on water [25].

As temperate change has seasonal patterns, time series of seasonal DTR, Tmax, and Tmin of the SBA were analysed to investigate the seasonal characteristics of DTR change, as illustrated in Figures. 2–5.Trends of seasonal DTR, Tmax and Tmin were summarized in Table1. Obviously, from Figures. 2–5 and Table1, Tmax and Tmin have different seasonal behaviours, and DTR

change demonstrates seasonal patterns. DTR has decreasing trend in spring and summer seasons, with the highest decrease rate in summer. While it shows the increasing trend in winter and autumn season, with the highest increasing rate in winter. In summer, Tmax has a highest decreasing rate but Tmin shows the lowest increasing rate among the four seasons, so DTR demonstrates the most significantly decreasing trend, at the rate of 0.263158 °C/year in this season. In winter season, the ascending slopes of trend lines of all parameters, DTR, Tmax and Tmin acknowledge the increase of temperature in this region. However Tmax demonstrates the highest increasing rate among all parameters in this season. Tmax increases with the rate of 0.210526 °C/year in winter season which indicates that winter in SBA is getting warmer. The DTR has shown the decreasing trend with the rate of 0.047368 °C/year but Tmax and Tmin have increasing trends during spring season. The winter season has also become hotter like winter. Tmax and Tmin demonstrate the decreasing trends during Autumn but DTR shows the increasing trend due to more rate of decreasing trend of Tmin than the decreasing rate of Tmax .

Tab. 1 - Trends of seasonal monthly maximum temperature(Tmax), minimum temperature(Tmin), and diurnal air temperature range(DTR) (unit: ^{o}C/yr) of the SBA.

	Winter	Spring	Summer	Autumn
Tmax	0.210526	0.368421	- 0.473684	-0.368421
Tmin	0.084211	0.421053	0.023684	- 0.421053
DTR	0.136842	- 0.047368	- 0.263158	0.115789

(a) Seasonal DTR (winter)

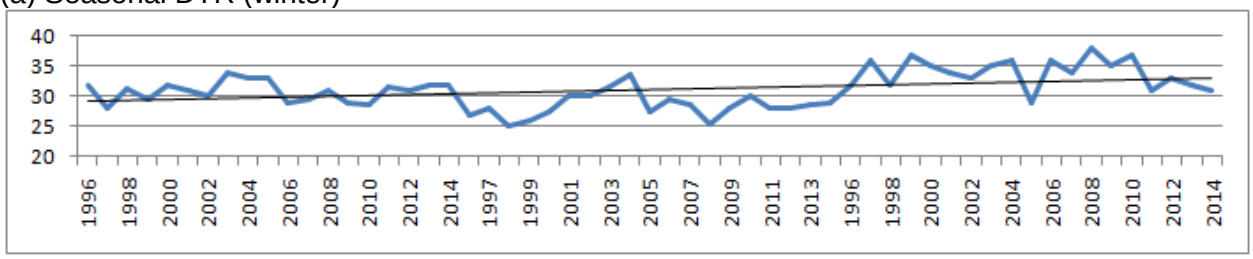

(b) Seasonal Tmax (winter)

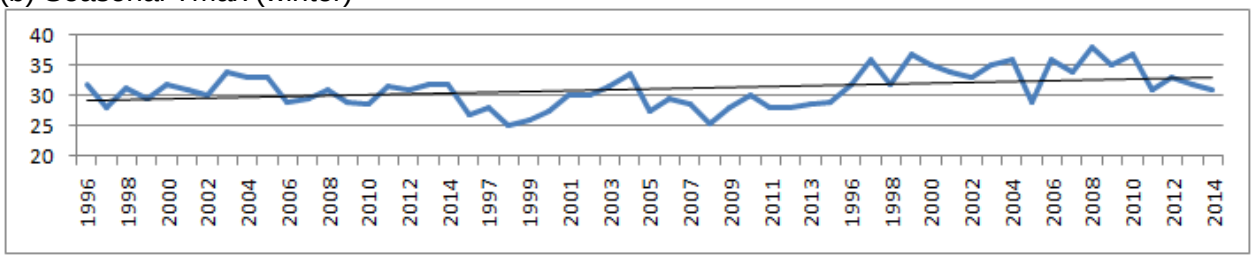

(c) Seasonal Tmin (winter)

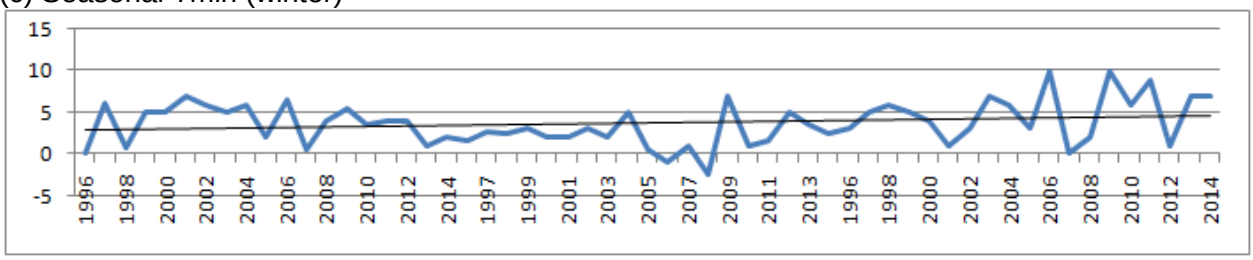

Fig. 2 - Air temperature variation of winter season in SBA (a) diurnal air temperature range (DTR) (b) maximum air temperature (Tmax) (c) minimum air temperature(Tmin)

DOI 10.14311/CEJ.2019.02.0015

(a) Seasonal DTR (spring)

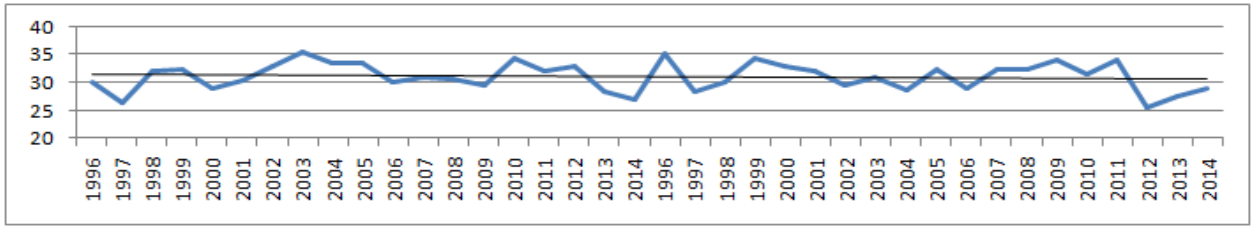

(b) Seasonal Tmax (spring)

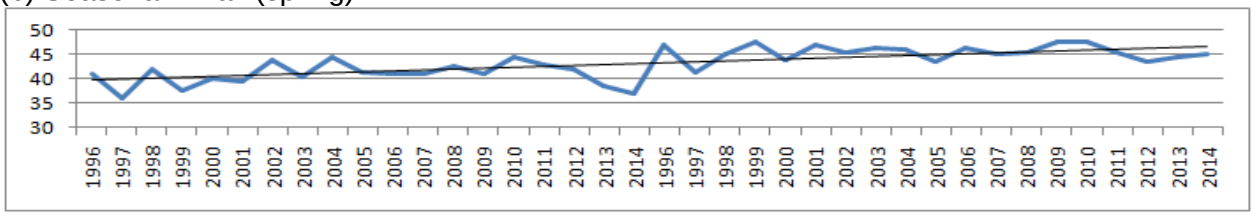

(c) Seasonal Tmin (spring)

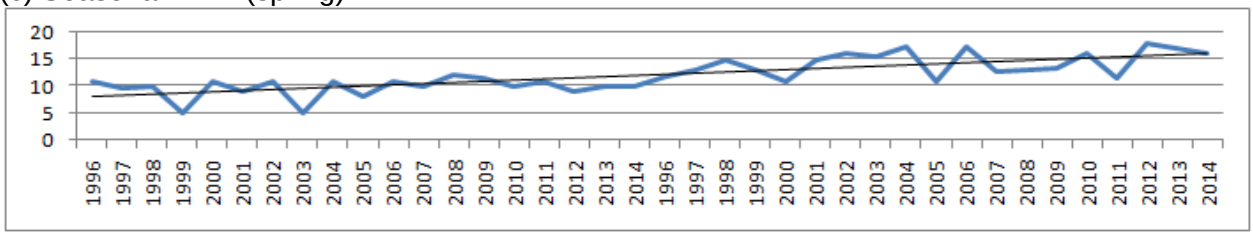

Fig. 3 - Air temperature variation of Spring season in SBA (a) diurnal air temperature range (DTR) (b) maximum air temperature (Tmax) (c) minimum air temperature(Tmin)

(a) Seasonal DTR (summer)

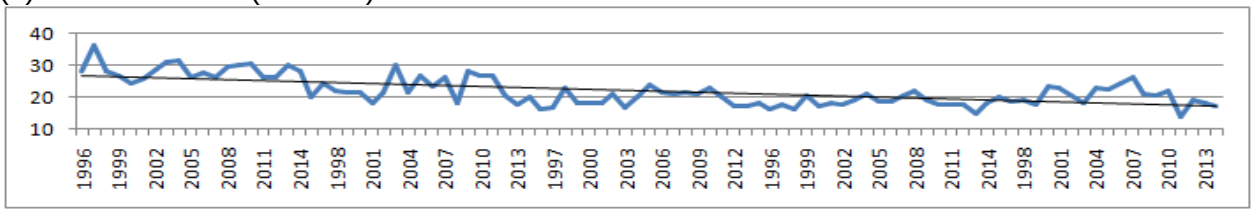

(b) Seasonal Tmax (summer)

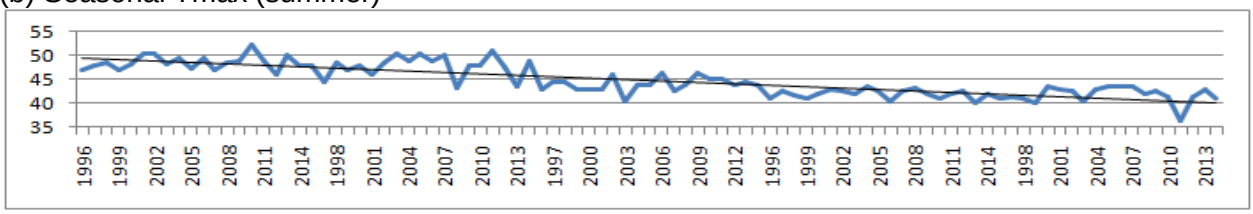

(c) Seasonal Tmin (summer)

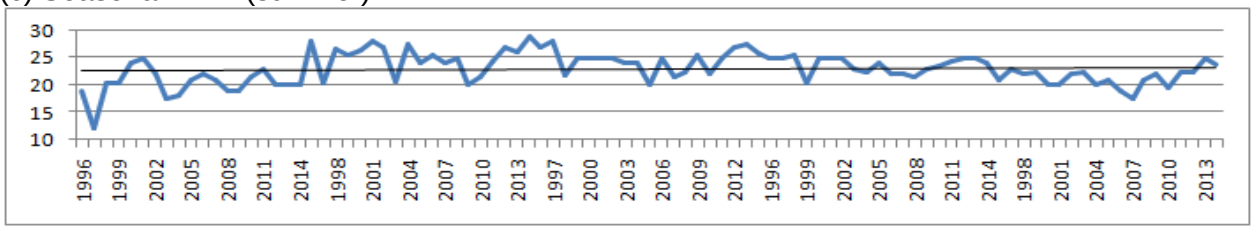

Fig. 4 - Air temperature variation of Summer season in SBA (a) diurnal air temperature range (DTR) (b) maximum air temperature (Tmax) (c) minimum air temperature(Tmin)

(a) Seasonal DTR (autumn)

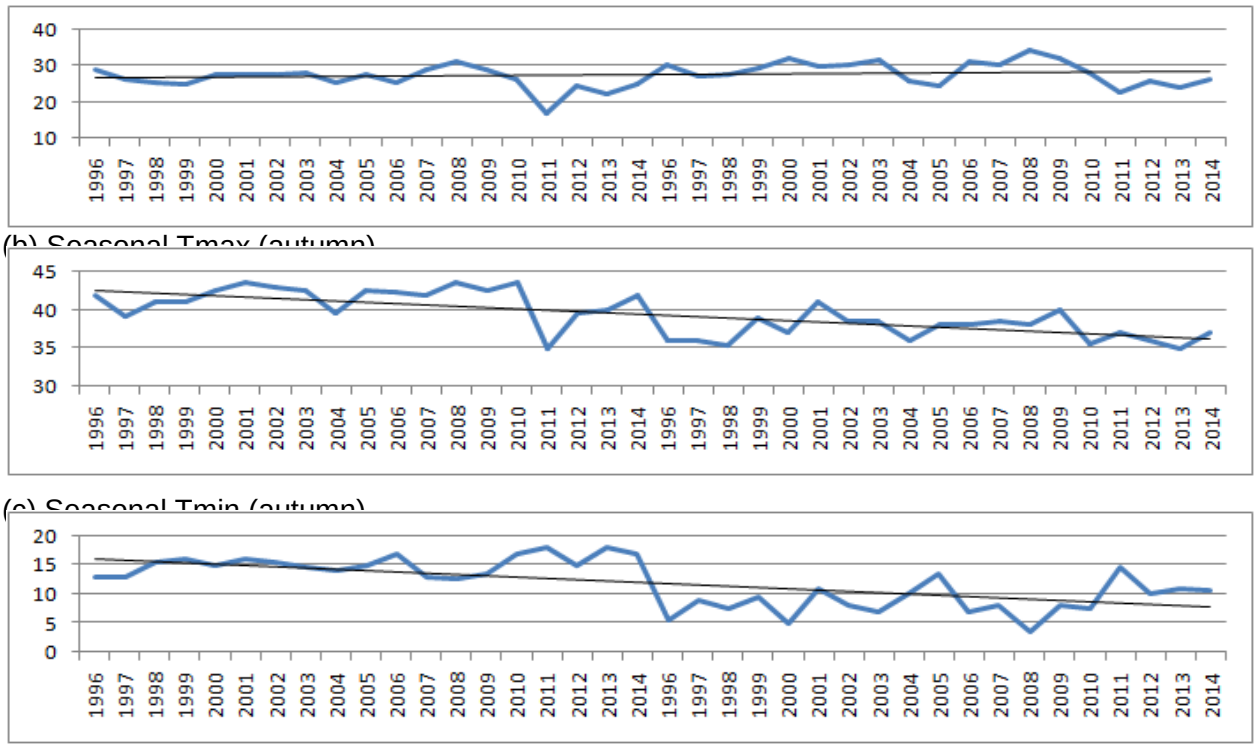

Fig. 5 - Air temperature variation of Autumn season in SBA (a) diurnal air temperature range (DTR) (b) maximum air temperature (Tmax) (c) minimum air temperature(Tmin)

Trend analysis by Mann-Kendall test and Sen's estimator

The Mann-Kendall test was performed on the all parameters in order to find out the statistics regarding the trends of temperature in Shaheed Benazir Abad. The results were summarized in the Table 2 and Table3 which were obtained by using Mann-Kendall test on the all parameters of temperature. The significance level was taken same (α = 5%) for all parameters of temperature.

Tab. 2 - Statistics by Mann-Kendall test of Temperature

Parameters	Mann-Kendall Statistic(S)	Kendall's Tau	P-value	Alpha	Test Interpretation
Tmax	-96.00	-0.004	0.533	0.05	Accept H_o
Tmin	571	0.022	0.309	0.05	Accept H_o
DTR	-1186	-0.047	0.850	0.05	Accept H_o
Tmax(winter)	355	0.228	0.007	0.05	Reject H_o
Tmin(winter)	129	0.083	0.188	0.05	Accept H_o
DTR(winter)	201	0.134	0.075	0.05	Accept H_o
Tmax(Spring)	339	0.491	0.0001	0.05	Reject H_o
Tmin(Spring)	401	0.591	0.0001	0.05	Reject H_o
DTR(Spring)	-38	-0.055	0.679	0.05	Accept H_o
Tmax(Summer)	-2610	-0.596	1	0.05	Accept H_o
Tmin(Summer)	-115	-0.026	0.643	0.05	Accept H_o
DTR(Summer)	-1751	-0.397	1	0.05	Accept H_o
Tmax(Autumn)	-326	-0.474	1	0.05	Accept H_o
Tmin(Autumn)	-253	-0.365	0.999	0.05	Accept H_o
DTR(Autumn)	87	0.125	0.139	0.05	Accept H_o

Tab. 3 - Nature of trends and their magnitudes

Parameters	Mann-Kendall Test Nature	Trend Significance	Sen's slope	Magnitude of Trend (°C/year)
Tmax	No change	No	0.00	0.00052
Tmin	Positive	No	0.003	0.06315
DTR	Negative	No	-0.006	0.05789
Tmax(winter)	Positive	Yes	0.067	0.21052
Tmin(winter)	Positive	No	0.018	0.084211
DTR(winter)	Positive	No	0.044	0.136842
Tmax(Spring)	Positive	Yes	0.182	0.36842
Tmin(Spring)	Positive	Yes	0.214	0.42105
DTR(Spring)	Negative	No	-0.025	- 0.04736
Tmax(Summer)	Negative	No	-0.094	- 0.473684
Tmin(Summer)	No change	No	0.00	0.023684
DTR(Summer)	Negative	No	-0.10	- 0.263158
Tmax(Autumn)	Negative	No	-0.168	-0.368421
Tmin(Autumn)	Negative	No	-0.206	-0.421053
DTR(Autumn)	Positive	No	0.056	0.115789

The results revealed that seven parameters have positive trends and six parameters have negative trends while two parameter show no change in trends which are indicated in Table 3. The P-values of twelve parameters are greater than Alpha value (significance level) as indicated in Table 2 which means that one cannot reject the hypothesis H_o. These values show that twelve parameters have insignificant trends. While the P-value of three parameters of time series of temperature are less than the value of Alpha which are interpreted that the hypothesis H_o should be rejected. It means that the significant positive trends were detected for Tmax(winter), Tmax(spring) and Tmin(spring) in Shaheed Benazir Abad during study period. The warming trend of winter season was also confirmed by MK test. The Sen's estimator of slope was used to find out the magnitude of slopes of trends of temperature in the study area. The result shows that Tmin(spring) exhibits significant increasing trend with slope of 0.214 and Tmin (Autumn) indicates the decreasing trend with slope of 0.206.

CONCLUSIONS

The all months and seasonal variation of Diurnal temperature range was investigated in Shaheed Benazir Abad from 1996 to 2014 by using the linear regression method, the trend magnitude, the Mann-Kendall test and the Sen's estimator of slope. The result reveals that there is decreasing trend in all months DTR which means that the variation range of temperature is reducing in the past 19 years, as demonstrated in this paper. A steadily decreasing trend of DTR over the SBA was identified statistically. The minimum temperature increased by 0.0631°C/year across SBA in the past 19 years, whereas the DTR decreased by 0.05°C/year which was mainly due to the increasing rate of minimum temperature. The trends of DTR, maximum air temperature and minimum air temperature have significant seasonal differences. The summer season demonstrate higher DTR decreasing rate than the spring season while, in winter and autumn, the DTR shows increasing trend. The significant positive trends were detected by MK test for Tmax(winter), Tmax(spring) and Tmin(spring) in Shaheed Benazir Abad during study period which means that the winter and spring are warmer now than in the previous years.

REFERENCES

[1] Shen, X., Liu, B., Li, G., Wu, Z., Jin, Y., Yu, P. and Zhou, D., 2014. Spatiotemporal change of diurnal temperature range and its relationship with sunshine duration and precipitation in China. Journal of Geophysical Research: Atmospheres, 119(23)..DOI: 10.1002/2014JD022326

[2] Lewis, S.C. and Karoly, D.J., 2013. Evaluation of historical diurnal temperature range trends in CMIP5 models. Journal of Climate, 26(22), pp.9077-9089..https://doi.org/10.1175/JCLI-D-13-00032.1

[3] Qu, M., Wan, J. and Hao, X., 2014. Analysis of diurnal air temperature range change in the continental United States. Weather and Climate Extremes, 4, pp.86-95. https:// doi.org/10.1016/ j.wace. 2014 .05.002

[4]. Vose, R.S., Easterling, D.R. and Gleason, B., 2005. Maximum and minimum temperature trends for the globe: An update through 2004". Geophysical Research Letters, 32(23)..DOI: 10.1029/2005GL024379

[5] Roy, S.S. and Balling, R.C., 2005. Analysis of trends in maximum and minimum temperature, diurnal temperature range, and cloud cover over India. Geophysical Research Letters, 32(12). DOI: 10.1029/2004GL022201

[6] Folland, C.K., Karl, T.R. and Vinnikov, K.Y., 1990. Observed climate variations and change. Climate change: the IPCC scientific assessment, 195, p.238.

[7] Rai, A., Joshi, M.K. and Pandey, A.C., 2012. Variations in diurnal temperature range over India: under global warming scenario. Journal of Geophysical Research: Atmospheres , 117(D2). DOI: 10.1029/2011JD016697

[8] Braganza, K., Karoly, D.J. and Arblaster, J.M., “Diurnal temperature range as an index of global climate change during the twentieth century”. Geophysical Research Letters ,31 (13) .2004. DOI: 10.1029/2004 GL019998

[9]. Easterling, D.R., Horton, B., Jones, P.D., Peterson, T.C., Karl, T.R., Parker, D.E., Salinger, M.J., Razuvayev, V., Plummer, N., Jamason, P. and Folland, C.K., 1997. Maximum and minimum temperature trends for the globe. Science, 277(5324), pp.364-367..DOI: jstor.org/stable/2892861

[10] Chaudhry, Q.U.Z., Mahmood, A., Rasul, G. and Afzaal, M., 2009. Climate change indicators of Pakistan. Technical Report No. PMD-22/2009, pp 1-43.

[11] Rebetez, M. and Beniston, M., 1998. Changes in sunshine duration are correlated with changes in daily temperature range this century: An analysis of Swiss climatological data. Geophysical Research Letters, 25(19), pp.3611-3613.

[12] Dai, A., Trenberth, K.E. and Karl, T.R.,. 1999. Effects of clouds, soil moisture, precipitation, and water vapor on diurnal temperature range. Journal of Climate, 12(8), pp.2451-2473. https ://doi.org /10.1175/ 1520-0442

[13] Englehart, P.J. and Douglas, A.V.,Changing behavior in the diurnal range of surface air temperatures over Mexico”. Geophysical Research Letters, 200532(1). DOI: 10.1029/2004GL021139

[14] Wang, K., Ye, H., Chen, F., Xiong, Y. and Wang, C., 2012. Urbanization effect on the diurnal temperature range: different roles under solar dimming and brightening. Journal of Climate, 25(3), pp.1022-1027. D.O.I.org/10.1175/JCLI-D-10-05030.1

[15] Lobell, D.B. and Bonfils, C., 2008. The effect of irrigation on regional temperatures: a spatial and temporal analysis of trends in California, 1934–2002. Journal of Climate, 21(10), pp.2063-2071. https://doi.org/10.1175/2007JCLI1755.1

[16]. TuTiempo. Average annual climate values 1996-2014.Available from: http://www.tutiempo.net/en/Climate

[17] Ahmad, I., Zhaobo, S., Weitao, D. and Ambreen, R., 2010. Trend analysis of January temperature in Pakistan over the period of 1961-2006: Geographical Perspective. Pakistan Journal of Meteorology, 7(13), pp.11-22.

[18] Sadiq, N. and Qureshi, M.S., 2010. Climatic variability and linear trend models for the five major cities of Pakistan. Journal of Geography and Geology, 2(1), p.83.

[19] Martinez, C.J., Maleski, J.J. and Miller, M.F., 2012. Trends in precipitation and temperature in Florida, USA . Journal of Hydrology, 452, pp.259-281.

[20] Shi, P., Ma, X., Chen, X., Qu, S. and Zhang, Z., 2013. Analysis of variation trends in precipitation in an upstream catchment of Huai River. Mathematical Problemsin Engineering, DOI. org/10. 1155/2013/ 929383.

[21] Yadav, G. and Mishra, D.N., 2015. Air Pollution Trend Analysis Using Sen Estimator Method. International Journal of Advanced Research in Computer Science and Software Engineering, 5(7), pp.1073-1080.

[22] Gavrilov, M.B., Marković, S.B., Jarad, A. and Korać, V.M., 2015. The analysis of temperature trends in Vojvodina (Serbia) from 1949 to 2006. Thermal Science, 19 (suppl. 2), pp.339-350. D.O.I. 10.2298/TSCI150207062G

[23] Tabari, H. and Talaee, P.H. 2011. Analysis of trends in temperature data in arid and semi-arid regions of Iran. Global and Planetary Change, 79(1), pp.1-10.

[24] O. Hoegh-Guldberg,D. Jacob, M. Taylor, M. Bindi, S. Brown, I. Camilloni, A. Diedhiou, R. Djalante, K. Ebi, F. Engelbrecht, J. Guiot, Y. Hijioka, S. Mehrotra, A. Payne, S. I. Seneviratne, A. Thomas, R. Warren, G. Zhou, 2018, Impacts of 1.5°C global warming on natural and human systems. In: Global warming of 1.5°C. An IPCC Special Report on the impacts of global warming of 1.5°C above pre-industrial levels and related global greenhouse gas emission pathways, in the context of strengthening the global response to the threat of climate change, sustainable development, and efforts to eradicate poverty [V. Masson-Delmotte, P. Zhai, H. O. Pörtner, D. Roberts, J. Skea, P.R. Shukla, A. Pirani, W. Moufouma-Okia, C. Péan, R. Pidcock, S.

Connors, J. B. R. Matthews, Y. Chen, X. Zhou, M. I. Gomis, E. Lonnoy, T. Maycock, M. Tignor, T. Waterfield (eds.)]. In Press.
[25] Y. Hijioka et al. 2014. Climate Change 2014: Impacts, Adaptation, and Vulnerability-Asia. Cambridge, United Kingdom, and New York, USA: Cambridge University Press. p. 1350.

Article no. 16

THE CIVIL ENGINEERING JOURNAL 2-2019

NUMERICAL ANALYSIS ABOUT BLASTING EFFECT OF DIGITAL DETONATOR AND MILLISECOND DETONATOR IN UPPER AND LOWER CROSS TUNNELS

LUO Gang[1], PAN Shao-kang[1], JIA Hang-hang[1], ZHANG Yu-long[1], CHEN Liang[2,3]

1. *Chang'an University,School of Highway, Xi'an, Shanxi, China; luogang@chd.edu.cn*
2. *Changsha University of Science & Technology,School of Civil Engineering, Changsha, Hunan, China;1113852332@qq.com*
3. *Guangxi Communications Investment Group, Nanning, Guangxi, China;*

ABSTRACT

In order to study on the vibration effect of the blasting in the upper and lower cross tunnels, depress the impact of blasting vibration on existing adjacent tunnel and acquire the sound way of tunnel blasting construction, the finite element software LS-DYNA was adopted to calculate what vibration effect of existing tunnel would be generated by the different detonation modes (simultaneous initiation and hole-by-hole initiation) and the different cut modes (parallel cut and oblique cut). In general, the results of numerical simulation compared with the results measured in real, they are generally consistent. Results show that the vibration velocity of hole-by-hole initiation of digital electronic detonator is 40% lower than ordinary simultaneous initiation of millisecond detonator, and the vibration acceleration is reduced by 24%. As regards vibration displacement, the distinction between the two detonation modes is small. The rule of velocity decay with increasing distance from the initiating position is similar in this two cases. Meanwhile, the vibration velocity of oblique cut is lower than parallel cut. But, for the vibration acceleration, the oblique cut is 15% higher than parallel cut. For oblique cut, the seismic waves show a pronounced periodicity and the energy is relatively concentrated. The fact is quite opposite when the parallel cut applied. In the case of explosion of hard rock strata, the effect of oblique cut is better than parallel cut.

KEY WORDS

Tunnel engineering, Explosion vibration, Numerical simulation, LS-DYNA

INTRODUCTION

In recent years, with the rapid economic growth in China and the booming development of the national transport industry, the subway construction has become an essential development project in large and medium-sized cities. In that cities, such as Chongqing, Xiamen and Qingdao, the drilling and blasting method usually used to subway construction in hard rock strata. In addition,

due to the outward expansion of the city and the characteristics of the original terrain, a lot of “mountain city” appeared. As a result, many mountain hard rock tunnels have emerged in the construction of municipal roads and subway traffic. So, the surrounding buildings, especially cultural building relics, will be impacted by blasting construction in central urban area. How to choose a reasonable tunnel blasting method to reduce the impact of blasting vibration on the surrounding buildings is a considerable issue.

As the science and computer technology progressed, the method of numerical simulation of blasting vibration effect and evaluating structural safety is widely used. Singh P K (2002) delved into the destruction problems of underground tunnels in the effect of adjacent tunnel blasting[1]. There are research results indicate that blasting vibrations induced by a new tunnel excavation might cause spalling, fissures, or even collapse of existing tunnel linings[2]. Yao et al. (2004) conducted numerical simulations on the blasting construction process of the road tunnels with small spacing under different support conditions[3]. Zhao et al. (2007) studied the response of blasting vibration of neighbourhood cross tunnel by numerical simulation and determined the influence range of blasting vibration[4]. Wen (2008) established the 3D model by MIDAS/GTS software to simulate the situation that the existing tunnel was impacted by the burst of adjacent tunnel. Under the different tunnel spacing and different surrounding rock grades, the vibration velocity, stress and strain of the lining and surrounding rock of adjacent tunnel during blasting were evaluated[5]. Li[6] (2010), Yang[7] (2011) and Zhang[8] (2011) used the finite element program ANSYS/LS-DYNA to implement the numerical simulations of tunnel blasting excavation in many different situations. The dynamic effect of the adjacent tunnel lining caused by blasting seismic wave was explored from two aspects -- the spatial distribution and time history of the particle vibration velocity and the spatial distribution and time history of the element strain. Sambuelli[9] and Liang[10] et al. have been studied some empirical or theoretical methods to calculate the blasting vibration velocity maximum based on in situ monitoring data. Zou (2011) simulated the tunnel blasting by using ANSYS/LS-DYNA and got the peak values of blasting vibration at different measuring points, and verified the feasibility of numerical simulation method for predicting the blasting vibration peak velocity[11]. Utilizing the empirical formula of the predecessor, Liang et al. (2012) calculated the blasting load and simplified it into 8 triangular-shaped impulsive loads and adopted numerical simulation to explain the impact of the newly built railway tunnel blasting on the existing railway tunnel. Observed results surfaced that the additional stress and the total stress peak appeared at the tunnel cross-section of the vault and wall feet[12]. Meng et al. (2015) inquired into the dynamic response of tridimensional cross tunnel blasting construction under many circumstances[13]. Yu et al. (2014) adopted numerical simulation to analyse the construction of Zoumagang diversion tunnel intersection. Based on the simulation results, the safety control area and corresponding construction scheme of the intersection were obtained[14]. Cai et al. (2015) availed of ANSYS/LS-DYNA software to simulate the construction that the Dawangshan tunnel built on the existing Shawan supply tunnel, and indicated the stress and particle vibration velocity of the supply tunnel below[15].

Currently, on the part of numerical simulation, there are mainly three methods for calculating tunnel blasting . Firstly, blasting vibration load in the form of uniform triangular pressure load acting on the tunnel wall along the normal direction. Secondly, blasting vibration load is applied in the form of equivalent load on the plane defined by the concentric line of the same row of blast holes and the

axis of the blast hole. The range of pressure effect is equal to the length of the charge section in the blast-hole. Thirdly, there will do a dynamic solution, when the blast-hole wall is applied the blasting vibration load which varies with the time history. Among the three methods, the third method can simulate the blasting process of blast-hole during tunnel excavation. In this paper, this method will be used to clarify the blasting process of the tunnel provided with a certain number of cutholes.

METHODS

Project profile

From FSDK11+ 205 to FSDK11+ 684, the excavation mileage of Shijingshan tunnel in Fengsha railway rebuilding project is 479 meters. The concealed excavation is located in the city center area. The depth of the tunnel is 4~32m. At the FSDK11 + 460 mileage, the new tunnel is built below the civil air defence tunnel (It is 2.17m from the civil air defence tunnel. The size of the civil air defence tunnel is 2m wide and 2.4m high.). The plane position of the new tunnel is approximately orthogonal to the civil air defence tunnel, as Figure 1 shows below. For the concealed excavation of new tunnel, the design surrounding rock grade is V. With the drilling and blasting method adopted, the three steps of excavation is applied in the new tunnel construction. The excavation footage is 0.8m, the number of cut holes on the top level is 6. The blast-hole depth is 1m. The single hole charge amount is 0.45kg. The engineering geology is mainly tufa at weak weathered and moderate weathered , uniaxial compression strength reach 109MPa.To ensure the safety of civil air defence tunnel during the construction of tunnel blasting, blasting vibration monitoring is conducted on the civil air defence tunnel.

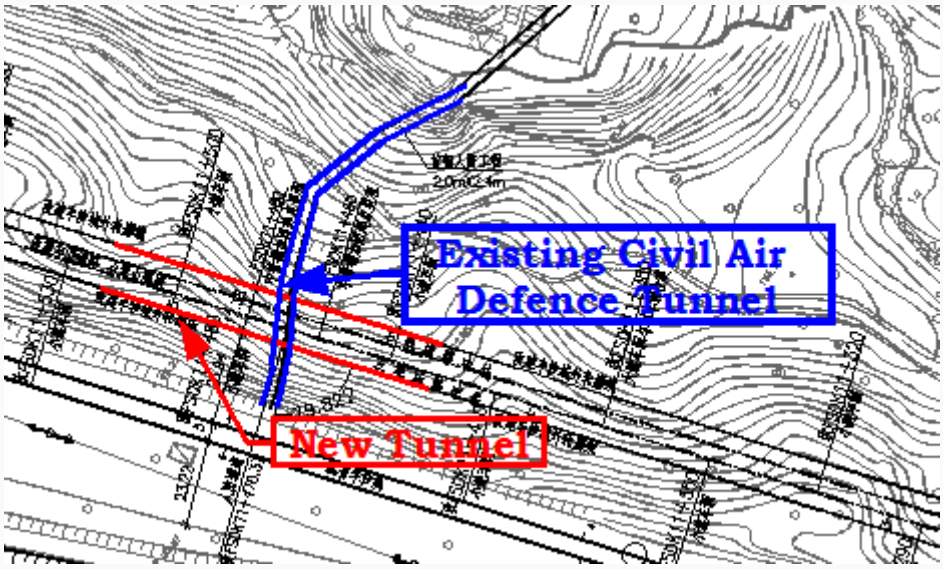

Fig.1 – Location relationship between new tunnel and civil air defence tunnel

Numerical simulation and analysis

Now, the major control blasting technique adopted by the drilling and blasting construction in the mountain tunnel is smooth blasting. The sectional blasting of initiation of millisecond detonator is the core content of smooth blasting. The cutholes are detonated at the same time in the sectional

blasting. The charge weight per delay interval is large, so the greater impact will be generated on the surrounding structure. The time interval between holes can be precisely controlled in the hole-by-hole initiating of digital detonator. This blasting method exploits the effect of the seismic wave among holes superimposed destructive interference to significantly reduce the vibration influence. Moreover, different cut modes also have different vibration effects on adjacent structures. Under normal circumstances, due to the large charge amount of cutholes and cutholes grasped by the rock mass, so the vibration velocity of neighbouring structures caused by cuthole blasting seismic wave is larger than the satellite hole and periphery hole. Therefore, this paper aims to reduce the vibration velocity of neighbouring structures caused by cuthole. And LS-DYNA will be adopted to study the detonation modes and cut modes of cutholes.

Element and arithmetic

Surrounding rock, explosives and air will employ solid-164 element. The rock uses constant stress solid element. This element uses pure Lagrange algorithm. When the structural deformation is huge, it is possible to cause severe distortion of the finite element mesh, which causes problems in numerical calculation, so the algorithm is not suitable for air and explosives. The coupling between explosives and air uses the ALE (Arbitrary Lagrangian-Eulerian) algorithm. The ALE algorithm can handle similar grid distortions arose from large deformations, such as explosives and air. The interaction among the air, rock and explosives will be considered by fluid-solid coupling method. There are usually two methods for fluid-structure interaction, one is common node and the other is by *CONSTRAINED_LAGRANGE_IN_SOLID. The first numerical simulation method is used in this paper. The air and explosives material are bound in an element algorithm with the keyword of *ALE_MULTI_MATERIAL_GROUP. Set the detonation point coordinates and detonation time by keyword of *INITIAL_DETONATION. Then, the termination time of blast set to 0.03s by keyword of *CONTROL_TERNITION.

Material parameters and equation of state

Air is defined by the *MAT_NULL material model and the *EOS_LINEAR_POLYNOMIAL linear polynomial equation of state. The equation expression is as follows.

$$P = C_0 + C_1\mu + C_2\mu^2 + C_3\mu^3 + (C_4 + C_5\mu + C_6\mu^2)E \qquad (1)$$

Where: $\mu = \rho/\rho_0 - 1$, ρ and ρ_0 are the mass density and the reference mass density, respectively. E is the material internal energy per unit volume. C_0, C_1, C_2, C_3, C_4, C_5, and C_6 are all real constants. The parameters are valued according to the ideal gas state equation (Table 1). V_0 represents the initial relative volume.

Tab. 1 - Material parameters of air[16]

ρ (kg/m^3)	C_0	C_1	C_2	C_3	C_4	C_5	C_6	E (J/m^3)	V_0
1.290	0	0	0	0	0.4	0.4	0	2.5×10^5	1.0

With *MAT_PLASTIC_KINEMATIC model adopted, surrounding rock is considered as the ideal elastic-plastic material. Yield condition:

$$\phi = \frac{1}{2}\xi_{ij}^2 - \frac{\sigma_y^2}{3} = 0 \qquad (2)$$

Where: stress deviator tensor $\xi_{ij} = s_{ij} - a_{ij}$, yield stress $\sigma_y = [1 + (\frac{\dot{\varepsilon}}{C})^{\frac{1}{P}}](\sigma_0 + \beta E_P \varepsilon_{eff}^p)$,

among left equation, s_{ij} is Cauchy ' s stress tensor, P and C are constants input. σ_0 and β are the initial yield stress and hardening parameters respectively. $\dot{\varepsilon}$ is the strain rate, $\dot{\varepsilon} = \sqrt{\dot{\varepsilon}_{ii}\dot{\varepsilon}_{ij}}$;

E_P is the plastic hardening modulus, $E_P = \frac{E_t E}{E - E_t}$. E and E_t is the elasticity modulus and tangent modulus respectively. ε_{eff}^p is the finite plastic strain. Core samples were drilled from the surrounding rock. The mechanical parameters of the rock were obtained from a triaxial compression test of the field laboratory. The parameters of rock are shown in the Table 2.

Tab. 2 - Parameters of rock mechanics

Density (g/cm^3)	Elasticity modulus (10^{3}MPa)	Shear modulus (GPa)	Poisson's ratio	Yield stress (MPa)	Cohesion (MPa)	angle of internal friction (°)
2.3	2	0.06	0.34	70	0.3	50

In the LS-DYNA program, *MAT_HIGH_EXPLOSIVE_BURN is adopted to represent the explosive material model and describe the relationship between gas pressure and volume. It is to calculate the detonation pressure that the JWL (Jones-Wilkens-Lee) equation of state is employed. JWL equation of state as follows:

$$P = A\left(1 - \frac{\omega}{R_1 V}\right)e^{-R_1 V} + B\left(1 - \frac{\omega}{R_2 V}\right)e^{-R_2 V} + \frac{\omega N}{V} \qquad (3)$$

Where: *P* — detonation pressure, *N* — internal energy of explosive detonates products, *V* — relative volume of explosive detonates products, *A*, *B*, R_1, R_2, ω — the constants of explosives nature. The parameters of explosive materials and the equation of state should generally be obtained from cylinder tests[17-19]. The related parameters valued refer to the previous research as a result of low experimental conditions (Table 3).

Tab. 3- Materials of explosive & parameters of state equation[20]

Density (kg/m^3)	Detonation velocity (m/s)	Detonation pressure (GPa)	*A* (GPa)	*B* (GPa)	R_1	R_2	ω	*E* (GPa)
1100	3500	4	214	0.182	4.15	0.95	0.3	4.192

Calculation model

This paper calculates and analyses the impact of tunnel blasting on the civil air defence tunnel under the three conditions of parallel cut (simultaneous initiation), parallel cut (hole-by-hole initiation) and oblique cut (hole-by-hole initiation). The specific calculation model size is 30m (width)×22m (height)×13.2m (length). The blasting holes of parallel cut perpendicular to the rock surface. The angle between the blasting holes of oblique cut and the rock surface is 120°. So, the model of oblique cut is more difficult to build. In order to improve the calculation accuracy, the meshes in the lateral and longitudinal ranges of the oblique blasting holes are refined. The local grid size of blasting holes and explosives is 0.005m. The basic grid size of other parts is 0.2m. The parallel cut model contains 1095636 elements, 1171446 nodes. The oblique cut model contains 1157923 elements, 1386325 nodes. Reverse uncoupled charge is adopted in the blasting process. The borehole diameter, explosives diameter, blast hole depth, the charge weight per delay interval and the time interval between holes are 42mm, 30mm, 0.8m, 0.45kg and 5ms respectively. The calculation models are shown in the Figure 2 and Figure 7.

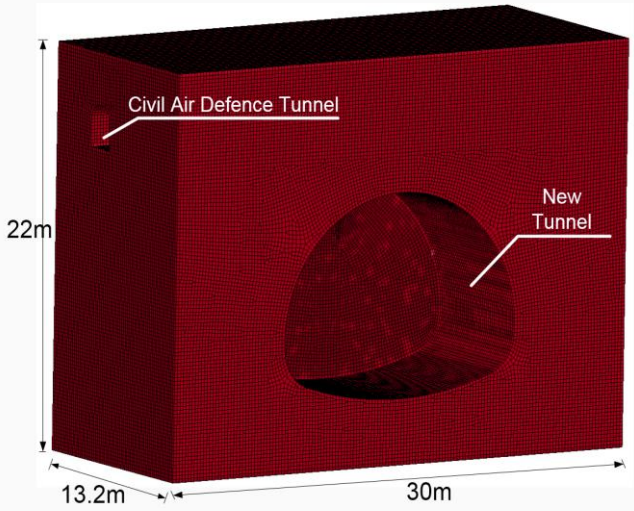

Fig.2 – The diagram of calculation model parallel cut

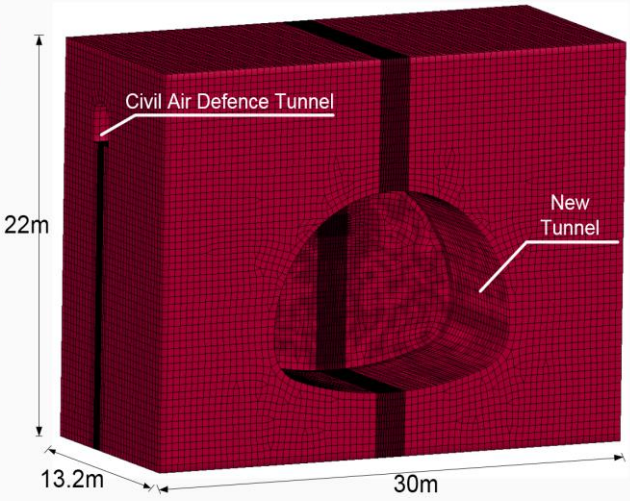

Fig.3 – The diagram of calculation model oblique cut

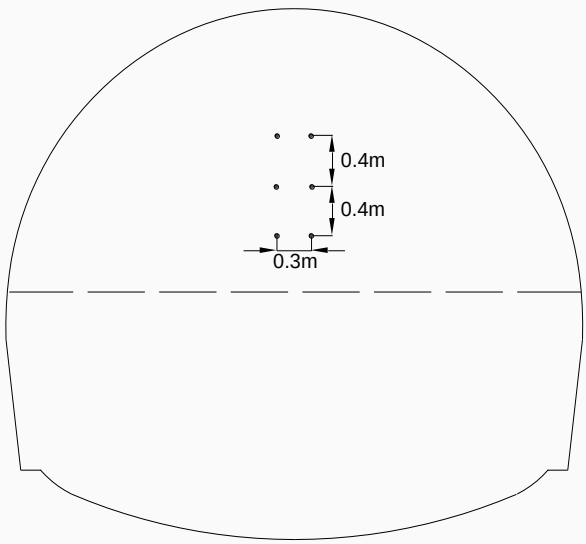

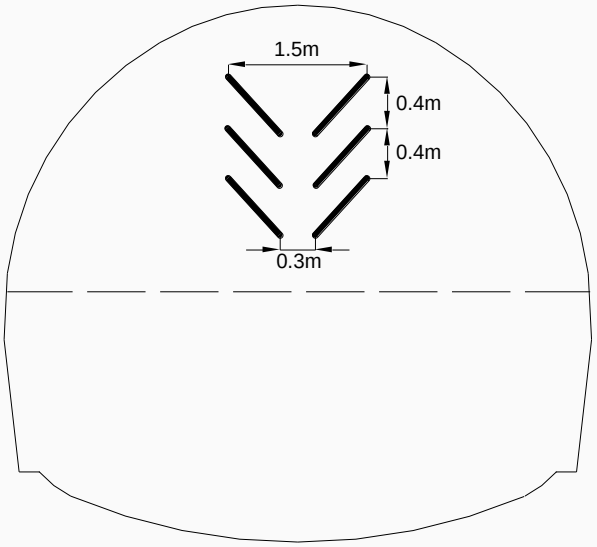

Fig.4 – Distribution of parallel cut

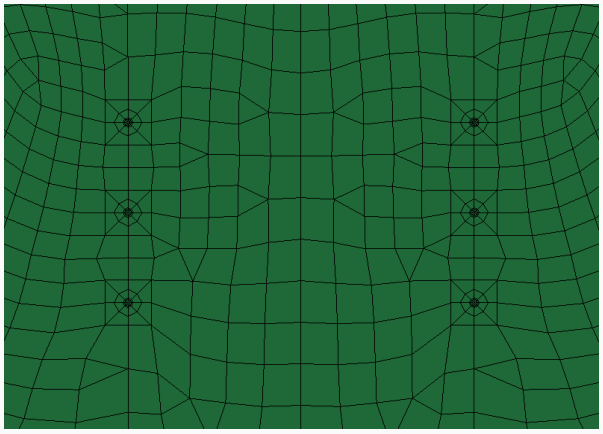

Fig.5 – Distribution of oblique cut

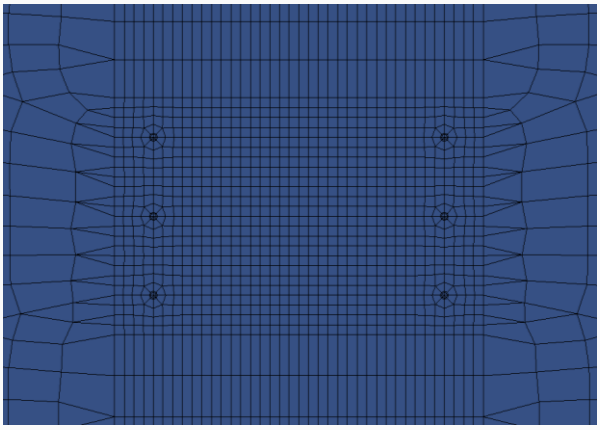

Fig.6 – Blasting holes of parallel cut

Fig.7 – Blasting holes of oblique cut

RESULTS

Experimental verification

Blasting vibration data are acquired by Chengdu ZKCK TC-4850N (Figure10) blasting seismometer acquisition. The instrument vibration monitoring frequency range is 5 to 500 Hz. And the resolution, sampling rate, and reading accuracy are 0.01, 100, and 0.1, respectively. The oblique wedge cut and hole-by-hole initiation of digital detonator are applied to site construction. With the new tunnel axis as the center line, the left and right sides of the tunnel should be equipped with a three-phase acceleration sensor at every 5m. There are 5 instruments in total. The specific figure of distribution and field test figure are shown at the Figure 8. The numerical calculation results and field test results of the vertical vibration velocity of the floor (monitoring point 3) of the civil air defense tunnel right above the new tunnel center-line are selected to make a comparative analysis. This is because the monitoring point 3 is closest to the newly built tunnel and the velocity in the vertical direction is the largest. Typical working conditions can more clearly reflect the physical laws implied by the data. The results are shown in the Figure 9.

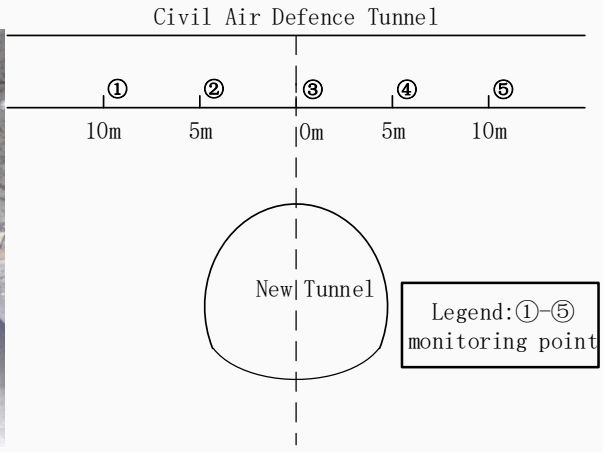

Fig.8a – Layout of monitoring points in civil

Fig.8b – Diagram of field test air defence tunnel

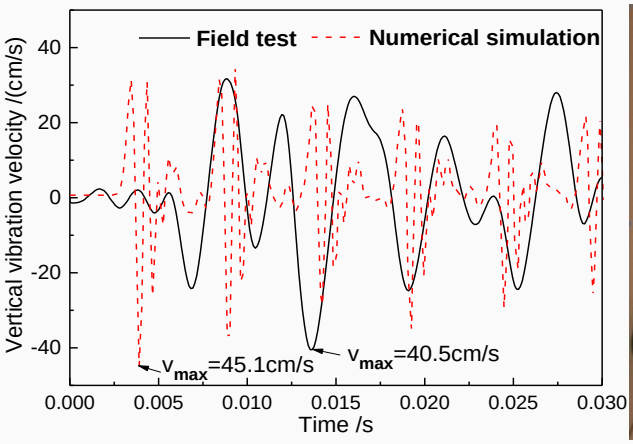

Fig.9 – Comparative analysis of test data

Fig.10 – Picture of TC-4850

It can be seen from Figure 9 that the maximum of vibration velocity measured at the monitoring point 3 is 0.405 m/s and the seismic wave period of each hole is between 3 and 4 ms. The hump phenomenon of vibration waveform appealed after the seismic waves of adjacent holes superimposed. The maximum vertical vibration velocity of numerical calculation is 0.451m/s, 11% higher than the measured results, the hole blasting seismic wave period between 2 ~ 3ms. The each hole blasting seismic waves have no superposition phenomenon. The amplitudes of the vibration-velocity curves of field-measured and numerical simulation both decrease with time. Overall, the numerical results are in good agreement with the results of field test, and the calculation method is reliable.

Analysis of detonation mode

The vibration effects of simultaneous initiation (millisecond detonator) and hole-by-hole initiation (digital detonator) on adjacent civil air defence tunnel are studied through the numerical simulation. The advantage of numerical simulation is that it can monitor the vibration at any point. This section selects the data of the four monitoring points (located at the left wall, the right wall, the crown and the floor) of the civil air defence to make a comparative analysis. The specific layout of the tunnel cross-section monitoring point is shown in Figure 11. The vibration velocity of X, Y and Z directions of the four monitoring points are listed in Table 4.

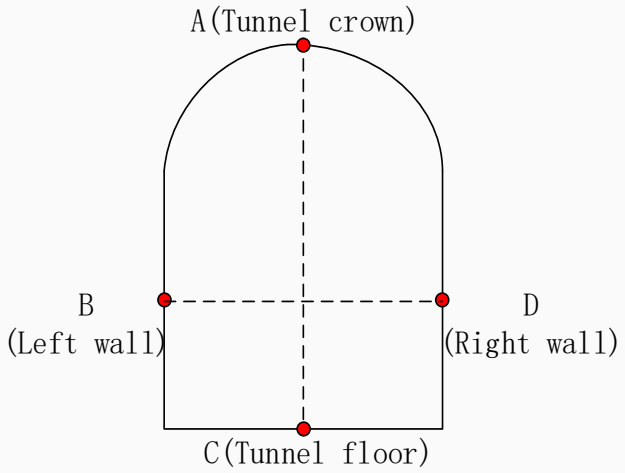

Fig.11 – Layout of monitoring points

Tab. 4- Vibration velocity in three directions (m/s)

Parameters	Parts	X (Tunnel longitudinal)	Y (Vertical direction)	Z (Tunnel transverse)	Comment
Velocity	Tunnel floor	-0.405	0.754	0.0124	simultaneous initiation
		0.238	-0.451	0.0983	hole-by-hole initiation
	Left wall	-0.214	-0.447	-0.00348	simultaneous initiation
		-0.114	-0.215	-0.0283	hole-by-hole initiation
	Right wall	-0.148	-0.246	0.00642	simultaneous initiation
		-0.0602	-0.105	-0.026	hole-by-hole initiation
	Tunnel crown	-0.0415	0.0592	0.00215	simultaneous initiation
		0.0209	0.0323	-0.00725	hole-by-hole initiation

As the Table 4 shows, the vibration velocity in the X and Y direction of hole-by-hole initiation are about 50% of simultaneous initiation. And the vibration velocity in the vertical direction under both conditions is faster than the other two directions. The vibration velocity in the Z direction caused by hole-by-hole initiation is larger than simultaneous initiation. However, the vibration velocity in the Z direction is small on the whole and does not have a large impact on the structural safety, so it is not the key point of research. Therefore, the vertical direction of the data is selected as the focus of comparative study in what follows in this passage. The Y-direction vibration (vertical direction) velocity of four monitoring points in the civil air defence tunnel shown in Figure 12.

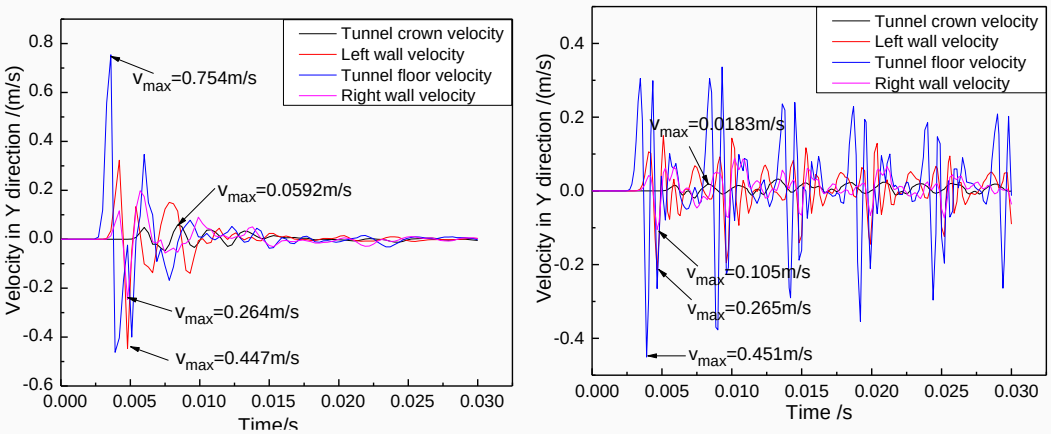

(a) Simultaneous initiation (millisecond detonator)

(b) Hole-by-hole initiation (digital electronic detonator)

Fig.12 – Vibration velocity in vertical direction

Comparing Figure 12(a) and Figure 12(b) shows that the maximum vibration velocity(0.754m/s) of simultaneous initiation is much larger than the maximum vibration velocity(0.451m/s) of hole-by-hole initiation. Digital detonators can reduce the maximum velocity by 40%. The moment of the peak of vibration velocity appears in the first three peaks, because the first wave of different detonation modes has no phenomenon of superimposition and cancellation between peak and trough. The vibration velocity caused by simultaneous initiation is almost attenuated to 0 after 0.015 s. The vibration velocity caused by hole-by-hole initiation is not linearly attenuated due to the mutual interference of different seismic waves, but the vibration velocity assignment decreases with time. The descending order of the vibration velocity of the four monitoring points of the civil air defence tunnel is the floor, left wall, right wall and crown. This is because the blast center distance of floor is nearest, and it has the maximum vibration velocity, the blast center distance of crown is farthest, and it has the minimum vibration velocity. The right wall is located in the upside of the tunnel excavated. Due to the existence of the free face (Fig 2 and 3), the vibration velocity of right wall is less than the velocity of left wall. And the vibration velocity of right wall is close to half of the left wall.

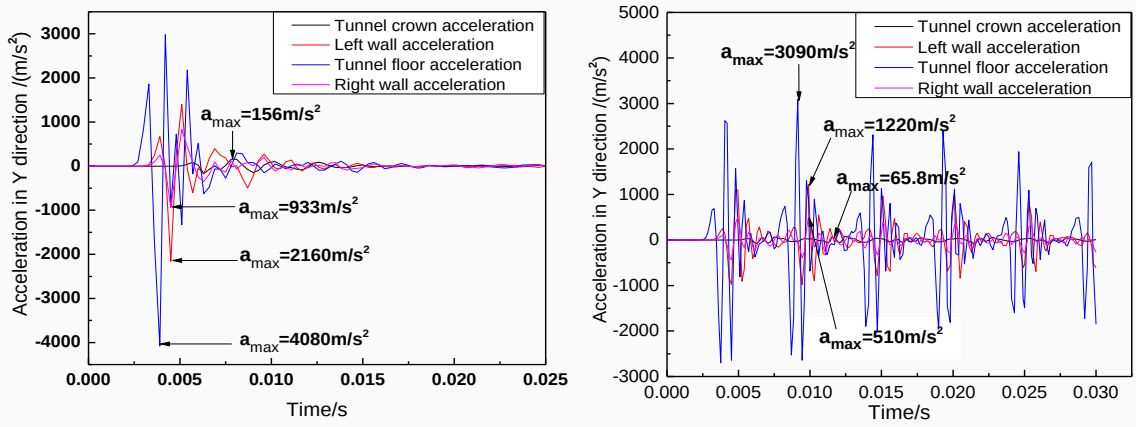

(a) Simultaneous initiation (millisecond detonator)

(b) Hole-by-hole initiation (digital electronic detonator)

Fig.13 – Vibration acceleration in vertical direction

Comparing Figure 13(a) and Figure 13(b), it can be seen that under both conditions, the peak acceleration of the floor is far greater than other parts. The peak acceleration of vibration (4080m/s^2) of simultaneous initiation is far greater than the peak acceleration of vibration (3090m/s^2) of hole-by-hole initiation. Digital detonators can lower the peak vibration acceleration by 24%. In the same time, the descending order of the vibration acceleration of the four monitoring points of the civil air defence tunnel is also the floor, left wall, right wall and crown. The law of acceleration is similar to the law of velocity change, which indicates that in blasting construction, increasing the free surface helps to reduce the adverse effects caused by blasting. It can be also found that the energy is relatively concentrated at the simultaneous initiation, and the spectrum shows a single peak phenomenon. After 0.015s, the acceleration of each part is almost attenuated to 0. The energy of hole-by-hole initiation is relatively dispersed, the spectrum shows multi-peak phenomenon. The vibration velocity of hole-by-hole initiation coincides with the vibration period of acceleration, which is about 9 ms. The curve of simultaneous initiation does not show significant periodicity. Most of the energy of simultaneous initiation is released at the beginning of the explosion, and the force generated is large, while hole-by-hole initiation has a process of energy release for a certain period of time.

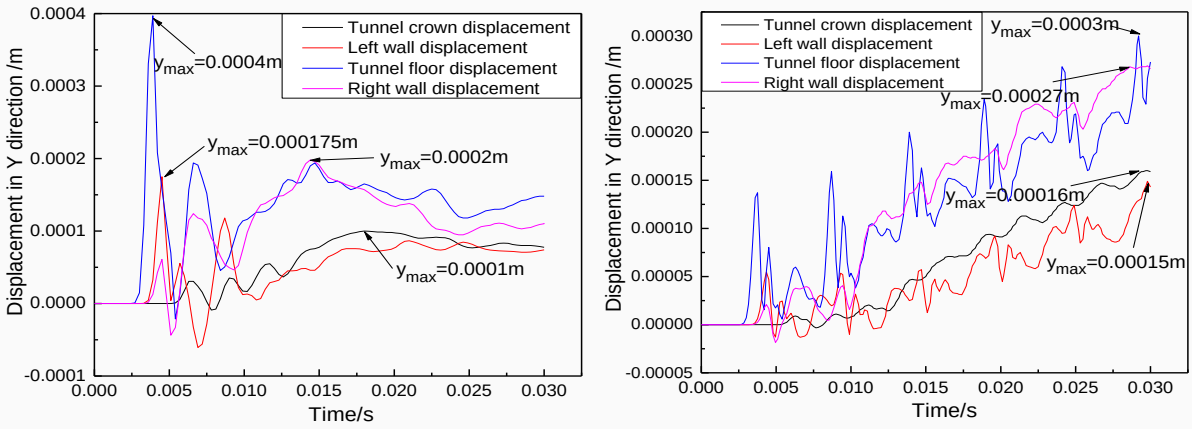

(a) Simultaneous initiation (millisecond detonator) *(b) Hole-by-hole initiation (digital electronic detonator)*

Fig.14 – Displacements in vertical direction

Comparing Figure 14(a) and Figure 14(b), it can be seen that under both conditions, the vibration displacement in the vertical direction is small. The maximum vibration displacement of the floor of simultaneous initiation and hole-by-hole initiation are 0.4mm and 0.3mm respectively. The reason is that the blasting time is extremely brief, and different detonation modes have less influence on the vibration displacement, and there is no significant divergence in the displacement extreme value. Hence, the vibration displacement should not be used as the evaluation criterion of vibration impact.

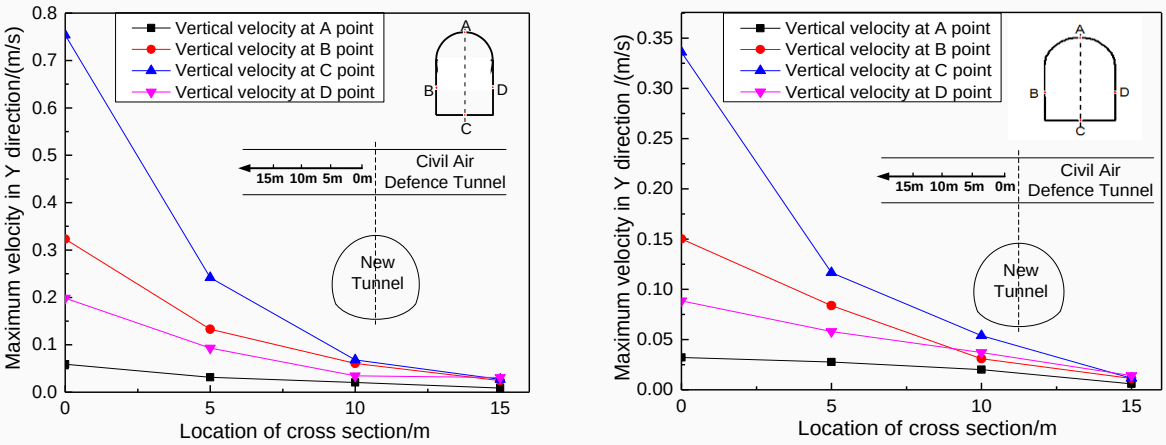

(a) Simultaneous initiation (millisecond detonator) *(b) Hole-by-hole initiation (digital electronic detonator)*

Fig.15 – Vibration velocity in different positions

As Figure 15 shows, under the two conditions of simultaneous initiation and hole-by-hole

initiation, the vibration velocity at different monitoring points decays with the distance from the initiation position increases in a similar law. Because the vibration velocity of the tunnel floor (C point) is the largest, it is the research object. Under the condition of simultaneous initiation, from monitoring point 3(0.754m/s) to monitoring point 4(0.240m/s), the maximum vibration velocity is reduced by 68%. Under the condition of hole-by-hole initiation, from monitoring point 3 (0.3336m/s) to monitoring point 4(0.120m/s), the maximum vibration velocity is reduced by 64%. Further analysis shows that the vibration velocity of C point decreases exponentially with distance increases. The blasting distance of C point is the smallest, although the vibration velocity is the largest, the attenuation is faster than other parts (A, B, D). Moreover, the vibration velocity of the civil air defence tunnel other than 15 m is close to, which indicate that the blasting vibration influence range is roughly 30m directly above the detonation point. This range of influence can provide a reference for the safety monitoring of civil air defence tunnel.

Analysis of cut modes

The quality of cut-holes has a direct influence on the dig velocity of hard-rock tunnel and the efficacy of smooth blasting. At present, the main cut modes are parallel cut and oblique cut. In this section, numerical simulation is used to explain the influence of parallel cut and oblique cut on blasting vibration. Figure 16, Figure 17 and Figure 18 show the time history of vertical vibration velocity, displacement and acceleration of civil air defence tunnel floor under two kinds of cut modes.

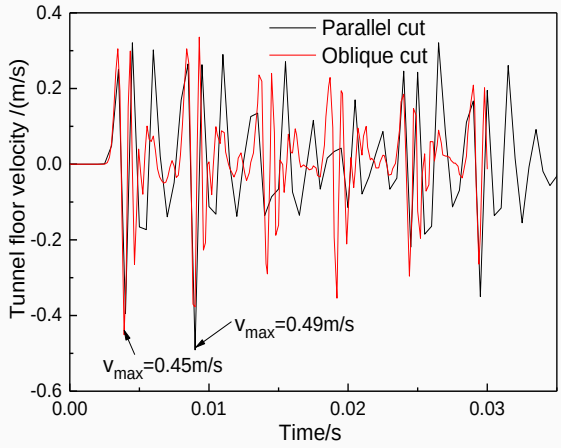

Fig.16 – Vibration velocity in vertical direction

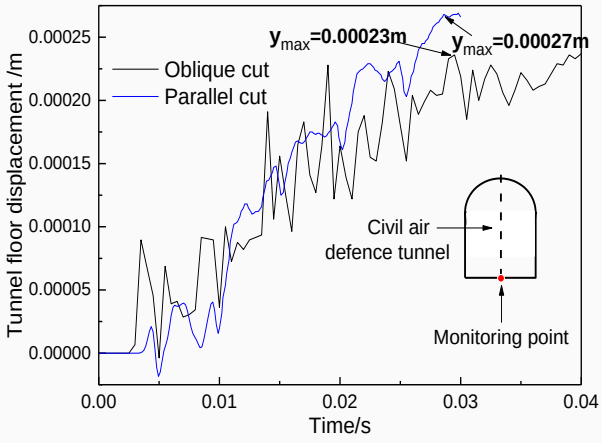

Fig.17 – Time history curve of vertical displacement

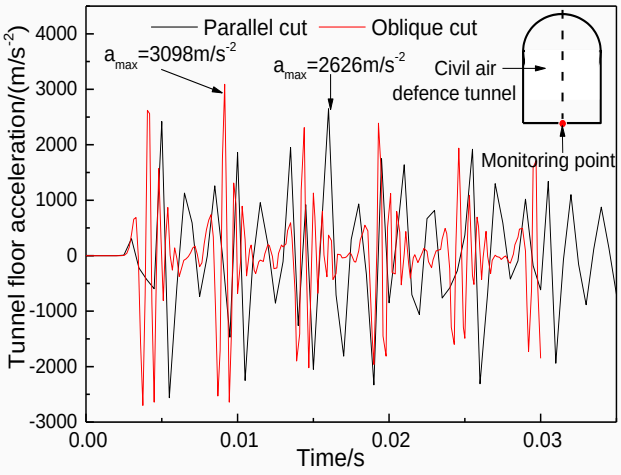

Fig.18 – Vibration acceleration in vertical direction

Knowing from Figure 16, the maximal vibration velocity of parallel cut is slightly larger than the maximum of oblique cut. Oblique cut shows a clear periodicity. The vibration period is approximately 5ms, and the energy is relatively concentrated, while the parallel cut does not have obvious periodicity, the energy is relatively dispersed. Therefore, in the condition of hard-rock, the rock-breaking effect of oblique cut is better than parallel cut, and the oblique cut has a slighter impact on the adjacent structure than parallel cut.

Observed results from Figure 17 generate that the vibration displacement maximum (0.27mm) of the parallel cut is slightly larger than that of the oblique cut (0.23mm), and the vibration displacement of the adjacent structure under both conditions is small. After the start of blasting, due to the vibration of the seismic wave, the displacement of the tunnel floor under the condition of two types of cut, but generally increased with time. However, the vibration displacement of the parallel cut tends to be stable after 0.03 s, and the vibration of the oblique cut continues to 0.04 s, which indicates that the oblique cut has a stronger vibration effect in hard rock blasting.

It can be seen from Figure 18, the maximum value (3098m/s^2) of the oblique cut vibration acceleration is 15% greater than the maximum value (2626m/s^2) of the parallel cut vibration acceleration, and the acceleration of oblique cut appears 9 ms earlier than parallel cut. The energy released after blast starting of the oblique cut is concentrated in the early stage of the blasting process. And in the later stage, the vibration acceleration of the oblique cut shows a more regular periodicity, and the attenuation velocity is slower. The results indicates that, compared with parallel cut, the oblique cut's the surrounding rock stress is greater. Through the above analysis, it can be materialized that the rock-breaking effect of oblique cut is better.

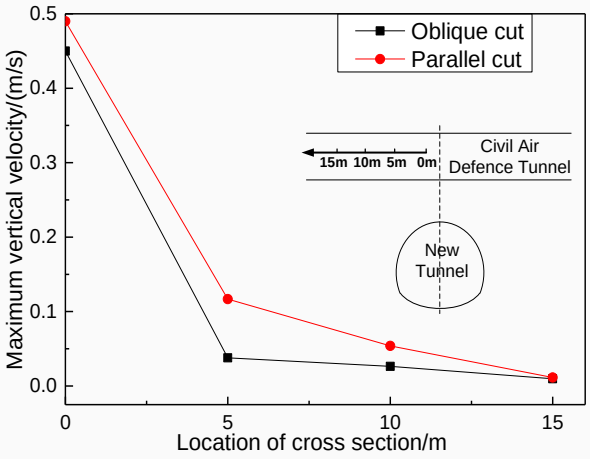

Fig.19 – Relationship between vibration velocity & distance

Obtained curves form Figure 19 shows that, under different positions, the vibration velocity of parallel cut is greater than that of oblique cut, and the change trend of the velocity with distance is similar under the two conditions. Further studies reveal that the trend shows an exponential decay. In the range of 0 to 5 m, the vibration velocity generated by the oblique cut is rapidly attenuated. In the range of 5 to 15 m, the vibration velocity is close to 0. Therefore, the oblique cut is more advantageous for the protection of the civil air defence tunnel.

CONCLUSION

In this paper, the reliability of the finite element method is verified by comparing the measured data with the results of LS-DYNA finite element program. Then, numerical simulation is used to illustrate the influence of different detonation modes and different cut modes on the vibration effect of adjacent structures. The main conclusions in this paper are as follows:

(1) As mentioned earlier, single-hole coupled blasting vibration analysis is carried out by using ALE algorithm. And the calculation results can accurately reflect the vibration characteristics of seismic waves of holes. The calculation parameters and methods are basically reasonable.

(2) The vibration velocity of hole-by-hole initiation (digital electronic detonator) is 40% lower than simultaneous initiation (millisecond detonator), and the vibration acceleration is reduced by 24%. The vibration velocity at different monitoring points decays with the distance from the initiation position increases in an exponential rule. The digital detonator is more suitable for the vibration damping control blasting of the tunnel under complex condition in the central urban area, but its cost is 6 to 8 times higher than that of an ordinary millisecond detonator.

(3) The vibration velocity of parallel cut on surrounding structure is larger than the oblique cut a bit. However, the vibration acceleration of oblique cut is 15% larger than the parallel cut, and has a better effect for rock-breaking. Consequently, the oblique cut is more fitting for hard rock tunnel blasting.

REFERENCES

[1] Singh P K. 2002.Blast vibration damage to underground coal mines from adjacent open-pit blasting. International Journal of Rock Mechanics & Mining Sciences, vol. 39(8): 959-973.

[2] Wang M, Pan X, Zhang C et al. 2004, Study of blasting vibration influence on close-spaced tunnel. Rock and Soil Mechanics, vol. 25(3):412–414.

[3] YAO Yong, HE Chuan, YAN Qi-xiang et al.2004, Numerical simulation of blasting control for small clear distance zone of Dongjiashan tunnel. Rock and Soil Mechanics, vol.25(s2): 501-506.

[4] ZHAO Dong-ping, WANG Ming-nian. 2007, Study on influence of blasting vibration on cross tunnels with small clearance. Chinese Journal of Geotechnical Engineering,vol.29(1):116-119.

[5] WEN Xi.2008.Study on Impact and Safety Evaluation of Existing Tunnels by Blasting and Excavation of Adjacent Tunnel. (Master dissertation, Wuhan University of Technology).

[6] LI Yu-xi.2010.Effect of Blasting excavation on the Structure Safety of Existing Tunnel Adjacent to the New Tunnel. (Master dissertation, Chongqing Jiao Tong University).

[7] YANG Guang.2011.Control and Analysis of an Existing Tunnel Vibration Induced by Blasting Construction of Nearby Tunnel. (Master dissertation, Central South University).

[8] ZHANG Zhan-hong. 2011. Influence of New Jiuyanshan Tunnel Crossing the Existing Operative Railway Tunnel.(Master dissertation, Southwest Jiao Tong University).

[9] Sambuelli L. 2009. Theoretical derivation of a peak particle velocity–distance law for the prediction of vibrations from blasting. Rock Mechanics & Rock Engineering,vol.42(3): 547-556.

[10] Liang Qing-guo , An Ya-fang , Zhao Lei , et al.,2011. Comparative Study on Calculation Methods of Blasting Vibration Velocity. Rock Mechanics & Rock Engineering,vol.44(1): 93-101

[11] ZOU Xin-kuan.2012.The Vibration Effect Study of Anchorage Tunnel under Blasting Power. (Master dissertation, Southwest Jiao Tong University).

[12] LIANG Q, LI J, LI D, et al.,2012. Effect of Blasting-induced Vibration form New Railway Tunnel on Existing Adjacent Railway Tunnel in Xinjiang, China.Rock Mechanics & Rock Engineering,vol.46(1): 19-39.

[13] MENG Dong, LIU Qiang, PENGLi-min, Lei Ming-feng.2015.Study on Construction Blasting Vibration Response in Railway Intercharge Tunnel. Journal of Hefei University of Technology (natural science), vol. (03): 363-368.

[14] YU Jian-xin, CHEN Wei-zhong, YANG Jian-ping, et al.,2014.Study of Blasting Vibration Control Technology of Up and Down Cross Tunnel. Rock and Soil Mechanics,vol. (S2): 445-452.

[15] CAI Lu-jun, ZHU Fang-min, WU Liang, et al.,2015.Influence of Blasting Vibration of Lower Water Supply Tunnel on the Excavation of Upper Tunnel. Highway Engineering,vol.(03): 28-32.

[16] GAO Xuan-neng, WANG Shu-peng, JIANG Yuan. 2010. Shock Wave Pressure Distribution on Large-Space Structures And Explosion Venting Under Blast Loading. Engineering Mechanics, vol.27(4):226-233

[17] Lan I F, Hung S C, Chen C Y, et al.1993. An improved simple method of deducing JWL parameters from cylinder expansion test. Propellants, Explosives, Pyrotechnics, vol.18(1): 18-24

[18] Wescott B L, Stewart D S, Davis W C.2005. Equation of state and reaction rate for condensed-phase explosives. Journal of Applied Physics, vol.98(5): 053514

[19] Chen Hua, Zhou Hai-bing, Liu Guo-zhao et al. 2017. Bayesian calibration for parameters of JWL equation of state in cylinder test. Explosion and Shock Waves, vol.37(4): 585-590

[20] SHEN Fei, WANG Hui, YUAN Jian-fei. 2014. A simple method for determining parameters of JWL

EOS. Journal of Vibration and Shock, vol.(9): 107-110

DOI 10.14311/CEJ.2019.02.0016

Article no. 17

THE CIVIL ENGINEERING JOURNAL 2-2019

STUDY ON FAILURE MECHANISM OF STRIP FOUNDATION BUILDINGS CAUSED BY SURFACE HORIZONTAL DEFORMATION IN MINING AREA

Xiaopeng Liu[1,2], Guangli Guo[1,2]*

1. *NASG Key Laboratory of Land Environment and Disaster Monitoring, China University of Mining and Technology, Xuzhou 221116, China; xp_liu001@163.com*
2. *School of Environment Science and Spatial Informatics, China University of Mining and Technology, Xuzhou 221116, China; guangliguo@cumt.edu.cn*

ABSTRACT

The surface deformation caused by underground coal mining will cause great damage to the surface buildings. Especially for the strip foundation buildings, the surface horizontal deformation will cause the walls to crack and open, threatening the safe use of buildings. However, there is lacking research on the failure mechanism of strip foundation buildings caused by surface horizontal deformation. Therefore, it is particularly important to study the mechanism. In this paper, a mechanical model of additional stress distribution in the strip foundation under surface horizontal deformation is established. Based on the model, the internal stress variation characteristics of the longitudinal wall of strip foundation buildings are studied with different factors: friction coefficient, surface curvature, foundation load and foundation length under the surface horizontal deformation. The internal stress variation of the transverse wall of the strip foundation buildings is analysed. The theory is verified by numerical simulation and a case study from Fengfeng coalmine China. Finally, the protection methods of the strip foundation buildings under the surface horizontal deformation are proposed.

KEY WORDS

Surface horizontal deformation, Strip foundation buildings, Failure mechanism, Numerical simulation

INTRODUCTION

The surface movement and deformation caused by underground coal mining is one of the common geological disasters in the mining area. Especially in the past ten years, with the rapid development of Chinese economy, the demand for coal increases gradually and the mining area increases rapidly, making the problem of surface movement and deformation in mining areas extremely serious [1]. Due to some of the earliest developed old mining areas are gradually depleted and the amount of coal under villages in the mining areas is huge, the coal mining under buildings is gradually included in the plan to maintain the normal operation of enterprises [2]. At this time, the movement and deformation of the surface in the mining area will definitely affect the surface buildings and even cause damage to the buildings, which becomes one of the important factors affecting the social security in the mining area.

Horizontal deformation, curvature deformation and oblique deformation are the three major forms of the surface movement and deformation caused by underground coal mining [3]. In China,

coal mining under buildings is mainly carried out in rural areas because of economic factors. Most of the rural houses are strip foundations, and the foundations are in full contact with the ground soil. The surface horizontal deformation will often drive the deformation of the building foundation and cause damage to the building. Therefore, horizontal deformation is the main cause of the destruction of rural strip foundation buildings [4]. Therefore, it is of great significance to study the failure mechanism of strip foundation buildings caused by the surface horizontal deformation.

In the past, a variety of different methods were used to study the damage of buildings caused by the surface movement deformation. Field measurement is one of the most important ways to study the surface movement deformation and building deformation, which can analyse the form of surface movement deformation and the condition of building deformation and damage, so that the damage degree of buildings under different surface deformations is estimated to make a prediction [5-7]. This kind of statistical-based method, with universal characteristics, can analyse a large amount of observation data. However, since there is no analysis for the internal mechanism of building damage, the results are often deviated from each other when applied to a single building. Compared with the analysis method based on measured data, the prediction method combining mathematical model and theoretical calculation is a simple and quick method to analyse the building damage under the surface movement deformation. Herein, the mathematical model can be established by simplification of surface deformation and building structure, and the internal stress changes caused by surface deformation are analyzed by theoretical calculation [8-10]. Establishing a scaled-down physical model with similar materials can intuitively analyse the damage of buildings caused by different deformations and different degrees of surface deformation, and study the causes of damage by analysing the damage form of buildings [10-11]. In recent years, numerical simulation experiments have been continuously applied to the study of soil-structure interactions. The finite element or finite difference method is used to simulate the interaction of foundation-structure. The extent of structural damage is estimated by analysing the plastic failure and internal stress changes of buildings [12-13]. This method is an ideal research method to simulate the interaction between soil and building foundation as well as the process of deformation from soil to building.

In this paper, a theoretical model of the additional force in the building foundation is established to study the additional stress distribution of the strip foundation buildings under the surface horizontal deformation. The distribution law of additional stress in the longitudinal wall and the transverse wall of the building under the surface horizontal deformation is revealed. The reasons for the additional stress deformation inside the longitudinal wall foundation of the building are analysed. The theory is verified by numerical simulation and a case study from Fengfeng coalmine China. Finally, the results of theoretical analysis are verified by numerical simulation

.

THEORETICAL ANALYSIS OF BUILDING DAMAGE CAUSED BY SURFACE HORIZONTAL DEFORMATION

Among the movements and deformations caused by mining subsidence, horizontal deformation of the surface (Figure 1) is one of the main causes of building damage. Assuming the horizontal deformation of the surface is parallel to the long axis of the longitudinal wall, the surface deformation will exert tensile stress on both the longitudinal wall and the transverse wall of the building, whose direction is parallel to the longitudinal wall and vertical to the transverse wall. At this time, the interaction between the foundation soil and the building foundation is mainly manifested in four aspects: a. The friction between the building foundation and the foundation soil generated by the building foundation reaction. b. The friction between the building foundation and the foundation soil generated by the lateral pressure of the foundation soil. c. The tension and compression exerted by the lateral pressure of the foundation soil on the transverse wall. d. The cohesion between the building foundation and the foundation exerts a tensile and compressive

effect on the building. Since the force of the surface horizontal deformation on the longitudinal wall foundation of the building is symmetric with respect to the midline of the long axis of the longitudinal wall of the building, only the effect of one side force is analysed below.

(a) Tensile deformation *(b) Compression deformation*

Fig. 1 - Horizontal deformation diagram

The following assumptions can be made when the horizontal deformation of the surface is used to theoretically analyze the basic effects of the building:

a. Assuming that the long axis direction of the longitudinal wall of the building is consistent with the horizontal deformation direction of the surface.

b. The lateral pressure of foundation soil on the building foundation conforms to the Rankine lateral pressure theory.

Additional stress inside the longitudinal wall foundation

a. Friction between the foundation base of the building and the foundation.

The friction of the bottom of the building foundation is the same as the deformation direction of the building foundation, which consists of two parts: one part acts on the bottom surface of the vertical wall foundation and the other part acts on the bottom of the transverse wall foundation. The friction is proportional to the bottom pressure of the building foundation $f = \mu N$, f is the friction, μ is the friction coefficient between the building foundation and the ground, and N is the pressure between the building foundation and the ground.

It is well known that the pressure of building foundation on the ground is equal to the ground reaction, and the surface horizontal deformation caused by the mining subsidence is often accompanied by the surface curvature deformation. When curvature deformation occurs on the surface, the compressive stress of each part of the bottom of the building foundation under the Winkel elastic foundation model is $\sigma_x = kw(x)$. Where k is the foundation coefficient of the ground soil, and w is the depth of the building foundation cutting into the ground soil. The calculation method can be found in the literature [14-15].

The friction at the bottom of the longitudinal wall foundation of the building is:

$$f_1 = \mu\sigma_x \tag{1}$$

At this time, the horizontal stress generated by the friction at the bottom of the longitudinal wall foundation at different positions is:

$$\sigma_1(x) = \frac{\int_0^x \sigma(t)dt}{bh_1} \qquad (0 < x < l_x / 2) \tag{2}$$

l_x is the length of the building longitudinal wall, b is the width of building foundation, h_1 is the height of building foundation.

The friction between the bottom of the transverse wall foundation of the building and the ground is:

$$f_2 = \mu l_y N_y \tag{3}$$

The length of the transverse wall is l_y, and the load of the building foundation is N_y.

Considering that a transverse wall acts on the front and rear longitudinal walls, the horizontal stress in a single longitudinal wall caused by the bottom friction of the transverse wall should be half of that of the whole transverse wall:

$$\sigma_2(x) = \frac{f_2}{2bh_1} \tag{4}$$

b. The effect of lateral pressure of foundation soil on building foundation.

The building foundation is located in the ground soil, which exerts lateral pressure on the building foundation. When the lateral pressure of the ground soil acts on the longitudinal wall, horizontal friction is generated between both sides of the longitudinal wall foundation. When the lateral pressure acts on both sides of the transverse wall foundation, the pressure difference on both sides will bend the transverse wall and generate tensile and compressive stress on the longitudinal wall of the building.

It is known from the basic assumptions that there is no deformation on the surface perpendicular to the longitudinal wall of the building, so the lateral pressure of the ground soil on both sides of the building longitudinal wall is static earth pressure. According to the Rankine lateral pressure theory, the lateral pressure at height h above the ground is:

$$P = k\gamma h \tag{5}$$

Where, P is the static earth pressure, k is the static earth pressure coefficient, and r is the unit weight of the foundation soil.

The friction generated by the lateral pressure on both sides of the longitudinal wall foundation is:

$$f_3 = 2\mu k\gamma \frac{h_1}{2} = \mu P \tag{6}$$

Due to the friction generated by the lateral pressure of the longitudinal wall is symmetrical about the center line of the longitudinal wall, the horizontal stress generated by the friction on one side of the longitudinal wall can be analyzed as follows:

$$\sigma_3(x) = \frac{\mu P x}{bh_1} \qquad \left(0 < x < l_x / 2\right) \tag{7}$$

According to the Rankine lateral pressure theory, after the foundation soil reaching equilibrium state under the surface movement deformation, both sides of the building transverse wall foundation will be affected by the active earth pressure and the passive earth pressure. When the surface is subjected to tensile deformation, the inner side of the transverse wall foundation is subjected to passive earth pressure, and the outer side is subjected to active earth pressure. When the surface is subjected to compression deformation, the inner side of the transverse wall foundation is subjected to active earth pressure, and the outer side is subjected to passive earth pressure.

The calculation formula for the total active earth pressure of cohesive soil is:

$$P_a = \frac{1}{2}\gamma h_1^2 K_a - 2ch_1\sqrt{K_a} + \frac{2c^2}{\gamma} \quad (8)$$

Where, K_a is the active earth pressure coefficient, and $K_a = \tan^2(45° - \frac{\phi}{2})$, C is the cohesion of the soil, and ϕ is the internal friction angle.

The formula of total passive earth pressure for cohesive soil is:

$$P_p = \frac{1}{2}\gamma h_1^2 K_p + 2ch_1\sqrt{K_p} \quad (9)$$

Where, K_p is the active earth pressure coefficient, and $K_p = \tan^2(45° + \frac{\phi}{2})$

When the surface is deformed horizontally, the horizontal stress generated by the lateral pressure of the transverse wall on the longitudinal wall is:

$$\sigma_4(x) = l_y(\frac{P_p - P_a}{2bh_1}) \quad (10)$$

c. The effect of cohesion between the building foundation and the ground on the building foundation.

When the building foundation and the surface produce relative motion, the cohesion between the building foundation and the ground is transformed into tensile and compressive stress acting on the building foundation to cause damage to the building.

Assuming that the cohesion between the building foundation and the ground soil is C, the tensile and compressive stress resulting from the cohesion on the bottom of the building transverse wall is as follows:

$$f_4 = \frac{l_y bC}{2bh_1} \quad (11)$$

The tensile and compressive stress generated by the cohesion on the bottom and side of the longitudinal wall is:

$$f_5(x) = \frac{bxC + 2h_1xC}{bh_1} \quad (0<x\leq ly/2) \quad (12)$$

$$\sigma_5(x) = f_4 + f_5 \quad (13)$$

From the above analysis, it can be seen that when the surface is deformed horizontally, the horizontal stresses around the longitudinal wall foundation of a building are:

$$\sigma_t(x) = \sigma_1(x) + \sigma_2(x) + \sigma_3(x) + \sigma_4(x) + \sigma_5(x) \quad (14)$$

Additional stress inside the transverse wall foundation

It can be seen from the above analysis that when the surface is deformed horizontally, if the deformation direction is parallel to the longitudinal wall, the stress will occur in the direction perpendicular to the transverse wall foundation of the building. Because the transverse wall foundation and the longitudinal wall foundation are connected, the two ends of the transverse wall foundation are difficult to rotate under pressure, so the transverse wall foundation can be regarded as a beam fixed at both ends under uniform load. At this time, the force on the beam includes the cohesion between the building foundation and the ground soil, the friction and the lateral pressure difference between the two sides of the transverse wall foundation. Their comprehensive stress is:

$$\sigma_h = \frac{P_p - P_a + Cb + \mu N_y}{bh_1} \quad (15)$$

According to the fixed beam model, the deflection of the beam is:

$$y = \frac{1}{EI}\left(-\frac{1}{24}qx^4 + \frac{ql}{12}x^3 - \frac{ql^2}{24}x^2\right) \ (0<x<ly) \quad (16)$$

The bending moment is:

$$M = -\frac{1}{2}qx^2 + \frac{ql}{2}x - \frac{ql^2}{12} \ (0<x<ly) \quad (17)$$

Shear is:

$$Q = q\left(-x + \frac{l}{2}\right) \ (0<x<ly) \quad (18)$$

Where, σ_h is the vertical stress acting on the transverse wall, y is the deflection deformation of the transverse wall, M is the internal bending moment of the transverse wall, and Q is the internal shear of the transverse wall.

RESULTS AND DISCUSSION

Under the surface horizontal deformation, additional stress is generated inside the building, changing the stress distribution inside the building, which may lead to the destruction of the building. The theoretical analysis indicates that the following factors play a major role in the distribution of stresses in buildings caused by the horizontal deformation of the foundations: (a) friction coefficient between the ground soil and the building foundation; (b) the surface curvature deformation value; (c) the building foundation load; (d) the length of the longitudinal wall foundation; (e) the transverse wall foundation of a building. Combined with the general situation of rural strip foundation buildings and the data in the literature [16], each factor can be valued as follows: friction coefficient is 0.8, clay cohesion is 10KPa, static earth pressure coefficient is 0.6, general building foundation load is 150kN/m^2, the length of longitudinal wall is 15m, the length of transverse wall is 5m, and the surface curvature is 4mm/m^2.

Additional stress distribution inside the foundation under surface horizontal deformation

In different locations of the building, the form of building damage caused by horizontal deformation of the surface is also different. Figure 2 shows the additional stress distribution inside the building under the horizontal deformation of the surface.

It can be seen from Figure 2(a) that when the surface produces tensile deformation paralleling to the direction of the longitudinal wall, tensile stress will be generated inside the longitudinal wall foundation. The stress distributes symmetrically about the building foundation, and the stress increases from the two ends to the middle. Due to the uneven distribution of the foundation reaction caused by the curvature deformation, the stress grows in a non-linear way and the stress growth rate increases from the two ends to the middle.

From the above analysis, it is concluded that the horizontal deformation of the surface along the longitudinal wall direction of the building will lead to the flexural deformation of the transverse wall, resulting in additional bending moment and shear inside the transverse wall. From Figure 2(b), it can be seen that under the tensile deformation of the surface, the extreme value of shear inside the transverse wall of a building appears at both ends of the transverse wall. The absolute value of shear decreases from both ends to the middle and reaches 0 in the middle. Under the surface tension deformation, the bending moment of the transverse wall is negative at both ends and positive in the middle, and the maximum value is obtained in the middle of the transverse wall foundation.

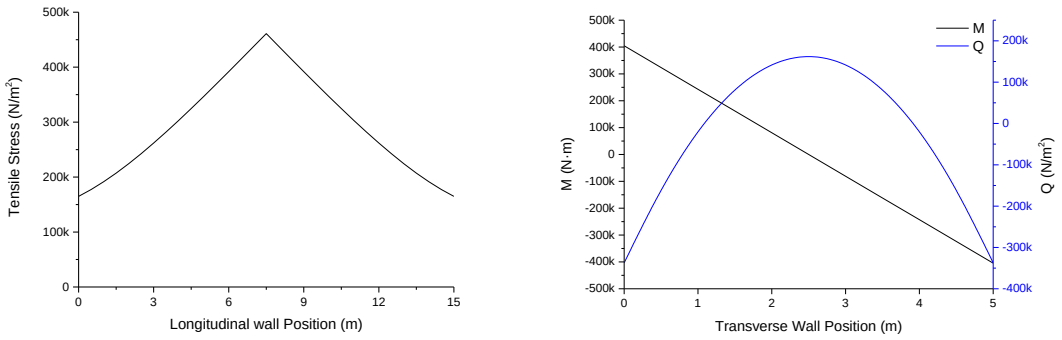

(a) Longitudinal wall *(b) Transverse wall*

Fig. 2 - Additional stress distribution inside the longitudinal wall and transverse wall of the building under the surface horizontal deformation

Additional stress distribution under different conditions

As shown in Figure 3(a), with the increase of friction coefficient between building foundation and ground soil, the tensile stress of the longitudinal wall foundation of building increases as a whole. This is due to the increase in friction coefficient, which increases friction in all parts of the building foundation, resulting in an increase in the overall tension. It can be seen that when the building foundation is easy to slide on the ground soil, the damage degree of the building can be reduced.

Figure 3(b) shows the tensile stress distribution of the longitudinal wall foundation of a building under different surface curvature deformations. It can be seen from the figure that when the curvature of the surface changes, there is no influence on the maximum stress of the building foundation, but on the stress distribution of the building foundation. That is, as the surface curvature deformation increases, the horizontal stress at both ends of the building foundation decreases. When the surface curvature is small, the growth rate of horizontal stress from the two ends of the foundation to the middle is consistent. With the increase of the surface curvature deformation, the difference in growth rate gradually increases.

It can be seen from Figure 3(c) that the change of the building foundation load has a direct impact on the change of tensile stress inside the building foundation. When the building foundation load increases, the tensile stress of the building longitudinal wall foundation increases overall. The

main reason is that when the building load increases, the pressure of the foundation bottom on the foundation soil increases, resulting in an increase in friction. This shows that the building foundation is more vulnerable to damage when the height of the building increases.

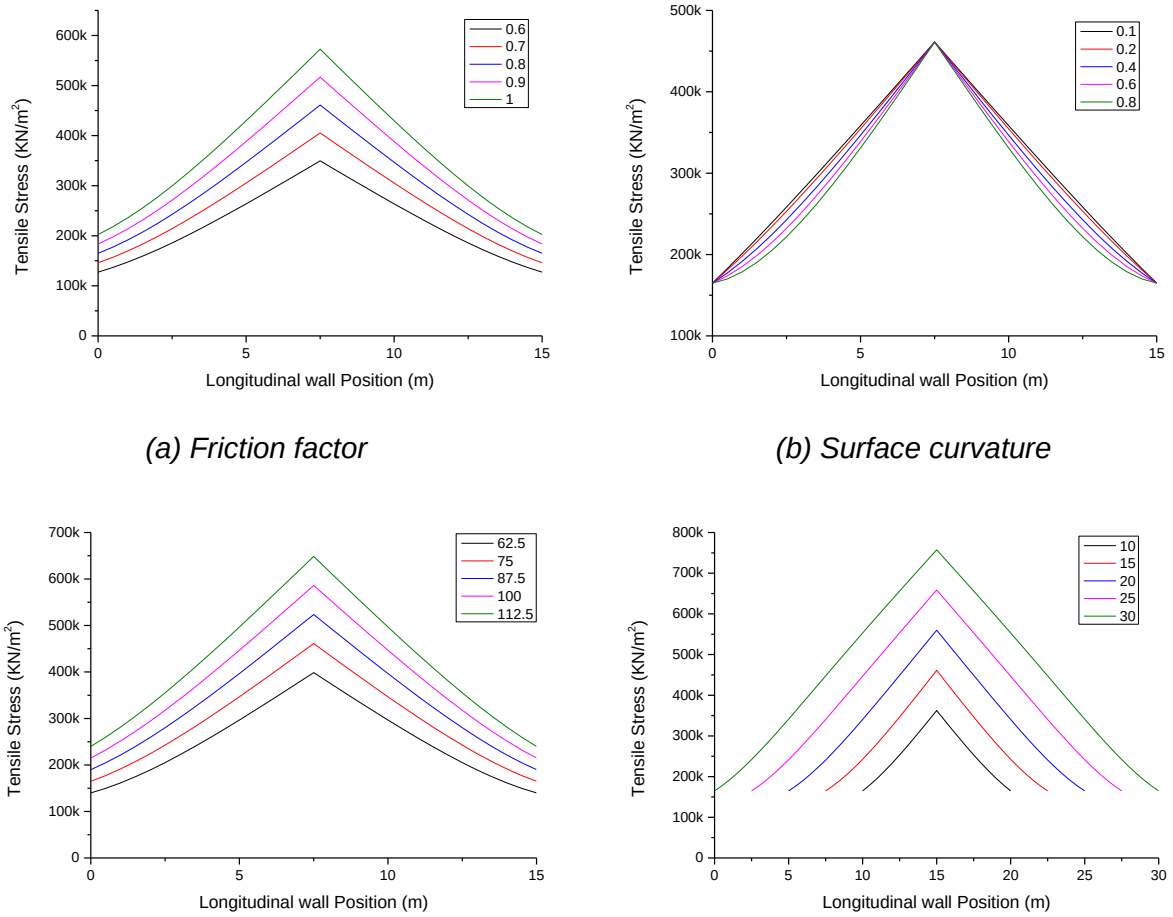

(a) Friction factor *(b) Surface curvature*

(c) Foundation load *(d) Building length*

Fig. 3 - Stress distribution of the longitudinal wall foundation of buildings under different conditions

As can be seen from Figure 3(d), when the length of the longitudinal wall foundation increases, the tensile stress at both ends remains unchanged, but the maximum tensile stress in the middle of the foundation increases continuously. It is because with the increase of the building length, the contact area between the bottom of the building foundation and the ground increases, and the maximum tensile stress increases. This indicates that buildings with longer length are more susceptible to tensile damage than buildings with shorter length.

NUMERICAL SIMULATION

Model establishment

This simulation takes the common bungalows in rural China as an example. The building consists of foundations, walls and structural columns. The structural columns are connected with the foundation, and the material model conforms to the Mohr-Coulomb yield criterion. The model is 20m long and 10m wide. The building is 15m long and 5m wide. The height of foundation is 1 m,

and the height of wall is 4 m. The thickness of building foundation and structural column is 0.5m, and the thickness of wall is 0.25m. The front of the building consists of four windows, one door, the back of the building and the transverse wall without doors and windows. The model is made up of 53760 units and 63185 nodes, as shown in Figure 4.

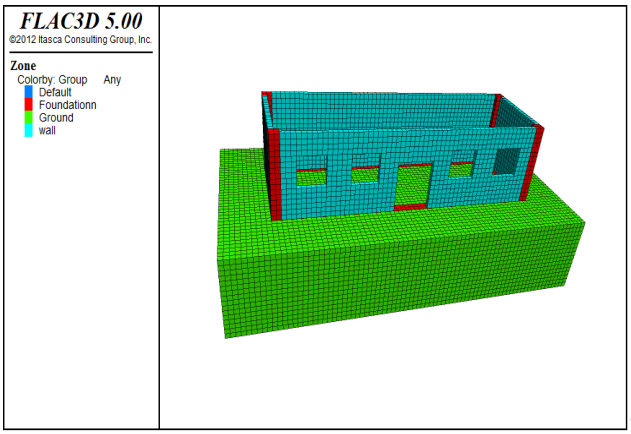

Fig. 4 - 3D model of the building

Boundary conditions and material parameters

In this experiment, the horizontal deformation of the surface is simulated by setting the displacement boundary conditions for the foundation soil. The velocity boundary conditions of the ground in the model are set uniformly changed along the x-axis direction, and the surface horizontal deformation of the model finally reaches 4 mm/m. The material parameters in the model are shown in Table 1.

Tab. 1- Material parameters of numerical simulation model

Parameter / Material	Bulk /MPa	Shear /MPa	Cohesion /MPa	Tension /MPa	Friction /°	Density /kg/m^3
Foundation soil	6.6	1.72	0.01	0.01	14	1800
Foundation	4460	2290	1.8	1.8	48	2500
Wall	2975	1530	1.25	1.25	47	2500

Influence of horizontal deformation on buildings.

From Figure 5(a), it can be seen that under the horizontal deformation of the surface paralleling to the direction of the longitudinal wall, additional tensile stress is generated inside the longitudinal wall of the building, and the additional stress is mainly concentrated on the building foundation and gradually spread to the building wall. The tensile stress gradually increases from the two ends of the building to the middle in the horizontal direction, getting the maximum value in the middle part, and decreases continuously from bottom to top in the vertical direction, obtaining the maximum value in the foundation part of the building. Figure 5(b) shows the horizontal stress distribution inside the transverse wall of the building under the horizontal deformation of the surface paralleling to the longitudinal wall. As shown in the figure, the outer ends of the transverse wall are compressive stress, the middle is tensile stress, the inner ends are tensile stress, and the middle is compressive stress. It can be inferred that the bending moment distribution is consistent with the theoretical analysis. Figure 5(c) shows the additional shear stress distribution inside the

transverse wall of the building. The absolute value of the shear stress decreases from the two ends to the middle and reaches 0 in the middle of the transverse wall. It can be seen that the numerical simulation experiment results are consistent with the theoretical analysis results, which verifies the correctness of the theory.

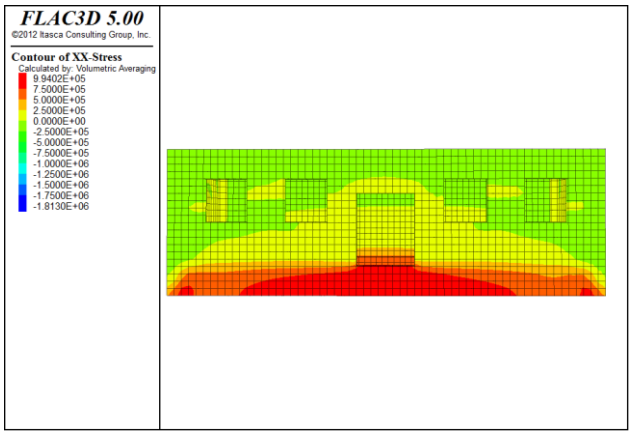

(a) Tensile stress distribution in the x-direction of the building under horizontal tension

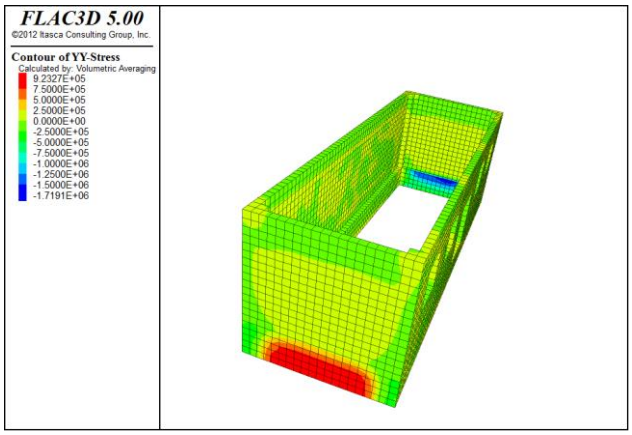

(b) Tensile stress distribution in the y-direction of the transverse wall under horizontal tension

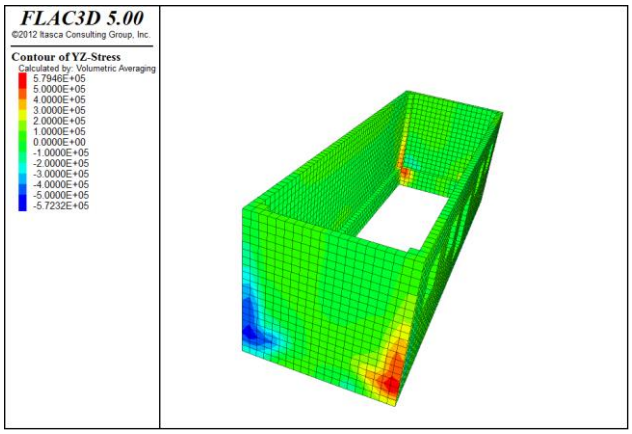

(c) Shear distribution of the transverse wall under horizontal tension

Fig. 5 - Diagram of building deformation and internal stress distribution under horizontal deformation

CASE ANALYSIS

Zhangzhuang Village is located in the northeast of Fengfeng mining area in Hebei Province, China. It is in the south of 2513, 2515 coal mining face. The mining of the working face has brought a large area of surface movement deformation and caused great damage to the interior house of Zhangzhuang Village[17]. Figure 6 shows that most of the houses in Zhangzhuang Village are located on the side of the coal wall in the goaf of 2515 working face, and a small number of houses are located on the upper part of the goaf. Most of the houses are brick-concrete structure buildings, which have strong compressive deformation resistance and weak tensile deformation resistance.

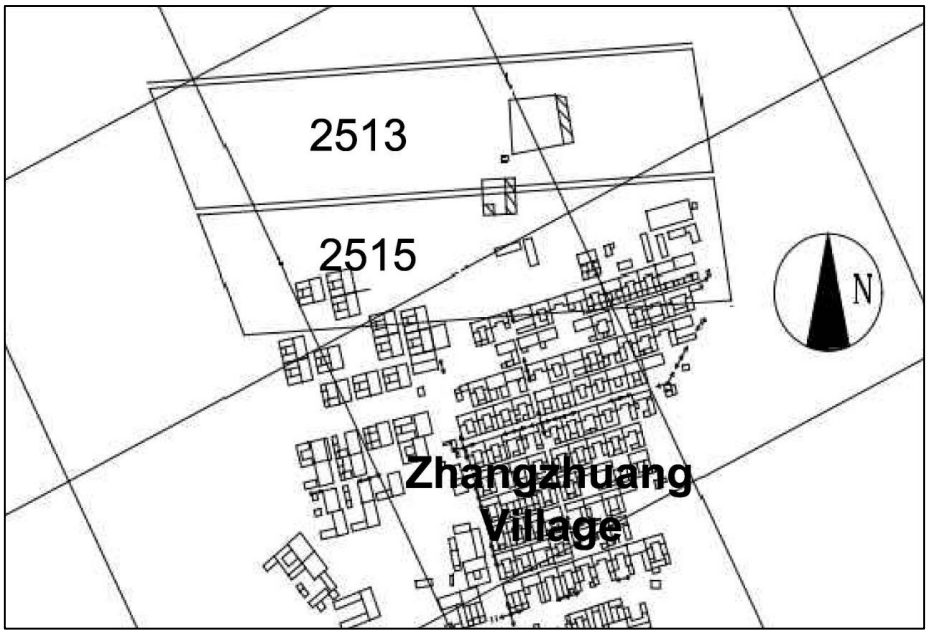

Fig.6 - The location relationship between working face and village

It can be known from the general law of mining subsidence (Figure 7), the houses on the side of the goaf are affected by surface compression deformation, and the houses on the side of coal wall are affected by surface tension deformation. According to the deformation parameters of the mining area, the surface horizontal deformation in the village is predicted with the probability integration method as follows: the maximum tensile deformation of the surface is 7 mm/m, and the maximum compression deformation is -6 mm/m.

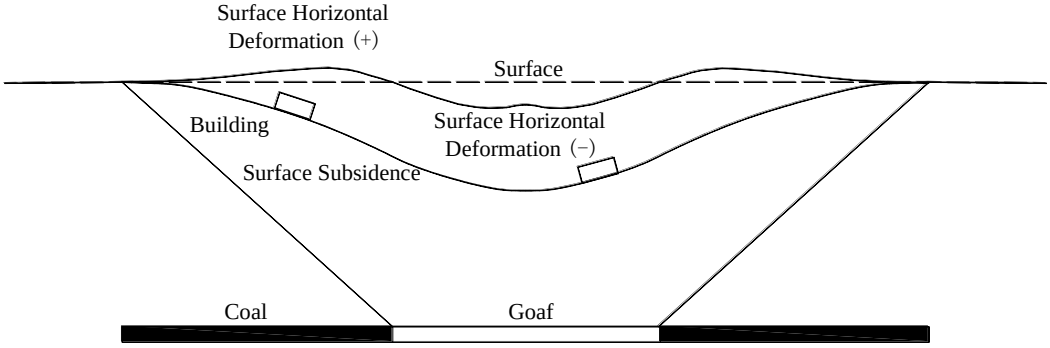

Fig.7 - Schematic diagram of surface horizontal deformation

According to the field survey and measurement of the damaged buildings in the mining area, it can be seen from Figure 8 that the vertical tensile cracks are generated in the middle of buildings under the effect of surface horizontal deformation. Herein the crack width of the house is about 6 mm in Figure 8(a), and the tensile crack of the house is 12 mm in Figure 8(b). From this we can see that the horizontal deformation of the mining area is likely to cause vertical damage in the middle of the building. It can be seen from Figure 9 that the joint between the transverse wall and the longitudinal wall of the house is damaged under the surface horizontal deformation, wherein the crack width in the corner of the house in Figure 9(a) is 13mm. In Figure 9(b), the crack in the wall corner of the house is distributed in the form of upper narrow and lower wide, and the width of the upper crack is 5 mm and the width of the lower crack is 33 mm. This shows that the two ends of the building are also susceptible to the surface horizontal deformation, and the

damage propagates from the bottom to the top of the building. Comparing Figure 8 with Figure 9, we can see that the damage degree at two ends of the building is greater than that in the middle of the building. The reason is that when damage occurs at two ends of the building, cracks block the propagation of stress from two ends to the middle of the building, resulting in the reduction of the stress concentration in the middle part of the building, so the damage degree is reduced. The damage forms of buildings in this area verify the theoretical analysis above.

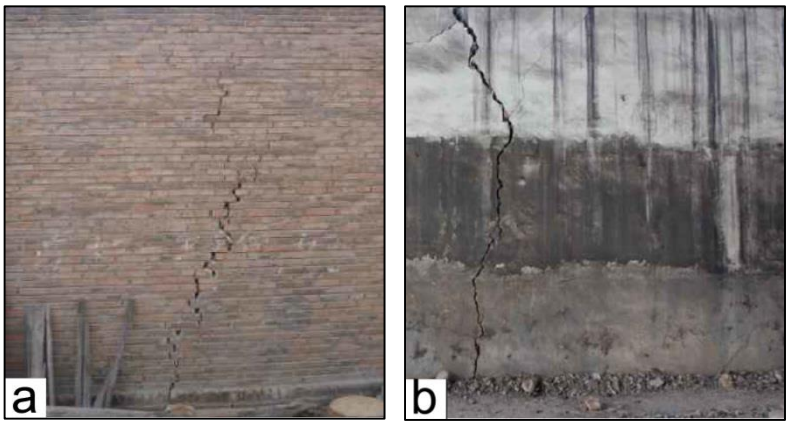

Fig.8 - Cracks in the middle of building walls

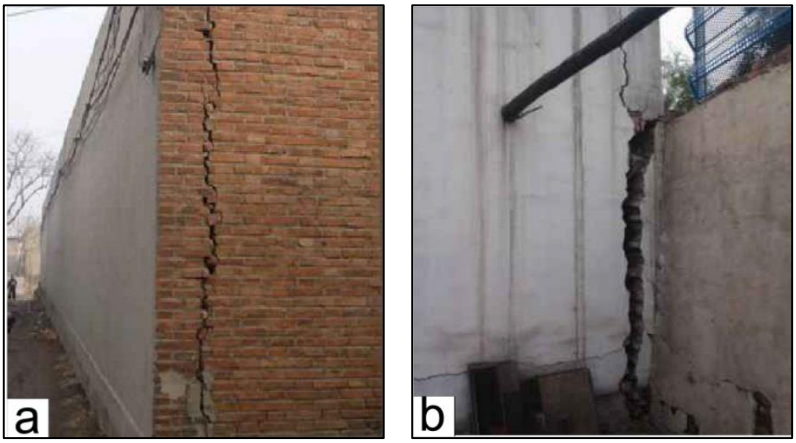

Fig.9 - Cracks at both ends of building walls

BUILDING PROTECTION UNDER SURFACE HORIZONTAL DEFORMATION

From the above analysis, it can be concluded that the horizontal stress along the axial direction of the longitudinal wall is the primary cause of buildings damage generated by the surface horizontal deformation. The greater the friction coefficient and cohesion between the building foundation and the ground soil are, the larger the internal horizontal stress will be. So a sliding layer can be set between the ground soil and the building foundation in the mining area, replacing the ground soil under the building foundation to reduce friction coefficient and cohesion. The longer the length of the building wall is, the greater the maximum horizontal stress inside the building is. Therefore, for buildings with longer length, deformation joints can be arranged in the middle of the building wall to divide a long-length building into a plurality of buildings with shorter length, so as to reduce the influence of building length.

CONCLUSIONS

The theoretical model of the internal additional stress variation in the strip foundation building under the surface horizontal deformation is established. It is considered that when the horizontal deformation direction of the surface is along the axial of the building transverse wall, the damage of the building longitudinal wall is caused by the additional tensile stress, and the destruction of the building transverse wall is caused by the additional bending moments and additional shear.

The extreme value of the internal additional stress in the strip foundation building increases with the increasing of friction factor, upper load and the building length.

The numerical simulation method is used to analyse the influence of horizontal deformation on the foundation and wall of the strip foundation building. It is found that the effect on the building foundation is consistent with the theoretical analysis, which verifies the correctness of the theoretical analysis.

The case analysis shows that the stress concentration caused by the surface horizontal deformation will cause damage in the middle and two ends of the building, which confirms the reliability of the theoretical analysis. In addition, the case analysis shows that the cracks at two ends of the building block the propagation of stress from two ends to the middle of the building, thus reducing the damage degree in the middle of the building.

By analysing the mechanism of building damage caused by horizontal deformation in the mining area, protection methods for the strip foundation building under horizontal deformation are proposed.

ACKNOWLEDGMENTS

This work was funded by the National Natural Science Foundation of China (Grant No. 51674249), China Postdoctoral Science Foundation Funded Project (No.2017M621873).

REFERENCES

[1] Ministry of Land and Resources, P. R. China, Report on Chinese Land Resource in 2014. Ministry of Land and Resources of the People's Repubic of China, Beijing (in Chinese)

[2] Guo, G. L., Zha, J. F., Miao, X. X., Wang, Q., & Zhang, X. N., 2009. Similar material and numerical simulation of strata movement laws with long wall fully mechanized gangue backfilling. Procedia Earth & Planetary Science, vol. 1: 1089-1094.

[3] Zhu, X., Guo, G., Zha, J., Chen, T., Fang, Q., & Yang, X., 2016. Surface dynamic subsidence prediction model of solid backfill mining. Environmental Earth Sciences, vol. 75: 1-9.

[4] Guo G L, Zhu X J, Zha J F, et al., 2014. Subsidence prediction method based on equivalent mining height theory for solid backfilling mining. Transactions of Nonferrous Metals Society of China, vol. 24: 3302-3308.

[5] Bennett, R. M., Drumm, E. C., Lin, G., Triplett, T., & Powell, L., 1996. Effects of ground subsidence on a house. Journal of Performance of Constructed Facilities, vol. 4: 152-158.

[6] Marino, G. G., & Gamble, W., 1986. Mine subsidence damage from room and pillar mining in illinois. International Journal of Mining & Geological Engineering, vol. 4: 129-150.

[7] Boone, S. J., 2001. Assessing construction and settlement-induced building damage: a return to fundamental principles. Underground Construction, vol. 34: 559-570.

[8] Namazi, E., & Mohamad, H., 2012. Assessment of building damage induced by three-dimensional ground movements. Journal of Geotechnical and Geoenvironmental Engineering, vol. 139: 608-618.

[9] Boscardin, M. D., & Cording, E. J., 1989. Building response to excavation-induced settlement. Journal of Geotechnical Engineering, vol. 115: 1-21.

[10] Son, M., & Cording, E. J., 2005. Estimation of building damage due to excavation-induced ground movements. Journal of geotechnical and geoenvironmental engineering, vol. 131: 162-177.

[11] Cording, E. J., Long, J. L., Son, M., Laefer, D., & Ghahreman, B., 2010. Assessment of excavation-induced building damage. In Earth Retention Conference 3 (pp. 101-120).
[12] Truong-Hong, L., & Laefer, D. F., 2008. Micro vs. macro models for predicting building damage underground movements. In Paper presented at CSM-2008 the International Conference on Computational Solid Mechanics, November 27-30, 2008, Ho Chi Minh City, Vietnam.
[13] Selby, A. R., 1999. Tunnelling in soils–ground movements, and damage to buildings in Workington, UK. Geotechnical & Geological Engineering, vol. 17: 351-371.
[14] TAN, Z. X., & DENG, K. Z., 2004. Coordinating Work Model of Ground, Foundation and Structure of Building in Mining Area [J]. Journal of China University of Mining & Technology, vol. 3: 7., in Chinese)
[15] TAN, Z. X., & DENG, K. Z., 2007. Study on change laws of additional ground reaction force of buildings in mining area [J]. Journal of China Coal Society, vol. 9: 2. (in Chinese)
[16] Ministry of Housing and Urban-Rural Development of the PR China., 2011. Code for design of masonry structures, China Construction Industry Press Beijing, Beijing, China. (in Chinese)
[17] WANG, B., 2017. The Research of Evaluation Method for Mining Damage to Buildings of Fengfeng Mining Area, Henan Polytechnic University, Jiaozuo, China. (in Chinese)

Article no. 18

THE CIVIL ENGINEERING JOURNAL 2-2019

NUMERICAL INVESTIGATION OF FRP-STRENGTHENED REINFORCED CONCRETE BEAMS AT HIGH TEMPERATURES

Osama El-Mahdy, Gehan Hamdy and Moustafa Abdullah

Department of Civil Engineering, Faculty of Engineering at Shoubra, Benha University, Shoubra, Cairo, Egypt; osama.alhenawy@feng.bu.edu.eg; os8294@hotmail.com

ABSTRACT

Fiber reinforced polymers (FRP) strengthening systems are mainly used to retrofit existing and deficient structural members. The performance of such strengthened structures at elevated temperatures is a critical issue that threatens the safety of the structure. Published research includes experimental testing of reinforced concrete (R.C) beams strengthened using FRP and subjected to fire tests. However, there is a need for numerical tools that simulate the performance of these FRP-strengthened elements in case of fire. This research work presents numerical modelling and nonlinear analysis conducted to assess the performance of reinforced concrete beams strengthened with externally bonded carbon FRP sheets when subjected to standard fire conditions. Finite element model using the general purpose software ANSYS 12.1 is developed and validated with experimental results published in the literature by other researchers.

The developed finite element model achieved good correlation with the experimental results. Further, application of the validated finite element model is extended into a parametric study to explore the influence of different variables on the performance of the FRP system when subjected to fire. Different aggregate types, moisture contents, concrete cover thickness, insulation material types and insulation material thickness are included in the study. The developed finite element model is thus regarded a valid and economical alternative to experiments for prediction of the performance of FRP strengthened and insulated R.C beams under fire conditions. Additionally, it can be used for estimation of the fire rating of such structures as well as for design of adequate fire protection layers.

KEYWORDS

Fire performance, Thermal insulation, Numerical modeling, Fiber reinforced polymers (FRP), Reinforced concrete beams; Flexural strengthening

INTRODUCTION

Fiber reinforced polymers (FRP) strengthening systems are mainly used to retrofit existing and deficient structural elements. Fire performance is pointed out as a critical factor that requires more research before FRP can be used with confidence in strengthening applications. Specifications and design guidelines limit the use, increase the load factor or limit the desired strength enhancement in order to meet fire hazard [1, 2]. There are still no design guidelines available for FRP-reinforced or strengthened concrete structures under fire conditions; which is one of the major threats to buildings and other structures. Experimental studies were carried out for FPR-strengthened reinforced concrete (R.C) members under elevated temperatures or fire by several researchers [3-10]. To provide protection of CFRP from direct fire exposure, a coating layer

of a thermal insulating material, typically gypsum products, was placed around the beam cross-section.

Few studies in the published literature addressed numerical modelling to predict the performance of FRP-strengthened R.C members subjected to fire [11-17] and the heat transfer through the different insulation layers during fire exposure [18]. Therefore, more research work is needed to model efficiently the performance of FRP-strengthened structures under elevated temperatures, in order to enable the analyst and designers to accurately predict the fire endurance and design efficiently the thermal insulation layers for such structures.

OBJECTIVE

The present paper aims at investigating numerically the behaviour of R.C beams strengthened by externally bonded FRP and thermally protected under standard fire test loading. Therefore, the paper provides an economical alternative to experiments for prediction of the performance of FRP strengthened and insulated RC beams under fire conditions. Additionally, it can be used for estimation of the fire rating of such structures as well as for design of adequate fire protection layers.

To achieve this aim, nonlinear finite element modelling is conducted and verified using the previously published experimental and numerical results [18, 23].

FINITE ELEMENT MODELLING

Nonlinear time analysis is performed using commercial software ANSYS 12.1 [19]. Finite element modelling is made for an R.C beam that has been subjected to fire test in the published literature [23]. The T-beam with span 3900 mm has the cross-section and reinforcement shown in Figure 1. The T-beam reinforcement details were as follows; the main steel reinforcement was two 20 mm diameter bars. Shear stirrups were 10 mm diameter bars spaced at 150 mm center to center. Concrete cover to the web stirrups was 40 mm and concrete cover for flange reinforcement was 25 mm. A CFRP laminate 1.3 mm thick and 100 mm wide is adhered to the bottom of the beam along the span and stopped at 100 mm from the support. A layer of vermiculite-gypsum (VG) plaster having thickness 25 mm is applied on the beam soffit and web and extends for a distance of 125 mm underneath the flange along the entire length of the beam. The element types used for transient thermal and structural finite element analysis are given in Table 1. The model accounts for the variation in thermal and mechanical parameters of the different materials with temperature.

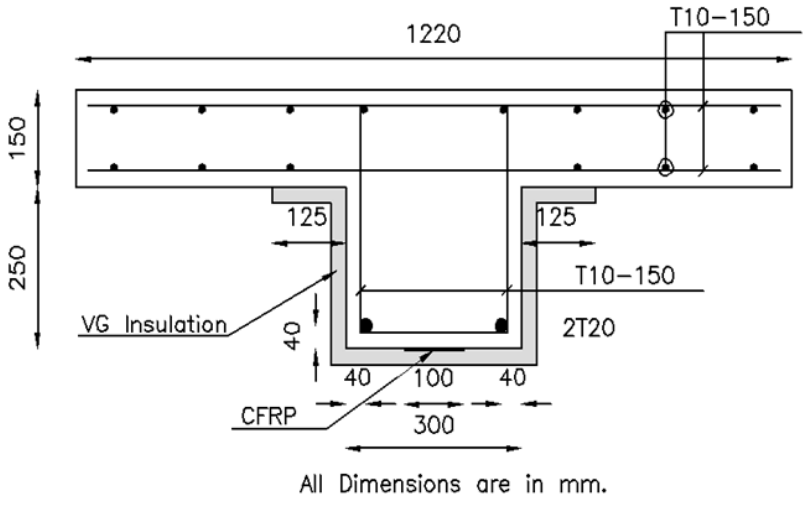

Fig. 1- Cross-section of experimentally tested T-beam [23]

DOI 10.14311/CEJ.2019.02.0018

Tab. 1 - Element types used for thermal and structural analyses

Material	Thermal analysis	Structural analysis
Concrete	SOLID70	SOLID65
Steel bars	LINK33	LINK8
CFRP layer	SHELL 57	SHELL 41
VG insulation	SOLID70	SOLID45

MATERIALS MECHANICAL AND THERMAL PROPERTIES

The concrete characteristic compressive strength is 41 MPa. The main steel reinforcement has yield and ultimate strengths of 500 and 650MPa, respectively. The 10mm diameter reinforcement bars have yield and ultimate strengths of 429 and 611MPa, respectively. The 1.3 mm-thick CFRP laminate possesses a design tensile strength of 460 MPa in the direction of the fibers and ultimate elongation of 2.2% at failure [23]. Table 2 gives the values for the materials mechanical and thermal properties at room temperature found in the literature [18, 20].

Tab. 2- Mechanical and thermal material properties at room temperature [18, 20]

Material	E_o MPa	K_o W/mm.K	C_o J/kg.K	μ	α	ρ_o Kg/m^3
Concrete	30200	2.7×10^{-3}	722.8	0.20	6.08×10^{-6}	2400
Steel bars	210000	5.2×10^{-2}	452.2	0.30	6.00×10^{-6}	7860
CFRP	228000	1.3×10^{-3}	1310	0.28	-0.90×10^{-6}	1600
VG Insulation	2100	2.5×10^{-4}	1654	0.30	1.70×10^{-5}	269

The thermal and mechanical properties at elevated temperature for concrete and steel are available in the literature [20-22, 27]. The variation of normalized density, modulus of elasticity, thermal conductivity, and specific heat with temperature for the constituent materials are shown in Figure 2.

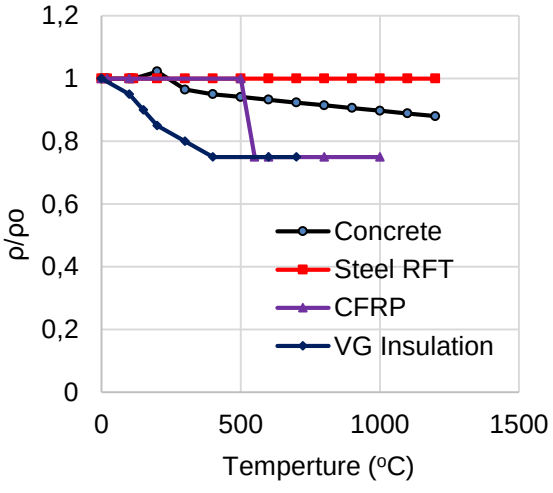

(a) Normalized density

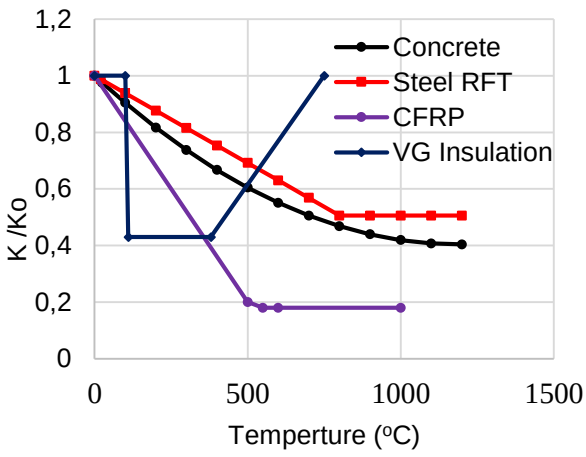

(b) Normalized thermal conductivity

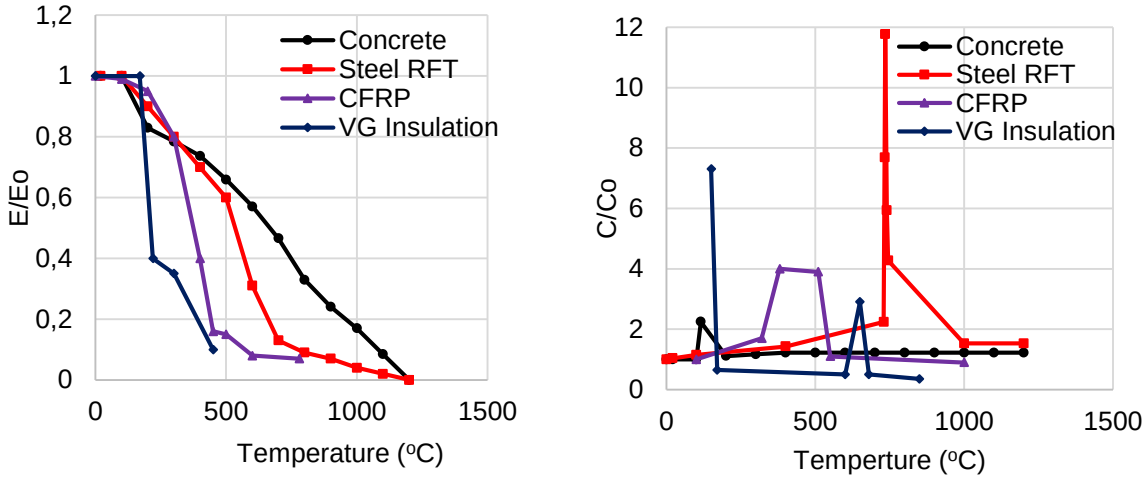

(c) Normalized stiffness *(d) Normalized specific heat*

Fig. 2 - Variation of mechanical and thermal properties of materials with temperature

The stress strain-curves for concrete in compression under elevated temperature adopted in the present study are shown in Figure 3(a), and the variation of concrete tensile strength with temperature is shown in Figure 2 (b) [18, 22]. The variation of the mechanical and the thermal properties of FRP and the materials used for thermal insulation is addressed in researches and not quite established. In this study, the thermal and mechanical properties of CFRP and VG insulation and their variation with temperature are based on the findings of other researchers [21, 24 - 25].

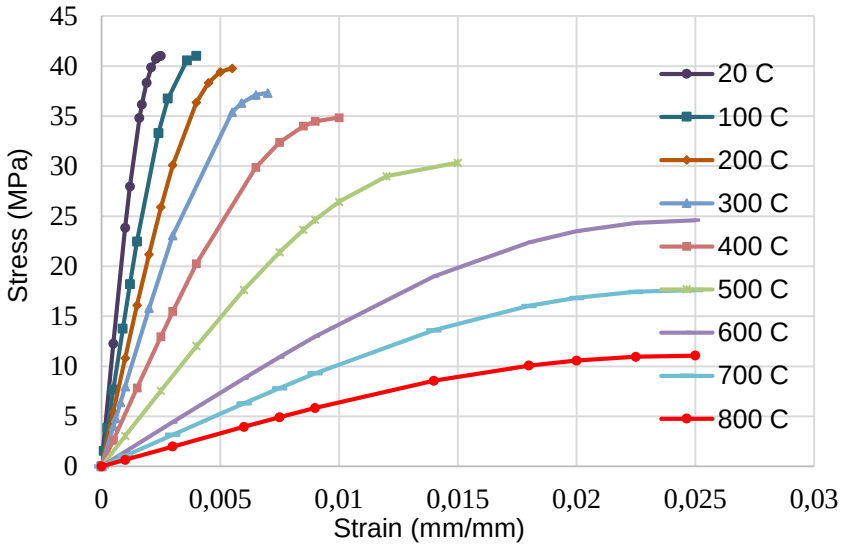

(a) Stress-strain curves in compression under elevated temperature

DOI 10.14311/CEJ.2019.02.0018

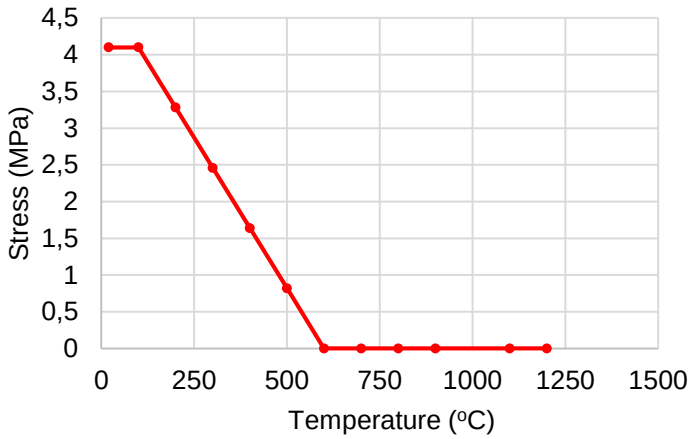

(b) Variation of concrete tensile strength with temperature

Fig. 3: Concrete mechanical behavior under elevated temperature [22]

ANALYTICAL PARAMETERS, LOADING TECHNIQUE AND BOUNDARY CONDITIONS

Concrete is modelled using the standard nonlinear constitutive concrete material model implemented within ANSYS [19]. The stress-strain temperature curves for concrete in compression and tension shown in Figure 3 are utilized. When a crack occurs, elastic modulus of the concrete element is set to zero in the direction parallel to the principal tensile stress direction. Crushing occurs when all principal stresses are compressive and are outside the failure surface; then the elastic modulus is set to zero in all directions and the element local stiffness becomes zero causing large displacement and divergence in the solution.

The analysis is carried out as two consecutive load cases. First, in the transient thermal analysis load case, standard temperature-time conditions described by ASTM E119 [26] and shown in Figure 4 are applied as nodal temperature-versus-time to the bottom surface of the T-beam. Equation 1 gives the ASTM E119 time temperature loading applied to the studied beam.

$$T = 20 + 750\left(1 - e^{-0.49\sqrt{t}}\right) + 22\sqrt{t} \qquad (1)$$

The thermal gradient distribution in the T-beam from the thermal analysis is next applied to the beam as nodal temperatures at several time load steps and sub-steps and structural stress analysis is performed. The beam has simply supported end conditions, and the experimentally applied sustained uniformly distributed load of 34 KN/m [23] is simulated by applying a pressure of 0.0278 MPa to the top surface of the T-beam flange.

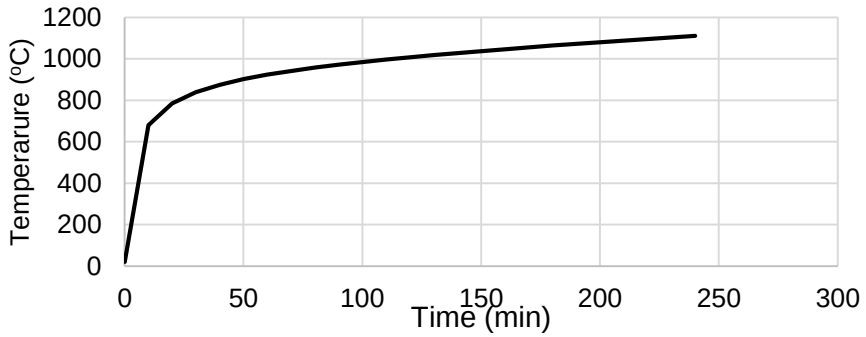

Fig. 4- Applied temperature conforming to Standard Fire Test Curve of ASTM E119

VERIFICATION OF RESULTS

In order to validate the accuracy of the developed model, the obtained finite elements results are compared to the available experimental and numerical results. The thermal analyses results are evaluated by checking the temperatures at key locations with temperature gradients between the key locations of the beam model. The nodal temperature distribution within the T-beam cross section after four hours of fire exposure is shown in Figure 5. The variation with time of the numerically calculated temperatures in VG, CFRP, and concrete at the same points that were measured in the experiment work [23] are plotted in Figure 6. It can be concluded from these figures that there is good agreement between the presented numerically predicted temperatures and the published experimental and numerical results [18, 23].

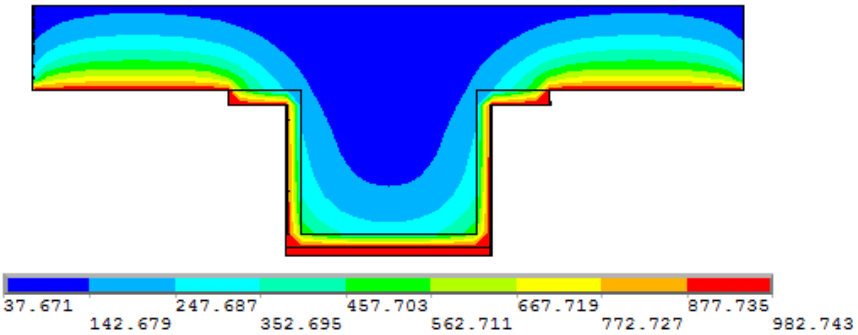

Fig.5 - Numerical predicted temperature distribution in beam cross-section (°C) after four hours

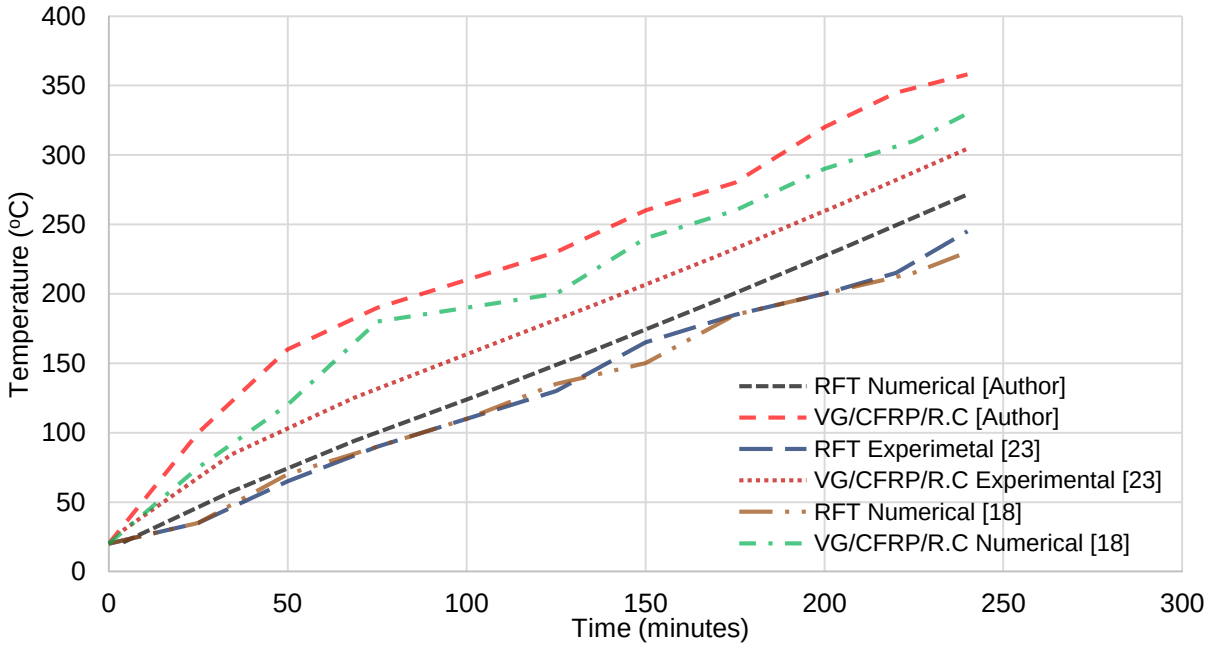

Fig. 6 - Numerical results of temperature versus time compared to experimental results

Figure 7 shows the numerically predicted and the experimentally measured mid-span deflection at the centerline of the cross section under the applied sustained uniformly distributed load as a function of fire exposure time. It can be concluded that the predicted mid-span deflection matches very closely the measured experimental one [23]. Furthermore, the adopted model is

demonstrated to provide a more enhanced description of the experimental results than the published numerical results [18]. The accuracy of the adopted model herein can be attributed to modelling the FRP system using shell elements rather than the solid elements used in the published model, in addition to proper description of the constituent materials properties and the finer meshing used in the present model.

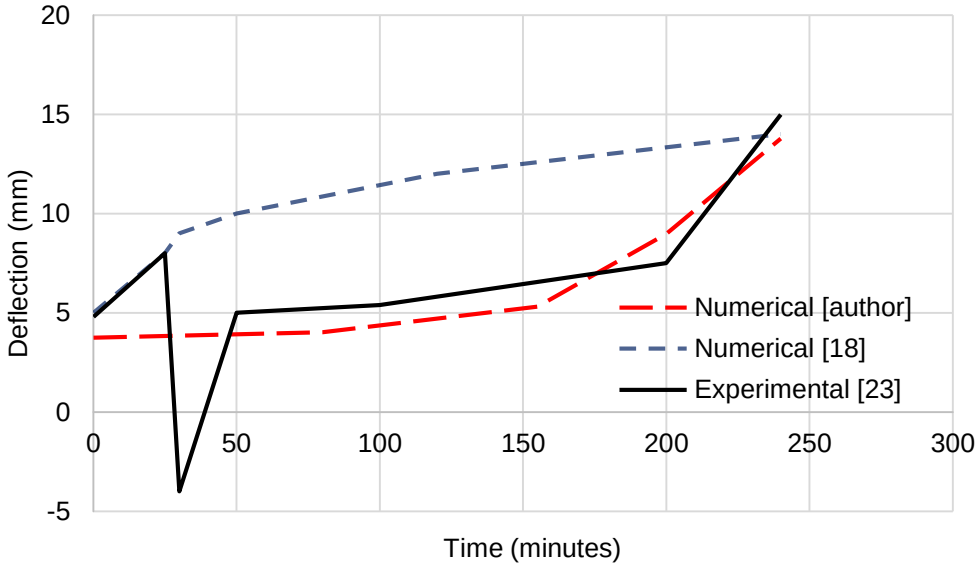

Fig. 7 - Variation of mid-span deflection with exposure time

PARAMETRIC STUDY

As the adopted finite element model achieved good correlation with the experimental program, a parametric study is designed to further investigate several different parameters on the performance of CFRP strengthened and insulated R.C beams, e.g. different aggregate types, moisture contents, concrete cover, insulation material thickness, different yield strength and concrete compressive strength. The following subsections show the results of studied parameters.

Concrete Aggregate Types

This section studies the effect of carbonate and siliceous aggregates on the behaviour of the CFRP strengthened R.C beams. The numerical results plotted in Figure 8 show that mid-span deflection of the R.C beam with carbonate aggregate in the concrete mix is 12 % less than that of a beam with siliceous aggregate, after 4 hours of exposure to standard fire conditions.

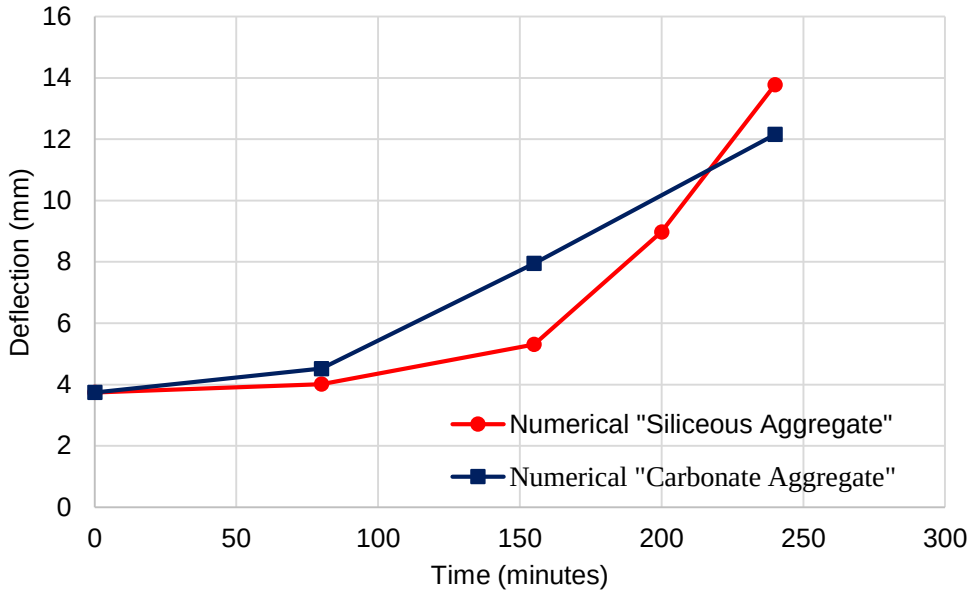

Fig. 8 - Mid-span deflection for different concrete aggregate types

Concrete Mix Moisture Content

As shown in Figures 9 (a) and (b), the temperature at steel reinforcement and VG/CFRP/R.C interface level increase with the decrease of moisture content in the concrete mix. This may be attributed to the absence of any water enough to absorb some of the thermal effects which leads to the increase in both steel reinforcement and VG/CFRP/R.C substrate temperature directly. Figure 10 shows also that at 0% moisture, the R.C beam deflection increases by 73% over the R.C beam deflection at 3% moisture. This emphasizes the importance of suitable moisture content in the concrete mixes.

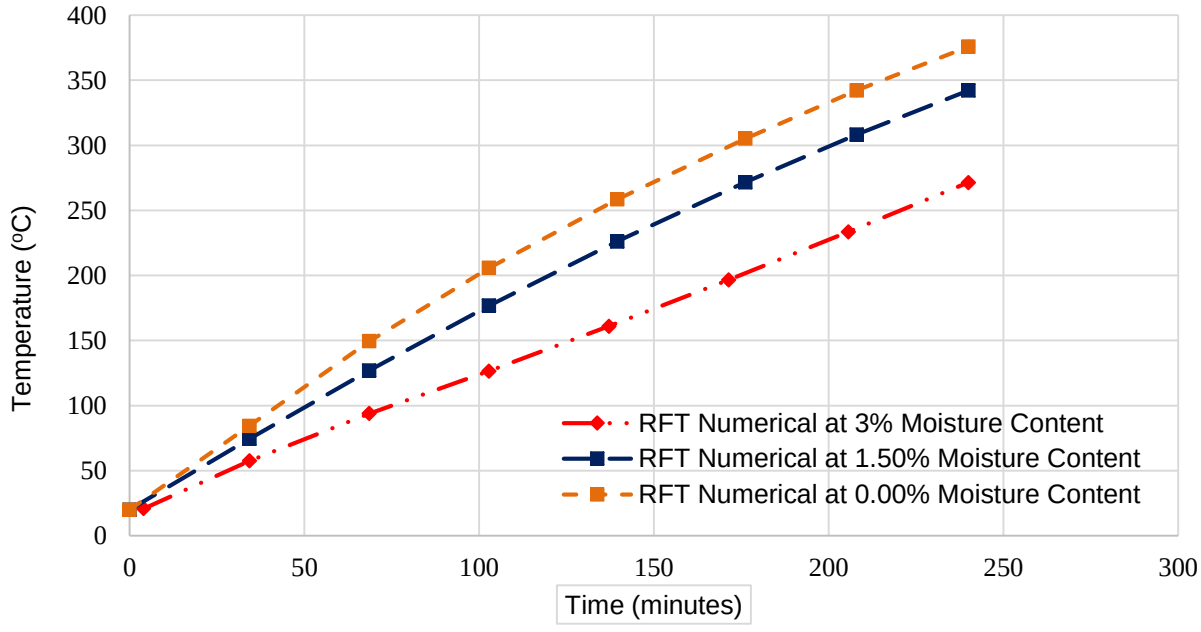

(a) Effect of moisture content on the thermal response of steel reinforcement

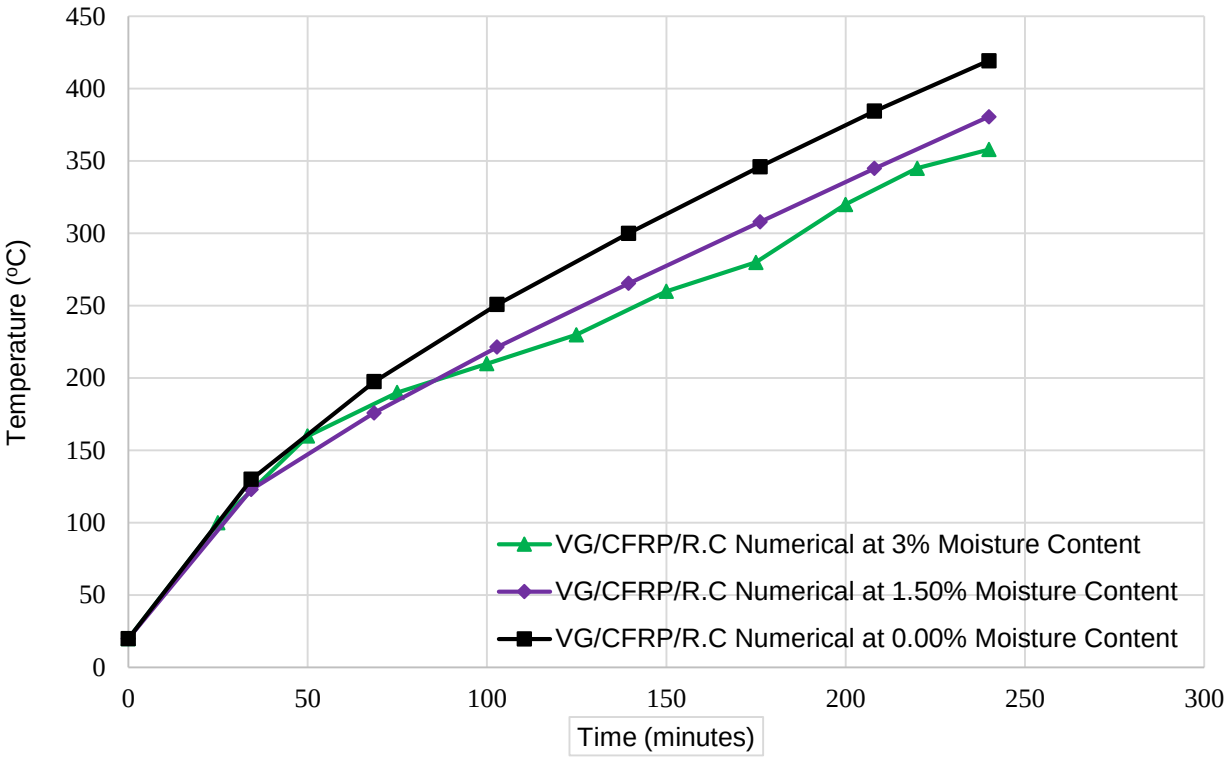

(b) Effect of moisture content on the thermal response of VG/CFRP/R.C interface

Fig. 9- Effect of moisture content on the thermal response of the beam

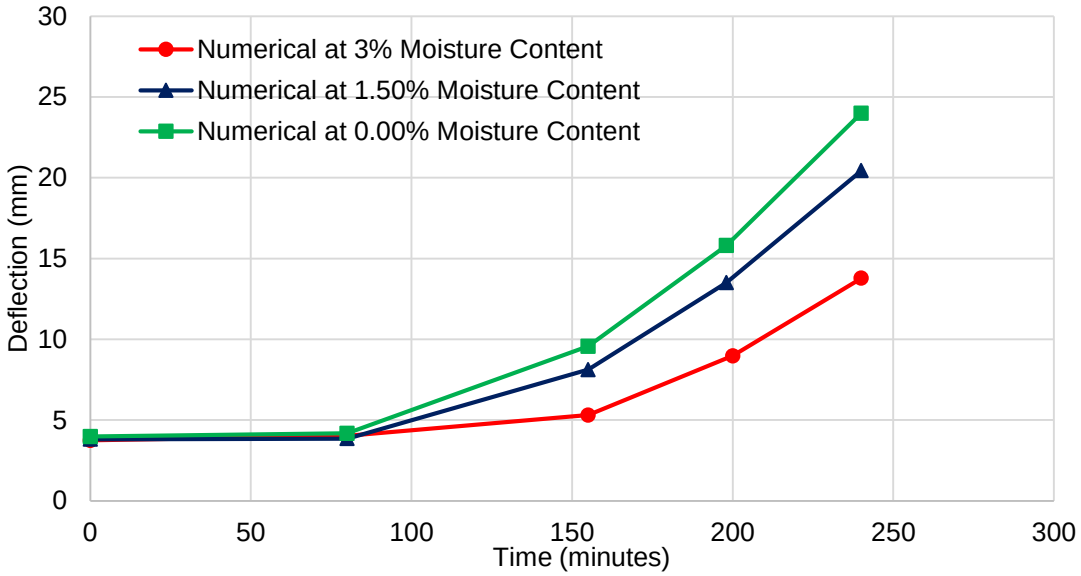

Fig. 10- Effect of moisture content on the structural response of the beam

Insulation Material Type and Thickness

Figure 11 presents the effect of increasing the VG insulation material thickness which decreases the temperature at both the steel reinforcement level and the CFRP/concrete level. Additionally, the mid-span deflection decreased with using a thicker VG material as plotted in Figure 12. This is due to the fact that a thicker insulation material with proper insulation properties is expected to decrease the thermal effect on the beam which in turn decreases the thermal strains and hence leads to a reduced mid-span deflection value.

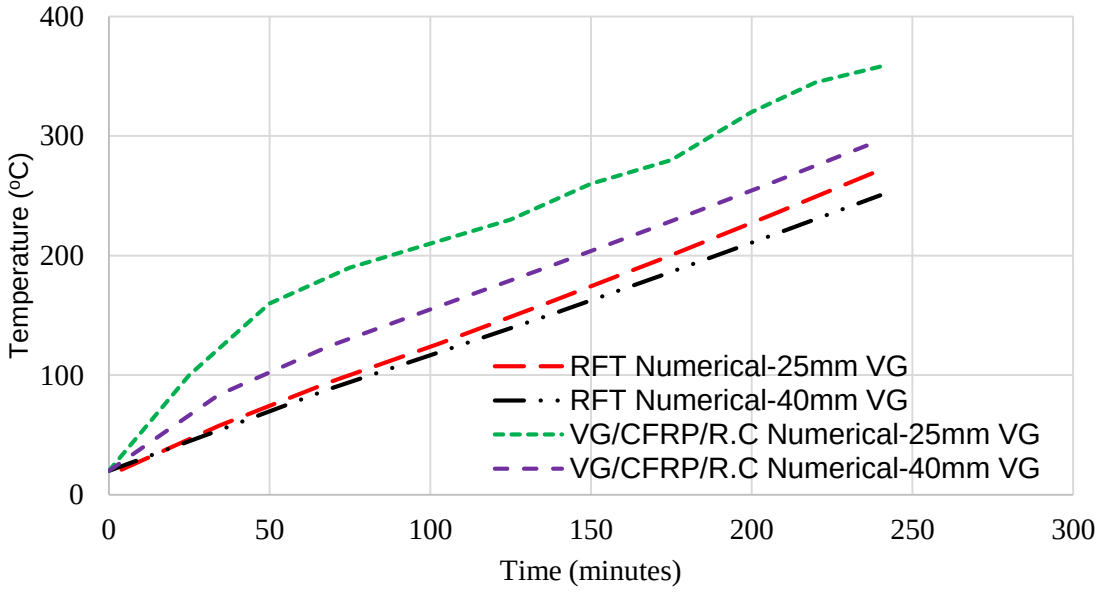

Fig. 11- Effect of changing VG thickness on thermal response of beam

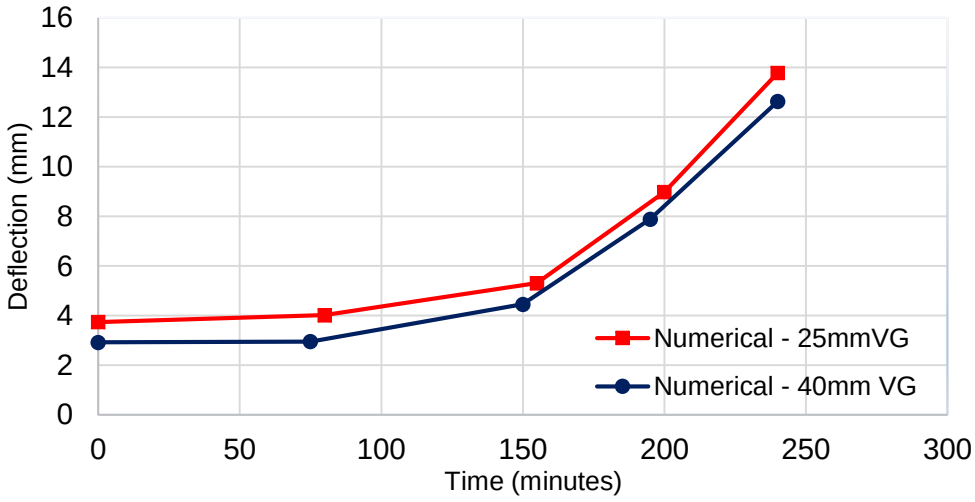

Fig. 12 - Effect of changing VG thickness on the structural response of beam

Concrete Cover

Concrete cover is an important parameter for fire rating and maintaining the durability of the R.C structural element. The increase of concrete cover thickness decreases the temperature at the steel reinforcement level as shown in Figure 13. Figure 14 presents the mid-span deflection of the

beam after four hours under the standard fire test. The increase of concrete cover thickness limits and reduces the thermal strains on the beam which is reflected on the tension cracks of the beam and hence reduces the mid-span deflection. According to ACI 318-14 [28], the beam with 20 mm thick cover is regarded as unsafe in deflection despite being safe in thermal response.

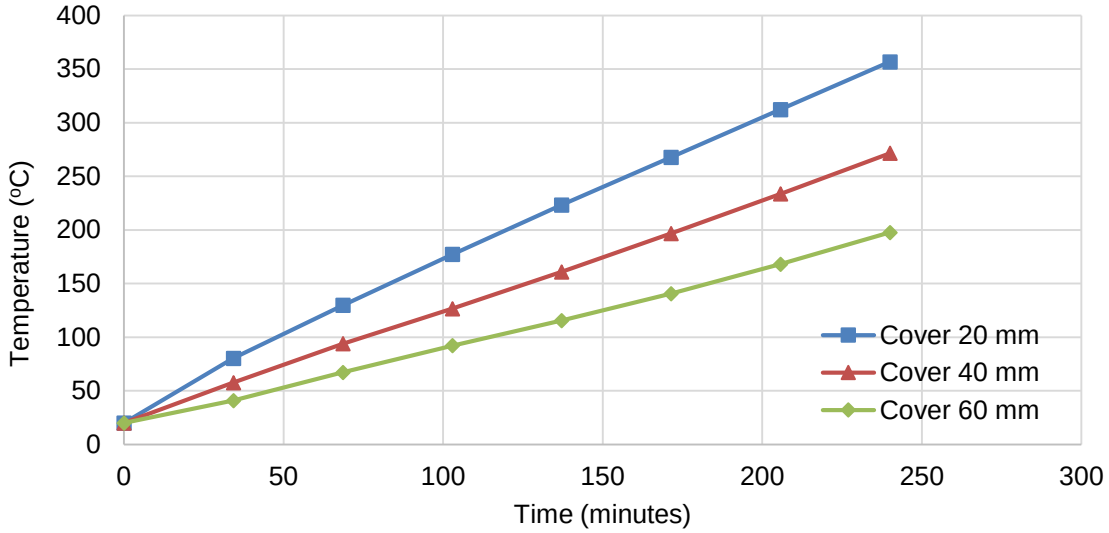

Fig. 13- Effect of changing the concrete cover thickness on thermal response of beam

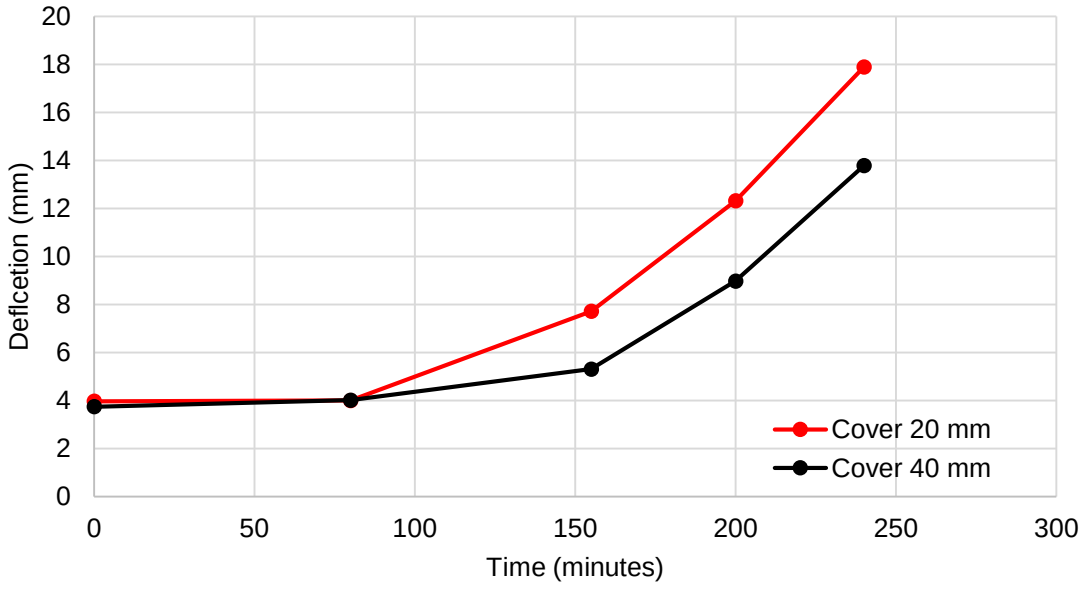

Fig. 14- Effect of changing the concrete cover thickness on structural response of beam

Steel Reinforcement Yield Strength

Despite being an important parameter in design of R.C beams, the steel reinforcement yielding strength has no vital effect on the mid-span beam deflection as shown in Figure 15.

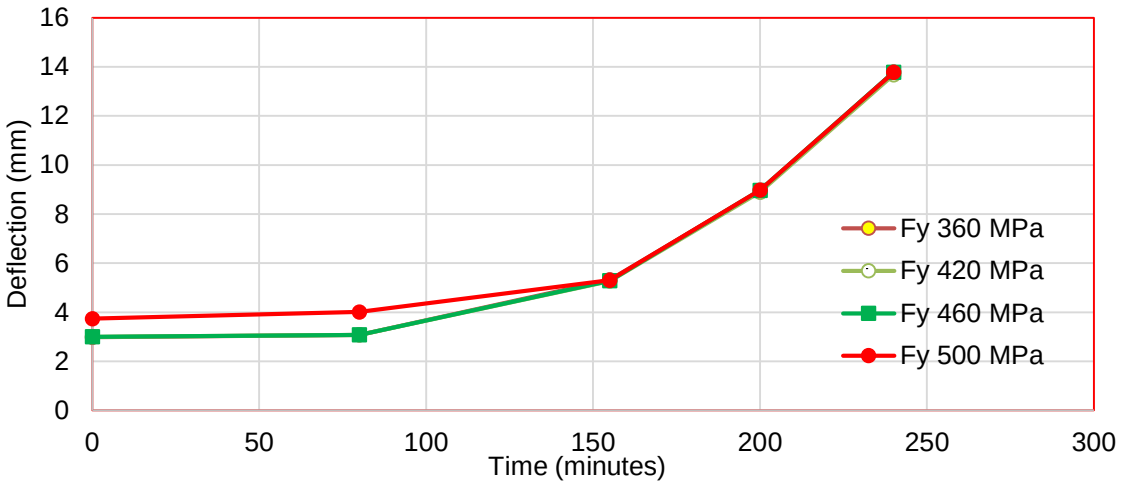

Fig. 15- Effect of changing reinforcement yield strength on structural response of beam

Concrete Compressive Strength

Concrete compressive strength has an important role in design of the R.C beam. Figure 16 shows the mid-span deflection of the R.C beam for different concrete compressive strength. The increase in compressive strength reduces the mid-span deflection as shown for concrete having C40 and C50.

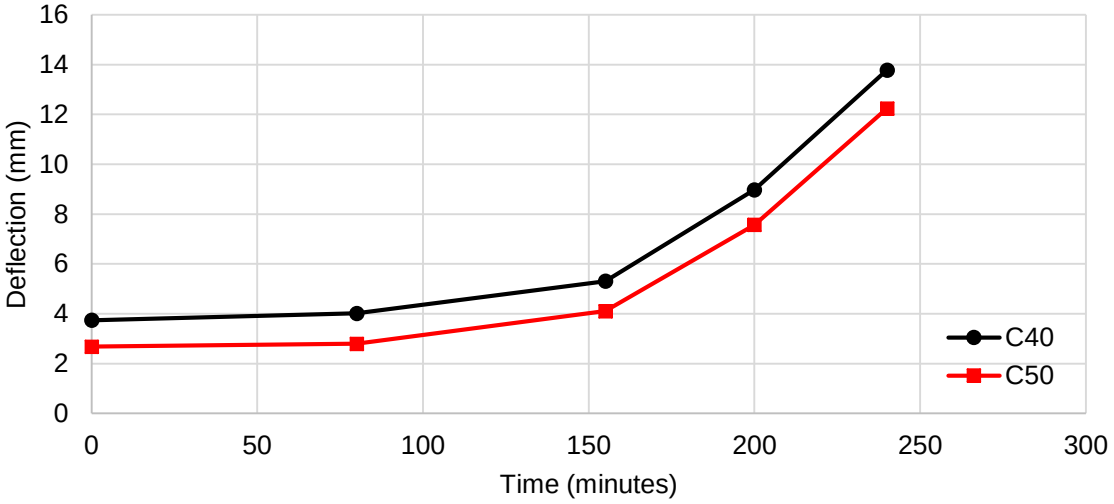

Fig. 16- Effect of changing concrete compressive strength on the structural response of beam

CONCLUSION

The paper presented numerical modelling procedure using finite elements that accurately simulates the behaviour of thermally insulated R.C beam strengthened in flexure with CFRP laminate when exposed to standard fire test. Numerical modelling and nonlinear analysis are performed using ANSYS 12.1 [19]. A parametric study is conducted for investigation of several parameters on the beam thermal behaviour. Based on the obtained numerical results the following conclusions can be drawn:

1. The numerical results of the proposed model are in good agreement with the published experimental ones regarding mid-span deflection and temperature distribution within the

cross-section throughout the elevated temperature time history.

2. The proposed model gives more accurate representation for mid-span deflection compared with published numerical results due to using shell elements for FRP, proper representation of the constituent materials used and the refined meshing used in the present model.
3. The developed models can be considered as an alternative solution for the time consuming and expensive fire testing.
4. Increasing insulation material thickness enhances the beam thermal response.
5. Mid-span deflection usually decreases with the increase of insulation thickness.
6. The concrete cover is a vital key element to protect the steel reinforcement from thermal effect and increase beams durability.
7. The steel yield strength has no important role in fire resistance of the structural element.
8. The carbonate aggregate is better than the siliceous aggregate in fire resistance of the R.C element.
9. Increasing the moisture content within the R.C structural element will enhance the thermal performance of the beam but care should be given so as not to affect the structural performance of the beam.
10. The concrete compressive strength is an important parameter that influences the thermal and structural performance of R.C beams.

REFERENCES

[1] American Concrete Institute (ACI), ACI 440.2R-08, “Guide for the design and construction of externally bonded FRP systems for strengthening concrete structures”, ACI Committee 440, Farmington Hills, MI, USA, 2008.

[2] ECP Committee 208, ECP 208-05: “Egyptian code of practice for the use of fiber reinforced polymer in the construction field”, ECP Committee 208, Ministry of Housing and Urban Communities, Egypt, 2005.

[3] Blontrock, H., Taerwe, L., and Vandevelde, P., “Fire tests on concrete beams strengthened with fiber composite laminate”, Third Ph.D. Symposium, Vienna, Austria, (2000), 10 pp.

[4] Blontrock, H., Taerwe, L, and Vandevelde, P., “Fire testing of concrete slabs strengthened with fiber composite laminate”, 5th Annual Symposium on Fiber-Reinforced-Plastic Reinforcement for Concrete Structures (FRPRCS-5), London, U.K., 2001, pp. 547–556.

[5] Williams, B., Bisby, L., Green, M., Kodur, V.K.R., and Su, J, Z., “An investigation on fire performance of FRP strengthened RC Beams”, 8th International Symposium on Fire Safety Science, Beijing, 2005, pp. 247–258.

[6] Gamage, J., Al-Mahaidi, R., and Wong, M.B., “Bond characteristics of CFRP plated concrete members under elevated temperatures”, Composite Structures, 75(1-4), 2006, pp.199–205.

[7] Klamer, E.L., Hordijk, D.A. and Hermes, M.C.J., “The influence of temperature on RC beams strengthened with externally bonded CFRP reinforcement”, Heron, 53(3), 2008, pp. 157–185.

[8] Yu, B., and Kodur, V.K.R., "Effect of temperature on strength and stiffness properties of near-surface mounted FRP reinforcement", Composites Part B: Eng. 58 (2014) 510-517.

[9] Firmo, J.P., Pitta, D, Correia, J.R., Tiago, C., and Arruda, M.R.T., "Experimental characterization of the bond between externally bonded reinforcement (EBR) CFRP strips and concrete at elevated temperatures", Cement Concrete Composites,60 (2015) 44-54.

[10] Firmo, J.P., and Correia, J.R., "Fire behaviour of thermally insulated RC beams strengthened with EBR-CFRP strips: experimental study", Composite Structures, 122 (2015) 144-154.

[11] O. El-Mahdy., G. Hamdy and M. Abdullah, (2018), "Numerical Investigation of The Performance of Insulated FRP-Strengthened Reinforced Concrete Beams in Fire", The Civil Engineering Journal (CEJ), Stavebni Obzor, Faculty of Civil Engineering, CTU in Prague, Czech Republic, No. 46, Issue 4, pp. 573-586

[12] Gao, W.Y., Dai, J.G., Teng, J.G., and Chen, G.M., "Finite element modeling of reinforced concrete

beams exposed to fire", Engineering Structures, 52 (2013) 488-501.
[13] Dai, J., Gao, W., and Teng, J., "Finite element modeling of insulated FRP-strengthened RC beams exposed to fire", Journal of Composites in Construction, 19(2) (2015)1-15.
[14] Arruda, M.R.T., Firmo, J.P., Correia, J.R., and Tiago, C., "Numerical modelling of the bond between concrete and CFRP laminates at elevated temperatures", Engineering Structures, 110 (2016) 233–243.
[15] Bisby, L.A., "Fire Behavior of Fiber-Reinforced Polymer Reinforced or Confined Concrete", Ph.D. thesis, Department of Civil Engineering, Queen's University, Kingston, Canada, 2003.
[16] Bisby, L.A., Green, M.F., and Kodur, V.K.R., "Modeling the behavior of FRP-confined concrete columns exposed to fire", J.Compos. Constr., 9(1), 2005, pp. 15–24.
[17] Bai, Y., Keller, T, and Vallée, T., "Modeling of stiffness of FRP composites under elevated and high temperatures", Compos. Sc. Techn., 68 (15-16), 2008, pp. 3309–3106.
[18] Hawileh, R., A., Naser, M., Zaidan, W., and Rasheed, H. A., "Modeling of insulated CFRP strengthened reinforced concrete T-beam exposed to fire", Eng. Struct., 31(12), 2009, pp. 3072–3079
[19] ANSYS. Finite Element Computer Code. Version 12.1.0. ANSYS Inc., Canonsburg, PA, 2009.
[20] Harmathy, T.Z., "Fire Safety Design and Concrete, Concrete Design and Construction Series", Longman, UK, 1993.
[21] Griffis, C. A., Masmura, R.A., and Chang, C.I., "Thermal response of graphite-epoxy composite subjected to rapid heating", Journal of Composite Materials., Vol. 15 (1981), pp. 427-442.
[22] Eurocode 2. EN 1992-1-2: Design of concrete structures. Part 1-2: General rules- Structural fire design, European Committee for Standardization, Brussels, Belgium, 2004.
[23] Williams, B., Kodur, V.K.R., Green, M.F., and Bisby, L.,"Fire endurance of fiber-reinforced polymer strengthened concrete T-beams, J. ACI Struct; 105(1), 2008, pp. 60–67.
[24] Cramer, S.M., Friday, O.M., White, R.H., and Sriprutkiat, G., "Mechanical properties of gypsum board at elevated temperatures", Fire and Materials, 2003, pp. 33–42.
[25] Park, S. H., Manzello, S., L., Bentz, D., P., and Mizukami, T., "Determining thermal properties of gypsum board at elevated temperatures", Fire and Materials, (2009), pp. 237-250.
[26] American Society for Testing and Materials (ASTM). ASTM E119: Standard Test Methods for Fire Tests of Building Construction and Materials, West Conshohocken, PA, USA, 2007.
[27] Eurocode 3. EN 1993-1-2: Design of steel structures. Part 1-2: General rules- Structural fire design, European Committee for Standardization, Brussels, Belgium, 2005.
[28] American Concrete Institute (ACI), ACI 318-14, "Building code requirements for structural concrete", ACI 318, Farmington Hills, MI, USA, 2014.

Article no. 19

THE CIVIL ENGINEERING JOURNAL 2-2019

A WIRELESS RAILWAY MONITORING SYSTEM OF PROBLEMATIC SUBSTRUCTURE IN TUNNEL

Yanxin Yang[1], Jianlin Ma[1] and Yong Huang[2]

1. *Southwest Jiaotong University, School of Civil Engineering, Department of Geotechnical Engineering, No.111, North 1st section, Erhuan Road, 610031 Chengdu, China; yanxinyangswjtu@foxmail.com(Yanxin Yang); majianlin01@126.com (Jianlin Ma)*
2. *Sichuan Provincial Transport Department Highway Planning, Survey, Design and Research Institute, No.1 Wuhou Heng Jie Street, 610041 Chengdu, China; 1043131035@qq.com*

ABSTRACT

The railway substructure needs to be monitored to determine whether the substructure is stable. In the paper, the damages to the substructure of the heavy-haul railway in the tunnel were recognized and the grouting technology and water pipes were used to avoid further damages. To monitor the state of the substructure in the tunnel, a wireless monitoring system was developed. The accelerometers, laser rangefinders, water level gauges, and cameras were used in the sensor module, the fiber optics and mobile telephony were used in data transferring module, and a data managing system was developed in the control center. To examine the measured date by the monitoring system, the measured vertical displacement and horizontal displacement, the settlement, and the water levels at the site were presented. The measured data showed that the underground voids still existed after the grouting technology and water pipes of installation were applied. The horizontal and vertical displacement and settlement were induced by the underground voids and the loading of the train. The water level varied at the three locations, and the change of the water level beneath the surface showed that the flowing water was drained due to the water pipes. The wireless monitoring system was successfully developed to monitor the real-time data of the substructure and determine if the substructures was stable.

KEYWORDS

Railway substructure, Monitoring system, Wireless, Sensors

INTRODUCTION

China heavy-haul railway is experiencing the growing demand for traffic and capacity. Due to the increasing number of cargo and passengers, the heavy-haul railway is playing an important role in the transportation system. The railway track [1], consisting of the superstructures and railway substructure, is governing the smooth rides of the train. One of the important factors needs to be considered during the operation of the heavy-haul railway is the health state of the railway track.

The performance of the railway track may be weakened by problematic railway substructure. The problematic railway substructure could be caused by various factors, such as repeat loading, high water content, loose soils, temperature and so on [1]. The railway track of heavy-haul railway is under large axle loading frequently, which results in the increasing vibration on the railway track and permanent deformation [2], so there is a high probability that the problematic railway substructure would occur in the railway track of heavy-haul railway.

To avoid further damages to the railway track, the status of railway track needs to be analysed for the heavy-haul railway. Several methods are available to monitor and analyse the railway track, including field monitoring method [3, 4] and numerical method [5, 6]. Some investigations [7,8] had been conducted on the dynamic response of the heavy-haul rail substructure using numerical simulation method. The dynamic response of the railway substructure varies with the site condition [9,10]. Although the numerical analysis was proved to be more accurate in the calculation of dynamic response of the substructure, detailed material properties and non-linear analysis of soil behaviors had to be taken into consideration. In engineering practice, the field monitoring gains a better understanding regarding the dynamic response of substructure with various instruments, such as inclinometers, acceleration sensors, and other measuring devices. The field monitoring could be used in the railway track, and various monitoring system [11, 12, 13, 14, 15, 16, 17] were developed for different purposes.

One of the challenges for the field monitoring of the railway substructure in the tunnel of the heavy-haul railway is that the field monitoring is limited to the space of the tunnel, and the conventional monitoring is difficult to be instrumented without the interruption of the train operation. Furthermore, the intense freight of the heavy-haul railway decreases the maintenance time. In such a situation, a stable, efficient and accurate system that monitors the railway track. As a result, a real-time, long-time monitoring system consisting of sensors, data station, and control center connected by wireless network [18,19] needs to be developed to monitor the structure health of the railway substructure and overcome the shortcomings of the conventional field monitoring.

The problematic substructure was identified in the railway tunnel of Jundushan, which was part of the Daqin heavy-haul line in China. To guarantee the further safety of the tunnel after the initial treatment, a monitoring system was proposed, which aimed to monitor the problematic substructure and evaluate the safety of the tunnel. In the paper, the monitoring system based on wireless transmission technology was developed for a long-term monitoring to monitor the state of railway substructure in the tunnel and provide real-time surveillance of the railway substructure. The framework of the monitoring system was introduced as well as the sensors used in the monitoring system. The monitored data such as displacement of railway substructure, settlement, and water levels were presented to illustrate the monitoring system and evaluate the safety of the substructure.

SITE CONDITION

The railway from Datong to Qinhuangdao, known as Daqing line, was heavy-haul transportation, which was the first double-lane and electrified line in China. The tunnel was located at the Southeast of County Yanqing and the total length of the tunnel was 8460m, which was the longest tunnel among the 52 tunnels of the line.

The geology condition of the site mainly consisted of magmatic rock, which was classified as hard rock. However, the weak surrounding rock for the section of the tunnel from the entrance extending to the length of 670 m was composed of loess sandy clay, and the weak surrounding rock for the section accounting for 500 m of the tunnel to the exit of the tunnel was composed of weathered granite. The concrete board sleeper and wall lining were used during the construction of the tunnel. The section of tunnel was designed as horseshoe shape for the hard-surrounding rock and egg shape for the weak-surrounding rock with the inverted arch. The underground water was found at the site and fissure water was recognized at the bedrock, so the drainage ditches were designed locating at two sides and the center of the tracks.

IN-SITU SURVEY

The tunnel was completed and opened in the year 1988. The tunnel included double tracks, one of the two tracks was used as heavy-haul, and the other one track was used as light-haul

transportation. As one track was used as a heavy-haul track, the heavy freights caused serve damages to the track. A preliminary in-situ investigation was conducted by observation, measurement and referring to the design sketch.

Severe damages were identified at the section K279+902-K279+962 (where K stands for kilometre). The damages to the railway substructure and tunnel lining were investigated and shown in Figure 1, and the damages were categorized into 4 different types.

Type 1is settlement of the substructure: the settlement of the railway substructure was observed at the center and side of the track close to the drainage ditch, which was the heavy-haul track out of the two tracks in the tunnel. The vibration of the sleeper and roadbed of the heavy-haul track were observed when the vehicle ran on the rails. The observation of settlement was shown in Figure 1 (a). The settlement of the substructure was identified along the heavy-haul track at the section K279+917-K279+947. The value of settlement was not measured during the in-situ survey due to the limited condition.

Type 2 is water pooling: water pooling was observed at the side drainage ditch close to the heavy-haul track. Figure 1 (b) showed the water pooling at the drainage ditch close to the heavy-haul track. The depth of water pooling was measured as 0.3m at the Section K279+927. The cracks of the concrete beneath the drainage ditch were observed at the side and center drainage ditch. At section K279+935-K279+937, the width of the cracks was as much as 200 mm. Flowing water was identified at the center drainage ditch in the tunnel. The road bed was stroked by the flowing water at the center drainage ditch, due to the vibration of the vehicle. Water wave was observed at the side drainage ditch and the amplitude of the water vibration was as much as 10 cm.

Type 3 is underground void: beneath the base of the substructure, the underground voids were observed. The height of the voids was ranging from 0.03 m to 0.15 m at the section K 279+907-K279+947. The vibration of the sleeper was observed when the vehicle was running on the trail. Figure 1 (c) showed the measurement of underground voids by steel scale.

Type 4 is water seepage and cracks: water seepage and cracks were observed along the tunnel lining. Figure 1 (d) showed the cracks observed along the tunnel lining.

(a) Settlement of substructure

Fig. 1 - Damages of the railway substructure and tunnel

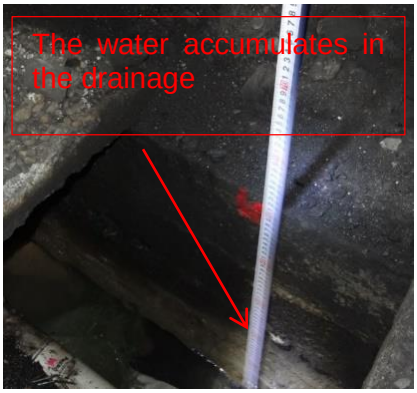

(b) Water pooling

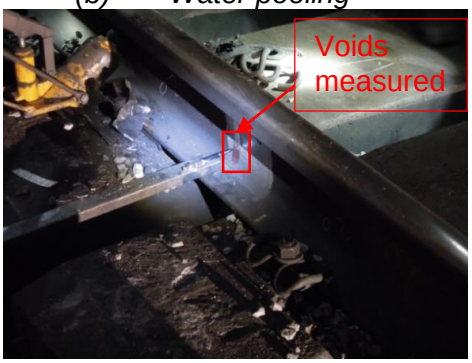

(c) Measurement of the underground voids

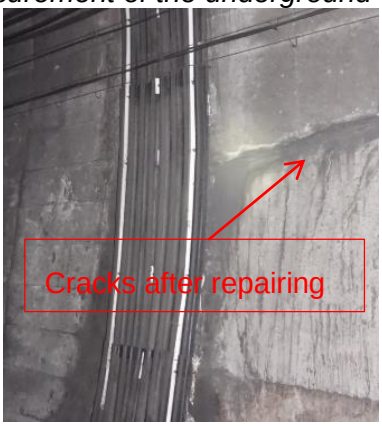

(d) Cracks of the lining

Fig. 1 - Damages of the railway substructure and tunnel: (a) Settlement of substructure; (b) Water pooling; (c) Measurement of the underground voids; (d) Cracks of the lining

COUNTERMEASURES TO FURTHER DAMAGES

For the heavy-haul track, the skylight time of the railway (the time interval between the two trains coming to the same location) was short and the traffic flow rate was high. The railway was undergoing the heavy axel loading frequently, so the cyclic loading resulted in rapid stress change vertically, which induced damages to the substructure. At the base of the substructure, the grouting technology was used to prevent the further occurrence of settlement and underground voids. While the grouting technology was limited to the site condition and due to its uncertain distribution beneath the ground surface, the damage may occur due to the existence of unfilled voids, thus the

monitoring would be conducted to decide if more grouts were required. As the water was found in the tunnel, water pipes were installed to drain water and prevent the flowing water from the adjacent sections.

The high performance of the railway required high safety levels, which could be achieved if the maintenance was scheduled correctly. A solution to a timely maintenance process was the application of monitoring system to monitor the health state of the substructure and avoided the damages to it.

The monitoring system needed to be developed based on the in-situ conditions. The substructure in the tunnel was located far from the control center of the line, the in-situ monitoring system was the alternative method if the real-time and long-term monitoring were required. The remote monitoring system integrated the monitoring data and video monitoring and recognized the damages remotely, in this way, the remote monitoring system would reduce the risk that the substructure would be damaged due to the heavy loading effectively. More measures could be taken for further treatment of the railway substructure based on the monitoring data if the damages occurred.

WIRELESS SENSOR NETWORK FRAMEWORK

The wireless sensor network required the sensors, data acquisition, data transferring, data processing and data management. A wireless sensor network, shown in Figure 2, was proposed to monitor the structural health of the substructure. The system included three major modules:

1. The sensor module, which attached the sensors to the substructure of the railway to measure the data and preliminary data processing;
2. The wireless transferring module which transferred the data from the sensor module to the control module;
3. The remote-control module, which consisted of data receivers, data management system.

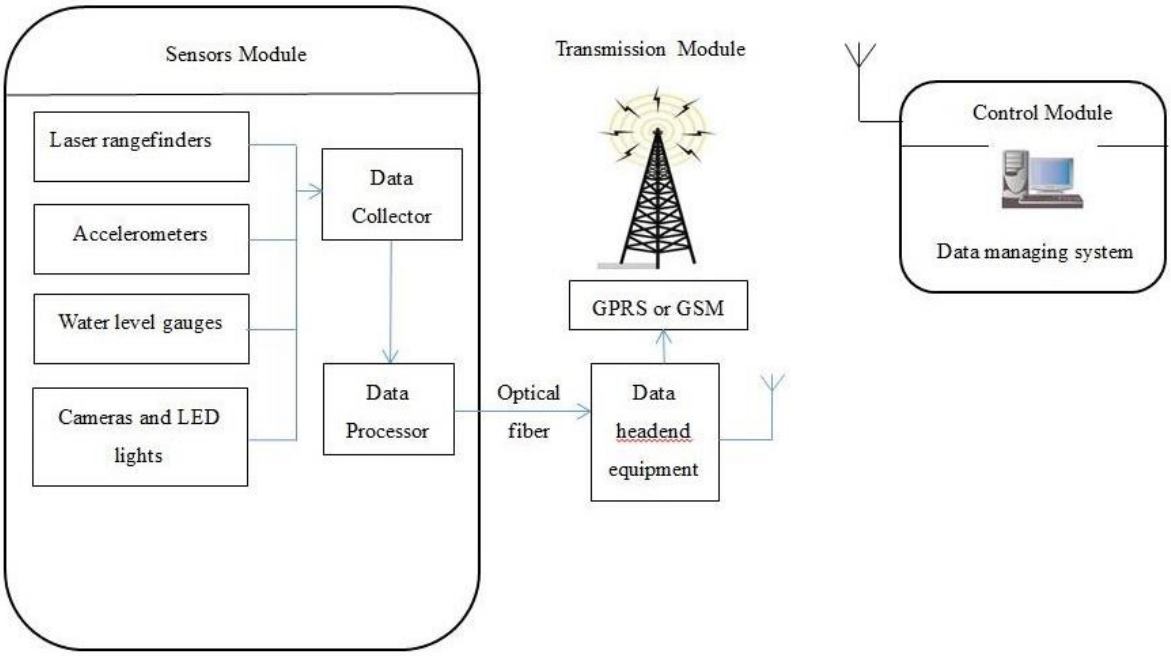

Fig. 2 - The wireless sensor network

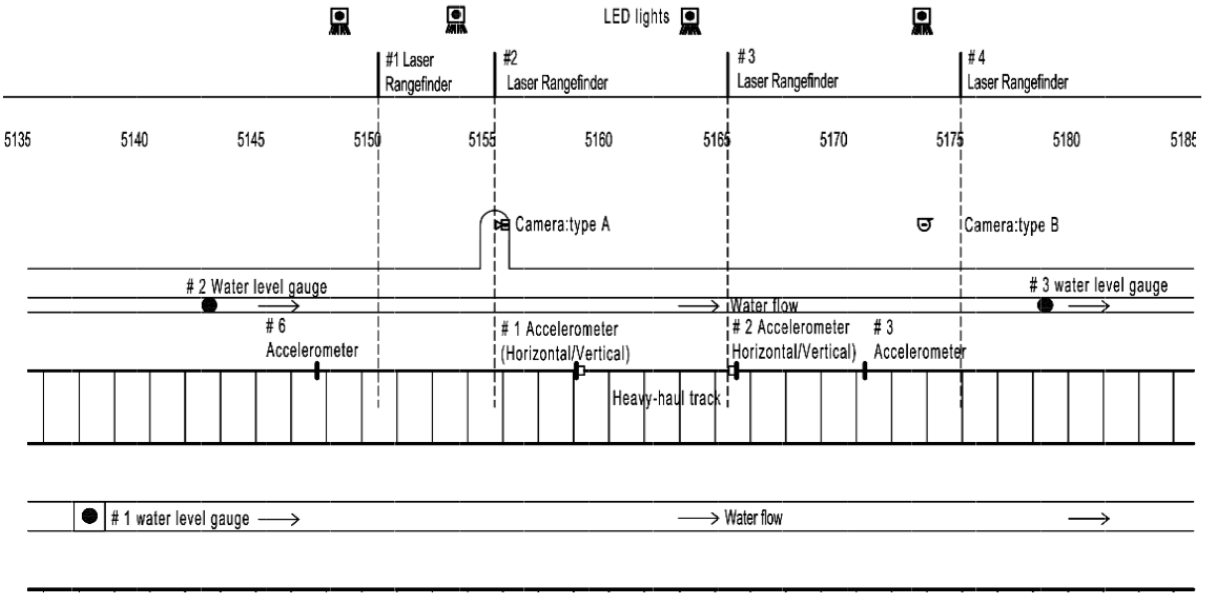

Fig. 3 - Layout of sensors

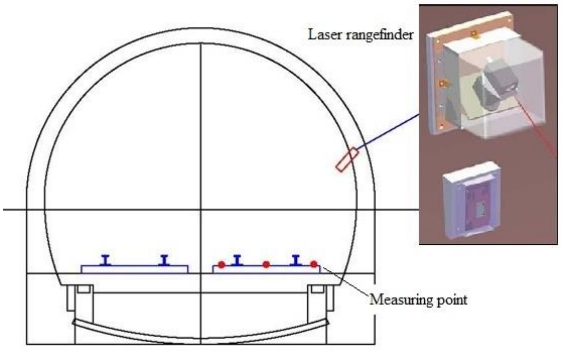

(a) Sectional view of the laser rangefinder

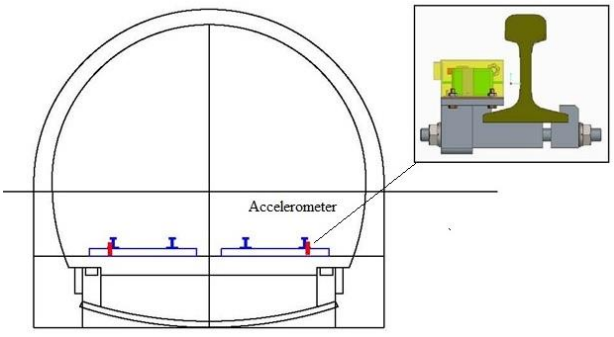

(b) Installations of accelerometers

Fig. 4 - Sectional views of the sensor module in the tunnel

DOI 10.14311/CEJ.2019.02.0019

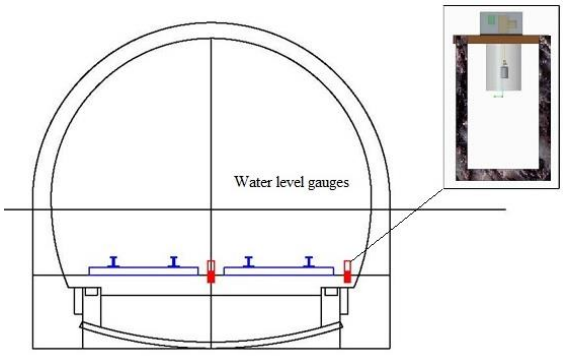

(c) Installations of water level gauges

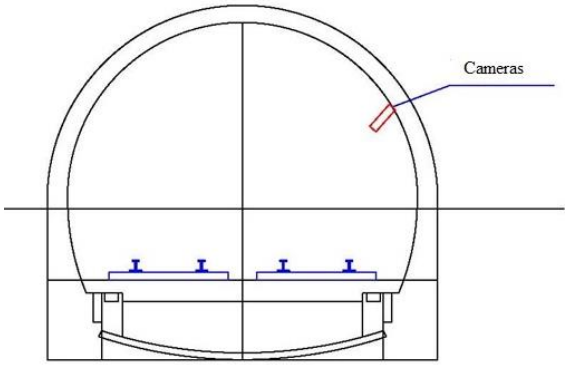

(d) Installations of cameras

Fig. 4 - Sectional views of the sensor module in the tunnel: (a) Sectional view of laser rangefinder; (b) Installations of accelerometers; (c) Installations of water level gauges; (d) Installations of cameras

In-place instruments located at the railway substructure and tunnel were used to determine the damage of the railway substructure, and various types of sensors were needed to develop the sensor module. The sensor module was aiming for the measurement of the condition that the train passes through the specific section. In the sensor module, several key parameters, such as settlement, dynamic displacement, and water levels needed to be monitored periodically. In addition, to realize the purpose of real-time monitoring, cameras were used to capture the images in the tunnel.

In Figure 3, the layout of the sensors was shown. Accelerometers were installed at the sleeper for vertical displacement and horizontal displacement monitoring. The vibration data monitored by the accelerometer were converted into displacement corresponding with various speeds of the heavy-haul train. The accelerometers were calibrated before the installation to reduce the stochastic error induced by the double integration. As the data was acquired frequently by the accelerometers, a data processor was used to filter the mass of data and obtain the vibration data every 4 seconds, and the data was regarded as the vibration data, the maximum displacement was used as the representative data for each day. Laser rangefinders were installed along the wall of the tunnel for settlement monitoring of the railway substructure. The distance between the laser rangefinder and the center of the sleeper was measured and the settlement was calculated based on the distance difference of two phases: before the train passage on the rails and when the train is passing through the section. The inclination angle between the height of the laser rangefinder and the measured distance was used to determine the settlement of the sleeper. Water level gauges installed at the drainage ditches were used to measure the water level during

the period that train passed on the rails. Cameras and Led lights were installed along the wall of the tunnel to capture the real-time image of the railway substructure. There were two types of cameras used in the system: the type-A camera was a dome camera and type-B camera was the outdoor camera. The video system could be switched on or off based on the demand of the user in the control module. Figure 4 (a) showed the sectional view of the laser rangefinder, and Figure 4 (b) showed the accelerometers installed at the sleeper of the rails. In Figure 4 (c), the water level gauges installation was shown, and in Figure 4 (d), the camera installation was shown. Before the data was transferred to the data management system, the measured data were collected and processed in the data collector and data processor, as shown in Figure 5.

Fig. 5 - Data collector and processor

In the wireless transferring module, as the distance between the monitoring system and control center was long, a two-stage data transferring was proposed: the data needed to be transferred through the tunnel to the entrance of the tunnel, and the data needed to be transferred from the tunnel entrance to the control module. In the module, the data were collected from the sensors and transmitted to the station at the entrance of the tunnel via optical fiber and then to the control center via GPRS or GSM. The fiber optics networks along the tunnel were used for data transmission inside the tunnel as well as for video transmission, and the mobile telephony was used for transmitting the signals outside the tunnel. In Figure 6, the data forwarder and antenna for data forwarding at the tunnel exit were shown in Figure 6 (a) and Figure 6 (b), respectively.

(a) Data forwarder at the tunnel exit
Fig. 6 - Transferring module

(b) Antenna for data forwarding at the tunnel exit

Fig. 6 - Transferring module: (a) Data forwarder at the tunnel exit; (b) Antenna for data forwarding at the tunnel exit

In the control module, the data was transferred and stored, and the data was accessible to the user. A data managing system was developed, which consisted of several functions: an introduction to the system, real-time monitoring and analysis, data inquiry, parameters setting and data managing. The introduction to the system provided the basic information of the data managing system. The real-time monitoring and analysis showed the measured data in the format of numbers and the curves. When the measured data was greater than the criteria value, the system sent alerts to the user. Data inquiry allowed the user to extract the history data in the format of numbers or curves. The parameter setting set the basic information of the project, the type of monitored data, the criteria value of the measured data, the receiver of the alert and the accessibility of the data. Data managing was aiming to collect and store the data. In Figure 7, the screenshot of the data managing system was shown.

Fig. 7 - Screenshot of data managing system

APPLICATION OF THE MONITORING SYSTEM

To study the capability of the remote monitoring system, the measured data at the site for a period were presented. A general analysis of the monitored data was presented. The measured

data consisted of the horizontal displacement of a sleeper, the vertical displacement of the sleeper, the settlement of the substructure and the variation of the water level.

Video surveillance

The cameras were used to capture the real-time image in the tunnel. The measured data was shown and analysed in the control module, once the irregular data was shown in the data managing system, the health state of the substructure needed to be examined by the real-time surveillance, and the video surveillance captured the image and video of the substructure for determining if an in-situ investigation was needed. Figure 8 showed a real-time image in the tunnel.

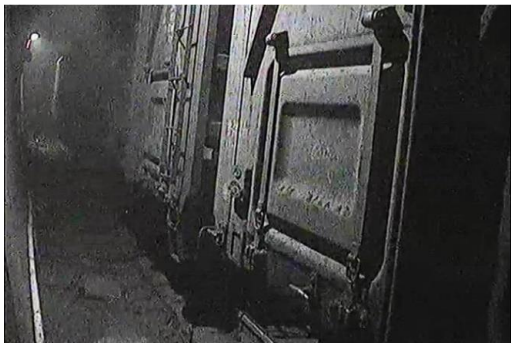

Fig. 8 - A real-time image in the tunnel

Vertical displacement

The dynamic displacements of the sleeper were recorded by the sensors installed at the sleeper. Along the heavy-haul track, the displacements by four sensors were recorded. The measured maximum displacements of each day by four sensors were shown in Figure 9 for 100 days from the beginning of the installation of the remote monitoring system. The magnitude of the displacement was affected by the heavy axel loading.

The displacement variations of the four sensors were different, and No.3 had less fluctuation compared to the other three sensors: for No.1 and No.6 sensors, the displacement varied from 6 mm to 8 mm; for No.3 sensor, the displacement varied from 2.32 mm to 4.0 mm; for No.2 sensor, the displacement varied from 4.4 mm to 5.5 mm. The greatest displacement was recorded by No.1 accelerometer. The maximum displacement was 8 mm on the day of 8. The smallest displacement was recorded by No.3 accelerometer, and the smallest displacement was 2.32 mm on the day of 21. The displacement varied with the time but within a certain range, and the integrity of the substructure was reflected by the trend of the dynamic displacements. The occurrence of the displacement was due to the existence of the underground voids and heavy axel loading on the substructure. When axel loading was acting on the sleeper, downward movements occurred and a maximum displacement was monitored. The variation of displacement of each day depended on the loading acted on the sleeper and the occurrence of underground voids. More underground voids existed under the location where the No.1 sensor was installed compared to No. 3 based upon the fluctuation of dynamic displacements.

Horizontal displacement

The curves of maximum horizontal displacements varying with time were shown in Figure 10. Two accelerometers were installed at different locations of a sleeper. As the axel loading and the horizontal displacement were orthogonal, the less fluctuation of the horizontal displacement was

observed. During the monitoring period, the horizontal displacement recorded by the two accelerometers slightly changed within a certain range. The displacement varied at the range from 0.54 mm to 0.61 mm during 88 days. The maximum horizontal displacement was 0.61 mm on the day of 23, and the minimum horizontal displacement was 0.54 mm on the day of 35. The underground voids had less influence on the horizontal displacement of the sleeper. No.2 accelerometer was more influenced by the underground voids comparing to No.1 accelerometer. In general, the horizontal dynamic displacements could be ignored as the maximum displacement was less than 1 mm. The axle loading of the heavy-haul train and the underground voids had less influence on the horizontal displacement of the sleeper.

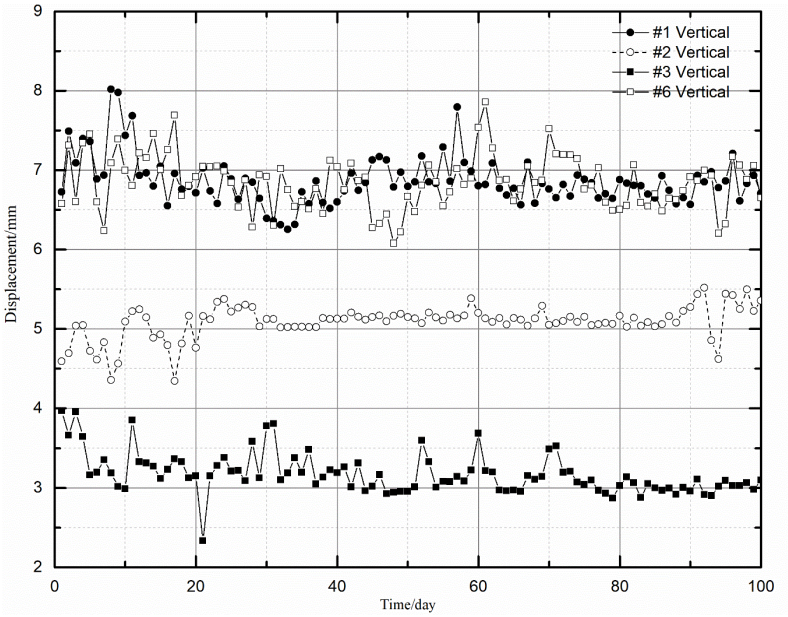

Fig. 9 - The maximum vertical displacement versus time

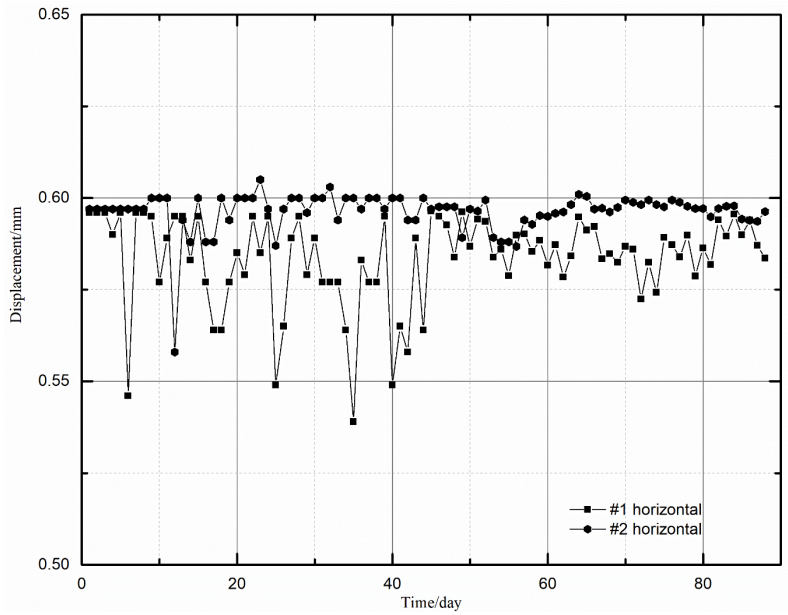

Fig. 10 – Maximum horizontal displacement versus time

Settlement of railway substructure

The settlements of the railway substructure were recorded by the laser rangefinders, and the curves of the settlement versus time were plotted in Figure 11. Figure 11 (a) showed the settlements by No.1 and No.2 laser rangefinders, and Figure 11 (b) showed the settlement by No.3 and No.4 laser rangefinders. If the settlement occurred during the monitoring, more measures to treat the substructure were needed.

The accuracy of the laser measurement was affected by many factors, such as temperature, atmosphere, and the environment. In the tunnel, the measurement of the laser rangefinder depended on the surface roughness of the measured object and the measuring vibration. The noisy or unstable measurement induced by the surface roughness, train vibration and the particles in the tunnel air would bring the uncertainty to the measurement of the settlement. In Figure 11, the measured settlement was induced by the underground voids under the loading of the train and the fluctuation may be attributed to the uncertainty of the measurement. The four laser rangefinders measured the different amplitude of displacements, and the amplitude for the four laser rangefinders were 1.40 mm, 1.05 mm, 1.56 mm and 1.29 mm, respectively. The settlement by different rangefinder showed the influence of the underground voids and loading of the train. During the 100 days of monitoring, the measuring error of the laser rangefinder was 1mm, and the settlement changed with the time but within a certain small range, so the railway substructure could be regarded as being stable. While before the grouting technology was applied, the settlement was observed at section K279+917-K279+947.

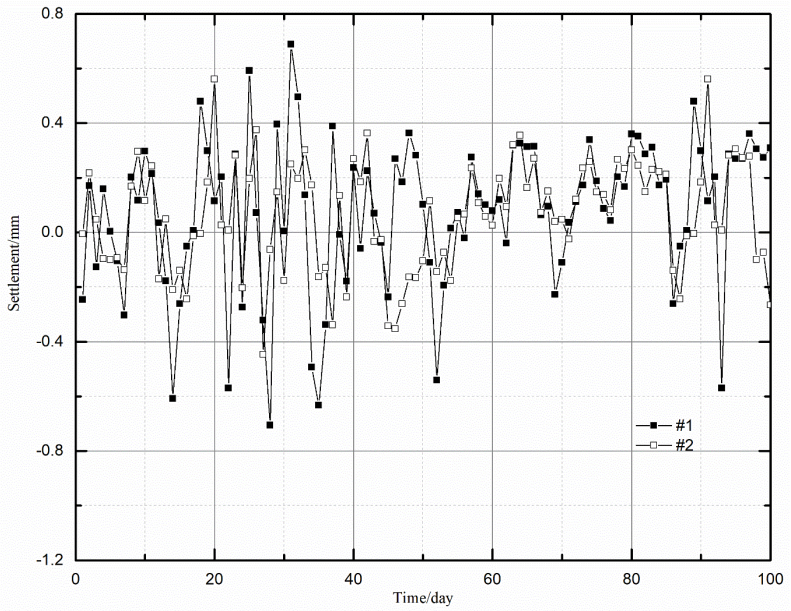

(a) Settlement by No.1 and No.2 laser rangefinder

Fig. 11- Settlement of the railway substructure

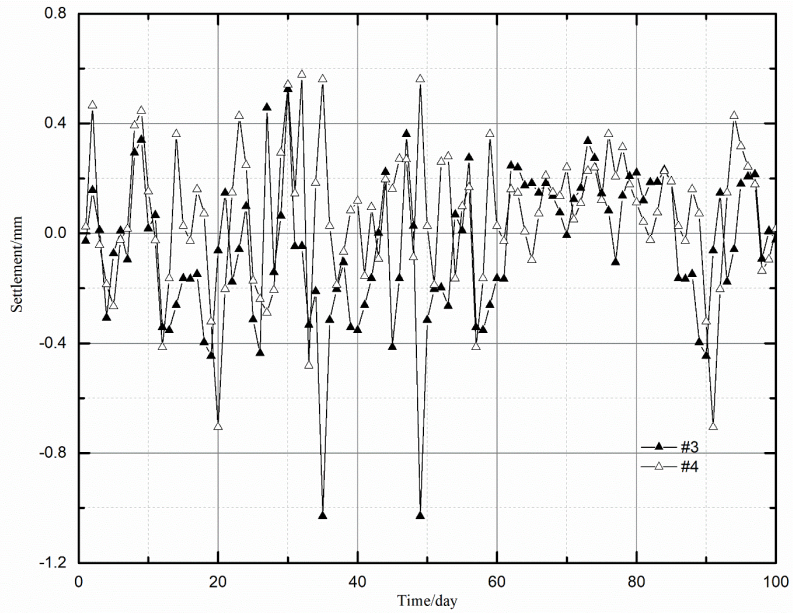

(b) Settlement by No.3 and No. 4 laser rangefinders

Fig. 11- Settlement of the railway substructure: (a) Settlement by No.1 and No.2 laser rangefinder; (b) Settlement by No.3 and No. 4 laser rangefinders

Water level

The amplitude was defined as the difference between the maximum water level and the minimum water level in the section. The amplitudes of water levels for each day were plotted in Figure 12. The variation of the water level was induced by the flowing water from the surroundings and the train. For the amplitude of No.1 and No.2 water level gauges, the amplitude decreased with time. The water level amplitude of water gauge No. 2 changed from 24 cm to 18 cm at the day of 100, while the water level amplitude of water gauge No. 1 decreased from 17.5 cm to lowest water level amplitude of 11.0 cm and then increased to 16 cm. For the No.3 water level gauge, the amplitude changed slightly. The water level amplitude varied at the range between 6 cm to 11 cm. The measured water levels were smaller than the measured maximum water level of 30 cm at section K279+927. It was noted that the underground voids were affecting the water levels measured by the water level gauges. The decreasing water level amplitudes indicated that although the water pipe was working for drainage, the water in the underground voids came out when the train was passing through the section. The influence of the underground voids could be determined by the amplitude of the water levels. As water level amplitude change recorded by No.2 was greater than the other two gauges, more underground voids close to No.2 water level gauge were assumed. The installation location of the water levels was influencing the variation of water level amplitude: the location of No.2 water level gauge was close to the drainage ditch and water pipe, so more water was drained comparing to the other two locations where the water level gauges were installed.

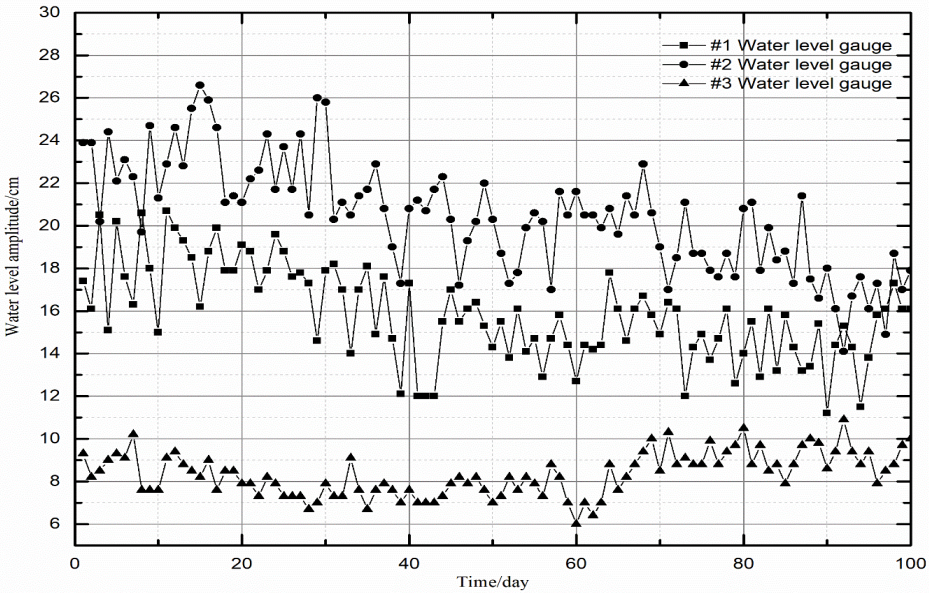

Fig. 12 - Water level amplitude versus time

CONCLUSION

In the paper, the damages to the substructure of the railway in the tunnel were investigated. The grouting technology and water pipes were used to mitigate the damages identified in the substructure. To monitor the further state of the substructure, a wireless monitoring system was proposed. The system has proved to be effective in monitoring the state of the substructure in the tunnel.

The wireless remote monitoring system was installed with three modules, the sensor module, the transferring module, and control module. The measured displacement, settlement, water level, and real-time image were transferred from the site to the control center.

The monitored results showed that the vertical displacement was more influenced by the underground voids comparing to the horizontal displacement, the fluctuation of the measured settlement was attributed to the vibration of the train, the particles in the tunnel air as well as the underground voids. The water level at the site was influenced by the flowing water and the drainage ditches locations. By applying the grouting technology and installing the water pipes, the settlement of the substructure was stable and the water was drained continuously to lower the water level.

According to the analysis of the measured curves, the existence of underground voids was affecting the measured displacement and settlement, so more measures were needed based on a long-term monitoring to eliminate the underground voids, and a further application of the monitoring system needs to be examined in the similar sites.

ACKNOWLEDGEMENTS

The authors would like to thank the financial support from the funding: National Key Research & Development Program of China (2016YFC0802203).

REFERENCES

[1] Aw, E. S., 2007. Low Cost Monitoring System to Diagnose Problematic Rail Bed: Case Study of Mud Pumping Site. PhD diss., Massachusetts Institute of Technology.

[2] Wang K., Wang L.J., 2017. Dynamic Investigation of Pile-compacted Subgrade under Heavy Haul Train, Boletín Técnico, vol. 55: 249-261.

[3] Bowness, D., Lock, A.C., Powrie, W., Priest, J.A. and Richards, D.J., 2007. Monitoring the Dynamic Displacements of Railway Track. In: Proceedings of the Institution of Mechanical Engineers, Part F: Journal of Rail and Rapid Transit, 221(1), 13-22. doi: 10.1243/0954409JRRT51.
[4] Ling, X.Z., Chen, S.J., Zhu, Z.Y., Zhang, F., Wang, L.N. and Zou, Z.Y., 2010. Field Monitoring on the Train-induced Vibration Response of Track Structure in the Beiluhe Permafrost Region along Qinghai–Tibet Railway in China. Cold Regions Science and Technology, vol. 60(1): 75-83. doi:10.1016/j.coldregions.2009.08.005.
[5] Brinkgreve, R.B.J., Engin, E., Swolfs, W.M., Waterman, D., Chesaru, A., Bonnier, P.G. and Galavi, V., 2012. Plaxis 3D 2012. Plaxis bv.
[6] Shahraki, M., Sadaghiani, M.R.S., Witt, K.J. and Meier, T., 2014. 3D Modelling of Train Induced Moving Loads on an Embankment. Plaxis Bulletin, vol. 36: 10-5.
[7] Shi, J., Burrow, M.P., Chan, A.H. and Wang, Y.J., 2013. Measurements and Simulation of the Dynamic Responses of a Bridge–embankment Transition Zone below a Heavy Haul Railway Line. In: Proceedings of the Institution of Mechanical Engineers, Part F: Journal of Rail and Rapid Transit, 227(3): 254-268. doi:10.1177/0954409712460979.
[8] Shi, J., Chan, A.H. and Burrow, M.P., 2013. Influence of Unsupported Sleepers on the Dynamic Response of a Heavy Haul Railway Embankment. In: Proceedings of the Institution of Mechanical Engineers, Part F: Journal of Rail and Rapid Transit, 227(6): 657-667. doi:10.1177/0954409713495016.
[9] Barke, D. and Chiu, W.K., 2005. Structural Health Monitoring in the Railway Industry: a Review. Structural Health Monitoring, vol. 4(1): 81-93. doi:10.1177/1475921705049764.
[10] Barke, D. and Chiu, W.K., 2005. Structural Health Monitoring in the Railway Industry: a Review. Structural Health Monitoring, vol. 4(1): 81-93. doi:10.1177/1475921705049764.
[11] Shan, Y., Albers, B. and Savidis, S.A., 2013. Influence of Different Transition Zones on the Dynamic Response of Track–Subgrade systems. Computers and Geotechnics, vol. 48: 21-28. doi:10.1016/j.compgeo.2012.09.006.
[12] Aw, E. S., 2004. Novel Monitoring System to Diagnose Rail Track Foundation Problems. PhD diss., Massachusetts Institute of Technology.
[13] Li, J., Chen, S., Yu, F., Guo, W. and Ojekunle, V.O., 2015. Development and Application of a Remote Monitoring and Analysis System for a High Speed Railway Subgrade Structure in Mountainous Areas. In: Innovative Materials and Design for Sustainable Transportation Infrastructure: 389-404. doi:10.1061/9780784479278.036.
[14] Ribeiro, D., Calçada, R., Ferreira, J. and Martins, T., 2014. Non-contact Mmeasurement of the Dynamic Displacement of Railway Bridges using an Advanced Video-based System. Engineering Structures, vol. 75: 164-180. doi:10.1016/j.engstruct.2014.04.051.
[15] Yang, J., Feng, Q., Zhang, B. and Cui, J., 2012. An Automatic Method and System for Measuring and Monitoring Subgrade Settlement using Inclinometer. Journal of Beijing Jiaotong University, vol. 36(6): 52-56.
[16] Roveri, N., Carcaterra, A. and Sestieri, A., 2015. Real-Time Monitoring of Railway Infrastructures Using Fibre Bragg Grating Sensors. Mechanical Systems and Signal Processing, vol. 60: 14-28. doi:10.1016/j.ymssp.2015.01.003.
[17] Bowness, D., Lock, A.C., Richards, D.J. and Powrie, W., 2005. Innovative Remote Video Monitoring of Railway Track Displacements. Applied Mechanics and Materials, vol. 3-4: 417-422. doi:10.4028/www.scientific.net/amm.3-4.417.
[18] Pinto, N., Ribeiro, C.A., Gabriel, J. and Calçada, R., 2015. Dynamic Monitoring of Railway Track Displacement using an Optical System. In: Proceedings of the Institution of Mechanical Engineers, Part F: Journal of Rail and Rapid Transit, 280-290. doi:10.1177/0954409713509980.
[19] Muthukumar, M. and Nallathambi, S., 2017. Remote Sensor Networks for Condition Monitoring: An Application on Railway Industry. In: IEEE International Conference on Electrical, Instrumentation and Communication Engineering, 1-5. doi:10.1109/iceice.2017.8191894.
[20] Jiang, P., Xia, H., He, Z. and Wang, Z., 2009. Design of a Water Environment Monitoring System based on Wireless Sensor Networks. Sensors, vol. 9(8): 6411-6434. doi:10.3390/s90806411.

Article no. 20

THE CIVIL ENGINEERING JOURNAL 2-2019

THE RESEARCH OF THE VARIATION LAWS OF SETTLEMENT AND INTERNAL FORCE OF PILE GROUPS OF RAILWAY BRIDGE CAUSED BY PUMPING BRINE

Guodong Li[1,2], *Huijun Wu*[1,2]*, *Yazhou Li*[1,2], *Zhongchang Wang*[1,2]

1. *Tunnel & Underground Structure Engineering Center of Liaoning, Dalian Jiaotong University, Dalian 116028, China*
2. *Institute of Civil Engineering, Dalian Jiaotong University, Dalian 116028, China; whj79629@sina.com*

ABSTRACT

Taking Yingzigou Bridge of Dezhou-Dajiawa railway as the engineering background, the three-dimensional fluid-solid coupling models of pile group caps were established on the basis of five-stage field monitoring data of the settlement and groundwater level drop by using FLAC3D software. On the basis of the field monitoring data checking, the variation of axial force and skin friction of piles at different positions under the condition of water level drop was simulated. The results show that with the underground water level dropped, the axial force of pile along the shaft increased first and then decreased. The cross section of maximum axial force moved down constantly. In the same ground water levels drop, the distance between the maximum axial force and neutral point of each pile and the top of the pile was corner pile > side pile> near borehole center pile > center pile. The size of the pile axial force and negative skin friction resistance was corner pile > side pile> near borehole center pile > center pile. The upper part of the pile was subjected to negative skin friction resistance. The skin friction resistance of each pile along the shaft increased first and then decreased. The lower part of the pile was subjected to positive skin friction resistance. The skin friction resistance of each pile along the shaft increased. The location of the maximum negative friction resistance was about 10m distance from the top of the pile. The maximum negative friction resistance of corner pile was -36.5kPa. The distance of neutral point of center pile from the top was 35.2m. The neutral point of each pile was in accordance with the position of the maximum axial force of the pile. A reliable basis was provided for high-speed railway survey and design and the prevention and control of land subsidence along the railway.

KEY WORDS

Skin friction, Pile groups, Pumping water, Groundwater level drop, Neutral point, Axis force

INTRODUCTION

The brine wells were densely distributed along Dezhou-Dajiawa railway. The regional subsidence in DK228+800-DK257+500 of Dezhou-Dajiawa railway resulted from the over mining of underground brine in the adjacent area of pile foundation of railway bridge. The skin friction

resistance was produced on the pile groups of the bridge (XIA et al 2012, WU et al 2008). It would adversely affect the bearing performance and settlement control of the pile and even the geometry of the line and the running quality of the train. To ensure the safety and efficiency of high-speed railway operation, it was very important to calculate the settlement and internal force of the pile caused by the groundwater level drop. At present, the main methods of calculating the settlement of the foundation pile are elastic theory method (ZHAO et al 2004, SHEN 2008), shear displacement method (ZHAO et al 2008), load transfer method (JIA et al 2015, HONG et al 2004), numerical analysis method (XIA et al 2012, COMODROMOS et al 2005), model experiment(YANG et al 2008, LIU 2015, HE et al 2002), field test (CHEN et al 2000, XIA et al 2009), and more[1-4]. According to the generation mechanism of skin friction resistance of the pile, the estimation of skin friction resistance could be attributed to the determination of the depth of neutral point and the strength of skin friction resistance. However, there were many factors that influenced the skin friction resistance of piles [5-8]. The current methods were approximate or empirical, and it was impossible to consider the fluid-solid coupling process of the foundation settlement of piles caused by pumping (WANG et al 2014, LIU et al 2013, and XU et al 2013). There are little literatures on the internal force of piles in field tests. Based on the measured settlement data in the field, it was an important method to study the settlement and internal force of pile foundation under pumping conditions by using numerical analysis method, which could consider various influencing factors. The reference could be provided for survey and design and the ground subsidence control along the high-speed railway [9-12].

MONITORING ANALYSIS OF PILE FOUNDATION OF BRIDGE DURING BRINE WELL MINING

The construction of Dezhou-Dajiawa railway started in November 2010. The monitoring of ground subsidence started on 21 April 2014. The settlement value was set at 0. The monitoring values for subsequent periods were added. The five stages of monitoring were conducted by 15 September 2015. The accumulated ground subsidence of DK246~DK249 and DK252~DK257 sections along Dezhou-Dajiawa railway was serious. The central distance of Yingzigou Bridge in the serious settlement area was DK247+724.0. The length of the bridge was 132.6m. The span of bridge was 5 spans. Each span was 24m. The upper structure of the bridge was continuous pre-stressed concrete T beam. The lower bridge deck adopted rib deck. The layout of settlement marks of the bridge piers was shown in Figure 1. The piers was cylindrical and the piers were frictional pile foundation. The piers contained nine single piles with 45m length and 1m diameter. The distribution of piles was rectangular distribution. The spacing of piled was 3.4m and 4.1m. The distance between the centers of the pile with the edge of the bearing bed was 1.15m. The pile and the bearing bed were rigid connection. The size of pile groups and bearing bed was shown in Figure 2.

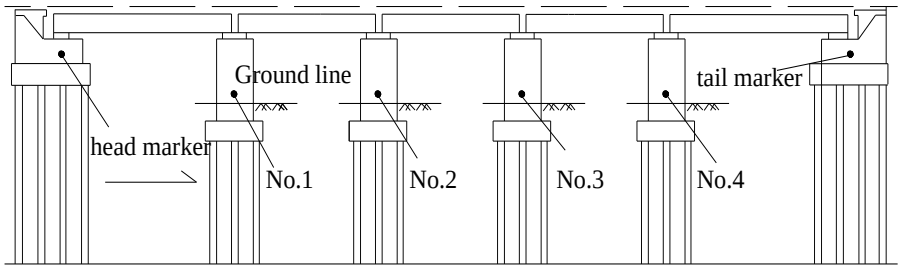

Fig. 1- Arrangement diagram of pier settlement observation mark

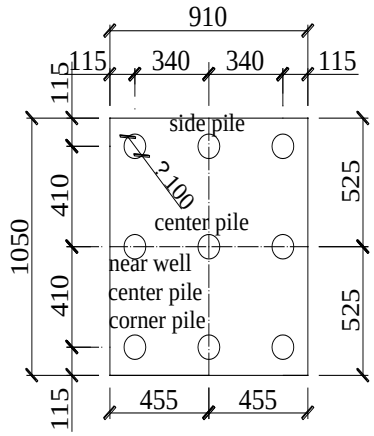

Fig.2 - The size of pile groups and bearing bed (unit: cm)

The settlement curves of the bridge piers at each stage were shown in Figure 3. The subsidence of the bridge piers was about -26mm in August 2014 to December. The maximum difference settlement between the two piers was 5.2mm and the difference settlement at the head and end of the bridge was 12.5mm and 17.7mm respectively. The settlement of bridge piers was relatively low in December 2014 to March 2015, and there was a trend to accelerate the settlement of bridge piers in March 2015 to September 2015. The maximum cumulative settlement was 106mm by September 2015. The bridge piers showed a trend of uneven settlement with a maximum difference of $3^{\#}$-$4^{\#}$ and a difference of 5mm. The brine mining is mainly carried out in the form of water well pumping. With the increase of the exploitation of brine water resources, the dynamic and static water level of brine continues to decline. The water level drop value reached -47.5m on September 15, 2015.The settlement values of $3^{\#}$ bridge piers and the monitoring values of the nearby groundwater level were shown in Table 1. With the decline of the groundwater level, the funnel-like settlement of the ground gradually increases, and the regional land subsidence along the railway seriously weakens the stability of the pile foundation of the railway bridge and makes the differential settlement of the bridge.

The three-dimensional fluid-solid coupling models of group piles with pile cap were established on the basis of five stage field monitoring data of the settlement and groundwater level drop by using $FLAC^{3D}$ software [13-17]. On the basis of the field monitoring data checking, the variation of axial force and skin friction of pile bodies at different position under different conditions of water level drop of pumping well was simulated.

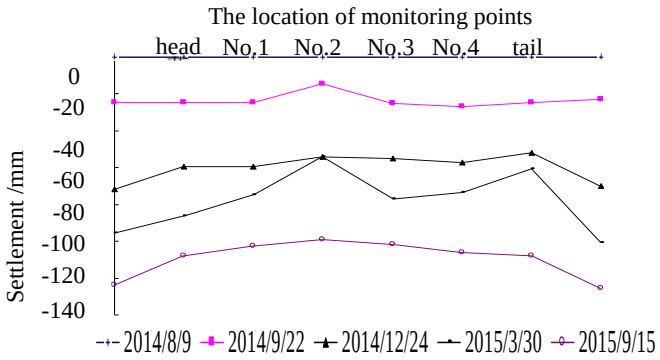

Fig.3 - Settlement curve of Yingzigou bridge piers

Tab.1 - Settlement of 3# pier and groundwater level at different time

Date	2014/8/9	2014/9/22	2014/12/24	2015/3/30	2015/9/15
Settlement/ mm	-6.6	-25.2	-55.2	-77.0	101.8
Groundwater level drop/m	-9	-26.7	-33.1	-40.2	-47.5

NUMERICAL SIMULATION OF SETTLEMENT AND INTERNAL FORCE OF PILE GROUPS DURING GROUNDWATER PUMPING

The fluid-solid coupling models of group piles with pile cap

The dimension of fluid-solid coupling models of pile group caps was 350m× 350m × 80m. The elastic-plastic material was used to simulate the behaviour of non-linear soil. The elastic model was adopted for concrete pile. The physical and mechanical parameters of soil and pile were shown in Table 2.

The pumping well was a square with 2m long and the depth was 80m. The center of well group was 47m away from the center pile groups. The pile-soil interface uses displacement method to establish the contact surface. The meshes of the soil and well under the bearing platform were closely divided. The meshes of the soil on both sides were sparse. The pile adopted the gradient radiation grid, and the finite difference model of soil and pile groups was shown in Figure 4.

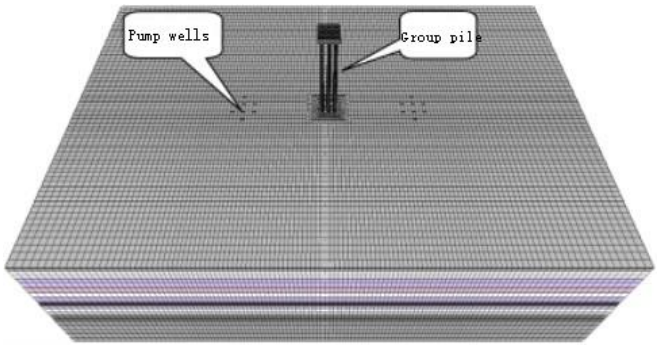

Fig. 4 - Finite difference model of soil and pile groups

Tab.2 - Calculation parameters of soil and pile group

The type of soil	Thickness/ m	Density / g/m^3	Moisture content	Porosity	Cohesion /KPa	Internal friction angle /^{o}	Bulk modulus /MPa	Shear modulus /MPa	Permeability coefficient; /m^2/Pa-sec
silty clay	2.5	1.88	31.3%	0.47	28.5	7.9	7.79	4.59	2×10^{-12}
silt	6.5	1.96	21.6%	0.38	20.5	30.5	4.78	3.28	5×10^{-11}
silty clay	7.9	1.88	23.3%	0.39	27.7	9.0	5.6	3.76	2.2×10^{-12}
silt	9.8	2.03	21.6%	0.36	20.5	30.5	4.95	3.56	3.2×10^{-12}
silty clay	6.4	1.91	23.1%	0.37	27.0	8.9	5.6	3.77	2.2×10^{-12}
silt	7.1	1.93	20.3%	0.37	28.0	11.4	5.31	3.59	2.1×10^{-12}
silt	7.3	1.98	20.4%	0.36	21.5	25.8	4.68	3.18	4.6×10^{-11}
silt	32.5	2.07	21.1%	0.36	22.5	26.8	17.53	4.78	3.2×10^{-12}
pile caps	2.5	2.5	-	-	-	-	15600	11700	0
Pile	45.0	2.5	-	-	-	-	15600	11700	0

The permeability coefficient of the soil in Table 1 decreased gradually with the continuous pumping water.

The vertical constraint was set at the bottom boundary. The horizontal constraints were set at the boundary along the side face direction. The bottom of the model was non-permeable boundary. The side and top of the model were permeable boundaries. When pumping simulation was carried out, the pore water pressure above the water level line in the well was fixed at 0. The Initial ground stress was obtained by applying gravity loads on the model. The pore water pressure was applied to the model according to the groundwater level. A uniform load of 2000kN was applied to the top of the platform. The groundwater level reduced from -9m to -47.5m in simulation, then remained stable. Since the pile foundation has been settled under the action of load and groundwater level drop from construction completion of the Yingzigou Bridge to the arrangement of monitoring points. The initial settlement was set to 0. The cumulative settlement value of the bridge pile foundation was fitted by adjusting soil parameters, permeability coefficient and precipitation

depth. On this basis, the groundwater level monitored on September 15, 2015 was taken as the final water level, the final settlement of pile foundation was predicted, and the settlement of pile and its internal force were analysed by considering the influence of water level drop of brine well and the quantity of pumping well. The calculation time of seepage flow in FLAC^{3D} software was consistent with the monitoring interval.

The effects of water level drop of brine well on the pile foundation of bridge

The research programme was as follows. Eight wells were arranged on each side of the pile foundation. The center distance of two wells was 6m. The water level in the well dropped to -9m, -26.7m, -33.1m, -40.2m, -47.5m respectively. The pressure above the water level line was set to 0Pa and the pore water pressure in the soil surrounding the group well was set according to the actual head. By reducing the water level to a specified level, the settlement of piles tended to be stabilized as the standard for the calculation of termination fluid solid coupling. The variation law of settlement and internal force of pile foundation under different water level was analysed.

The effects of water level drop of brine well on the surface settlement of well groups

The pore water pressure at the bottom of the well was converted to the height of water surface. The infiltration curve of soil at different groundwater level drop was shown in Figure 5. It can be seen that the water level in the well and the soil layers was the same. The infiltration curve was funnel-shaped. The influence range of water pumping increased. And the water level in the soil layers at the same location decreased with the continuous drop of water level in the well.

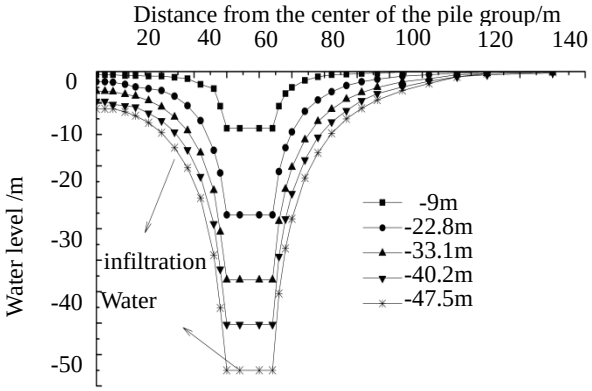

Fig. 5 - The infiltration curves of soil layer around the well groups at different water level drop

The ground subsidence curve within 100 m of the center of well groups at different groundwater level drop was shown in Figure 6. It can be seen that the ground subsidence at the same position increased, the range of ground subsidence increased with the continuous drop of water level in the well. The ground subsidence curve was funnel-shaped. The settlement of the ground in the center of the group well was severe and the settlement was large.

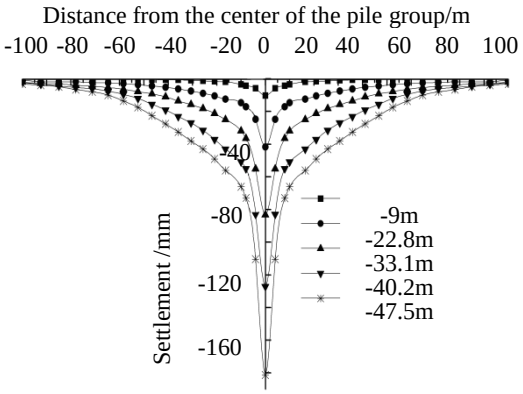

Fig. 6 - Ground settlement curve at different water level drop in wells

The effects of water level drop of brine well on the initial force of pile groups

The settlement curve of the top of pile groups at different groundwater levels drop was shown in Figure 7. It can be seen that the settlement of the piles increased gradually with the decrease of the water level in the pumping well. When the water level in the well is lower than 9m, the settlement of the pile was smaller. The settlement of the top of pile groups was proportional to the drop depth of water level in well.

.

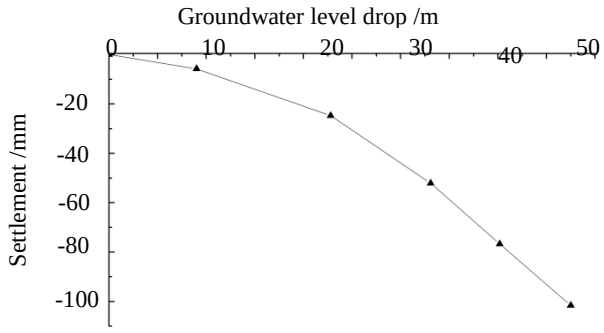

Fig. 7 - The settlement curve of the top of pile groups at different groundwater levels drop

The variation curves of axial force of different piles at different groundwater levels drop were shown in Figure 8. It can be seen that with the continuous drop of groundwater level in the well, the axial force of the piles along the shaft increased first and then decreased. The axial force of the piles increased and the position of cross section of the maximum axis force moved downward. When the groundwater level drop was -47.5m, the axis force of corner pile was the largest. The maximum axial force was 6054.8kN. In the same groundwater level drop, the size of axial force of the file was corner pile>side pile>near borehole center pile > center pile. The order of the distance from the cross section of maximum axial force to the top of the pile was center pile>near well center pile> side pile >corner pile. When the groundwater level drop was -47.5m, the maximum distance from the cross section of maximum axial force to the top of the center pile was 36.1m.

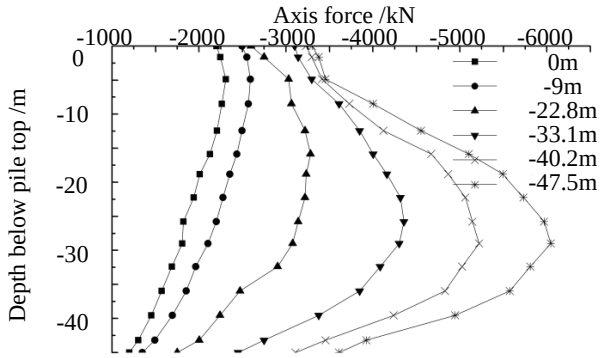

(a) Corner pile

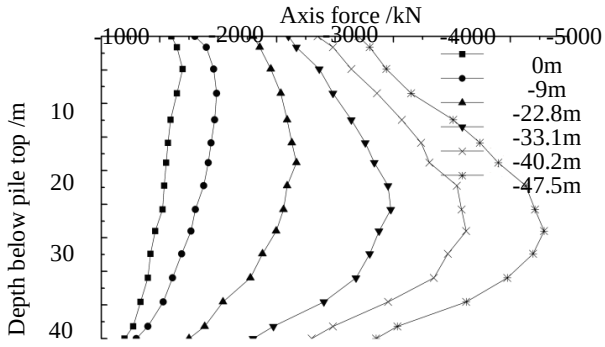

(b) Side pile

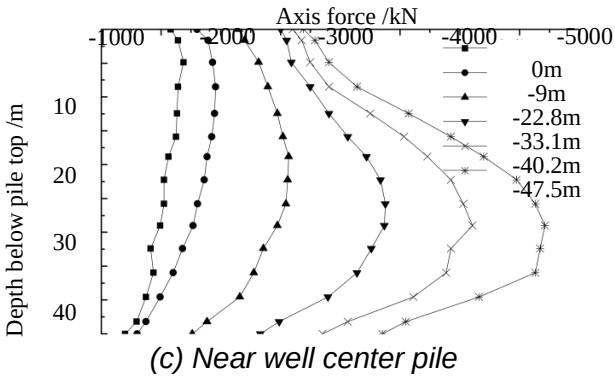

(c) Near well center pile

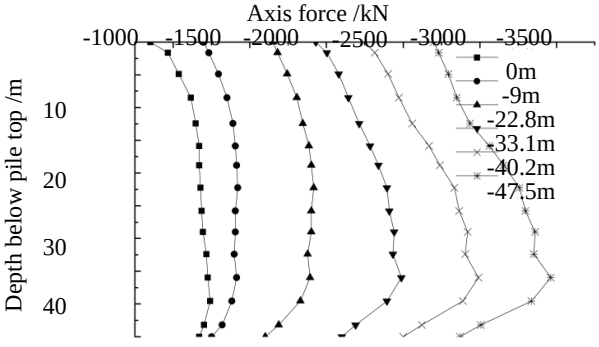

(d) Center pile

Fig.8 - The variation curve of axial force of different piles along the pile shaft at different groundwater levels drop

The variation curve of the skin friction resistance of the corner pile along the pile shaft along the pile shaft at different water level drop was shown in Figure 9. It can be seen that:

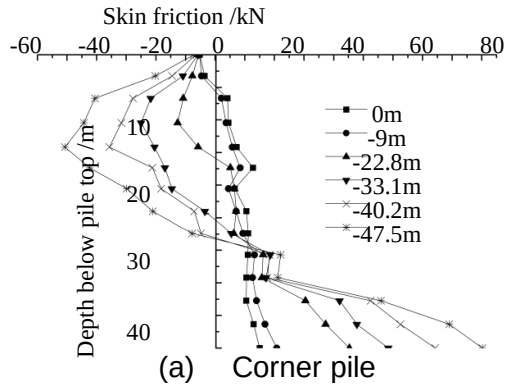

(a) Corner pile

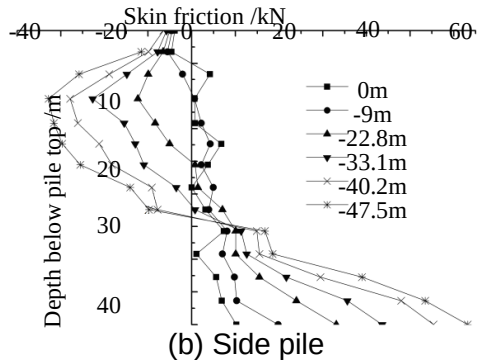

(b) Side pile

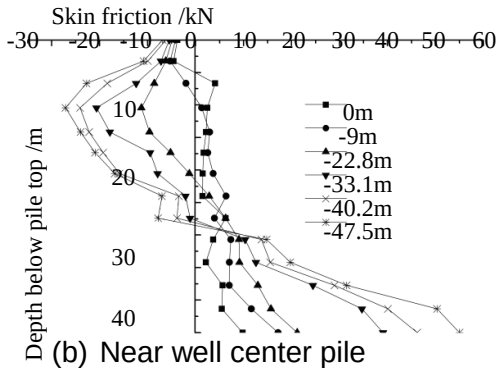

(b) Near well center pile

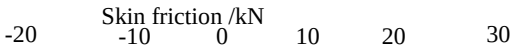

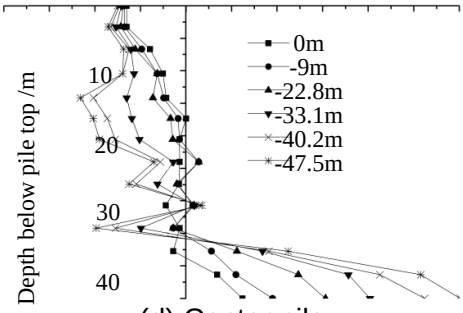

(d) Center pile

Fig.9- The variation curve of the skin friction resistance of different piles along the pile shaft at different groundwater levels drop

The pile around the top of the pile was subjected to negative skin friction resistance at different water level drop. When the water level drop in the well was lower than 9m, the pile was mainly affected by positive skin friction resistance, which increased gradually along the pile shaft. With the constant drop of water level in the well, the scope of the negative friction resistance in the upper part of the corner pile became larger and larger. In the negative friction resistance area, the negative friction resistance increased firstly and then decreased with the increase of depth of the pile. The position of the maximum negative skin friction resistance of corner pile, side pile and near well center pile was about 10m below the top of the pile. The order of negative friction resistance of corner pile was -36.5kPa.

With the drop of the groundwater level, the neutral point of each pile gradually moved down, and each pile was affected by positive friction below the neutral point and increased gradually along the pile shaft, the skin positive skin friction resistance reached the maximum in the bottom of the pile. When the groundwater level drop was -47.5m, the maximum positive skin friction resistance of corner pile was 90kPa. In the same ground water levels drop, the size of positive skin friction resistance was corner pile > side pile> near well center pile > center pile. The order of the distance between neutral point of each pile and the top of the pile was center pile > near well center > side pile > corner pile. When the groundwater level drop was -47.5m, the maximum distance from neutral point to the top of the center pile was 35.2m. The position of the neutral point of each pile was basically the same as the position of cross section of the maximum axial force of the pile.

The central pile was mainly affected by negative skin friction resistance in the range of 0 ~ 35m below the top of the pile. The pile was mainly affected by positive skin friction resistance in the range of 35m ~ 45m below the top of the pile. The cross-section position of the neutral point of the central pile was less affected by the water level in the well. There were multiple neutral points in center pile.

CONCLUSIONS

1) The curves of infiltration and ground subsidence were funnel-shaped. The influence range of water pumping increased. And the water level in the soil layers at the same location decreased with the continuous drop of water level in the well. The ground subsidence at the same position

increased, the range of ground subsidence increased with the continuous drop of water level in the well. The settlement of the ground in the center of the group well was severe and the settlement was large.

2) With the continuous drop of groundwater level in the pumping well, the axial force of the piles along the pile shaft firstly increased then decreased. The axial force of the piles increased and the position of cross section of the maximum axis force moved downward. In the same groundwater level drop, the size of the pile axial force was corner pile > side pile> near borehole center pile > center pile. The order of the distance from the cross section of maximum axial force to the top of the pile was center pile > near well center pile > side pile >corner pile. When the groundwater level drop was -47.5m, the maximum distance from the cross section of maximum axial force to the top of the center pile was 36.1m.

3) With the drop of the groundwater level, the neutral point of each pile gradually moved down, and each pile was affected by positive friction below the neutral point and increased gradually along the pile shaft, the skin positive skin friction resistance reached the maximum in the bottom of the pile. In the same ground water levels drop, the size of positive skin friction resistance was corner pile > side pile> near well center pile > center pile. The order of the distance between neutral point of each pile and the top of the pile was center pile > near well center > side pile > corner pile. The position of the neutral point of each pile was basically the same as the position of cross section of the maximum axial force of the pile.

4) The central pile was mainly affected by negative skin friction resistance in the range of 0 ~ 35m below the top of the pile. The pile was mainly affected by positive skin friction resistance in the range of 35m ~ 45m below the top of the pile. The cross-section position of the neutral point of the central pile was less affected by the water level in the well. There were multiple neutral points in center pile.

ACKNOWLEDGEMENTS

This work was supported by Liaoning province natural science foundation of China (No. 20170540143 and No. 20180550804) and the National Natural Science Foundation of China (No. 51774199 and No. 51579039).

REFERENCES

[1] Vanmarcke.E.H., Lee.G.C, 2015. On the distribution of the first-passage time for normal stationary random processes. Application of Mechanics, 42:1254-1261.

[2] Berrah M K, Eduardo Kausel, 2013. A modal combination rule for spatially varying seismic motions. EESD, 22:791-800.

[3] Dejus T, 2015. Evaluation of work safety control systems in construction. Civil Engineering and Management, 10(2):93-97.

[4] F.Leonhardt, 2016. Long Span Prestressed Concrete Bridges in Europe. Journal of the Pressed

Concrete institute, 8(1):98-103.

[5] Yamamura N, Hiroshi Tanaka, 2016. Response analysis of flexible MDF systems for multiple-support excitations. EESD, 19:345~357

[6] Kiureghian A D, Neuenhofer A, 2015. Response spectrum method for multi-support seismic excitaions.Earthquake Engineering and Structural Dynamics, 21:713~740

[7] J.T.P.Yao, 2016. ConcePt of Structure Control. Journal of structural Division, Vol.98(7):128-132.

[8] Shun-ichi Nakamura, 2015. New structural Forms for Steel Concrete Composite Bridges. Structural Engineering International, (1):204-212.

[9] Komatsu S, akimoto T, 2016. Nolinear Analysis of Spatial Frames Consisting of Members with Closed Cross-Section. Proc, JSCE, 252:85-91.

[10] Sakimoto T, Komatsu S, 1979. Ultimate Strength of Steel Arches under Lateral Loads Proceedings. Japan Society of Civil Engineer, 292:121-128.

[11] COMODROMOS EM, BAREKA SV, 2015. Evaluation of negative skin friction effects in pile foundations using 3D nonlinear analysis, Computers and Geotechnics, 32(4): 210-221.

[12] LIU ZS, 2015. Field tests on negative skin friction of steel pipe piles in high backfilling soils, Chinese Journal of Geotechnical Engineering, 37(2): 337-342.

[13] Li Guo-hao, 1992. Stability and vibration of bridge structures [M].BeiJing: China Railway Publishing House. (In Chinese)

[14] LI GC, MA ZQ, ZHANG N, et al, 2015. Research on failure characteristics and control measuresof roadways affected by multiple overhead mining in Huaibei mining area. Journal of Mining & Safety Engineering, 30(2): 181-187 (in Chinese).

[15] SHEN BW, 2016. Nonlinear analysis of single piles under negative skin friction, Journal of Hefei University of Technology (Natural Science), 31(12): 2024-2027 (in Chinese).

[16] JIA Y, SONG FG, WANG BL, YANG LC, 2015. Modified load transfer method for calculation of foundation pile settlement due to dewatering, 36(1): 68-74(in Chinese).

[17] HONG X, LEI GH, SHI JY, 2014. Unified load-settlement solution of single piles based on bilinear load transfer, Chinese Journal of Geotechnical Engineering, 26(3): 428-431(in Chinese).

Article no. 21

THE CIVIL ENGINEERING JOURNAL 2-2019

W/C REDUCTION FOR FLEXURAL STRENGTHENING OF R.C BEAMS HAVING PLASTIC AGGREGATE

Akhtar Gul, Saad Tayyab, Asad Ullah, Kamal Shah, Faisal Mehmood and Fazal Haq

Civil Engineering Department, UET Peshawar, Satellite Campus-Bannu 28100, Pakistan;akhtarwazir@uetpeshawar.edu.pk

ABSTRACT

Due to the greater availability and low biodegradability plastic waste became a great concern for the researchers worldwide, because this waste is one of the main environmental issues. Nowadays harmful industrial waste can be helpful in place of conventional aggregate in concrete mix, which in turn will also save natural resources. A similar effort has been made in this research study for making concrete having replaced percentage of plastic aggregate along with plasticizer and reduced water cement ratio. Total of fifty-seven concrete cylinders and six beams were cast, and after curing period, these were tested for compression and flexural strength respectively. Compression strength decreases by increasing the percentages of plastic aggregates while reducing the w/c, the compression strength increases. The strength of beams in flexure increases by 57% through reduction of W/C from 0.68 (normal concrete/fc'=3000psi) to 0.3, and with further replacement of 40% plastic aggregate the increase in strength as compared to the normal concrete was still 3%.

KEYWORDS

Plastic Aggregate (PA), Flexural Strength (FS), Compressive Strength (CS), Water Cement Ratio (W/C), Superplasticizer (SP)

INTRODUCTION

A significant increase for aggregate demand is just because of increase in population day by day. The changed life style of human being adds much solid waste to the environment. We can reduce some of the problems caused by these solid waste through productive use of the waste and thus we can benefit our world in the form of reduced environmental pollution, saving and sustaining natural resources and recycling energy products. Nowadays many research works are conducted to determine the possible disposal of plastic waste to be replaced in place of mineral aggregates, especially in situations where the main concern is dead weight reduction rather than strength.

Many research works have been conducted to modify the concrete mix by replacing some of the components of concrete such as coarse and fine aggregates and cement with different industrial and solid waste materials. In concrete, these materials are beneficial to be added either as a part of mineral aggregate or as a partly replacement of fine aggregate. Due to heavy weight of concrete, it can be used in skyscrapers because use of plastic aggregate will make the concrete light and then eventually the entire structure [1].

Plastic aggregates which are non-biodegradable and can be successfully replaced with mineral aggregates in concrete mix, which reduce the bulk density of concrete and it light weight. By replacing 10% to 50% of mineral aggregates with recycled plastic aggregates, bulk density decreases in the range of 2.5% to 13% as compare to the concrete having 0% of plastic aggregates. The replacement of 10% to 50% of recycled plastic aggregates with mineral coarse aggregates in

concrete mix reduces compression strength of concrete in the range of 34% to 67% compare to normal concrete [2].

Another research work was carried out by replacing 20% of plastic aggregates with the mineral coarse aggregate. After testing the concrete cylinders, it was concluded that the CS and split-tensile strength of concrete mix were reduced than that of concrete having only mineral coarse aggregates. Hence, it is advised that concrete having recycled PA should be used in non-structural applications of civil engineering where the strength requirement is up to 25 Mpa (3626 Psi). Eventually, this will reduce the cost of non-structural concrete [3].

Kou et al. concluded from their research work that increasing the plastic aggregates percentage, reduction occurs in the CS of concrete mix as well as in the split tensile strength. On the other hand, the poisson's ratio increased and modulus of elasticity decreased due to which ductility increased and chloride ion & drying shrinkage were also enhanced [4].

Saikia et al. in 2012 demonstrated that several strength related properties of the concrete having plastic aggregates will decrease, regardless of the percentages and type of PA. The reason behind the decrease in the concrete strength is the weak bonding between binding material and PA. By replacing 20% of mineral course aggregates with PA in concrete, CS of the resulting concrete was reduced up to 72% than that of control specimen. And by replacing 50% of fine aggregate by volume with the fine particles of plastic, the compressive strength reduction was reported up to 16%. It is concluded from the above results that either replacing course aggregates or replacing fine aggregates in the concrete with PA, the CS will reduce. The difference in the behaviour of concrete in each case (replacing fine or course aggregates) is due to the difference in shape, size and workability of concrete mixture [5].

The decrease in the CS of concrete mixture is directly proportional to the addition of PA in concrete mix. Also by increasing the PA in the concrete mix, the modulus of elasticity decreases but the ductility of concrete increases by increasing plastic aggregates compare to the normal concrete. It is cleared that concrete containing plastic aggregates can be used in stone curb and park benches etc. where they are not exposed to heavy loads [6].

In 2016 Colangelo et al. reported that the CS as well as concrete density decreases by replacing mineral aggregates with plastic aggregates in concrete. The reduction in the concrete density indicates that PA has lower density than mineral aggregates. Another reason for reduction in concrete density is the air trapped during mixing of plastic aggregates [7].

In 2016 another research work was carried out by Gu et al. and concluded that FS, split tensile strength, elastic modulus and CS decreases with the increase in PA in concrete mix. Moreover, the above strength related properties decreases more gently for concrete containing non-uniform shaped recycled plastic aggregates compare to concrete containing uniformly shaped plastic aggregates. By adding plastic aggregates in concrete, ductility improves but result in lower peak stress as compared to traditional concrete [8].

In 2005 a research work was carried out and demonstrated that 2–6% reduction in weight is possible through the addition of plastic aggregate as related to that of ordinary weight concrete. Although, the reduction of strength in compression was about 33% as compared to that of conventional concrete [9]. The same results were obtained from the experimental investigation of Batayeneh et al. (2007) in which the decrease of strength in compression was directly proportional to the increase in the addition of plastic aggregate [10].

Another research work investigated the physical, chemical and mechanical behaviour of concrete mix incorporated with plastic aggregate. Their findings showed that there would be no substantial alteration in the concrete mechanical behaviour if we incorporate plastic aggregate in quantity less than 10% by volume in the concrete matrix [11].

In one of the research polyethylene, terephthalate fibers were used to determine the concrete mechanical properties; with the main concern to measure the influence of various dimensions and geometries on the concrete mechanical properties. Marthong's conclusions declare that the workability effected by a very small amount by changing the fibers geometry [12].

In another research work researcher replaced various percentages of sand in concrete mix with the waste plastic. Concrete was investigated in hardened state as well as in wet state with the main concern on the toughness index test. The research declared that with replacement of sand through waste plastic the generation of micro cracks can be arrested because a fabric form shape is provided by plastic waste to concrete mixture [13].

The basic assumption, which is supported by experimental data reveals that the strength of hardened form of cement paste is the main agent that controls the structural concrete strength, which in turn is in the control of W/C and is defined as the quantity of water present in the fresh concrete mixture to the quantity of cement. Thus, it is clear that the relation between water cement ratios versus concrete strength is the base for modern concrete technology.

Concrete produced with 10%, 20%, 30%, 40% and 50% plastic aggregate. The plastic aggregate addition up to 20% in place of mineral aggregate will still give strength value with in permissible range. Beyond 20%, replacement of mineral aggregate with that of PA will reduce the density of concrete mix [14].

The concrete mechanical properties, such as CS and FS having polymer based on recycled Polyethylene terephthalate, and the results showed that energy saving along with reduction in material cost is possible [15].

Plastic aggregate is lightweight aggregate and incorporation of plastic aggregate in concrete mixture will give much better results than the addition of other naturally used lightweight aggregate. The poor mechanical properties in most of the studies are because of reduced bond strength between cement paste and plastic coarse aggregate [16].

Thus, the above discussions lead to study and promote the replacement of higher percentages of PA replacement with mineral coarse aggregate in concrete mix. This research work has been conducted to discover the concrete CS and FS of concrete containing higher percentages of PA with reduced w/c.

SELECTION AND LABORATORY TESTING OF MATERIALS

The test conducted on all the material used such as fine aggregates, coarse aggregate and cement had all the values within allowable limit according to the ASTM codes.

Plastic aggregates were made by crushing plastic waste i.e. PET (Polyethylene Terephthalate) bottles, plastic shopping bags, straws, plastic packing and other plastic items. These Plastic coarse aggregates are shown in Figure 1.

Fig. 1 – Curing stage of concrete cylinder

Additives are usually added to modern concert, which may be added either in chemical form or in mineral form. To improve workability of concrete mix we usually add superplasticizer and plasticizers, which are high range water reducers and reducers respectively, and both are chemical admixtures. There will be inverse relation between the concrete strength and added water or water cement ratio when the added water is not enough in the concrete mix. Plasticizer or superplasticizer will be required for greater workability when added water is too less for producing stronger concrete. Addition of 1-3% superplasticizer by weight of cement is usually sufficient as higher percentages are not advisable because it will cause excessive concrete segregation [17].

To maintain the workability of concrete mix, organic polymer blend superplasticizer (Chemrite 520 BA-S) was used. The slump test was carried out as per BS EN 12350 (2000) standard. The advisable range of superplasticizer is 0.6-3% per unit weight of cement for Chemrite 520 BA-S. Three trials were performed for each type of concrete to define the percentage of superplasticizer for the given W/C. Thus, superplasticizer of 0.75% per unit weight of cement was defined to be added for a W/C of 0.5, 1% super plasticizer per unit weight of binder (cement) for a W/C of 0.4 and 2.5% superplasticizer per unit weight of binder for a W/C of 0.3. Table 1 shows Mix Design for Concrete Specimen.

Tab. 1- Concrete Mix Design

Ratios	Cement : Fine Aggregate : Coarse Aggregate : PA				
	W/C = 0.68	W/C = 0.56	W/C = 0.5	W/C = 0.4	W/C = 0.3
0 % PA	1:3.1:4.4:0.0	1: 2.4:3.5:0	1:2:3.2:0.0	1:1.5:2.6:0.0	1:0.9:1.9:0.0
15 % PA	×	1:2.4:3.0:0.3	×	×	×
20 % PA	×	1:2.4:2.8:0.4	×	×	×
25 % PA	×	×	1:2:2.4:0.4	1:1.5:2:0.3	1:0.9:1.4:0.3
30 % PA	×	×	1:2:2.2:0.5	1:1.5:1.8:0.4	1:0.9:1.3:0.3
35 % PA	×	×	1:2:2:0.6	1:1.5:1.7:0.5	1:0.9:1.3:0.4
40 % PA	×	×	1:2:1.9:0.7	1:1.5:1.5:0.6	1:0.9:1.2:0.4

According to the ASTM standard C470/C470M-15 three concrete cylinders for each mix were prepared having dimensions of 1 feet height and ½ feet diameter. Total of 57 concrete cylinders were caste for different percentages of plastic aggregates having different water to cement ratios, as shown in the test matrix in Table 2.

Tab. 2- Test Matrix

Percentage of Plastic aggregates	No of Cylinders for W/C = 0.68	No of Cylinders for W/C = 0.56	No of Cylinders for W/C = 0.5	No of Cylinders for W/C = 0.4	No of Cylinders for W/C = 0.3
0% PA	3	3	3	3	3
15% PA	×	3	×	×	×
20% PA	×	3	×	×	×
25% PA	×	×	3	3	3
30% PA	×	×	3	3	3
35% PA	×	×	3	3	3
40% PA	×	×	3	3	3
Total	3	9	15	15	15
57					

According to the ASTM standard these concrete cylinders were tested through Universal Testing Machine (UTM) for compression strength after twenty-eight days of curing as shown in Figure 2 and 3 (a) and (b).

.

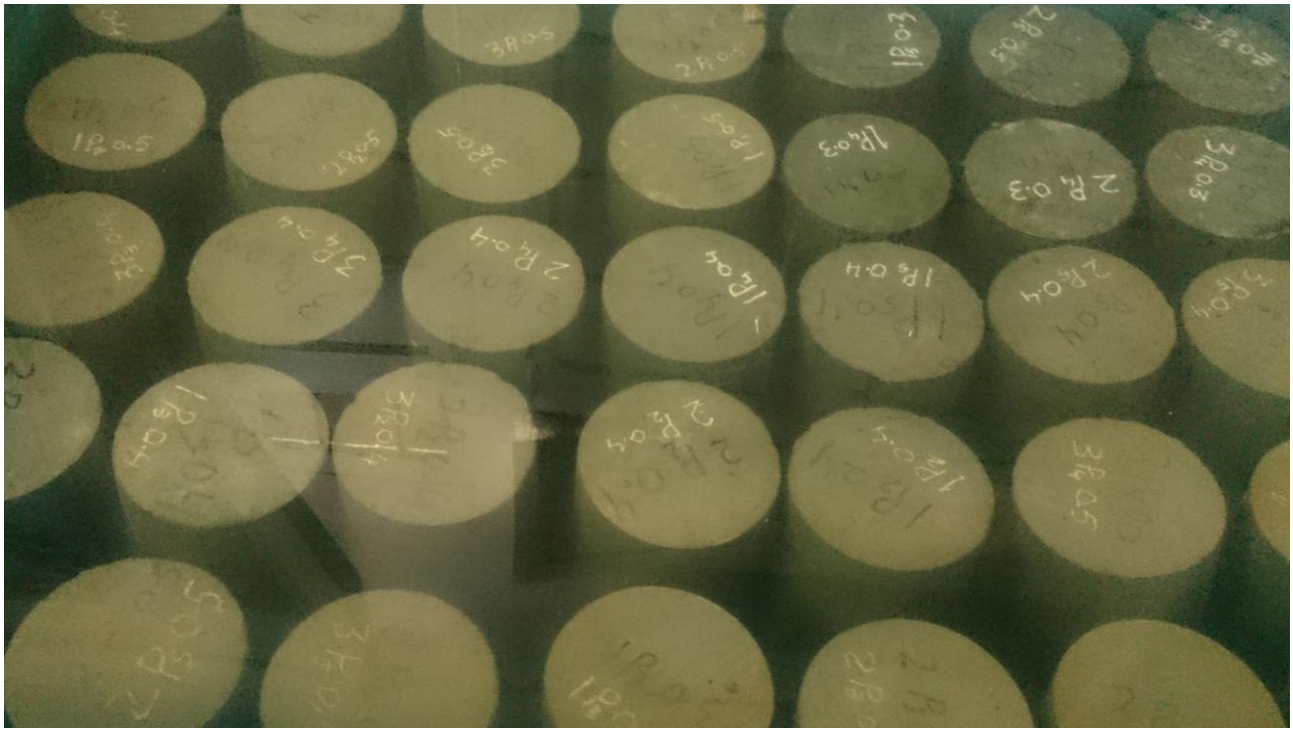

Fig. 2 – Curing stage of concrete cylinder

DOI 10.14311/CEJ.2019.02.0021

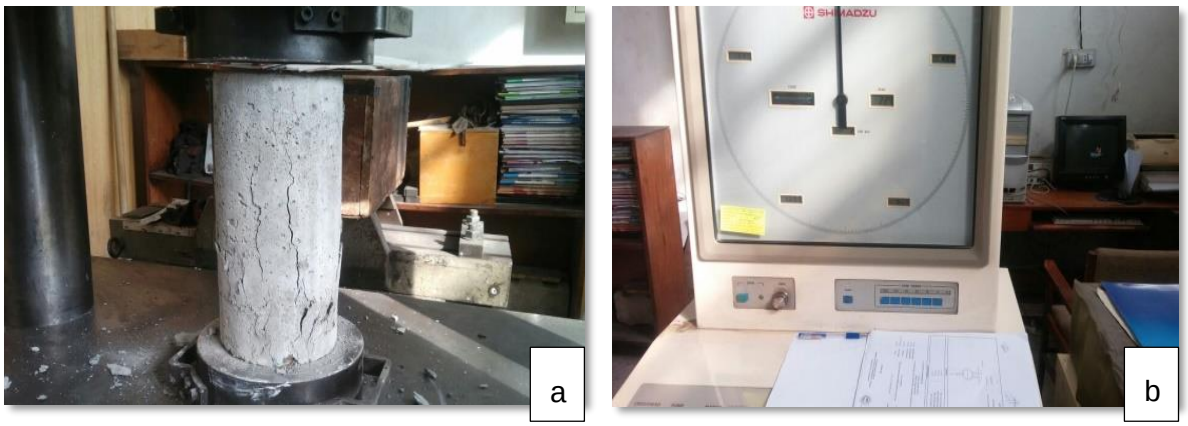

Fig. 3 – (a) & (b) Compressive test of concrete cylinder

The average compression strength of concrete cylinders obtained from the testing of concrete cylinders through UTM are shown in Table 3.

Tab. 3- Average CS ofcConcrete cylinders

	W/C = 0.68	W/C = 0.56	W/C = 0.5	W/C = 0.4	W/C = 0.3
Plastic Aggregate Percentage	Average CS of Concrete (Psi)	Average CS of Concrete (Psi)	Average CS of Concrete (Psi)	Average CS of Concrete (Psi)	Average CS of Concrete (Psi)
0	3008	3609	3936	5048	6712
15	×	3254	×	×	×
20	×	2983	×	×	×
25	×	×	2918	3432	3674
30	×	×	2798	3136	3555
35	×	×	2637	2996	3037
40	×	×	2466	2878	2953

Based on compression test results six beams were designed and cast for flexural testing with clear span equals six feet and cross sectional area of 6x9 in^2. Among them two were controlled beams (fc'=3000psi and provided with flexural reinforcement based on minimum steel reinforcement as per the ACI-318-08). Two beams with w/c of 0.3 containing PA of 0% while the last two beams had a w/c of 0.3 containing PA of 40% with compression strength (fc') of 6700psi which was obtained from compression test conducted on concrete cylinders as per ASTM standard C470/C470M-15. The beams were tested for flexural strength as per ASTM C78/78M-10 using the third point loading criteria, as shown in Figure 4.

Fig. 4 – Third point loading

The load application rate was 0.2 ton/sec by the loading cells having a total capacity of 100 ton. The data is tabulated in Table 4 and Figure 5, 6 and 7 shows flexural strength results.

Tab. 4- Flexural strength testing results

	Avg: Ultimate load (kips)	Avg: Deflection (mm)
Normal concrete (fc'= 3000 psi)	10.40	25.16
0 % Plastic Aggregate, W/C=0.3	16.40	38.23
40 % Plastic Aggregate, W/C=0.3	10.73	53.08

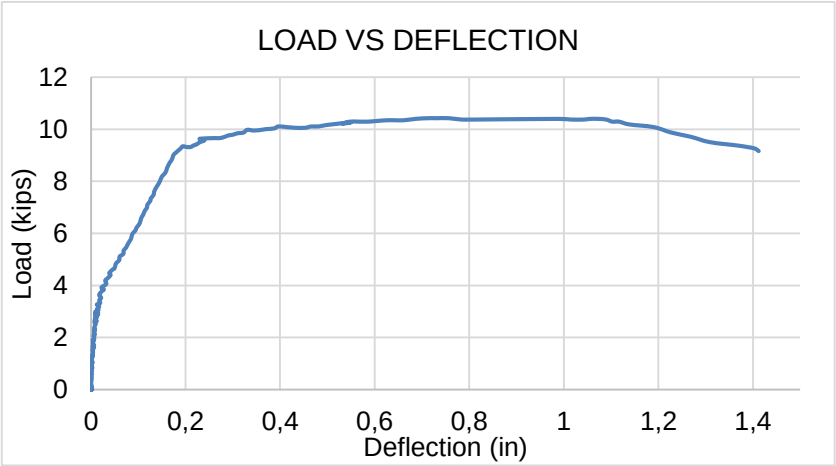

Fig. 5 – Average load vs. deflection curves for beams having W/C=0.68, PCA=0%

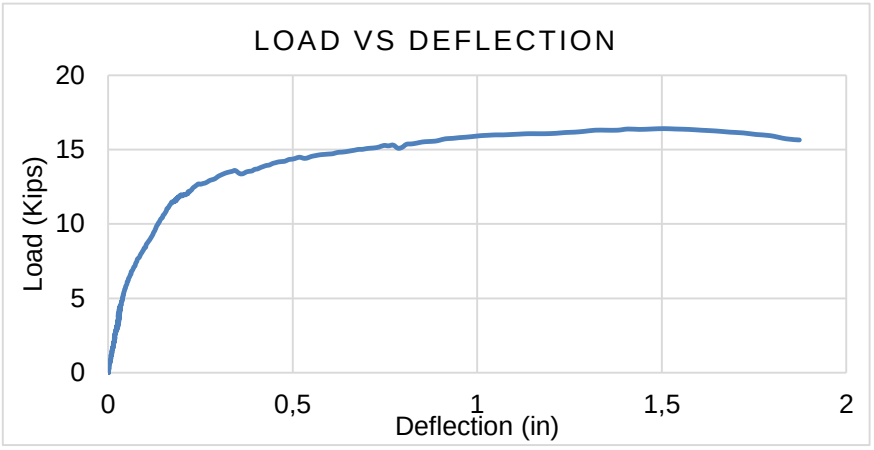

Fig. 6 – Average load vs. deflection curves for beams having W/C=0.3, PCA=0%

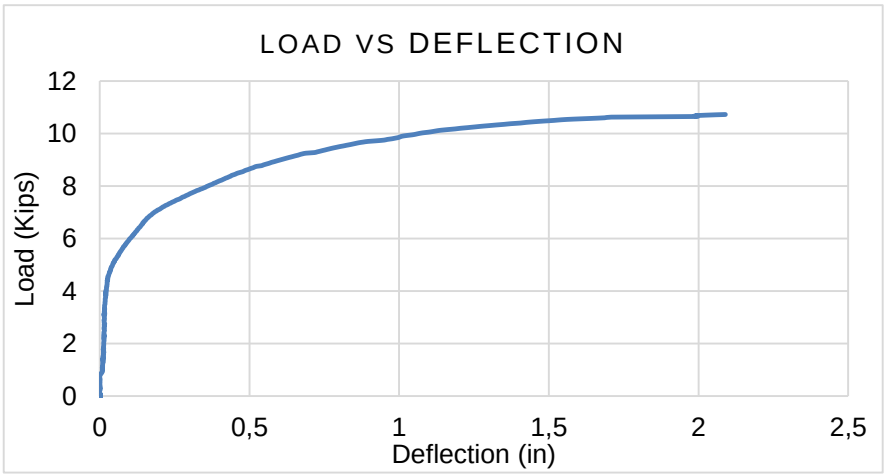

Fig. 7 – Average load vs. deflection curves for beams having W/C=0.3, PCA=40%

The specimens with the plastic coarse aggregate replacement of 40% took more load than the specimens having W/C of 0.68, with the increase in flexural strength equals 3% only. Although the increase in flexural strength of specimens with 0% plastic aggregate and W/C 0.3 was 57% as related to that of traditional concrete.

Since all the specimens were designed for maximum shear, therefore no shear cracks were observed. All the cracks observed were purely flexural cracks as shown below in Figure 8.

Fig. 8 – Crack pattern in 40% PCA specimen

DOI 10.14311/CEJ.2019.02.0021

CONCLUSION

From this research work, following decisions were made.

- The reduction in slump value because of plastic coarse aggregate addition best suits this concrete mix for situation where we need lower workability.
- By replacing 40% plastic aggregates with natural coarse aggregates, weight of concrete can be reduced up to 25-30% as compared to normal concrete.
- Higher percentages of plastic aggregates can be utilized in concrete mixture by reducing their w/c with the help of superplasticizers.
- As increasing the percentage of plastic aggregates in concrete from 0% replacement to 40% replacement of natural coarse aggregates, reduction in the CS of concrete occurs. The reduction in the CS of concrete having PA is due to weak bond between PA and the cement paste, which disturb the concrete interlocking arrangement.
- However, by reducing the w/c by using superplasticizers, the CS of concrete having PA increases.
- Concrete beam cast using PA as a replacement of mineral coarse aggregates increases ductility.
- The increase in ductility as a result of plastic aggregate addition can help to stop the cracks that can be generated during concrete mechanical failure.
- The strength of beams in flexural increases to 57% by lowering of W/C from 0.68 (normal concrete) to W/C of 0.3.
- Furthermore, by adding of plastic course aggregate of 40% to the mix having the same W/C of 0.3, FS decreases, and the obtained average value of flexural strength is only 3% more than that of normal concrete mix having W/C equal to 0.68.
- Thus, increasing the percentages of plastic aggregate with reduced W/C gives equal or even better performance in flexural strength than conventional concrete and thus can be used where dead load reduction is of prime concern.

CONFLICT OF INTEREST

The authors of this research paper, whose names are listed on title page, certify that they have developed this research entirely on the basis of their personal efforts made under the sincere guidance of the supervisor. The authors also certify that they have carried out this research work as final year project for the fulfilment of their graduate degree course through self-financing.

REFERENCES

[1] Girija, B.G., Sailaja, R.R.N. and Madras, G., 2005. Thermal degradation and mechanical properties of PET blends. Polymer Degradation and stability, 90(1), pp.147-153.

[2] Siddique, R., Khatib, J. and Kaur, I., 2008. Use of recycled plastic in concrete: A review. *Waste management*, *28*(10), pp.1835-1852.

[3] Batayneh, M., Marie, I. and Asi, I., 2007. Use of selected waste materials in concrete mixes. *Waste management*, *27*(12), pp.1870-1876.

[4] Kou, S.C., Lee, G., Poon, C.S. and Lai, W.L., 2009. Properties of lightweight aggregate concrete prepared with PVC granules derived from scraped PVC pipes. *Waste Management*, *29*(2), pp.621-628.

[5] Saikia, N. and De Brito, J., 2012. Use of plastic waste as aggregate in cement mortar and concrete preparation: A review. *Construction and Building Materials*, *34*, pp.385-401.
[6] Sharma, R. and Bansal, P.P., 2016. Use of different forms of waste plastic in concrete–a review. *Journal of Cleaner Production*, *112*, pp.473-482.
[7] Colangelo, F., Cioffi, R., Liguori, B. and Iucolano, F., 2016. Recycled polyolefins waste as aggregates for lightweight concrete. *Composites Part B: Engineering*, *106*, pp.234-241.
[8] Gu, L. and Ozbakkaloglu, T., 2016. Use of recycled plastics in concrete: A critical review. *Waste Management*, *51*, pp.19-42.
[9] Choi, Y.W., Moon, D.J., Chung, J.S. and Cho, S.K., 2005. Effects of waste PET bottles aggregate on the properties of concrete. Cement and concrete research, 35(4), pp.776-781.
[10] Batayneh, M., Marie, I. and Asi, I., 2007. Use of selected waste materials in concrete mixes. Waste management, 27(12), pp.1870-1876.
[11] Pezzi, L., De Luca, P.A., Vuono, D., Chiappetta, F. and Nastro, A., 2006. Concrete products with waste's plastic material (bottle, glass, plate). In Materials Science Forum (Vol. 514, p. 1753). Trans Tech Publications.
[12] Marthong, C., 2015. Effects of PET fiber arrangement and dimensions on mechanical properties of concrete. The IES Journal Part A: Civil & Structural Engineering, 8(2), pp.111-120.
[13] Ismail, Z.Z. and Al-Hashmi, E.A., 2010, June. Validation of using mixed iron and plastic wastes in concrete. In Second International Conference on Sustainable Construction Materials and Technologies. Ancona (pp. 393-403).
[14] Arduini, M. and Nanni, A., 1997. Parametric study of beams with externally bonded FRP reinforcement. ACI Structural Journal, 94(5), pp.493-501.
[15] Byung-Wan, J.O., Park, S.K. and Cheol-Hwan, K.I.M., 2006. Mechanical properties of polyester polymer concrete using recycled polyethylene terephthalate. ACI structural journal, 103(2), p.219.
[16] Saikia, N. and De Brito, J., 2012. Use of plastic waste as aggregate in cement mortar and concrete preparation: A review. Construction and Building Materials, 34, pp.385-401.
[17] Aitcin, P.C., 1992. The use of superplasticizers in high performance concrete. High performance concrete–from material to structure, pp.14-33.

Article no. 22

THE CIVIL ENGINEERING JOURNAL 2-2019

DESIGNS FOR T SHAPE FISHWAYS

Xi Mao[1,2,] , Jiehao Zhang[1], Kai Tang[1], Weiyang Zhao[2]*

1. *Sichuan Agricultural University, College of Water Conservancy and Hydropower Engineering, Yaan, Road Xinkang 46, China; maowhiteknight@163.com*
2. *Water Research Laboratory, School of Civil and Environmental Engineering, The University of New South Wales, Sydney, King Street 110, Australia*

ABSTRACT

This paper presented results of a numerical study on seven designs of T shape fishways. The trajectory equation of the maximum velocity line and the V/V_a equation of the T shape fishways were obtained from the results. It was found that a width of $1.5b_s$ for the T lateral baffle, a width of $5b_s$ and a length of $6.25b_s$ for the pools were very satisfactory for the dimensional design of T shape fishways, where b_s was the slot width. From the seven designs studied, design 3 (D3, D denotes “design”) was recommended for practical use.

KEYWORDS

Fishway, Civil engineering measures, Hydrodynamics, Hydraulics, Numerical simulation

INTRODUCTION

Fishways (or fish passes, fish passages) are structures that facilitate the upstream or downstream migration of aquatic organisms over obstructions to migration such as dams and weirs. Although constructing fishways does not eliminate the basic ecological damage caused by dams, such as loss of river habitat or loss of longitudinal connectivity, this measure attenuates the negative ecological impact of these obstructions to a certain extent, and thereby increases their ecological compatibility [1], [2].

Three types of technical fishways are commonly used in engineering:

(1) Denil fishways [3], [4], [5]
(2) pool and weir fishways [6], [7], [8]
(3) vertical slot fishways [9], [10], [11]

The Denil fishway is impressionable to fluctuating water levels and is prone to clogging up with silt and debris, so it needs to operate at higher water levels than other types of fishways. The pool and weir fishway is inadaptable to large water level fluctuations, and does not allow fish passing across the entire cross section. The vertical slot fishway is adaptable to frequent water level fluctuations, and allows fish to pass across the entire cross section and is not prone to be blockage. Another problem arises, however, which is that the velocity is extremely high in some areas, such as vertical slot zone.

Mao et al [12] first put forward a new kind of fishway called a T shape fishway by means of numerical simulation and physical experimentation. The T shape fishway consists of consecutive and identical pools, and includes a series of inlet lateral baffles and T shape baffles. The T shape baffle is named for its shape, which is composed of the T lateral baffle and the T central baffle.

Compared to these three traditional technical fishway types, the T shape fishway has plane symmetry, and the following obvious features:

(1) it can meet the migratory requirements of these fish with poor swimming and jumping capability, in terms of velocity and flow pattern

(2) the main flow travels from one slot to the next through the pool as a two-dimensional curved flow with gentle slope (S≤10%), where S is the slope of the fishway [9], [12].

This paper aims to understand the hydraulics of the T shape fishway, to develop simpler pool designs by means of numerical simulation.

METHODS

A commercial CFD solver (Fluent) was used to create a numerical model to solve the optimal control problem related to the optimal management of T shape fishways. The mathematical model uses the finite-volume method to solve the three-dimensional Navier-Stokes equation using the standard k-ε turbulence model. Complete details of the mathematical model, including the solution method, boundary conditions, and mesh conditions, is provided in works by Mao *et al*. By using the experimental method, the mathematical model was validated by Mao *et al*, and it was found that the rationality of the numerical simulation and experiments validate the overall controlling error within 8% [12].

Numerical simulation

Seven designs of T shape fishways were studied by using numerical simulation. These seven T shape fishway models were all set in the same water channel, with 24.5 m long, 2.0 m wide, and 1.2 m high. Baffles were set vertically within the water channel for each design with the slope of the flume set as S=2.6%. In each design, there were six regular pools in the flume, with two transition pools, one at the beginning of the water channel and the other at the end. The flow discharge in each design was Q=400 L/s. Figures 1 (a) and (b) show the details of the seven designs.

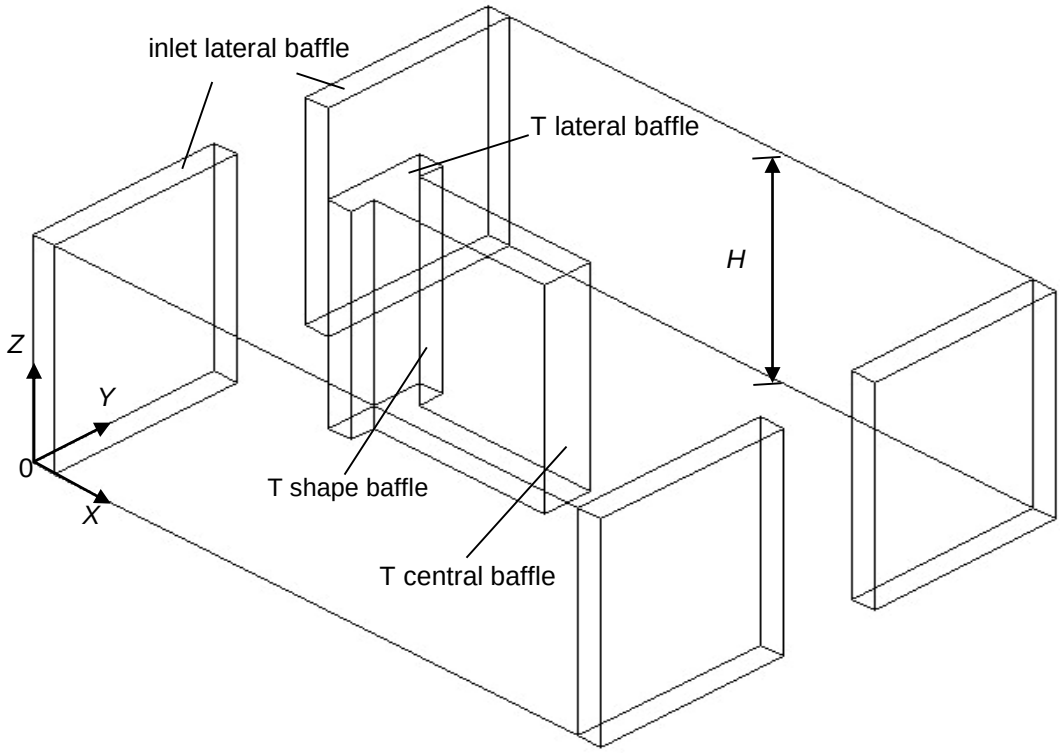

Fig. 1 (a) – Three-dimensional stereogram of fishway designs considered in this study

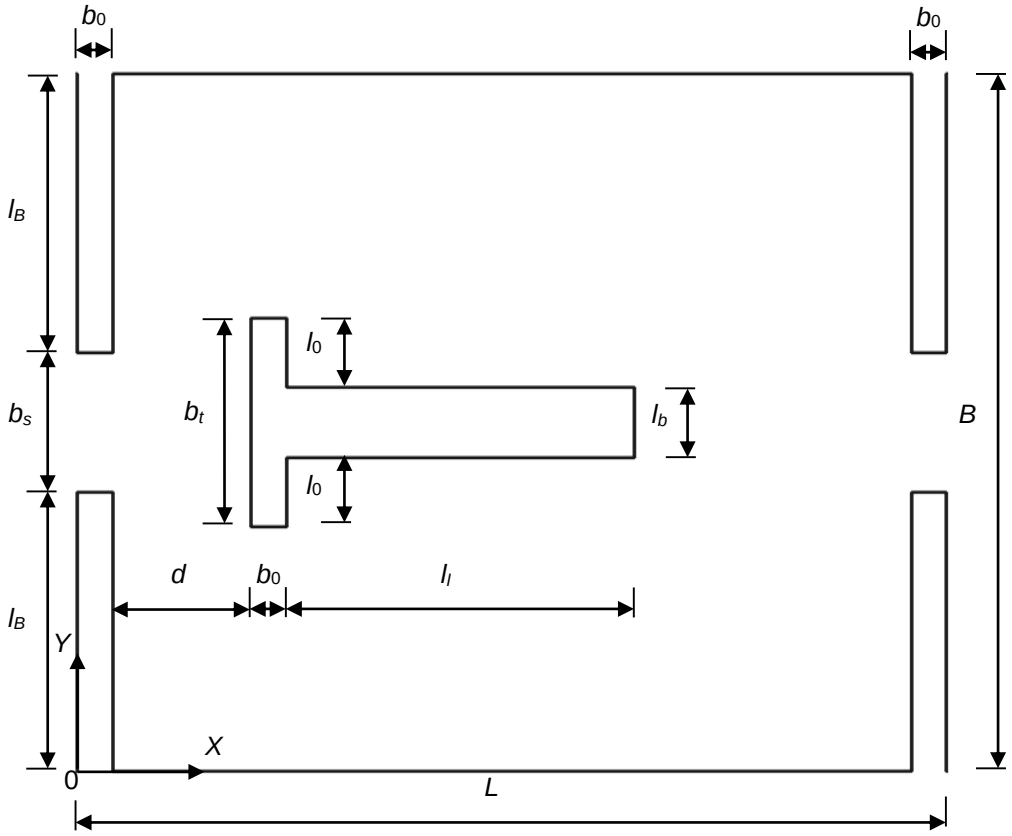

Fig 1 (b) – Planar graph of fishway designs considered in this study

The sizes of all of the seven designs in this study are shown in Table 1, where *L*, *B*, and *H* represent the length, width, and height of the single regular pool, respectively. b_s is the width of the slot, l_B is the length of the lateral baffle, and b_0 is the width of the inlet lateral baffle and the T lateral baffle. l_l and l_b represent the length and the width of the T central baffle, respectively. b_t is the length of the T lateral baffle, and *d* is the distance between the slot and the T lateral baffle.

Tab. 1- Sizes of the seven fishway designs under study (D denotes "design")

D	l_l (m)	l_b (m)	l_B (m)	b_0 (m)	b_s (m)	*B* (m)	*H* (m)	b_t (m)	l_0 (m)	*d* (m)	*L* (m)	*B*/*L*
1	1.0	0.2	0.8	0.1	0.4	2.0	1.2	0.6	0.2	0.4	3.0	2/3
2								0.6	0.2	0.4	2.0	1/1
3								0.6	0.2	0.4	2.5	4/5
4								0.4	0.1	0.4	2.5	4/5
5								0.8	0.3	0.4	2.5	4/5
6								0.6	0.2	0.2	2.5	4/5
7								0.6	0.2	0.6	2.5	4/5

DOI 10.14311/CEJ.2019.02.0022

Numerical models

The governing equations in numerical models include the continuity, momentum, and *k-ε* equations [13], [14]. In this paper, the water density ρ was assumed to be a constant, $\rho = 10^3$ kg/m^3.

The continuity equation is written as:

$$\frac{\partial u}{\partial x}+\frac{\partial v}{\partial y}+\frac{\partial w}{\partial z}=0 \quad (1)$$

The momentum equations as:

$$\frac{\partial u}{\partial t}+u\frac{\partial u}{\partial x}+v\frac{\partial u}{\partial y}+w\frac{\partial u}{\partial z}=-\frac{1}{\rho}\frac{\partial p}{\partial x}+(\mu+\mu_t)(\frac{\partial^2 u}{\partial x^2}+\frac{\partial^2 u}{\partial x\partial y}+\frac{\partial^2 u}{\partial x\partial z}) \quad (2)$$

$$\frac{\partial v}{\partial t}+u\frac{\partial v}{\partial x}+v\frac{\partial v}{\partial y}+w\frac{\partial v}{\partial z}=-\frac{1}{\rho}\frac{\partial p}{\partial y}+(\mu+\mu_t)(\frac{\partial^2 v}{\partial x\partial y}+\frac{\partial^2 v}{\partial y^2}+\frac{\partial^2 v}{\partial y\partial z}) \quad (3)$$

$$\frac{\partial w}{\partial t}+u\frac{\partial w}{\partial x}+v\frac{\partial w}{\partial y}+w\frac{\partial w}{\partial z}=g-\frac{1}{\rho}\frac{\partial p}{\partial z}+(\mu+\mu_t)\left(\frac{\partial^2 w}{\partial x\partial z}+\frac{\partial^2 w}{\partial y\partial z}+\frac{\partial^2 w}{\partial z^2}\right) \quad (4)$$

And the *k-ε* equation as:

$$\frac{\partial k}{\partial t}+u\frac{\partial k}{\partial x}+v\frac{\partial k}{\partial y}+w\frac{\partial k}{\partial z}=\frac{\partial}{\partial x}\left(\frac{\mu_t}{\sigma_k}\frac{\partial k}{\partial x}\right)+\frac{\partial}{\partial y}\left(\frac{\mu_t}{\sigma_k}\frac{\partial k}{\partial y}\right)+\frac{\partial}{\partial z}\left(\frac{\mu_t}{\sigma_k}\frac{\partial k}{\partial z}\right)+\frac{G_k}{\rho}-\varepsilon \quad (5)$$

$$\frac{\partial \varepsilon}{\partial t}+u\frac{\partial \varepsilon}{\partial x}+v\frac{\partial \varepsilon}{\partial y}+w\frac{\partial \varepsilon}{\partial z}=\frac{\varepsilon}{k}C_{1\varepsilon}\frac{G_k}{\rho}-C_{2\varepsilon}\frac{\varepsilon^2}{k}+\frac{\partial}{\partial x}\left[\left(\mu+\frac{\mu_t}{\sigma_\varepsilon}\right)\frac{\partial \varepsilon}{\partial x}\right]+\frac{\partial}{\partial y}\left[\left(\mu+\frac{\mu_t}{\sigma_\varepsilon}\right)\frac{\partial \varepsilon}{\partial y}\right]$$
$$+\frac{\partial}{\partial z}\left[\left(\mu+\frac{\mu_t}{\sigma_\varepsilon}\right)\frac{\partial \varepsilon}{\partial z}\right] \quad (6)$$

Where,

$$G_k=\mu_t\{2\left[\left(\frac{\partial u}{\partial x}\right)^2+\left(\frac{\partial v}{\partial y}\right)^2+\left(\frac{\partial w}{\partial z}\right)^2\right]+\left(\frac{\partial u}{\partial y}+\frac{\partial v}{\partial x}\right)^2+\left(\frac{\partial u}{\partial z}+\frac{\partial w}{\partial x}\right)^2+\left(\frac{\partial v}{\partial z}+\frac{\partial w}{\partial y}\right)^2\} \quad (7)$$

$$\mu_t=\rho C_\mu\frac{k^2}{\varepsilon} \quad (8)$$

In Equations (1) – (8), *u, v,* and *w* represent the velocity in the *X*, *Y*, and *Z* direction, respectively, in units of m/s;

p is time-averaged pressure, in Pa;

μ and μ_t are the molecular viscosity coefficient and turbulence eddy viscous coefficient of the water, respectively, in m^2/s;

g is the acceleration of gravity in the *Z* direction, in m/s^2;

k is the turbulence kinetic energy, in m^2/s^2; *ε* is dissipation rate of the turbulence kinetic energy, in m^2/s^3;

σ_k and σ_ε are the Prandtl numbers corresponding to *k* and ε, respectively; $C_{1\varepsilon}$, $C_{2\varepsilon}$ and C_μ are empirical constants, with σ_k=1.0, σ_ε =1.3, $C_{1\varepsilon}$ =1.44, $C_{2\varepsilon}$ =1.92, and C_μ =0.09; and G_k is the generation term of the turbulence kinetic energy *k*, and it is caused by the mean velocity gradient.

Solution method and boundary conditions

The pressure implicit with splitting operators (PISO) method was used in this study, in which the "velocity inlet" is taken as the inlet boundary condition, and the value of the velocity is the average velocity taken from earlier experimental work [12]. The values of k and ε are taken as:

$$k=0.0144u_i^2 \quad (9)$$

$$\varepsilon=k^{0.5}/(0.5h_i) \quad (10)$$

In Equations (9) - (10), u_i and h_i are the velocity and the depth of the inlet, respectively. The hex-shaped grid was used in the entire model, and the time step was set as 0.002 s.

Mesh

In order to obtain a mesh-independent solution, a mesh-convergence analysis was carried out on the designs, and three block-structured meshes with different spatial resolutions were tested, namely Mesh-1, Mesh-2, and Mesh-3. The number of elements in each mesh was 48120, 95256, and 212254, and the average element size was 1.0067×10^{-3}, 5.032×10^{-4}, and 2.245×10^{-4} m^3. No significant differences were found in the results obtained using the two finer meshes (Mesh-2 and Mesh-3). Therefore, an average element size of 5.032×10^{-4} m^3 (Mesh-2) was adopted, with a slightly higher mesh density in the slot region.

RESULTS

In the case of gentle slope (S=2.6%, <10%), the main flow travels from one slot to the next through the pool as a two-dimensional curved flow [9][12]. Meanwhile, previous study has shown that the flow pattern in each pool is approximately the same for the most regular pools of the fishway, as mentioned before, and thus, Figures 2 (a) to (g) show the two-dimensional nephograms of the seven designs studied. Table 2 provides only the two-dimensional results of the third regular pool (pool 3) among the seven designs considered.

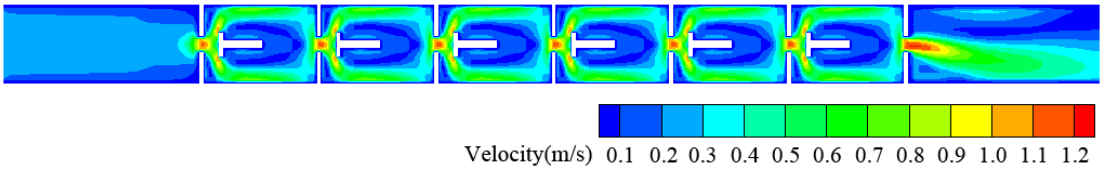

(a) - D1

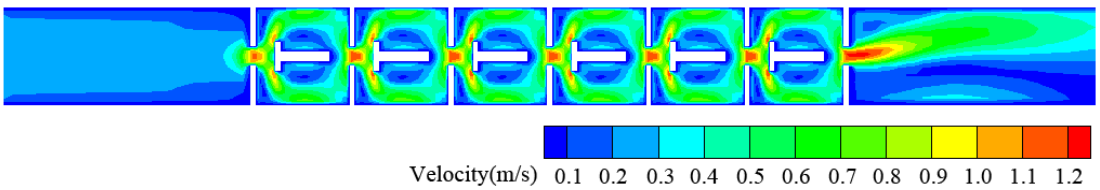

(b) - D2

Fig. 2 - Two-dimensional nephogram

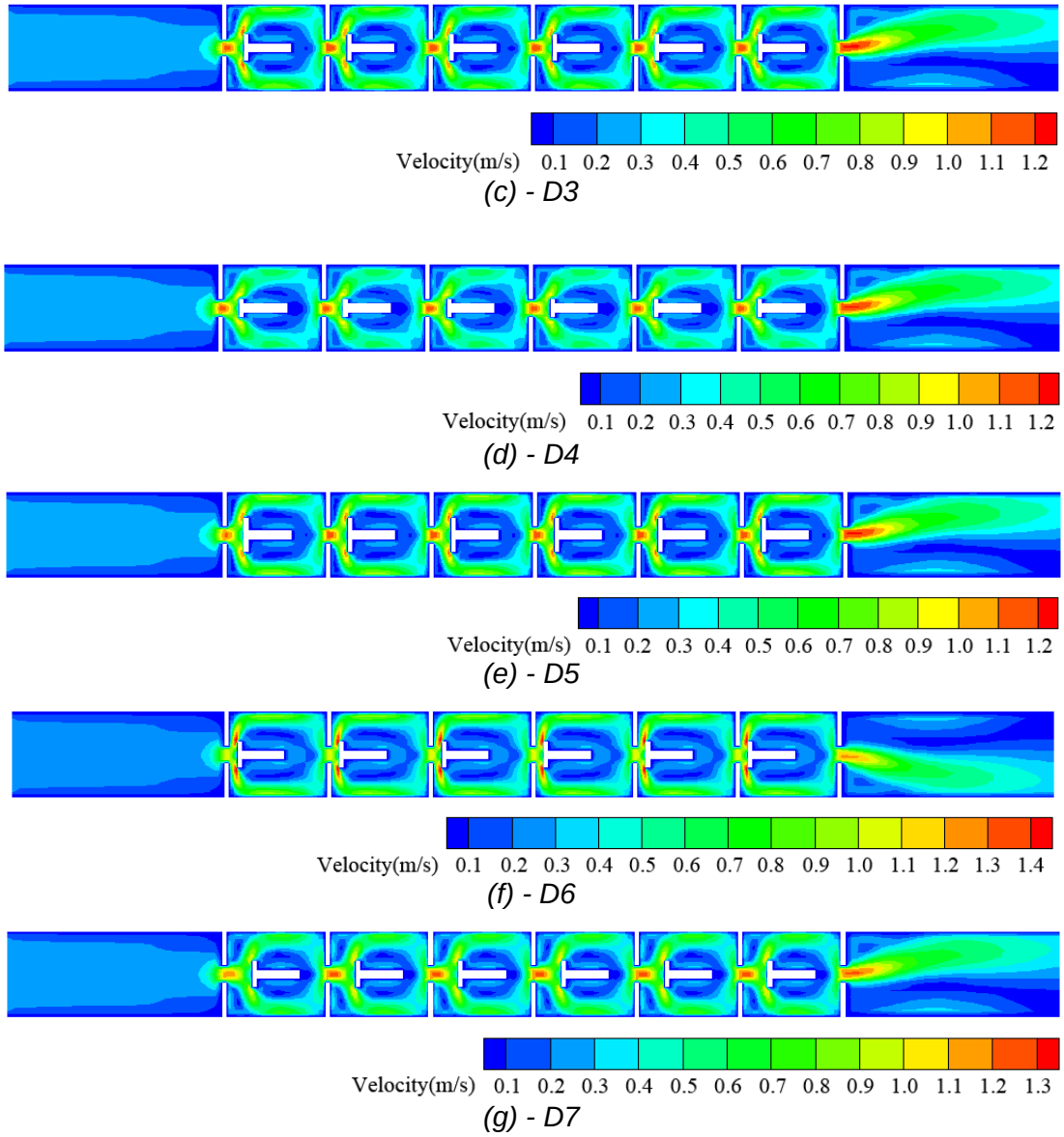

Fig. 2 - Two-dimensional nephogram

Under the given conditions, when the distance between the slot and the T lateral baffle was: (1) d=0.4 m (for D1–D5), the maximum velocity was approximately 1.2 m/s, as shown in Figure 2 (a)-(e); (2) d=0.2 m (for D6), the maximum velocity was approximately 1.4 m/s, as shown in Figure 2 (f); (3) d=0.6 m (for D7), the maximum velocity was approximately 1.3 m/s, as shown in Figure 2 (g).

Table 2 lists the two-dimensional results for pool 3, where X/b_s is the specific value between the X value and the width of the slot, b_s, V is the maximum velocity and the Y value indicates the location of V. V_a is the average velocity of the slot section (X=0), and V/V_a is the specific value between the maximum velocity of each section and the average velocity of the slot section.

According to the data of Table 2, the maximum velocity points in each column for the seven designs studied can be given, as shown in Figures 3 (a) and (b).

Tab. 2- Two-dimensional results of pool 3 in D1–D7 (D denotes "design")

D	V_a (m/s)	X (m)	Y (m)	V (m/s)	X/b_s	V/V_a	X (m)	Y (m)	V (m/s)	X/b_s	V/V_a
D1	1.03	0	1.12	1.04	0	1.01	0.5	0.61	1.08	1.25	1.05
		1	0.09	0.74	2.5	0.72	1.5	0.08	0.75	3.75	0.73
		2	0.08	0.67	5	0.65	2.5	0.08	0.49	6.25	0.48
D2	1.05	0	1.12	1.08	0	1.03	0.5	0.61	1.12	1.25	1.07
		1	0.09	0.76	2.5	0.72	1.5	0.08	0.62	3.75	0.59
		2	0.96	1.01	5	0.97	2.1	1.04	1.18	5.25	1.13
D3	1.03	0	1.12	1.05	0	1.02	0.5	0.61	1.1	1.25	1.07
		1	0.09	0.75	2.5	0.73	1.5	0.08	0.74	3.75	0.72
		2	0.08	0.48	5	0.47	2.5	0.96	1.16	6.25	1.13
D4	1.03	0	1.12	1.04	0	1.01	0.5	0.7	1.01	1.25	0.5
		1	0.11	0.51	2.5	0.5	1.5	0.13	0.53	3.75	0.52
		2	0.19	0.35	5	0.34	2.5	0.96	1.14	6.25	1.11
D5	1.03	0	1.12	1.05	0	1.02	0.5	0.53	1.05	1.25	1.02
		1	0.08	0.84	2.5	0.82	1.5	0.08	0.8	3.75	0.78
		2	0.07	0.54	5	0.52	2.5	0.96	1.16	6.25	1.13
D6	1.02	0	1.12	1.06	0	1.04	0.5	0.09	0.76	1.25	0.74
		1	0.08	0.97	2.5	0.95	1.5	0.08	0.89	3.75	0.87
		2	0.08	0.62	5	0.61	2.5	1.04	1.07	6.25	1.04
D7	1.05	0	1.12	1.07	0	1.02	0.5	0.95	0.81	1.25	0.78
		1	0.09	0.63	2.5	0.6	1.5	0.08	0.76	3.75	0.73
		2	0.08	0.52	5	0.5	2.5	0.96	1.2	6.25	1.15

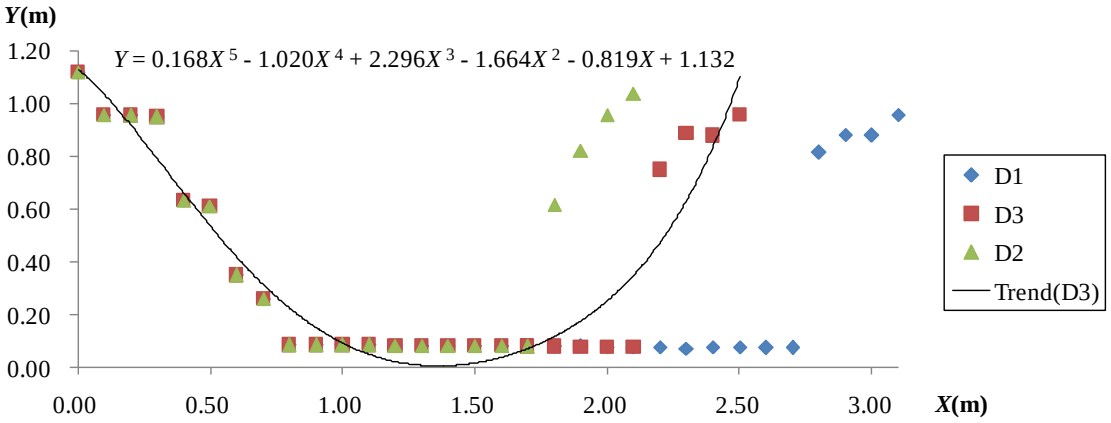

Fig. 3 (a) - Maximum velocity points in each column (D1–D3)

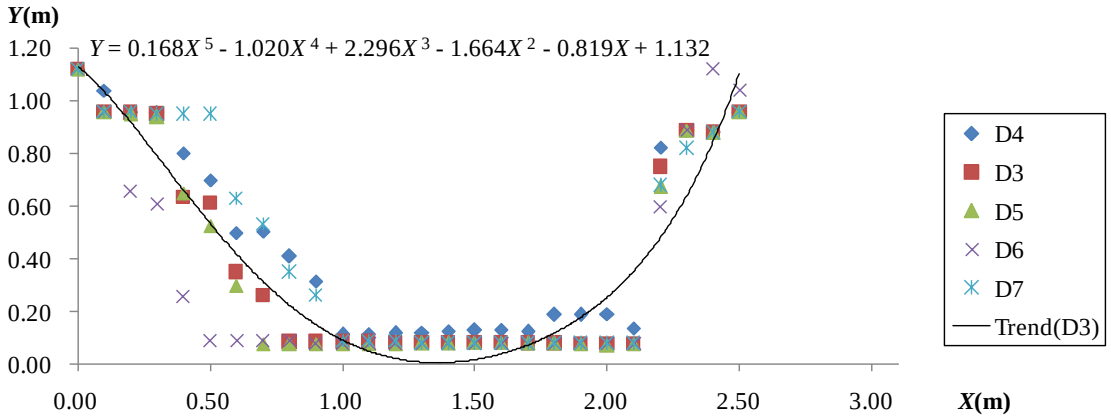

Fig. 3 (b) - Maximum velocity points in each column (D3–D7)

The trajectory equation of the maximum velocity line was defined to indicate the location of the maximum velocity (V) in each column. According to Table 2 and Figures 3 (a) and (b), the trajectory equation of the maximum velocity lines of the T shape fishways can be described as a "U" shape line, and can be expressed by the trend line of $D3$: $Y=0.168X^{5}-1.020X^{4}+2.296X^{3}-1.664X^{2}-0.819X+1.132$. The water is blocked by the T shape baffle after entering the slot of the regular pool, and then it symmetrically flows downstream from both sides of the T shape baffle.

According to the data of Table 2, the relationship between X/b_s and V/V_a can be given, as shown in Figures 4 (a) and (b).

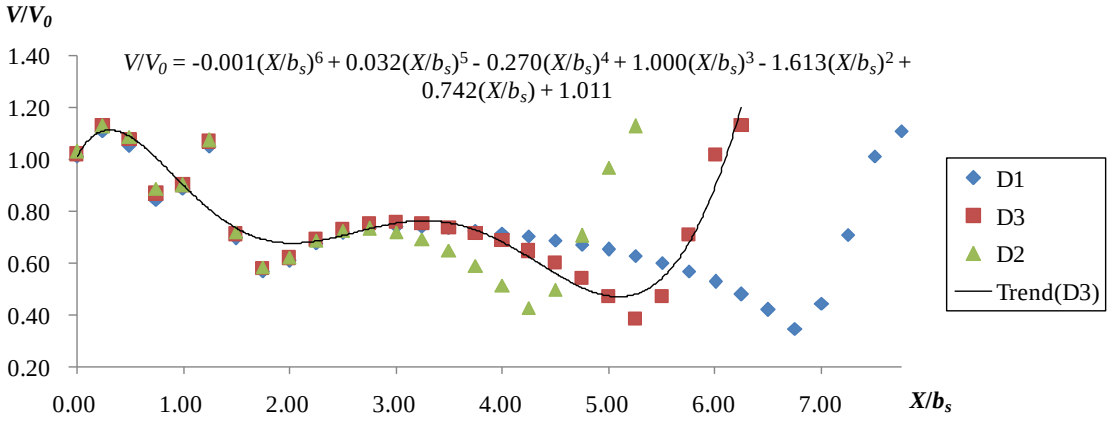

Fig. 4 (a) - Relationship between X/b_s and V/V_a (D1–D3)

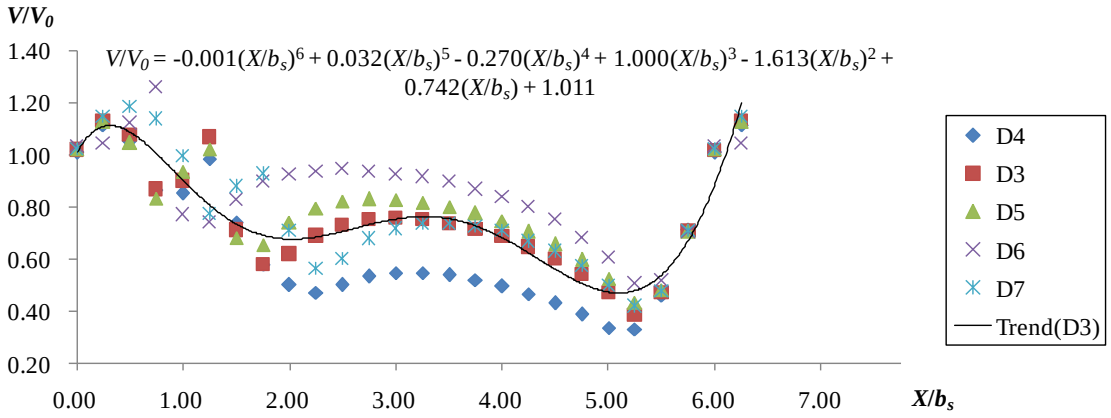

Fig. 4 (b) - Relationship between X/b_s and V/V_a (D3–D7)

The V/V_a equation was defined to indicate the ratio of the maximum velocity to the average velocity. According to Table 2 and Figure 4, the V/V_a equation of the T shape fishways can be described as a "W" shape line, and can be expressed by the trend line of *D*3: $V/V_a=-0.001(X/b_s)^6+0.032(X/b_s)^5-0.270(X/b_s)^4+1.000(X/b_s)^3-1.613(X/b_s)^2+0.742(X/b_s)+1.011$.

DISCUSSION

(1) The overall length of the seven designs was 24.5 m. According to Table 1, the length of the single regular pool of D3 was L=2.5 m, while the length of the single regular pool of D1 was L=3.0 m and the length of the single regular pool of D2 was L=2.0 m. As a result, the length of the transition pool of D3 was about 2 times that of the regular pool (about 4.8 m), while the length of the transition pool of D1 was approximately equal to the regular pool (about 3.2 m), and the length of the transition pool of D2 was about 3 times that of the regular pool (about 6.3 m). According to the literature [15], the appropriate size of the recirculation area can provide a resting place for fish, while an overly large area of recirculation will cause the fish to lose their way. Consequently, from Figures 2 (a)–(c) we can see, compared to D3 that the area of the recirculation zone in D1 was much larger and, in D2, was much smaller. Therefore, D3 is better than D1 and D2 in terms of the length of the regular pool.

(2) The length of the T lateral baffle was b_t=0.6, 0.4, and 0.8 m in D3, D4, and D5, respectively, as shown in Table 1. Figures 2 (c)–(e) show that the area of the recirculation zone in D4 was much

smaller compared to D3. The area of the recirculation zone in D5 was almost the same, compared to that in D3, but the cost of construction was greater than that of D3. Thus, D3 is better than D4 and D5 in terms of the length of the T lateral baffle, as well as in terms of the cost of construction.

(3) The distance between the slot and the T lateral baffle was d=0.4, 0.2, and 0.6 m in D3, D6, and D7, respectively, as shown in Table 1. Figures 2 (c), (f), and (g) show that the maximum velocity in D6 and D7 was larger than in D3. Therefore, D3 is better than D6 and D7 in terms of the distance between the slot and the T lateral baffle.

(4) The data in Table 2 and Figure 4 show that the maximum V/V_a was approximately 1.26 when X/b_s was approximately 0.75, which was near the T shape baffle; the minimum V/V_a was approximately 0.33 when X/b_s was approximately 5.25.

CONCLUSION

In this paper, the author presented the results of a numerical study of the hydraulics of T shape fishways that were constructed using seven different structural designs.

In the pools of T shape fishways, water is blocked by the T shape baffle after entering the slot of the regular pool, and then it symmetrically flows downstream from both sides of the T shape baffle.

The trajectory equation of the maximum velocity line of T shape fishways can be expressed as: $Y=0.168X^5-1.020X^4+2.296X^3-1.664X^2-0.819X+1.132$.

The V/V_a equation of T shape fishways can be expressed as: $V/V_a=-0.001(X/b_s)^6+0.032(X/b_s)^5-0.270(X/b_s)^4+1.000(X/b_s)^3-1.613(X/b_s)^2+0.742(X/b_s)+1.011$. Under the given conditions, the range of V/V_a was found to be between 0.33 and 1.26 ($0.33 \le V/V_a \le 1.26$); that is, for the seven different T shape fishway designs considered, the maximum and minimum values of the velocity can be calculated approximately as long as the average velocity of the slot section is known. In addition, the migratory requirements can be simultaneously checked, as to whether they satisfy the fish or not.

Of the seven designs studied, design 3 (D3) was found to be the most suitable design in terms of helping fish migrate the fishway efficiently. For D3, l_l=1.0 m, l_b=0.2 m, l_B=0.8 m, b_0=0.8 m, b_s=0.4 m, B=2.0 m, H=1.2 m, b_t=0.6 m, l_0=0.2 m, d=0.4 m, and L=2.5 m. According to the results, $d=b_s$, $b_t=1.5b_s$, $B=5b_s$, $L=6.25b_s$, and B/L= 4/5 are very satisfactory parameters for the dimensional design of T shape fishways.

ACKNOWLEDGEMENTS

This study was supported by Education Department of Sichuan Province (035Z1994), and by Sichuan Agricultural University (065H0600, 1921993122).

REFERENCES

[1] Food Agriculture Organization, 2002. Fish passes: design, dimensions and monitoring (Rome, FAO, in arrangement with DVWK) 119 pp.

[2] Mao X., 2018. Review of Fishway Research in China. Ecological Engineering, vol. 115: 91-95.

[3] Schwalme K., Mackay W., Lindner D., 2011. Suitability of Vertical Slot and Denil Fishways for Passing North-Temp, Canadian Journal of Fisheries & Aquatic Sciences, vol. 42: 1815-1822.

[4] Mallen-Cooper M., Stuart I., 2007. Optimising Denil fishways for passage of small and large fishes, Fisheries Management & Ecology, vol. 14: 61-71.

[5] Schwalme K., Mackay W. C., Lindner D., 1985. Suitability of Vertical Slot and Denil Fishways for Passing North-Temperate, Nonsalmonid Fish, Canadian Journal of Fisheries and Aquatic Sciences, vol. 42:1815-1822.

[6] Fuentes-Pérez J., Sanz-Ronda F., Azagra A., García-Vega A., 2016. Non-uniform hydraulic behavior of pool-weir fishways: a tool to optimize its design and performance, Ecological Engineering, vol. 86: 5-12.
[7] Larinier M. et al., 2002. Fishways: biological basis , design criteria and monitoring (Rome, FAO of the United Nations, DVWK) 208pp.
[8] Landsman S. J., Mclellan N., Platts J., Heuvel M., 2018. Nonsalmonid versus Salmonid Passage at Nature-Like and Pool-and-Weir Fishways in Atlantic Canada, with Special Attention to Rainbow Smelt, Transactions of the American Fisheries Society, vol. 147: 94-110.
[9] Wu S., Rajaratnam N., Katopodis C.,1999. Structure of Flow in Vertical Slot Fishway, Journal of Hydraulic Engineering, vol. 125: 351-360.
[10] Quaranta E., Katopodis C., Comoglio C., 2019. Effects of bed slope on the flow field of vertical slot fishways, River Research and Applications, vol. 35: 1-13.
[11] Stamou A. I., Mitsopoulos G., Rutschmann P., Bui M., 2018. Verification of a 3D CFD model for vertical slot fish-passes, Environmental Fluid Mechanics, vol. 18: 1435 –1461.
[12] Mao X., Fu J., Tuo Y., An R., Li J., 2012. Influence of structure on hydraulic characteristics of T shape fishway, Journal of Hydrodynamics, vol. 24: 684 – 691.
[13] John A., 1995. Computational fluid dynamics: the basics with applications (McGraw-Hill, New York, USA) 381pp.
[14] Oberkampf W. L., Trucano T. G., 2007. Verification and validation in computational fluid dynamics, Advances in Mechanics, vol. 38: 209-272.
[15] Mao X., 2015. Study of Fish-friendly Fishway Hydraulics in Mountainous Rivers of Southwest China (Sichuan University, Chengdu, China, in Chinese), PhD Thesis.

Article no. 23

THE CIVIL ENGINEERING JOURNAL 2-2019

MULTI-OBJECTIVE OPTIMIZATION OF SUPPORTING PLAN FOR DEEP FOUNDATION USING ENTROPY-BASED UM-DEA

*Shi Huawang, Du Jingkun and Yang Jing**

*Hebei University of Engineering, Department of Civil Engineering, Handan, China; stone21st@163.com, 81158626@qq.com, *shw2016@sohu.com*

ABSTRACT

In regard to optimize the supporting plan of deep foundation pit, this paper used the unascertained measurement (UM) and data envelopment analysis (DEA) to conduct. In order to determine the relationship between influencing factors and the best bid plan, an evaluation model for deep foundation pit support schemes based on UM was developed. First, the information entropy (IE) was introduced to determine the weight of discriminant indices which consider the confidence identification criteria as the judgment principle of evaluation. Then, the optimal solution from all feasible support schemes was investigated. Finally, Fuzzy comprehension assessment-data envelopment analysis (FCA-DEA) was utilized to analyse the effectiveness of design plans, which was evaluated by UME subsequently. Applicability of the proposed UM-DEA model was tested with four real design cases of foundation projects. Results compared with other methods have shown the developed model is useful for concept design and decision making of supporting plan for deep foundation.

KEYWORDS

Deep foundation pit, Unascertained measurement evaluation, Data envelopment analysis, Information entropy

INTRODUCTION

With the rapid development of civil engineering projects, deep foundation pit construction with large amounts of land and the complicated influence of surrounding environment is becoming much more common. Deep foundation pit construction is the key and basis of building construction. Its safety and reliability has direct relationship with high-rise building's safety, stability and longevity. The successful level of any foundation construction projects can be argued to construct largely on selecting the most competent design plan. Accordingly, the selection of a design plan is one of the most important issues in construction projects. The complexity of foundation projects with comprehensive and uncertain conditions result in the process of design becoming a research topic which is full of high difficulty and high risk. The accident rate of the deep foundation pit engineering in high-rise buildings accidents accounted for nearly 10%. Both the economic losses and threat to safety of the workers are also serious [1,2]. Therefore, how to choose the best supporting system of deep foundation pit is closely related to the safety and economy of the whole project. In the design phase of deep foundation pit engineering, firstly, several kinds of feasibility supporting schemes are provided by experts [3]. Then, selecting the most appropriate plan for deep foundation pit is the most important issue. The optimization of each plan of the deep foundation pit supporting scheme will be evaluated and selected according to multiple targets [4,5].

To address those issues, this research rigorously identified the main influence factors affecting the selection process to incorporate criteria other than the factors inherited in foundation

project. The influential criteria were selected based on experts' opinions and the ideas from the literature. And UM and entropy were utilized to address the uncertainty and interdependency among criteria [6,7]. The entropy is a powerful tool that can quantify the uncertainty inherited in respondents' weighting of criteria to decrease the subjective and arbitrary decisions. Then, DEA[8,9] was introduced to evaluate the effectiveness of the plan selected and identified the relationship between criteria and results. Finally, a model which can select the most appropriate design support schemes for deep excavation was developed with using those tools. And the validity of the proposed model was tested with real cases.

METHODS

The developed methodology, as shown in Figure1, starts with a brief literature review to illustrate varies of approaches utilized by researchers for design plan selection methods of deep foundation projects.

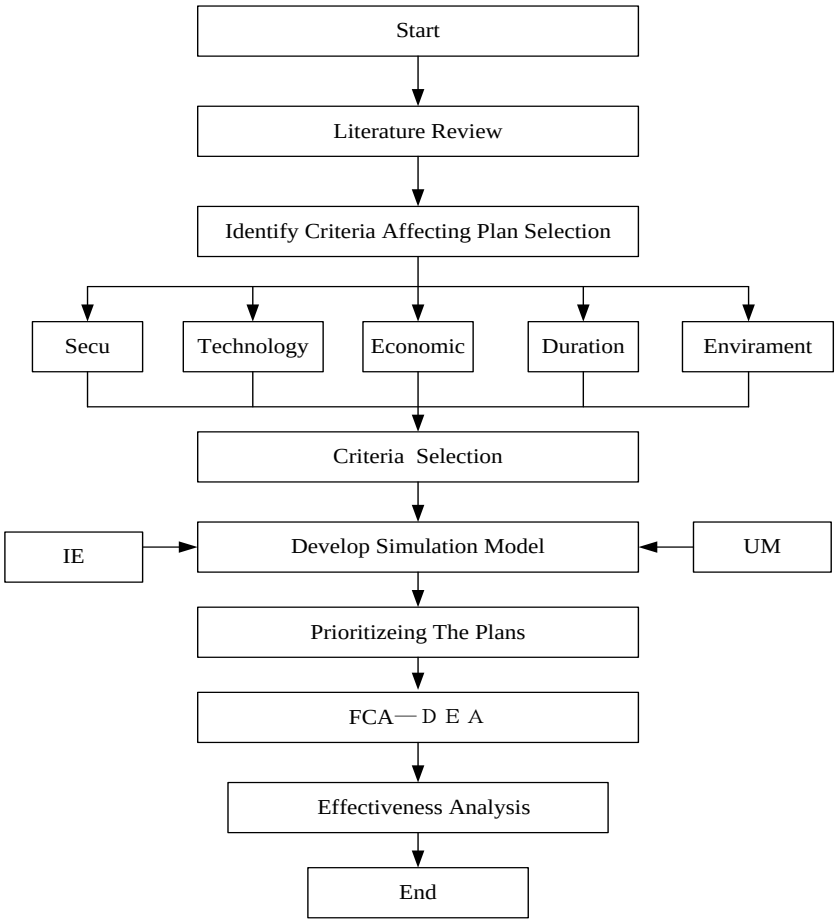

Fig.1- Research techniques

The criteria needed were selected from two stages. The first stage was prepared from the literature requesting, thereafter, experts specialized in the safety, economy, environment, duration and quality to fill out a form that asked for a list of the most influential criteria in design plan selection. When the most important affected criteria of deep foundation design plan selection were identified, according to the collected data, relative weights of criteria were determined using the IE technique. The criteria weights obtained from IE analysis were then used as input for the proposed simulation model for deep foundation design plan selection based on UM. Finally, the developed

model was tested using case foundation projects, and an effective analysis was conducted to show the effectiveness of outputs to any changes in the inputs. This integration considered factors' interdependency (using UM), made decisions under uncertainty (using simulation/UM), and handled decisions that involved large numbers of variables.

The uncertainty measure theory is different from fuzzy mathematics, grey theory and the random information, and it is a kind of new uncertainty theory[10,11].In the model, there are n evaluate samples that can be expressed using $x_1, x_2, \ldots x_n$, and the sample space can be used $U = \{x_1, x_2, \ldots, x_n\}$ to express. Any object x_i consists of m evaluation indexes. And the index space can be used $I = (I_1, I_2, \ldots, I_m)$ to express, when $x_i \in U$, x_{ij} is the observed values I_j of j index in the sample x_i, the evaluation space can be used $L = (L_1, L_2, \ldots, L_k)$ to express, L_k = the k th grade, $1 \le k \le K$, where, K is grade of evaluation.

Single-index uncertainty measure

If there is a fixed object $x_i \in U$ and an indicator I_j, the observed value of x_i for I_j can be expressed by x_{ij}, when the map μ exists, A is the arbitrary set, and the object is subject to satisfy:

$$\mu_{\bigcup_c A_c} = \sum_{c=1} (x_{ij}) \tag{1}$$

$$0 \le \mu_A(x_{ij}) \le 1 \tag{2}$$

$$\mu_U(x_{ij}) = 1 \tag{3}$$

Where, i=1,2..., n, j=1,2...,m, the formula (1) is expressed "additive property "; the formula(2) is expressed "nonnegative bounded "; the formula (3) is expressed "polarity ". When the above three kinds of characteristics are satisfied, can $\mu_A(x_{ij})$ be called uncertainty measure function, namely measure.

According to the principle of the uncertainty measure, abiding by the law of the curve of the index, we construct a suitable single index measure function:

$$\mu_i = \begin{pmatrix} \mu_{i11} & \mu_{i12} & \cdots & \mu_{i1k} \\ \mu_{i21} & \mu_{i22} & \cdots & \mu_{i2k} \\ \vdots & \vdots & \ddots & \vdots \\ \mu_{im1} & \mu_{im2} & \cdots & \mu_{imk} \end{pmatrix} = (\mu_{ijk})_{m \times n} \tag{4}$$

Determination for weight of index

The entropy method is a kind of objective weighting method, and the index weight can be calculated by the size of information through each indicator contained. The entropy method determines index weight by the relationship between the original data to decrease the subjective and arbitrary decisions, so the overall evaluation results are more objective [12].

When the measurement value x_{ij} and evaluation index are given, the measured value of the attribute is given, and each weight is calculated by the measured value. According to the theory of information entropy, the weight of index is determined:

$$v_{ij} = 1 + \frac{1}{\log k} \sum_{k=1}^{K} \mu_{ijk} \log \mu_{ijk} \tag{5}$$

In the formula, the size of v_{ij} can reflect the importance or match the index I_j, then the weight of the index I_j is defined as:

$$w_j = v_{ij} / \sum_{j=1}^{m} v_{ij}, \quad 0 \le w_j \le 1, \quad \sum_{j=1}^{m} w_j = 1 \tag{6}$$

Multi index comprehensive measure matrix

The single-index uncertainty measure can be calculated by formula (4), and the weight vector of the index can be calculated by formula (5) and formula (6):

$$p = w_j \bullet (\mu_{ijk})_{m \times n} \tag{7}$$

Multi index comprehensive measure matrix can be expressed by $P = (P_1, P_2, \ldots, P_k)$.

Confidence criterion

Introducing "confidence" as the recognition criteria, according to the confidence threshold value λ ($\lambda \ge 0.5$, usually in the range of [0.6, 0.8].

$$k_0 = \min_k \left(k : \sum_{l=1}^{k} \mu_{il} \ge \lambda \ , \ 1 \le k \le K \right) \tag{8}$$

Then the evaluation results are considered as the L_{k_0} evaluation grades of k_0.

Priority ranking

When $L_1 > L_2 > \cdots > L_k > \cdots > L_K$, the assignment of L_t is C_t, and $C_t > C_{t+1}$, then:

$$Q_{R_i} = \sum_{i=1}^{K} C_t \mu_{ik} \tag{9}$$

Q_{R_i} is the degree of uncertainty of the evaluation scheme R_i, $Q = \{Q_{R_1}, Q_{R_2}, \cdots Q_{R_n}\}$ is called the vector of the degree of uncertainty, according to its superior ranking.

Effective analysis of design scheme based on FCA-DEA

Using the method of the evaluation of the uncertainty measure, a set of comprehensive measures evaluation can be ranked, and the optimal design plan could be obtained. However, when making a plan decision, only the pros and cons of each obtained design plan may not be sufficient, the following questions are more important. What is insufficient of each design scheme is that it cannot make sure whether can we turn it into effective suitable design plan, etc. This paper introduces the method of data envelopment analysis to deal with these problems.

If there are n design plans for a project, and p is used to represents any plan, i indicates analysis index. The single-index uncertainty measure matrix is $\{\mu_{ijk}^{(p)}\}_{n \times m}$, $\mu_{ijk}^{(p)} \in [0,1]$.

Based on the theory of uncertainty measure, $\{\mu_{i1k}{}^{(p)} / \sum_{j=1}^{c} \mu_{ijk}{}^{(p)}, \mu_{i2k}{}^{(p)} / \sum_{j=1}^{c} \mu_{ijk}{}^{(p)}, \ldots, \mu_{ijk}{}^{(p)} / \sum_{j=1}^{c} \mu_{ijk}{}^{(p)}\}$ is got for basic distribution information of all the results evaluated by the scheme p relative to the index i. According to the information entropy, the total value $Q_i{}^{p}$ of index i can be calculated as follows:

$$Q_i{}^{p} = \sum_{j=1}^{c} \frac{\mu_{ijk}{}^{(p)}}{\sum_{t=1}^{c} \mu_{itk}{}^{(p)}} w_j = \frac{\sum_{j=1}^{c} \mu_{ijk}{}^{(p)} w_j}{\sum_{j=1}^{n} \mu_{ijk}{}^{(p)}} \tag{10}$$

Where $Q_i{}^{p} = \mu_{ijk}{}^{(p)}$ and $Q^{p} = (Q^{p}{}_1, Q_2{}^{p}, \ldots, Q_i{}^{p})$ indicates that the characteristics and status of each indicator of the plan p. According to the production theory in DEA, the possible compositions of the production mainly contain three conditions: convex, non-effective and minimal. The set needed is:

$$LDT = \{y \mid y_i \le \sum_{p=1}^{n} \frac{\sum_{j=1}^{c} \mu_{ijk}{}^{(p)} w_j}{\sum_{j=1}^{c} \mu_{ijk}{}^{(p)}} \lambda_p\},\ i = 1, 2, \ldots n, \sum_{p=1}^{n} \lambda_p = 1 \tag{11}$$

According to formula (11), we can define supporting scheme FCA-DEA effectiveness. Three theorems are given as follows:

Theorem 1: The design scheme p_0 for the FCA-DEA is valid when and only if

$$(F-D)\begin{cases} \min\left[\varphi - \sum_{i=1}^{n} \frac{\sum_{j=1}^{c} \mu_{ijk}{}^{(p_0)} w_j}{\sum_{j=1}^{c} \mu_{ijk}{}^{(p)}} U_i\right] = V_{F-D} \\ s.t. \varphi - \sum_{i=1}^{n} \frac{\sum_{j=1}^{c} \mu_{ijk}{}^{(p_0)} w_j}{\sum_{j=1}^{c} \mu_{ijk}{}^{(p)}} U_i \le \varphi \\ \sum_{i=1}^{n} U_i = 1, U_i \ge 0, i = 1, 2, \ldots, n \\ p = 1, 2, \ldots, n \end{cases} \tag{12}$$

Theorem 2: The design scheme p_0 for the FCA-DEA is valid when and only if the optimal value is: $V_{F-DD} = 0$.

$$(F-DD)\begin{Bmatrix} \min(-e^t s) = V_{F-DD} \\ s.t.\sum_{p=1}^{n} \dfrac{\sum_{j=1}^{c} \mu_{ijk}{}^{(p)} w_j}{\sum_{j=1}^{c} \mu_{ijk}{}^{(p)}} \lambda_x - s_i = \dfrac{\sum_{j=1}^{c} \mu_{ijk}{}^{(p_0)} w_j}{\sum_{j=1}^{c} \mu_{ijk}{}^{(p_0)}} i = 1,2,...,n \\ \sum_{p=1}^{n} \lambda_p = 1, \lambda \geq 0, s \geq 0 \end{Bmatrix} \quad (13)$$

Theorem 3: If the plan p_0 does not satisfy the FCA-DEA, the optimal solution of $(F-DD)$ is $\bar{\lambda}, \bar{s}$, then the $Q^{p_0} + \bar{s}$ must be able to achieve FCA-DEA effective.

Where, $(F-D)$ and $(F-DD)$ are the fuzzy decision of multi-objective optimization and the duality problem of $(F-D)$, respectively. From the above three theorems, we can construct the DEA model, carry out the scheme of FCA-DEA validity analysis.

RESULTS

Affected criteria of design plan selection

This project included the construction of an area of 8100m^2 underground car park with depth of 6.2m. In the direction of east, west and south, project site is adjacent to highway, office building is away from about 15m in the north direction, and there is an athlete field in the north-west direction. The influence of the building, road, underground lines and the plenum of the pipeline is affected by the settlement. Soil is composed of plain fill, fine sand, silt, fine sand, silty soil and there is strong weathered mudstone from top to bottom. Engineering geological conditions and characteristics are shown in Table 1.

Tab. 1- Engineering geological condition and characteristics

Soil classification	Soil characteristics	Soil thickness(m)	Indicators		
			Soil gravity γ (kN/m³)	Internal friction angle φ(°)	Cohesion C(kPa)
Plain fill	Made up of sand, gravel, clay	2.5	17.2	15	10
Fine sand	Containing 20% of silt, loose, saturated	2.5	17.8	30	6
Silt	Dark grey, plastic flow, saturated	4	16.8	12	5
Sand	Gray, little compaction saturated	2.6	19.0	30	6
Silty clay	Containing a small amount of powder sand, hard plastic	1.6	16.9	25	30

According to the main characteristics of foundation pit engineering, there are some ideas which are suitable for the primary support scheme: (1) Dense rows of bored piles with reinforced concrete interior support + single row deep mixing pile cut-off wall; (2) Retaining structure with double row piles and single row deep mixing pile cut-off wall; (3) Spraying the anchor net supporting + single row deep layer mixing pile cut-off wall; (4) Arching cement soil + steel casing drilling pile space combination support.

Following the model testing methodology, the below main characteristics need to be considered: the influence factors of the surrounding environment, engineering geology and hydro geology of the foundation pit of the engineering project, the safety, economy, environment, duration and quality, as shown in Figure2, were determined based on the selected criteria and sub criteria.

According to relevant specification and documents [9], etc., index values of deep excavation were determined, as shown in Table 2, therefore, through formula (1)-(4), the main technical and economic index values were calculated, as shown in Table 3.

Tab. 2 - Standard values of selection criteria

Criteria	Excellent	Good	Poor	Very poor
Reliability of construction technology $\mathbf{C_1}$	≥1	[0.85,0.95]	[0.75,0.85]	≤0.75
Coefficient of safety stability） $\mathbf{C_2}$	≥2	[1.7,1.9]	[1.5,1.7]	≤1.5
Difficulty of construction $\mathbf{C_3}$	≤0.7	[0.7,0.8]	[0.8,0.9]	≥1
Reliability of design theory $\mathbf{C_4}$	≥1	[0.85,0.95]	[0.75,0.85]	≤0.75
Comprehensive cost $\mathbf{C_5}$	≤200	[200,225]	[225,275]	≥300
Surrounding buildings $\mathbf{C_6}$	≤0.7	[0.7,0.8]	[0.8,0.9]	≥1
Surrounding distribution utilities and underground structures and utilities $\mathbf{C_7}$	≤0.7	[0.7,0.8]	[0.8,0.9]	≥1
Surrounding road transportation $\mathbf{C_8}$	≤0.7	[0.7,0.8]	[0.8,0.9]	≥1
Construction duration $\mathbf{C_9}$	≤30	[30,40]	[40,60]	≥70
Maximum horizontal Displacement $\mathbf{C_{10}}$	≤20	[20,25]	[25,35]	≥40
Effectiveness of precipitation $\mathbf{C_{11}}$	≥1	[0.85,0.95]	[0.75,0.85]	≤0.75
Waterproof effects $\mathbf{C_{12}}$	≥1	[0.85,0.95]	[0.75,0.85]	≤0.75

Tab. 3 - Technical and economic values of schemes

Criteria	Excellent	Good	Poor	Very poor
$\mathbf{C_1}$	0.90	1.00	0.80	0.95
$\mathbf{C_2}$	1.68	1.83	1.95	1.89
$\mathbf{C_3}$	0.95	0.85	1.00	0.90
$\mathbf{C_4}$	1.00	1.00	0.70	0.90
$\mathbf{C_5}$	335.10	283.70	252.30	223.90
$\mathbf{C_6}$	0.95	0.85	0.95	0.80
$\mathbf{C_7}$	0.95	0.85	0.90	0.80
$\mathbf{C_8}$	0.95	0.80	0.95	0.80
$\mathbf{C_9}$	65.00	60.00	70.00	40.00
$\mathbf{C_{10}}$	47.00	26.00	29.00	34.00
$\mathbf{C_{11}}$	0.90	0.87	0.85	0.83
$\mathbf{C_{12}}$	0.93	0.92	0.90	0.80

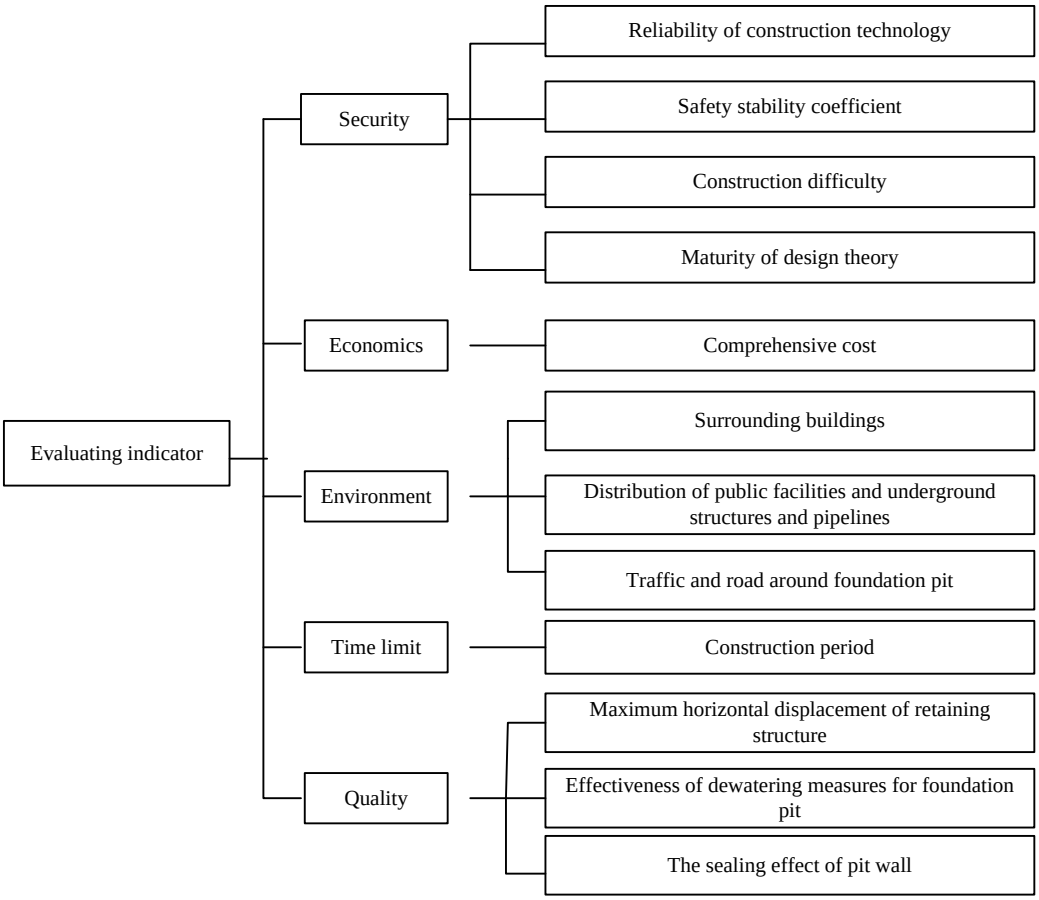

Fig. 2. Selection for Criteria Affecting Plan

Determination of single-index measure matrix

Through the classification of all the individual indicators, the evaluation level can be considered as excellent, good, poor and very poor. The main technical and economic indexes of each plan were obtained through the investigation of experts, and the single-index of the four kinds of supporting schemes was calculated as follows:

$$(\mu_{1jk})_{12\times4}=\begin{pmatrix}0 & 0.5 & 0.5 & 0\\ 0 & 0 & 0.9 & 0.1\\ 0 & 0 & 0.5 & 0.5\\ 1 & 0 & 0 & 0\\ 0 & 0 & 0 & 1\\ 0 & 0 & 0.5 & 0.5\\ 0 & 0 & 0.5 & 0.5\\ 0 & 0 & 0.5 & 0.5\\ 0 & 0 & 0.5 & 0.5\\ 0 & 0 & 0 & 1\\ 0 & 0.5 & 0.5 & 0\\ 0 & 0.8 & 0.2 & 0\end{pmatrix} \quad (\mu_{2jk})_{12\times4}=\begin{pmatrix}1 & 0 & 0 & 0\\ 0 & 0.65 & 0.35 & 0\\ 0 & 0.5 & 0.5 & 0\\ 1 & 0 & 0 & 0\\ 0 & 0 & 0.652 & 0.348\\ 0 & 0.5 & 0.5 & 0\\ 0 & 0.5 & 0.5 & 0\\ 0 & 1 & 0 & 0\\ 0 & 0 & 1 & 0\\ 0 & 0.9 & 0.1 & 0\\ 0 & 0.2 & 0.8 & 0\\ 0 & 0.7 & 0.3 & 0\end{pmatrix}$$

$$(\mu_{3jk})_{12\times4}=\begin{pmatrix} 0 & 0 & 0.5 & 0.5 \\ 0.5 & 0.5 & 0 & 0 \\ 0 & 0 & 0 & 1 \\ 0 & 0 & 0 & 1 \\ 0 & 0.454 & 0.546 & 0 \\ 0 & 0.5 & 0.5 & 0 \\ 0 & 0 & 1 & 0 \\ 0 & 0.5 & 0.5 & 0 \\ 0 & 0 & 0 & 1 \\ 0 & 0.6 & 0.4 & 0 \\ 0 & 0 & 1 & 0 \\ 0 & 0.5 & 0.5 & 0 \end{pmatrix} (\mu_{4jk})_{12\times4=}\begin{pmatrix} 0 & 1 & 0 & 0 \\ 0 & 0.95 & 0.05 & 0 \\ 0 & 0 & 1 & 0 \\ 0 & 0.5 & 0.5 & 0 \\ 0.044 & 0.956 & 0 & 0 \\ 0 & 1 & 0 & 0 \\ 0 & 1 & 0 & 0 \\ 0 & 1 & 0 & 0 \\ 0 & 1 & 0 & 0 \\ 0 & 0.1 & 0.9 & 0 \\ 0 & 0 & 0.8 & 0.2 \\ 0 & 0 & 0.5 & 0.5 \end{pmatrix}$$

Where, $(\mu_{ijk})_{12\times4}$, $(\mu_{2jk})_{12\times4}$, $(\mu_{3jk})_{12\times4}$ and $(\mu_{4jk})_{12\times4}$ indicate the single-index unascertained measure matrices of scheme 1, scheme 2, scheme 3 and scheme 4 respectively.

Weight(W_i) determination for plan optimization

According to formula (5) and formula (6), the weight vectors of the four programs were determined respectively:

W_1 =(0.0632 0.0957 0.0632 0.127 0.127 0.0632 0.0632 0.0632 0.127 0.0632 0.0809)

W_2 =(0.1172 0.0626 0.0586 0.1172 0.0626 0.0586 0.0586 0.1172 0.1172 0.0897 0.0749 0.0656)

W_3=(0.0587 0.0587 0.1174 0.1174 0.0591 0.0587 0.1174 0.0587 0.1174 0.0604 0.1174 0.0587)

W_4 =(0.0987 0.0846 0.0987 0.0493 0.0859 0.0859 0.0987 0.0987 0.0987 0.0987 0.0754 0.0631 0.0492)

According to the formula (7), the final comprehensive measure of the evaluation vectors were obtained respectively as in Table 4.

The confidence degree is 0.6, based on formula (8), four evaluation grades of deep foundation pit supporting scheme of the comprehensive evaluation results of the uncertainty measure were given. In Table 4, it can be concluded that the results of four optimal deep foundation pit support schemes are “poor, good, general and good“. According to the principle of superiority ranking, the superiority of all schemes is calculated as (1.9603 2.8344 1.8579 2.9928), therefor the superiority ranking is scheme 4 > scheme 2 > scheme 1 > scheme 3.The scheme4 of arch cement soil + type steel drilling pile space combination supporting is the optimal supporting structure. The results are the same as actual supporting structure scheme. And the evaluation results of the grey fuzzy variable decision model in Table 5, were compared and analysed. The optimal results are basically in line with the feasibility.

Tab. 4 - Results of the uncertainty measurement evaluation

Scheme No.	Synthetic uncertainty measure				Discriminate result	Priority ranking
	Excellent	Good	General	Bad		
1	0.127	0.1279	0.3235	0.4216	Bad	1.9603
2	0.2344	0.3874	0.3564	0.0218	Good	2.8344
3	0.0294	0.1805	0.4086	0.3816	General	1.8579
4	0.0038	0.6882	0.2705	0.0372	Good	2.9928

Tab. 5 - Results of grey- fuzzy variable evaluation

Scheme No.	model parameter $\alpha=1$ $p=1$	$\alpha=1$ $p=2$	$\alpha=2$ $p=1$	$\alpha=2$ $p=2$	Average relative membership degree	Sort
1	0.410	0.373	0.327	0.261	0.343	4
2	0.709	0.601	0.856	0.694	0.715	2
3	0.497	0.563	0.493	0.624	0.544	3
4	0.864	0.833	0.976	0.961	0.908	1

Effectiveness analysis

The values Q_i^p is $R=(R_1,R_2,R_3,R_4,R_5)$, and the five indicators respectively correspond to the safety, economy, environment, construction period and quality. Then the $F-DD$ models were calculated, the results can be shown in Table 6.

Tab. 6 - Values of criteria s and the optimal value V_{F-DD}

Variables	Scheme 1	Scheme 2	Scheme 3	Scheme 4
s_1	0.1631	0.2021	0.3044	0.2573
s_2	0.2542	0.1255	0.0871	0
s_3	0.1854	0.0848	0.1263	0.0575
s_4	0.2045	0.2064	0.3034	0
s_5	0.1437	0	0.0956	0.1078
V_{F-DD}	0.9509	0.6188	0.9168	0.4226

From Table 6, it can be concluded that the optimal value V_{F-DD} of scheme 4 is minimum, if the size of s_1, s_3 and s_5 can be adjusted, reaching the state of s_1=0, s_3=0 and s_5=0. Then scheme 4 can achieve the effectiveness of FCA-DEA. In addition, comparing several kinds of supporting scheme to arched soil cement + steel drilling pile space combination support the supporting scheme, it is not possible to be more effective than scheme 4, but it can be helpful to improve some indicators of performance.

In the feasibility research of the support scheme, the application of double row pile retaining + single row deep mixing pile anti-seepage curtain wall supporting scheme (scheme 2) can be clearly shown. Through the above analysis, it is proved that scheme 2 of unascertained measure evaluation has its advantaged compared to scheme 4. So it also has reference to other scheme contains information, analysis of the deficiencies, and to explore whether there can be further improved. According to Table 6, double row piles supporting + single row deep mixing pile cut off curtain wall of a program s_1, s_2, s_3, s_4 and s_5 are not 0. That is to say that the indicators of safety, economy, environment and time limit for a project have not reached effectively compared to FCA-DEA, it needs to be improved. If the security, economic, environmental, duration and other indicators of the scheme 2 are increased

$$(Q_1^p+s_1,Q_2^p+s_2,Q_3^p+s_3,Q_4^p+s_4)=(0.2943,0.6233,0.3747,0.4364)$$

Then, the scheme 2 can achieve the effective state of FCA-DEA.

CONCLUSION

It is vital to choose reasonable supporting scheme for deep foundation pit, the paper used unascertained measurement principle and data envelopment analysis theory to optimize the supporting scheme. The following conclusions can be drawn:

(1) Evaluation of supporting schemes for deep foundation pit is generally subject to a number of evaluation indices to determine in the process of the evaluation indicators of uncertainty, the aspects of safety, environment and quality are considered with using the unascertained measure theory. And the construction of deep foundation pit supporting scheme optimization of unascertained measure evaluation model can be established;

(2) The use of information entropy theory can determine the index weight to avoid subjective random;

(3) The DEA model was used to analyse deep foundation design plans, showing the validity of FCA-DEA in the deep foundation pit.

REFERENCES

[1] R. L. Lu, Q. H. Jiang. Reinforcement Scheme and Numerical Simulation for Sequential Excavation of the Deep Foundation Pit. Applied Mechanics & Materials, 2012, 204-208:359-365.
[2] J.Y. Lin, T.M. Zeng, X.G. WU, .L.M. Zhang. Safety assessment of deep foundation pit engineering based on Extenics. Material Science and Environmental Engineering, 2016: 740-749.
[3] Horkoshi, K. And Randolph, M. F. A Contribution to optimum Design of Pi led Rafts. Geotechnique. 1998, 48(3): 301-317.
[4] Poulos H.G. Pi led Raft Foundation: Design and Application Geotechnique. Geotechnique,2001, 51(2) : 95-113.
[5] R. Li et al., The Technique of Deep Foundation Pit and Pile Foundation Construction, Applied Mechanics and Materials, 2012, 204-208:308-311,
[6] Audun Jøsang. Subjective Logic: A Formalism for Reasoning Under Uncertainty. Springer, Heidelberg, 2016.
[7] David Sundgren and Alexander Karlsson. Uncertainty levels of second-order probability. Polibits, 2013, 48:5-11.
[8] Yang Guoliang, Liu Wenbin, Zheng Haijun. A review of the data envelopment analysis method (DEA). Journal of systems engineering, 2013,(06):840-860.
[9] Cook, W.D., Tone, K., and Zhu, J., Data envelopment analysis: Prior to choosing a model, OMEGA, 2014, 44:1-4.
[10] Park, B., L. Simar and V. Zelenyuk. Categorical data in local maximum likelihood: theory and applications to productivity analysis. Journal of Productivity Analysis. 2015,43(2): 199-214.
[11] Sherman H.D, Zhu J. Analyzing performance in service organizations. Sloan Management Review. 2013, 54(4): 37-42.
[12] Antunes, Ricardo; Gonzalez, Vicente. A Production Model for Construction: A Theoretical Framework. Buildings. 2015,5(1): 209-228.

Article no. 24

THE CIVIL ENGINEERING JOURNAL 2-2019

PRIORITY METERING CONTROL FOR AN URBAN CIRCULAR INTERSECTION

Xinlu Ma[1], Ping Yi[1,2], Vinod Bolla[2]

1. *Chongqing Jiaotong University, Chongqing,400074,China*
2. *The University of Akron, Department of Civil Engineering, United States, pyi@uakron.edu*

ABSTRACT

Circular intersections have been used in transportation systems since the 1900s. Three types of circular intersections have been used in the United States: traffic circles, rotaries and roundabouts. While the use of traffic circles and rotaries in recent decades was found to have resulted in high crash rates, safety issues have been mitigated for roundabouts through the use of improved geometric designs.

Nevertheless, all three types of circular intersections face capacity problems during periods of high traffic volume, resulting in long queues and delays. Signal metering was introduced to reduce long queues and delays on the dominant approaches to circular intersections by stopping the flow of traffic from other approaches. This methodology was found to ease congestion for circular intersections with historically high traffic volumes. However, most signal metering at those intersections employ fixed signal timing, in which the metering rate is not responsive to changes in traffic condition. This study investigates the performance of an adaptive metering system for circular intersections. The system was implemented on a real traffic circle having high and unbalanced volumes. The model was calibrated, and a case study was simulated for peak-hour traffic conditions. Using the PTV VISSIM application programming interface, the algorithm was tested and the performance of the system was compared to the current intersection operation. The results showed that adaptive metering can significantly reduce delays and queues at a traffic circle. This preliminary study can be a useful reference for the development of priority-controlled circular intersections.

KEYWORDS

Metering control, Circular intersection, Simulation, Adaptive control.

INTRODUCTION

Circular intersections are intersections with a circulating roadway where multiple roads intersect, allowing all vehicles to travel in one direction around a central island. Three types of circular intersections are used in the United States: traffic circles, rotaries, and roundabouts. Traffic circles and rotaries were the first circular intersections to be developed, and they were designed with large diameters to enable high-speed merging and weaving of vehicles.

Roundabouts were developed in order to help overcome the safety issues associated with circles and rotaries [1,2]. Roundabouts were first developed in the United Kingdom in 1966 with a priority rule that required approaching vehicles to yield to the circulating traffic [3]. This new rule brought significant improvement in intersection safety, when compared with rotaries and traffic circles [4]. As a result, some traffic circles and rotaries were retrofitted with the same priority rule, while others were modified into roundabouts; however, many circles and rotaries are still in use today due to geometric or budget constraints.

Regardless of the type of circular intersection in use, all have safety issues, and drivers will experience longer delays and queues when traffic flows are high and unbalanced. As a result, signalization came into use to help reduce long queues and delays during peak periods [5,6,7]. Commonly used signal control for circular intersection signalization is based on fixed time control, where a historical flow profile is used to determine a fixed cycle time at fixed locations, either activated by a detector or scheduled according to the time of day. However, these control modes are beneficial only at locations where traffic conditions are predictable [8,9,10,11,12]. When traffic conditions are unpredictable, a more flexible type of traffic control is desirable.

To reduce the impact of high and unbalanced flows, an adaptive metering system for the priority control of circular intersections is explored in this study. This research implements a method for metering an upstream flow when a queue is detected at a downstream approach to the intersection. Unlike fixed signal timing used only at the selected approach, in adaptive metering, all approaches may be metered and controlled. When more than two approaches have high flows, vehicle arrival and waiting time are used as constraints for the selection of the approach to be serviced first. When a metered signal is activated, the queues and arriving demand on that approach is monitored in real time, and the metering may be switched off to avoid excessively long delays based on the updated priority order for service.

In order to investigate the performance of the adaptive metering system at a priority controlled circular intersection, we used the PTV VISSIM application program interphase (API) to build an algorithm to use in the implementation of the system. A traffic circle located in Tallmadge, Ohio, was selected for the analysis, as this intersection has suffered from long queues and delays due to unbalanced flows during rush hour. Peak-hour video data for the intersection was obtained, and the corresponding VISSIM model was built and calibrated to the prevailing traffic conditions observed in the video footage. The adaptive metering system was implemented for peak hour conditions, and the results showed that the delay and queue lengths were reduced significantly.

TALLMADGE CIRCLE

Tallmadge Circle, located in Tallmadge, Ohio, was selected for this study due to its high traffic volumes during peak periods with long queues and delays. Tallmadge Circle is a traffic circle with eight intersecting legs and a one-lane circulating roadway. The approaches are named according to the compass direction of travel away from the circle, as shown in Figure 1. All eight legs of the traffic circle have one-lane entries and one-lane exits. The island inside the circle is occupied by a historic church and low trees that do not block the view of drivers. This intersection is otherwise not connected to any other roads and there are no nearby parking facilities or gas stations. Currently, traffic controlled is made through yield signs, where arriving vehicles on each approach yield to the circulating traffic.

Fig. 1 – Arial image of Tallmadge Circle

The traffic circle in Tallmadge operates without much delay during non-rush periods, when traffic volumes are low. However, as traffic volumes in the approaches increase, the delays increase. Long queues of more than 20 vehicles have been observed on one or more approaches during evening rush hour, when the volumes on the approaches reach the daily maximum. The levels of service (LOS) of the circle during morning and evening rush hours were found to be “C” and “F”, respectively, in a study conducted in 2014 by DMZ Ohio, Inc., for the Akron Metropolitan Area Transportation Studies (AMATS) that was performed to investigate congestion problems at the circle. Data collection for this study was conducted using a video camera mounted at the bottom of a hot air balloon.

The data collected on Tallmadge Circle as part of the AMATS study was converted to hourly volumes, as shown in Table 1. From an operational analysis and crash investigation, it was determined that when gaps in traffic are insufficient to allow vehicles to enter into the circle, rear-end collisions often occur at the intersection. This problem was attributed to drivers’ anxiety/impatience to enter the traffic circle following a long delay. As a result, improving the performance of the circle and reducing delays was recommended as the primary solution.

Tab. 1- Volumes during morning and evening peak hours

AM SCENARIO									
FROM	TO								Total
	North	North-west	West	South-west	South	South-east	East	North-east	
North	0	4	34	55	59	42	25	2	221
Northwest	2	0	4	19	38	38	61	6	168
West	13	4	0	8	34	32	50	13	154
Southwest	53	21	4	0	21	21	32	40	192
South	124	101	57	13	0	32	40	29	396
Southeast	99	84	120	36	8	2	4	13	366
East	27	109	122	32	19	4	0	11	324
Northeast	11	15	80	50	25	6	0	0	187
Total	329	338	421	213	204	177	212	114	2008
PM SCENARIO									
FROM	TO								Total
	North	North-west	West	South-west	South	South-east	East	North-east	
North	0	8	38	36	131	59	33	7	312
Northwest	6	1	16	18	101	75	81	12	310
West	26	4	1	2	72	66	127	39	337
Southwest	63	9	17	0	74	68	122	69	422
South	155	114	108	13	1	23	67	87	568
Southeast	74	66	56	14	18	1	14	35	278
East	62	90	125	39	48	8	2	21	395

Northeast	11	21	91	39	55	18	16	2	253
Total	397	313	452	161	500	318	462	272	2875

MODEL DEVELOPMENT

The VISSIM simulation tool [13] was used as the platform for the analysis in this study. VISSIM is a microscopic simulation tool that can simulate individual driver behaviour and traffic characteristics. VISSIM uses a link-connector to define any type of intersection in its interface, and it provides a high level of detail. Various parameters, including reduced speed areas and conflict areas, are estimated in the model calibration process. The model was first built using Google images to obtain the geometric features of the traffic circle and the approaches, and the traffic volumes associated with the circle and its approaches were used as inputs. The data collection videos cover the peak volumes in both the morning (from 7:00–7:30 AM) and the afternoon (4:00–6:00 PM). Both the morning (AM) and afternoon (PM) conditions were studied.

MODEL CALIBRATION

The VISSIM model was calibrated to ensure that it can accurately reproduce local traffic conditions and vehicle merging behaviour. For this, the travel time for each vehicle at each approach was measured in the video from a fixed starting point to a fixed endpoint. The same starting point and endpoint were selected in the model so that the travel times in each segment would match as closely as possible. Adjustments were made for various parameters in the conflict areas, including front gap, rear gap, visibility and safety distance factor (SFD). Our model included a total of eight conflict areas, one at each approach. Only SFD has a major influence on travel times, as it can reflect the local roadway and environment conditions that influence driver behaviour. Thus, the default SFD value was increased if an approach was found to have longer travel times, and it was decreased if the travel times for an approach were lower than those indicated from the videos. Numerous trials were performed; for each trial, a Student's t-test was conducted to determine if the difference between the actual travel time and the simulated travel time was significant. The AM and PM models were calibrated separately, and the final parameters selected are shown in Table 2.

Tab. 2- Calibrated parameters and t-test results

AM SCENARIO				
Route	Safety Distance Factor	t-test for model and video		Travel time different after calibration?
		t-statistics	P-value	95% confidence level
North – South	2.5	0.66	0.51	No
Northeast – Southwest	1	−0.97	0.337	No
East – West	1.5	0.14	0.889	No
Southeast – West	1.5	0.51	0.613	No
South – North	1.5	−0.57	0.571	No
Southwest – Northeast	1.5	1.06	0.304	No
West – East	1.5	0.58	0.57	No
Northwest – East	1.5	−0.82	0.42	No

PM SCENARIO				
Route	Safety Distance Factor	t-test for model and video		Travel time different after calibration?
		t-statistics	P-value	95% confidence level
North – South	1.6	1.2	0.23	No
Northeast – West	1.3	0.34	0.737	No
East – West	0.9	−0.31	0.755	No
Southeast – North	0.9	−0.63	0.53	No
South – North	0.7	−0.27	0.788	No
Southwest – East	0.5	0.69	0.489	No
West – East	2.1	0.38	0.702	No
Northwest – South	1.2	−1.23	0.24	No

ADAPTIVE METERING CONTROL

Adaptive metering control has been developed to make the metering system more efficient by controlling all approaches and determining the appropriate metering rate (signal durations) based on real-time arrival data. The goal of this method is to improve the performance of the intersection by balancing queues when high flows are present in more than one approach. To achieve this, a C++ program with the required control logic has been developed using detector functions deployed through the API. Two adaptive metering methods with different timing strategies have been implemented for comparison purposes. Both methods control all signals, but the first method adaptively switches off the signal from a metered approach if desired, while the second method uses a fixed red time whenever a metered approach is activated. The methods are discussed in greater detail in the following sections.

Adaptive metering signals based on the average gap

For the method that uses adaptive metering signals based on the average gap (AMS-AG), four detectors are used for each approach to determine available gaps, entry flow rates, and upstream arrival flow rates as well as to detect queues. Table 3 describes the detectors used, and Figure 2 presents a diagram showing three of the eight approaches to Tallmadge Circle, including the locations of detectors on each approach. The small red lines before the entry detectors (E_1, E_2, and E_3) represent traffic signal heads, which are placed at a distance of 50 feet from the entry point to the circular road. The queue detectors for each approach were placed at a distance of 175 feet from the entry point, and the demand detectors were placed at a distance of 400 feet from the entry point.

Tab. 3- Description of detectors

Detector. No.	Detector extension	Purpose
1	E_i	To determine entry flow rate
2	Q_i	To detect queues
3	C_i	To determine gaps in circulating flow
4	D_i	To determine arrival flow rate

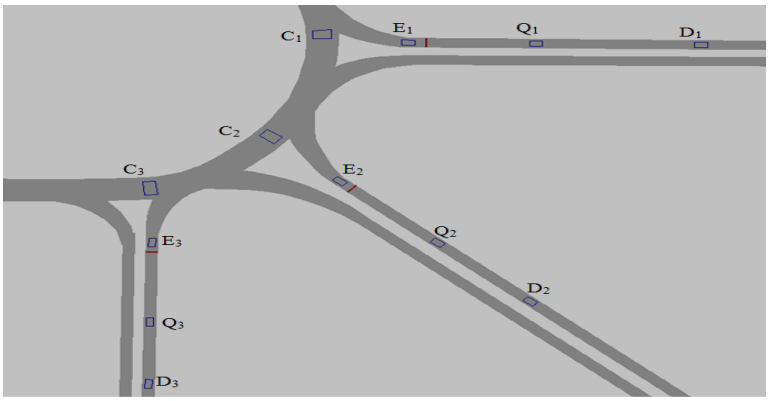

Fig. 2 – Detector setup in the adaptive model

It is difficult to predict the exact number of vehicles that can enter the circulating traffic flow for a given time period. Therefore, vehicle arrival rates, the average gap, and departure rates are used along with queue detectors to prioritize the approaches, decide if an approach should be controlled, and determine when to turn off the signals from metering. In the adaptive metering system, the signals on the metered approaches only use yellow and red lights. No cycle time is used, and the signals become activated or switched off following changes in traffic conditions. A fixed duration of 3 seconds is used for the yellow light, while the duration of the red light depends on the control strategy employed. The stepwise process for this method is explained below:

- A controlling approach is first selected based on the status of the queue detectors on all approaches. If a queue is detected on only one approach, that approach is selected as the controlling one. If a queue is detected in more than one approach, then the one with the highest arrival rate is selected as the controlling approach.
- After selecting the controlling approach, the closest upstream approach (i.e., the one that feeds traffic on the circle to the controlling approach) will be selected as a metered approach, and the signal control will be activated, starting with a yellow light for a duration of 3 seconds, after which it changes to red to prevent any vehicles on that approach from entering the intersection.
- The signal on the metered approach maintains a red light until the queue on the controlling approach is discharged or until a queue is detected on the metered approach. The average gap between vehicles in the circulating flow at the controlling approach is measured. If the gap is found to be less than the safe merging gap obtained from video data at different circulating flow speeds, then the second closest upstream approach to the controlling approach will also be metered. This process continues until no queue is detected on the controlling approach.
- A minimum red time (5~30 seconds) for a signal is used to gradually release vehicles into the intersection from the metered approach if the gaps detected on the circulating flow begin to increase, a strategy that allows limited access. The metering rate increases as conditions continue to improve through shortening the red time on the signal at that approach.
- Once the signal on a metered approach is switched off, a new controlling approach may be selected after 10 seconds. This time lag between each phase allows the system to collect data to aid in selecting the next approach with highest demand.

A flow chart explaining this control logic is shown in Figure 3 below.

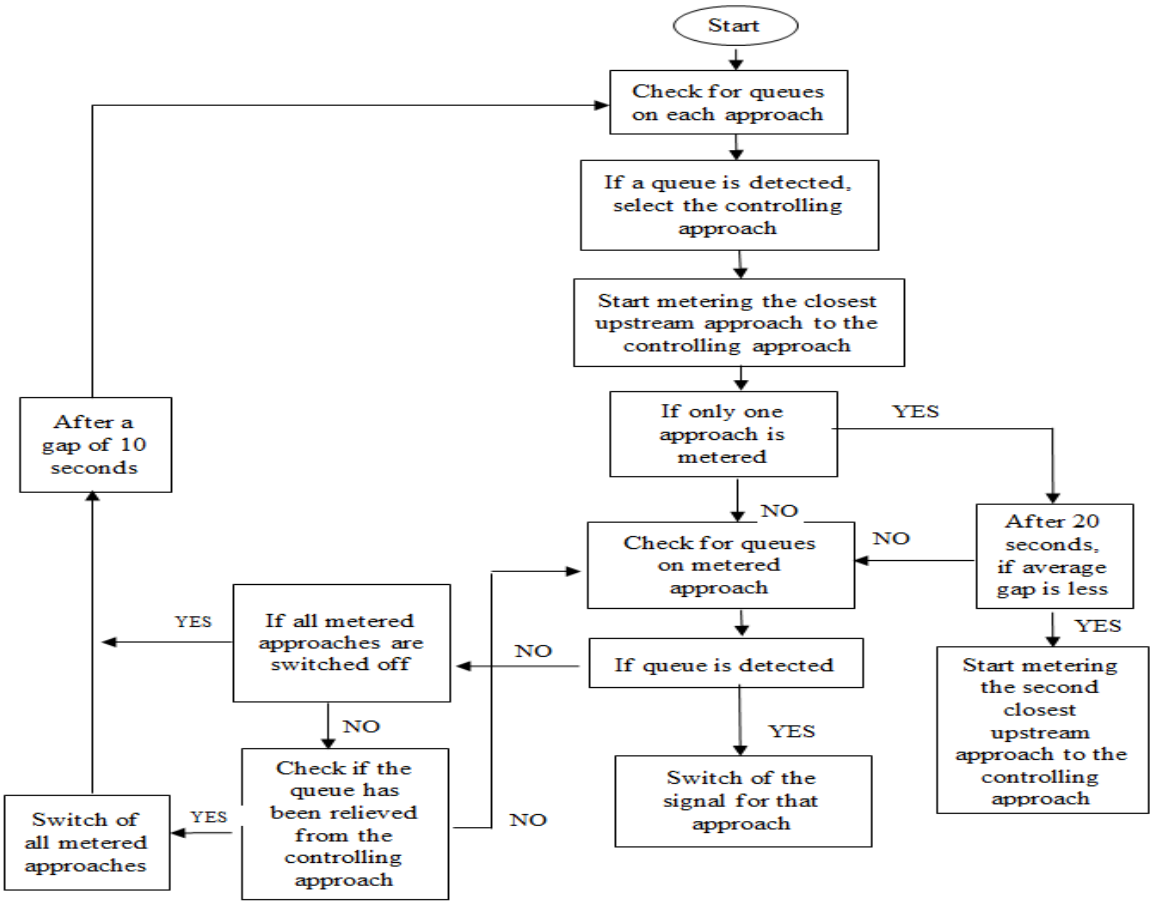

Fig. 3 – Flow chart for AMS-AG method

Adaptive metering signals based on a fixed signal time

A second adaptive metering method, which employs adaptive metering based on a fixed signal time (AMS-FS), has been developed for comparison purposes. This method uses a fixed red light duration for a signal instead of the flexible duration used in the first method. In this method, in order to simplify the implementation, only one approach is used to stop vehicles from entering the circular road, and no gap detectors are used in the circulating flow. The same process is used for selecting a controlling approach as the one used in the AMS-AG method. A yellow light duration of 3 seconds and a red light duration of 25 seconds is used for the signal whenever an approach becomes metered. The 25-second red light duration was selected as the best time interval following an evaluation of all volume conditions. Once the back queue is reduced, the controlling approach is either switched to another approach or is completely eliminated once metering control is no longer needed. A time lag of 25 seconds is used after the completion of a red signal on one controlling approach, before the next controlling approach is selected. Figure 4 shows a flow chart that summarizes the control logic for the AMS-FS method.

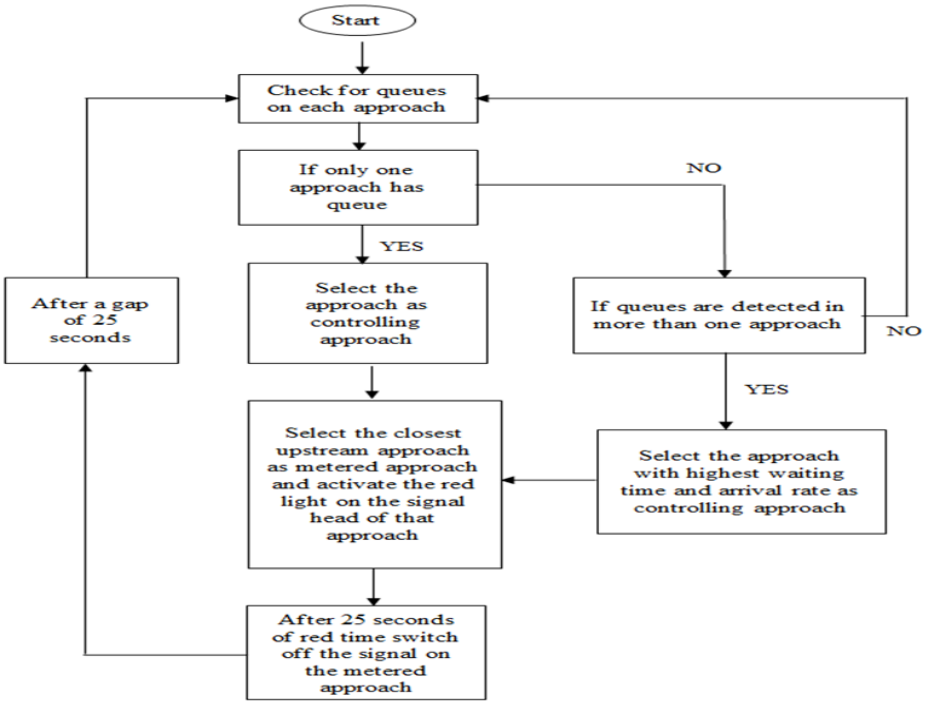

Fig. 4 – Flow chart for AMS-FS method

RESULTS AND ANALYSIS

The results from the two adaptive methods were compared with the current traffic circle operation (i.e., with no signal control). Four scenarios for traffic volume were used in the comparison, including two current AM and PM peak hour conditions and two future traffic conditions that assume a 15% increase over the current peak volumes. The simulations of the future conditions used the same calibration parameters and routing information as the current AM and PM conditions.

In the United States, the Transportation Research Board's *Highway Capacity Manual* [14] recommends comparing the delay for the entire intersection during intersection analysis. In addition, McShane and Roess [15] suggest that the "length of queue at any given time is a useful measure and is critical in determining when a given intersection will begin to impede the discharge from an adjacent upstream intersection". Hence, four measures of effectiveness (MOEs) — the average delay per vehicle, total delay, average queue size, and maximum queue size — were selected in order to compare the performance of the different control scenarios. Six simulation runs were performed for each scenario, and the average for each was used for comparison purposes. A Student's t-test was also conducted to determine if the differences between the adaptive methods and the current (no signal) control are statistically significant. The results for AM, Future AM, PM and Future PM traffic conditions are shown in Tables 4, 5, 6 and 7, respectively.

Tab. 4- Summary of results for AM scenario

Method	AM	% reduction	t-test
	Average delay time per vehicle (s)	Compared with no control	95% significance
AMS-AG	13.59	40.66	YES
AMS-FS	12.5	45.41	YES
No control	22.9	N/A	N/A
Method	Total delay time (h)		95% significance
AMS-AG	7.88	40.71	YES
AMS-FS	7.15	46.20	YES
No control	13.29	N/A	N/A
Method	Average queue length (ft)		95% significance
AMS-AG	10.29	61.02	YES
AMS-FS	8.65	67.23	YES
No control	26.4	N/A	N/A
Method	Maximum queue size (ft)		95% significance
AMS-AG	172.06	38.60	YES
AMS-FS	154.04	40.70	YES
No control	228.73	N/A	N/A

Table 5: Summary of results for Future AM scenario

Method	FUTURE AM	% Reduction	t-test
	Average delay time per vehicle (s)	Compared with no control	95% significance
AMS-AG	38.33	60.98	YES
AMS-FS	35.81	63.55	YES
No control	98.24	N/A	N/A
Method	Total delay time (h)		95% significance
AMS-AG	25.49	60.13	YES
AMS-FS	23.82	62.74	YES
No control	63.93	N/A	N/A

Method	Average queue length (ft)		95% significance
AMS-AG	60.04	71.28	YES
AMS-FS	56.06	73.18	YES
No control	209.06	N/A	N/A
Method	Maximum queue size(ft)		95% significance
AMS-AG	369.88	51.88	YES
AMS-FS	305.92	51.73	YES
No control	520.10	N/A	N/A

It can be seen from the above results that adaptive metering is able to reduce delay and queue length by a large proportion with statistical significance. The results also show that there is little difference in the effectiveness between the two adaptive metering methods in handling the moderate AM traffic.

Tab. 6- Summary of results for PM scenario

Method	PM	% reduction	t-test
	Average delay time per vehicle (s)	Compared with no control	95% significance
AMS-AG	71.9	30.32	YES
AMS-FS	91.17	11.65	NO
No control	103.19	N/A	N/A
Method	Total delay time (h)		95% significance
AMS-AG	58.83	30.69	YES
AMS-FS	74.67	12.03	NO
No control	84.88	N/A	N/A
Method	Average queue length (ft)		95% significance
AMS-AG	159.56	42.17	YES
AMS-FS	182.14	33.99	YES
No control	275.91	N/A	N/A
Method	Maximum queue size (ft)		95% significance
AMS-AG	607.43	37.79	NO
AMS-FS	626.29	27.81	YES
No control	716.27	N/A	N/A

Tab. 7- Summary of results for Future PM scenario

Method	Future PM	% reduction	t-test
	Average delay time per vehicle (s)	Compared with no control	95% significance
AMS-AG	194.01	16.50	YES
AMS-FS	214.8	7.55	NO
No control	232.34	N/A	N/A
Method	Total delay time (h)		95% significance
AMS-AG	176.02	15.38	YES
AMS-FS	193.89	6.79	NO
No control	208.02	N/A	N/A
Method	Average queue length (ft)		95% significance
AMS-AG	560.35	16.19	YES
AMS-FS	549.35	17.84	YES
No control	668.6	N/A	N/A
Method	Maximum queue size (ft)		95% significance
AMS-AG	1132.08	0.62	YES
AMS-FS	1111.58	0.62	YES
No control	1214.10	N/A	N/A

For the PM peak, the results in Tables 6 and 7 show an overall increase in the MOEs due to high traffic volumes and especially in a scenario with a 15% growth over current peak volumes. Nevertheless, a similar cross-the-board reduction in delays and queue lengths is observed after adaptive metering methods are applied. Moreover, the flexible metering rate method is able to outperform the fixed metering rate method due to its policy of allowing metering at multiple intersection approaches at the same time, resulting in a more strict metering control to help maintain smooth traffic circulation within the intersection. During modelling, we also observed that the queue length increased for approaches with a low volume, but the increase in queue length was much smaller when compared to the corresponding decrease in queue length from the high-volume approaches. This indicates that more vehicles were able to enter the intersection when the metering is under adaptive control, demonstrating that the metering is effective in redistributing and reducing the queues for unbalanced flows. The t-tests generally show the difference between adaptive metering (especially the flexible metering rate method) and no metering control is significant; the results would have become significant in all cases if a 90-percent significance level was used.

CONCLUSION

In this study, an adaptive metering system was developed and tested for circular intersections. The method was implemented for a traffic circle with eight legs having an unbalanced flow, where backup queues exceed 600 ft on two or more approaches. The traffic circle simulation was calibrated to the peak hour conditions, and the results of the computer simulation for both adaptive metering methods (flexible metering rate and fixed metering rate) were compared to the data on the current operation of the traffic circle without any signal control.

The modelling results showed that adaptive metering methods can bring significant improvements to the traffic circle in terms of mitigating delays and queues. The decrease in delay is over 30%, and the average queue length is reduced by more than 40% for the highest PM peak hour traffic volume. For the future PM scenario, the gain in delay and queue length control becomes smaller (reduced by approximately 15%). This indicates when traffic volumes are too high, congestion can form on all approaches as a result of queue balancing, thus diminishing the advantage of metering control. Therefore, other traffic management countermeasures, such as arrival demand diversion before reaching the roundabout and geometric improvements at the entrances/exits or addition of a circulation lane, should be used in conjunction with metering control. In summary, for all scenarios tested with existing conditions, the flexible metering rate method is most effective for reducing delays and controlling queues, and it should be further studied and tested in future research efforts. It should be noted that the system and settings of adaptive metering discussed in the paper represents only a basic proposal; if practically implemented in the field, the system would require execution of a multivariable program that is able to address many conditions according to input variables and limitations by technical standards.

ACKNOWLEDGEMENTS

This work is supported by the National Natural Science Foundation of China（61403052）and Chongqing Basic and Frontier Research Project (cstc2016jcyjA0576).

REFERENCES

[1] National Cooperative Highway Research Program, 2010. Roundabouts: An informational guide. NCHRP Report 672 ,Transportation Research Board, Washington D.C., USA

[2] Roundabouts: An Informational Guide, 2000. [cited1.02.2008], Available at http://www.tfhrc.gov/safety/00068.htm.

[3] Russell E. R., Rys M., Luttrell G., 2000. “Modelling Traffic Flows and Conflicts at Roundabouts.” Mac-Blackwell Report. Intersections.

[4] Federal Highway Administration, 2008. Operational Improvements at Traffic Circles, Report no. FHWA-NJ-2008-012: U.S Department of Transportation, Washington, D.C., USA

[5] Jacquemart, G. 1998. Modern Roundabout Practice in the United States. NCHRP Synthesis of Highway Practice 264, Transportation Research Board, Washington, D.C., USA

[6] Deshpande, N., Eadavalli, V. 2011. “Simulation Based Operational Performance of Roundabout with Unbalanced Traffic Volumes.” In Institution of Traffic Engineers, Annual Meeting: Anchorage, Alaska, USA.

[7] Akcelik, R, 2004. “Roundabouts with Unbalanced Flow Patterns.” In Institute of Transportation Engineers, Annual Meeting: Lake Buena Vista, Florida, USA.

[8] Akçelik, R., 2005 “Capacity and Performance Analysis of Roundabout Metering Signals.” In Transportation Research Board National Roundabout Conference: Vail, Colorado, USA.

[9] Toolbox to Evaluate the Impacts of Roundabouts on a Corridor or Roadway Network, 2008,

available from: http://www.lrrb.org/media/reports/200824.pdf.

[10] Rodegerdts, L., Blogg, M., Wemple, E., Myers, E., et al, 2007. “National Cooperative Highway Research Program.” Roundabouts in the United States - NCHRP Report 572, Transportation Research Board, Washington, D.C., USA

[11] Stevens, C.R, 2005. “Signals and Meters at Roundabouts.” In Mid-Continent Transportation Research Symposium: Iowa State University, Ames, Iowa, USA.

[12] Federal Highway Administration, 2004. Traffic Analysis Toolbox Vol. III: Guidelines for Applying Traffic Microsimulation Modelling Software. U.S Department of Transportation, McLean, Virginia, USA.

[13] PTV(2016) VISSIM 9 User Manual, available from: https://edoc.site/vissim-9-manual-pdf-free.html

[14] Highway Capacity Manual, 2010.Transportation Research Board: Washington, D.C.

[15] McShane W.R., Roess R.P., Prass E.S., 1998. *Traffic Engineering*. 2nd ed. Upper Saddle River, New Jersey: Prentice Hall.